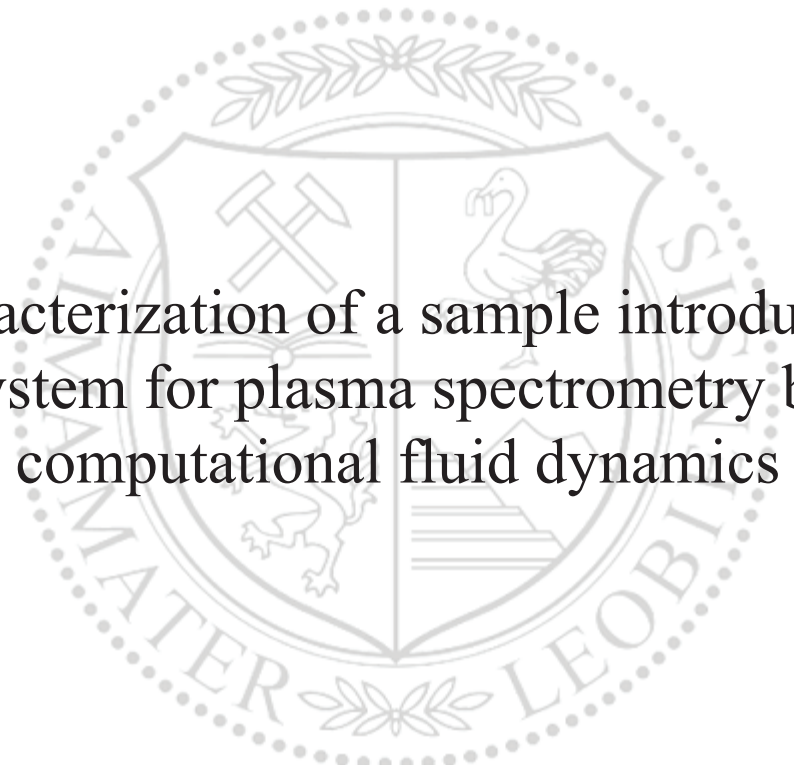




Chair of General and Analytical Chemistry

Doctoral Thesis



Characterization of a sample introduction  
system for plasma spectrometry by  
computational fluid dynamics

Dipl.-Ing. Elke Fasch

May 2024



**EIDESSTÄTLICHE ERKLÄRUNG**

Ich erkläre an Eides statt, dass ich diese Arbeit selbstständig verfasst, andere als die angegebenen Quellen und Hilfsmittel nicht benutzt, den Einsatz von generativen Methoden und Modellen der künstlichen Intelligenz vollständig und wahrheitsgetreu ausgewiesen habe, und mich auch sonst keiner unerlaubten Hilfsmittel bedient habe.

Ich erkläre, dass ich den Satzungsteil „Gute wissenschaftliche Praxis“ der Montanuniversität Leoben gelesen, verstanden und befolgt habe.

Weiters erkläre ich, dass die elektronische und gedruckte Version der eingereichten wissenschaftlichen Abschlussarbeit formal und inhaltlich identisch sind.

Datum 06.05.2024

Unterschrift Verfasser/in  
Elke Fasch

*"The more we learn about the world and the deeper our learning, the more conscious, specific, and articulate will be our knowledge of what we do not know, our knowledge of our ignorance. For this, indeed, is the main source of our ignorance the fact that our knowledge can be only finite, while our ignorance must necessarily be infinite."*

Sir Karl Popper in *Conjectures and Refutations: The Growth of Scientific Knowledge* (1963)

# Abstract

Sample introduction systems play a crucial role in obtaining reliable analytical data. These systems are chosen and refined in accordance with the specifications of the analysis and the kind of sample that will be examined. In mass spectrometry, particularly in inductively coupled plasma mass spectrometry (ICP-MS), spray systems are used to convert liquid samples into fine droplets and introduce them into the plasma, where they are atomized and ionized. Typically, these involve nebulizers used in combination with an appropriate spray chamber. The primary function of the spray chamber is to modify the aerosol generated by the nebulizer by adjusting properties such as droplet size distribution, aerosol concentration, or particle velocity. An ideal sample introduction system should introduce only droplets with a diameter  $< 10 \mu\text{m}$  into the plasma and effectively separate all droplets  $> 10 \mu\text{m}$ . In practice, a significant proportion of useful smaller droplets is lost through contact with the walls [Fasch et al., 2022], [Fasch et al., 2023].

Understanding these processes of aerosol modification, including impact, droplet breakup or coalescence, evaporation, and turbulence effects, requires control of the flow conditions, which is difficult to access empirically. In this thesis, a computational fluid dynamics (CFD) approach is used to investigate the aerosol flow conditions produced by a micro-uptake glass concentric nebulizer in a Scott type spray chamber. Phase Doppler anemometry (PDA), laser diffraction, and particle imaging velocimetry (PIV) are used in experiments to determine the droplet size distribution produced by the nebulizer itself (primary aerosol), the droplet size distribution at the exit of the Scott spray chamber (tertiary aerosol), and velocity distributions [Fasch et al., 2022], [Fasch et al., 2023].

These data are used for the numerical calculations, both as input parameters and for validation of the CFD model. The results provide a representation of the most important transport phenomena in the chamber. The assumption that only a small fraction of the introduced sample reaches the plasma as droplets is confirmed. After varying conditions in the spray chamber, it is also verified that cooling the chamber enhances the efficiency of the sample introduction system by reducing the solvent load on the plasma. Quantitative measurements of analyte transport demonstrate that as the spray temperature increases, the mass of transported solvent increases as well, while the analyte transport efficiency stays almost constant within the investigated temperature range ( $2 \text{ }^\circ\text{C}$  to  $40 \text{ }^\circ\text{C}$ ) [Fasch et al., 2022], [Fasch et al., 2023].

# Kurzfassung

Probeneintragsysteme spielen eine entscheidende Rolle bei der Gewinnung zuverlässiger Analysedaten. Diese Systeme werden je nach Anforderungen der Analyse und der Art der zu analysierenden Probe ausgewählt und optimiert. In der Massenspektrometrie, insbesondere in der Induktiv gekoppelten Plasma-Massenspektrometrie (ICP-MS), werden Sprühsysteme eingesetzt, um flüssige Proben in feine Tröpfchen zu zerstäuben und in das Plasma einzubringen, wo sie atomisiert und ionisiert werden. Gewöhnlich handelt es sich hierbei um Zerstäuber, die in Kombination mit einer geeigneten Sprühkammer verwendet werden. Die Hauptfunktion der Sprühkammer besteht darin, das vom Zerstäuber erzeugte Aerosol hinsichtlich der Tröpfchengrößenverteilung, der Aerosolkonzentration und der Geschwindigkeit der Partikel zu modifizieren. Ein ideales Probeneintragsystem sollte nur Tröpfchen mit einem Durchmesser von  $< 10 \mu\text{m}$  in das Plasma einbringen und alle Tröpfchen  $> 10 \mu\text{m}$  effektiv abscheiden. In der Realität geht jedoch ein erheblicher Anteil der nützlichen kleineren Tröpfchen durch Kontakt mit den Wänden verloren [Fasch et al., 2022], [Fasch et al., 2023].

Um die in der Sprühkammer stattfindenden Prozesse der Aerosolmodifikation – wie Aufprall, Tröpfchenaufbruch bzw. Koaleszenz, Verdampfung – und Turbulenzeffekte zu erfassen, sind Kenntnisse der Strömungsbedingungen unerlässlich, welche experimentell nur schwer zugänglich sind. In dieser Arbeit werden mit Hilfe eines Computational Fluid Dynamics (CFD) – Ansatzes die Strömungsverhältnisse des von einem konzentrischen Mikrozerstäuber aus Glas produzierten Aerosols in einer Scott-Sprühkammer untersucht. Mittels Phasen-Doppler-Anemometrie (PDA), Laserbeugung und Particle Imaging Velocimetry (PIV) werden die vom Zerstäuber erzeugte Tröpfchengrößenverteilung (Primäraerosol), die Tröpfchengrößenverteilung am Auslass der Scott-Sprühkammer (Tertiäraerosol) und die Geschwindigkeitsverteilungen experimentell bestimmt [Fasch et al., 2022], [Fasch et al., 2023].

Diese Daten werden für die numerischen Berechnungen, einerseits als Eingangsparameter und andererseits zur Validierung des CFD-Modells verwendet. Die Ergebnisse liefern eine Darstellung der wichtigsten Transportphänomene in der Kammer und bestätigen die Tatsache, dass im Verhältnis zur eingebrachten Probe nur eine geringe Menge als Tröpfchen das Plasma erreichen kann. Unter Berücksichtigung verschiedener Bedin-

gungen in der Sprühkammer wird auch bestätigt, dass die Kühlung der Kammer die Effizienz des Probeneintragsystems verbessert, indem die Lösungsmittelbeladung des Plasmas verringert wird. Messungen des Analyttransportes zeigen, dass mit zunehmender Temperatur der Sprühkammer die Masse des transportierten Lösungsmittels zunimmt, während die Analyttransporteffizienz in dem untersuchten Temperaturbereich (2 °C bis 40 °C) nahezu unverändert bleibt [Fasch et al., 2022], [Fasch et al., 2023].

# Acknowledgements

This thesis would not have been possible without the guidance and assistance of a number of individuals who, in one way or another, provided their valuable support in the preparation and completion of this study.

I am deeply indebted to my supervisor, Em.O.Univ.-Prof. Dipl.-Ing. Dr.techn. Wolfhard Wegscheider, for providing me with the topic, the resources and the necessary freedom to develop my skills.

Sincere thanks go to Univ.-Prof. Dipl.-Ing. Dr.techn. Thomas Prohaska who acted as an “unofficial-official” mentor and facilitator in the final years of this thesis.

I would like to express my deepest gratitude to Ao.Univ.-Prof. Dipl.-Ing. Dr.techn. Christian Weiß for being my mentor and supporting me with his profound knowledge. In particular, I would like to highlight the measurements he made possible at the Chair of Process Engineering and Environmental Protection. This endeavor would not have been possible without the assistance of Dipl.-Ing. Mario Peysa und Dipl.-Ing. Dr.mont. Jan Eisbacher-Lubensky.

I would like to extend my sincere thanks to Dipl.-Ing. Dr.techn. Hermann Maier who was a more than valuable support in the time of greatest despair, not only in terms of software, but also with his experience in multiphase flows and helpful discussions.

Words cannot express my gratitude to Dipl.-Ing. Dr.techn. Franz Landertsamer who has been by my side since the very beginning of this project and introduced me to the “cunning and pitfalls” of CFD using FIRE.

Many thanks to the company AVL, who made my research work possible by providing the simulation software FIRE™. I am particularly grateful to Dipl.-Ing. Alexander Ruth for his great technical support and for sharing his broad expertise. His enthusiasm for multiphase flows was more than infectious.

Finally, I would like to give special thanks to my husband Michael Markus and my children Paulina and Felix Maximilian for their continuous support when undertaking my research and writing my thesis.

*Dedicated to my father with love*



# Contents

<b>NOMENCLATURE</b>	<b>I</b>
<b>1. INTRODUCTION</b>	<b>1</b>
1.1 MOTIVATION AND SCOPE OF WORK	1
1.2 HISTORY OF INDUCTIVELY COUPLED PLASMA MASS SPECTROMETRY	2
1.3 SUMMARY OF CHAPTERS	4
<b>2. STATE OF THE ART</b>	<b>5</b>
2.1 SAMPLE INTRODUCTION IN ATOMIC SPECTROMETRY	5
2.1.1 <i>Liquid sample introduction</i>	5
2.1.1.1 Pneumatic nebulizers	5
2.1.1.2 Non-pneumatic aerosol generation	7
2.1.1.3 Spray chambers	9
2.1.2 <i>Solid sample introduction</i>	11
2.1.3 <i>Gaseous sample introduction</i>	11
2.2 COMPUTATIONAL FLUID DYNAMICS (CFD)	12
2.2.1 <i>Introduction</i>	12
2.2.2 <i>CFD investigations of sample introduction systems in ICP spectrometry</i>	13
<b>3. PERFORMANCE REQUIREMENTS OF A LIQUID SAMPLE INTRODUCTION SYSTEM TO BE USED WITH AN ICP</b>	<b>15</b>
3.1 GENERAL CONSIDERATIONS	15
3.2 DESOLVATION, VAPORIZATION AND IONIZATION IN THE ICP	16
3.3 ORGANIC SOLVENTS	17
3.4 IDEAL AEROSOL/ SAMPLE INTRODUCTION SYSTEM	18
3.5 PARAMETERS IN AEROSOL DROPLET CHARACTERIZATION	20
3.5.1 <i>Properties of size distributions and mean diameters</i>	20
3.5.2 <i>Span of a droplet size distribution</i>	25
3.5.3 <i>Velocity of droplets and droplet time of arrival</i>	25

---

3.5.4	<i>Volume flux of droplets and aerosol concentration</i>	26
3.5.5	<i>Mass transport rate of solvent</i>	26
3.5.6	<i>Mass transport rate of analyte</i>	26
3.6	AEROSOL MODIFICATION PROCESSES	27
3.7	LIMITATIONS OF CURRENT INSTRUMENTAL SETUPS OF PNEUMATIC NEBULIZERS AND SPRAY CHAMBERS	28
3.8	MODELING OF SAMPLE INTRODUCTION SYSTEMS	29
<b>4.</b>	<b>NUMERICAL SIMULATION</b>	<b>30</b>
4.1	INTRODUCTION	30
4.2	MODELLING OF THE FLOW	31
4.2.1	<i>Governing equations of fluid dynamics</i>	32
4.2.1.1	Conservation principle	32
4.2.1.2	Conservation of mass – continuity equation	36
4.2.1.3	Conservation of momentum	37
4.2.1.4	Conservation of energy	39
4.2.1.5	Species transport	40
4.2.1.6	Generalized form of transport equations	40
4.2.1.7	Ideal gas law	41
4.2.2	<i>Turbulence</i>	42
4.3	MODELING OF THE DISPERSED PHASE	48
4.3.1	<i>Formation of droplets</i>	48
4.3.1.1	Primary breakup	49
4.3.1.2	Secondary breakup	55
4.3.2	<i>Motion of droplets</i>	57
4.3.3	<i>Droplet – turbulence interaction</i>	59
4.3.4	<i>Droplet – wall interaction</i>	60
4.3.5	<i>Droplet – droplet interaction</i>	63
4.3.6	<i>Droplet evaporation</i>	64
4.4	DISCRETIZATION	69
4.5	ACCURACY OF NUMERICAL SOLUTIONS	71

---

4.6	REALIZATION OF NUMERICAL SIMULATION	72
4.6.1	<i>Software</i>	72
4.6.2	<i>Hardware</i>	72
4.6.3	<i>Numerical grid</i>	72
4.6.4	<i>Boundary conditions</i>	74
4.6.5	<i>Numerical model</i>	75
4.6.5.1	Gas flow solver	75
4.6.5.2	Spray	76
4.6.5.3	Wall film	79
4.6.5.4	Thin walls	81
<b>5.</b>	<b>LABORATORY EXPERIMENTS</b>	<b>83</b>
5.1	DROPLET SIZE AND VELOCITY DISTRIBUTION MEASUREMENTS	83
5.1.1	<i>Phase Doppler anemometry (PDA) measurements</i>	83
5.1.2	<i>Particle imaging velocimetry (PIV) measurements</i>	84
5.1.3	<i>Fraunhofer laser diffraction measurements</i>	86
5.1.4	<i>Instruments and equipment</i>	88
5.2	MASS TRANSPORT EFFICIENCY MEASUREMENTS USING THE CONTINUOUS WEIGHING METHOD	89
5.2.1	<i>Specification of the measurand</i>	89
5.2.2	<i>Identifying and analyzing uncertainty sources</i>	93
5.2.3	<i>Quantifying uncertainty components</i>	96
5.2.4	<i>Calculating the combined standard uncertainty</i>	97
5.2.5	<i>Conclusive result</i>	100
5.3	MASS TRANSPORT EFFICIENCY MEASUREMENTS USING THE WASTE COLLECTION METHOD	101
5.3.1	<i>Specification</i>	101
5.3.2	<i>Identifying and analysing uncertainty sources</i>	104
5.3.3	<i>Quantifying uncertainty components</i>	107
5.3.4	<i>Calculating the combined standard uncertainty</i>	109
5.3.5	<i>Conclusive result</i>	112

---

5.4	ANALYTE TRANSPORT EFFICIENCY MEASUREMENTS	113
<b>6.</b>	<b>RESULTS AND DISCUSSION</b>	<b>116</b>
6.1	MASS TRANSPORT EFFICIENCY (MTE)	116
6.1.1	<i>Mass transport efficiency - continuous weighing method</i>	116
6.1.2	<i>Mass transport efficiency – waste collection method</i>	117
6.2	ANALYTE TRANSPORT EFFICIENCY (ATE) – WASTE COLLECTION METHOD	119
6.2.1	<i>Mass transport – vs. analyte transport</i>	119
6.3	DROPLET SIZE AND VELOCITY DISTRIBUTION	126
6.3.1	<i>Spray droplet velocity and size distribution downstream of the nozzle exit in absence of the spray chamber – primary aerosol</i>	126
6.3.2	<i>Spray droplet velocity and size distribution downstream of the spray chamber plasma outlet – tertiary aerosol</i>	136
6.4	NUMERICAL SIMULATION RESULTS	143
6.4.1	<i>Flow field in the Scott spray chamber/ Argon jet</i>	143
6.4.2	<i>Numerical simulation of the droplet phase</i>	150
6.5	CONSIDERATIONS FOR THE OPTIMIZATION OF THE SCOTT-TYPE SPRAY CHAMBER	166
6.5.1	<i>Spray chamber model 1</i>	166
6.5.2	<i>Spray chamber model 2 and spray chamber model 3</i>	168
<b>7.</b>	<b>CONCLUSIVE SUMMARY AND OUTLOOK</b>	<b>171</b>
<b>8.</b>	<b>APPENDICES</b>	<b>173</b>
8.1	APPENDIX A: NUMERICAL SIMULATIONS – FIRE™ V7.3	173
8.1.1	<i>Numerical simulation and boundary conditions</i>	173
8.1.2	<i>Results and discussion</i>	174
8.1.2.1	<i>Scott-type double-pass spray chamber</i>	174
8.2	APPENDIX B: LIST OF FIGURES	181
<b>9.</b>	<b>REFERENCES</b>	<b>186</b>

# Nomenclature

## Latin letters

$\bar{a}$	[m s <sup>-2</sup> ]	acceleration
$A$	[m <sup>2</sup> ]	area, cross sectional area
$A_d$	[m <sup>2</sup> ]	projected area of the particle or droplet in the direction of the relative velocity
$A_j$	[m <sup>2</sup> ]	internal wall faces not in contact with the fluid or the environment
$A_s$	[m <sup>2</sup> ]	droplet surface area
$b$	[g min <sup>-1</sup> ]	slope of a (straight) line
$B_j$	[m <sup>2</sup> ]	internal wall faces in contact either with the fluid or with the environment
$c_p$	[J K <sup>-1</sup> kg <sup>-1</sup> ]	specific heat at constant pressure
$\bar{c}_{p,F}$	[J K <sup>-1</sup> kg <sup>-1</sup> ]	average vapor specific heat in the film
$C_D$	[-]	drag coefficient
CMD	[m]	count median diameter
$\bar{d}$	[m]	mean diameter
$d_{10}$	[m]	count mean diameter
$d_d$	[m]	particle diameter
$d_g$	[m]	geometric mean diameter
$d_i$	[m]	midpoint diameter of the $i$ th group
$d_L$	[m]	diameter of the cylindrical orifice
$d_{lm}$	[m]	length mean diameter
$d_{\bar{m}}$	[m]	diameter of average mass

$d_{mm}$	[m]	mass (volume) mean diameter
$d_{32}$	[m]	surface mean diameter
$d_p$	[m]	particle diameter
$d_{voli}$	[m]	droplet diameter below which the $i$ percentile of the cumulative aerosol volume is found
$D$	[m <sup>2</sup> s <sup>-1</sup> ]	diffusion coefficient
$\bar{D}_g$	[m <sup>2</sup> s <sup>-1</sup> ]	vapor/ air binary diffusion coefficient
$D_i$	[m <sup>2</sup> s <sup>-1</sup> ]	diffusion coefficient of the species $i$
$D_{vm,K}$	[m]	calculated droplet mean diameter using the <i>Kataoka droplet correlation model</i>
$e$	[J]	internal energy
$\vec{f}$		acceleration vector due to external volume forces
$f_{vs}$	[kg m <sup>-2</sup> s <sup>-1</sup> ]	vapor mass flux
$F$	[cm <sup>3</sup> s <sup>-1</sup> cm <sup>-2</sup> ]	volume flux of droplets
$F$	[N]	force
$F$	[-]	relative change of film thickness
$F_D$	[N]	drag force
$F_G$	[N]	gravity
$F_L$	[N]	buoyancy
$g$	[m s <sup>-2</sup> ]	gravitational acceleration
$h$	[J kg <sup>-1</sup> ]	specific enthalpy
$\dot{H}$	[J s <sup>-1</sup> ]	heat transfer
$k$	[W m <sup>-1</sup> K <sup>-1</sup> ]	thermal conductivity
$k$	[m <sup>2</sup> s <sup>-2</sup> ]	turbulent kinetic energy

$\bar{k}_g$	[W m <sup>-1</sup> K <sup>-1</sup> ]	average thermal conductivity of the gas mixture in the film
$K$	[-]	dimensionless droplet velocity (i.e., characteristic parameter to distinguish between different impingement regimes)
$l$	[m]	turbulence length scale
$L$	[J kg <sup>-1</sup> ]	latent heat of evaporation
$L_{BU}$	[m]	unbroken length of the liquid jet
LMD	[m]	length median diameter
$m$	[kg]	mass
$\dot{m}$	[kg s <sup>-1</sup> ]	droplet vaporization rate
$m_d$	[kg]	particle mass
$m_i$	[kg kg <sup>-1</sup> ]	mass fraction
$M_{r,j}$	[kg kmol <sup>-1</sup> ]	molecular weight of the component $j$
MMD	[m]	mass (volume) median diameter
$n$	[-]	number of species
$n_i$	[-]	number of particles in the $i$ th group
$N$	[-]	total number of particles in sample
$N_C$	[-]	total number of classes
$p$	[Pa]	pressure
$\vec{q}$	[W ]	heat flux vector
$q_s$	[W m <sup>-2</sup> ]	heat flux at particle surface
$Q$	[W]	heat
$Q$	[W m <sup>-3</sup> ]	specific heat exchange source

$\dot{Q}$	[W]	convective heat flux
$\dot{Q}_G$	[L min <sup>-1</sup> ]	nebulizer gas flow rate
$\dot{Q}_L$	[g min <sup>-1</sup> ]	liquid uptake rate
$\dot{Q}_{ND}$	[g min <sup>-1</sup> ]	nebulizer drain rate
$\dot{Q}_{SPL}$	[g min <sup>-1</sup> ]	solvent mass transported to the plasma per time unit
$R$	[J K <sup>-1</sup> mol <sup>-1</sup> ]	gas constant
$R_s$	[J K <sup>-1</sup> kg <sup>-1</sup> ]	specific gas constant
$S$		source or sink term
$S_{tot}$	[mg min <sup>-1</sup> ] or [μg s <sup>-1</sup> ]	total mass solvent transport rate
SMD	[m]	surface median diameter
$t$	[s]	time
$T$	[K]	temperature
$T_S$	[K]	spray temperature
$T_W$	[K]	wall temperature
$T^*$	[-]	dimensionless wall temperature
$u_c$		combined standard uncertainty
$u_{d,\perp}$	[m s <sup>-1</sup> ]	droplet velocity normal to the wall
$u_i$	[m s <sup>-1</sup> ]	velocity of the species $i$
$u_r$	[m s <sup>-1</sup> ]	relative velocity
$u_{te}$	[m s <sup>-1</sup> ]	relative velocity of the shear boundary layer
$u(b)$		uncertainty of the slope of the regression line



$U$	[m s <sup>-1</sup> ]	(average) velocity
$U$		expanded uncertainty
$U_L$	[m s <sup>-1</sup> ]	jet exit velocity
$v, \vec{v}$	[m s <sup>-1</sup> ]	velocity, velocity vector
$V$	[m <sup>3</sup> ]	volume
$w$	[-]	mass fraction
$W_{\text{tot}}$	[μg min <sup>-1</sup> ] or [μg s <sup>-1</sup> ]	total mass analyte transport rate
$Y$	[-]	mass fraction
$Y_{\text{vs}}$	[-]	ratio of the vapor content at the surface of the droplet
$Y_{\infty}$	[-]	ratio of the vapor content in the surrounding phase

### Greek letters

$\alpha$	[-]	volume fraction
$\alpha$	[W m <sup>-2</sup> K <sup>-1</sup> ]	convective heat transfer coefficient
$\alpha_c$	[-]	volume fraction of the continuous phase
$\alpha_d$	[-]	volume fraction of the dispersed phase
$\beta$	[K <sup>-1</sup> ]	coefficient of volumetric expansion
$\Gamma$	[-]	diffusion tensor
$\delta$	[m]	film thickness
$\varepsilon$	[m <sup>2</sup> s <sup>-3</sup> ]	turbulent dissipation
$\lambda$	[W m <sup>-1</sup> K <sup>-1</sup> ]	thermal conductivity
$\mu$	[kg m <sup>-1</sup> s <sup>-1</sup> ]	dynamic viscosity

$\mu_c$	[kg m <sup>-1</sup> s <sup>-1</sup> ]	viscosity of the continuous phase
$\mu_t$	[kg m <sup>-1</sup> s <sup>-1</sup> ]	turbulent eddy viscosity
$\xi$	[-]	velocity scale ratio
$\rho$	[kg m <sup>-3</sup> ]	density
$\rho_d$	[kg m <sup>-3</sup> ]	density of the particle
$\rho_c$	[kg m <sup>-3</sup> ]	density of the continuous phase
$\sigma$	[N m <sup>-1</sup> ]	surface tension
$\sigma$		standard deviation
$\Rightarrow$ $\tau$	[-]	stress tensor
$\tau_{ij}$	[-]	viscous part of the stress tensor
$\tau_p$	[s]	particle relaxation time
$\tau_V$	[s]	Stokes relaxation time
$\bar{\phi}$		time-averaged quantity
$\phi'$		fluctuation about a time-averaged quantity
$\Phi$	[-]	dissipation function

### Superscripts and overscore

0	initial state
-	average value
*	modified value

### Subscripts

c	continuous phase
cr	critical

---

d	droplet, dispersed phase
ent	entrainment
ev	evaporation
f	film, wall film
F	film
G	gaseous
<i>i</i>	sequential number, Cartesian coordinates
imp	impingement
IM	Ishii-Mishima
<i>j</i>	sequential number, Cartesian coordinates
L	liquid
M	mass diffusion problem
ND	nebulizer drain
P	particle
R	relative gaseous
Res	residual
s	surface
SH	Schadel-Hanratty
SPL	solvent plasma load
tot	total
turb	turbulence
T	thermal problem
vs	vapor content at the surface of the droplet
W	wall

0	initial state
$\infty$	particle far-field conditions

**Dimensionless quantities**

$B_Y$	mass transfer number
$B_T$	heat transfer number
$Le$	Lewis number
$Nu$	Nusselt number
$Oh$	Ohnesorge number
$Pr$	Prandtl number
$Re$	Reynolds number
$Rn_i$	random number from $[0 < Rn_i < 1]$
$Sh$	Sherwood number
$Sc$	Schmidt number
$St$	Stokes number
$T$	Taylor parameter
$We$	Weber number

**Acronyms**

AES	atomic emission spectrometry
CFD	computational fluid dynamics
CV	control volume
DDM	discrete droplet method
DES	detached eddy simulation

---

DNS	direct numerical simulation
ESI	electrospray ionization
HPLC	high-performance liquid chromatography
ICP	inductively coupled plasma
ID	inner diameter
LES	large eddy simulation
MALDI	matrix-assisted laser desorption/ ionization
MMN	MicroMist nebulizer
MS	mass spectrometry
PDA	phase Doppler anemometry
PIV	particle imaging velocimetry
PN	pneumatic nebulizer
RANS	Reynolds-averaged Navier-Stokes
REE	rare earth elements
SC	spray chamber
SCR	selective catalytic reduction
SI	spark - ignition
SIMPLE	semi-implicit method for pressure-linked equations
TOF	time of flight
USN	ultrasonic nebulizer

# 1. Introduction

## 1.1 Motivation and scope of work

Inductively coupled plasma mass spectrometry (ICP-MS) has been a very powerful, sensitive and robust analytical method in inorganic trace analysis since its introduction in the early 1980s. Since then, there have been important advancements on both the hardware and software. Nevertheless, it must be noted that sample introduction has a substantial influence on the performance of spectroscopic methods and still represents the weakest link in the analytical process. That is why it is often referred to as "the Achilles' heel of atomic spectroscopy" [Browner et al., 1984]. Essentially, systems based on the principles of pneumatic atomization<sup>1</sup> described by Gouy at the end of the 19<sup>th</sup> century are still in use today. Alternatives to the concentric nebulizer have been developed, but almost all nebulizer types have one thing in common: the use of a spray chamber.

The most important method of sample introduction in ICP-MS is the use of a nebulizer and a suitable spray chamber. The primary function of the spray chamber is to prepare the aerosol produced by the nebulizer by adjusting the particle size, particle velocity and aerosol concentration in order to make it suitable for spectroscopic analysis. It must also mitigate the turbulence in the chamber caused by the nebulization process. An ideal sample introduction system should only introduce droplets with a diameter  $< 10 \mu\text{m}$  into the plasma, while all droplets  $> 10 \mu\text{m}$  are efficiently separated. In practice, a significant proportion of the valuable smaller droplets are usually lost through contact with the spray chamber walls [Fasch et al., 2023], [Fasch et al., 2022].

Understanding the processes of aerosol modification in the spray chamber (i.e., impacts, droplet breakup and coalescence, evaporation, decay of turbulence etc.), requires knowledge of the flow dynamics which is difficult to access experimentally. This thesis uses computational fluid dynamics (CFD) to study the aerosol flow in a Scott-type spray chamber fitted with a micro-uptake glass concentric nebulizer for the first time. Phase Doppler anemometry (PDA), laser diffraction, and particle imaging velocimetry (PIV)

---

<sup>1</sup> Note: Atomization is here referred to the process of producing an aerosol, which is a colloidal suspension of fine solid particles or liquid droplets in a gas.

measurements are used to experimentally determine the properties of the nebulizer, including the aerosol size distribution generated by the nebulizer itself (primary aerosols), the aerosol size distribution at the outlet of the Scott spray chamber (tertiary aerosols), and velocity distributions. These data are used for the numerical approach, both as input parameters and for validation of the CFD model. The results provide a representation of the most important transport phenomena taking place inside the spray chamber. [Fasch et al., 2023], [Fasch et al., 2022].

## 1.2 History of inductively coupled plasma mass spectrometry

Inductively coupled plasma (ICP) mass spectrometry (MS) is an analytical technique that studies systems that cause the formation of gaseous ions and sorts them based on their mass-to-charge ratios and relative abundances.

The origins of mass spectrometry go back to physical and chemical investigations of gas discharges in the middle of the 19<sup>th</sup> century. Eugen Goldstein observed the so-called “canal rays” in gas discharges under low pressure. Wilhelm Wien could deflect and separate these positively charged rays by strong magnetic fields according to their mass-to-charge ratio. In 1913, Sir Joseph John Thomson presented his “parabola mass spectrograph” within the Bakerian Lecture: “rays of positive electricity” of the Royal Society of London. Based on the work of Wien he could demonstrate the isotopic nature of elements by directing a stream of ionized neon through a magnetic and electric field. The positive rays were deflected and impacted on a photographic plate placed perpendicular to the axis of the stream. By observing two different parabolas of deflection on the plate, Thomson concluded that neon gas must consist of atoms of two different masses (neon-20 and neon-22) [Thomson, 1913a], [Nature Milestones in Mass Spectrometry, 2015].

Although the history of mass spectrometry has involved many scientists, Thomson must be credited with the invention of the first mass spectrograph and with the publication of the first mass spectrum. Since then he has been considered as “father of mass spectrometry”. Also in 1913, he published a book with the title “Rays of Positive Electricity and their Application to Chemical Analyses”. In the preface he wrote in a visionary manner: “... *one of the main reasons for writing this book was the hope that it might induce others, and*

*especially chemists, to try this method of analysis. I feel sure that there are many problems in chemistry, which could be solved with far greater ease by this than by any other method. The method is surprisingly sensitive – more so even than that of Spectrum Analysis, requires an infinitesimal amount of material, and does not require this to be specifically purified; the technique is not difficult if appliances for producing high vacua are available. ...”* [Thomson, 1913b].

In 1919 Thomson’s student Francis William Aston reported on his first mass spectrometer. He used electromagnetic focusing technique and was able to identify isotopes of chlorine, bromine and krypton among others. Almost at the same time (1918), Arthur Jeffrey Dempster designed the first modern mass spectrometer that became the basis of later commercially developed devices [Mahrer et al., 2015].

The next decades were affected by the development of new ionization techniques like electrospray ionization or matrix-assisted laser desorption/ ionization (MALDI) and of mass spectrometer design, in particular the “time of flight” (TOF) mass analyzer, quadrupole mass filters, and tandem mass spectrometry (MS/MS) setup, respectively. Coupling chromatographic separation techniques with mass spectrometry made mass spectrometry not only a well-established tool in chemical research but also in the biological area.

In 1961, Thomas Reed invented the inductively coupled plasma (ICP) torch that could produce an electrode-free plasma at atmospheric pressures by inductively heating the plasma gas with a radiofrequency coil. It took another two decades that Alan Gray, together with researchers from the Ames Laboratory in Iowa, in particular Robert Samuel Houk and Velmer Fassel, connected the ICP torch to a mass spectrometer, which led to a real revolution in elemental and isotope analysis techniques. From now on, it was possible to cleanly atomize and ionize a sample to produce singly charged ions [Nature Milestones in Mass Spectrometry, 2015].

Scientific-instrument manufacturing companies like SCIEX and VG Isotopes realized immediately the enormous potential of this new technology. The first commercially available instrument was launched in 1983 (Sciex ELAN 250). More than 90% of the elements in the periodic table with detection limits ranging from 0.5 to 10 parts per billion (ppb) could be analyzed. Today, ICP-MS is a highly accurate and powerful analytical tool with a large dynamic range up to 12 orders of magnitude capable of analyzing a great number of elements at very low trace amounts from parts per trillion (ppt) to parts per million (ppm) [Nature Milestones in Mass Spectrometry, 2015], [Ramos, 2008].



## 1.3 Summary of chapters

Chapter 1 explains the purpose of this thesis and provides a brief introduction to the history of inductively coupled plasma mass spectrometry.

In chapter 2, general aspects of sample introduction in atomic spectrometry are summarized concerning the sample form and instrumental equipment. Moreover, it includes an overview of computational fluid dynamic approaches for investigating sample introduction systems in ICP spectrometry.

Chapter 3 focuses on the performance requirements of liquid sample introduction systems and the phenomenology of aerosol modification processes.

The equations and models required for the numerical calculation of both continuous and dispersed flow in a spray chamber are provided in chapter 4. In addition, the numerical model describing the flow conditions in the investigated nebulizer - spray chamber system is presented in detail.

The measurements required experimentally for the validation of the numerical model are discussed in chapter 5. It describes the methods used for droplet sizing and the investigation of mass and analyte transport.

Chapter 6 deals with the results of the experimental measurements and numerical calculations. Furthermore, it presents the validation of the model by real spray measurements and laboratory experiments.

Finally, chapter 7 offers a conclusion and an outlook of the present work.

## 2. State of the art

### 2.1 Sample introduction in atomic spectrometry

The selection of the adequate sample introduction system primarily depends on the physical state (liquid, solid or gaseous) of the sample. Furthermore, it must be considered whether the sample quantity is limited, whether discrete or continuous sample introduction techniques are to be used or whether there are special requirements regarding matrix components, speciation information or the number of analyses per unit of time.

The following is an overview of the various sample introduction techniques, without claiming to cover them completely.

#### 2.1.1 Liquid sample introduction

The vast majority of samples in atomic spectrometry are in the form of solutions. Nebulization is the necessary step to convert the liquid into a fine spray (also known as atomization). It should be noted that an ICP can typically handle about 20  $\mu\text{L min}^{-1}$  of water accompanied by an equivalent vapor flow without compromising robustness or even extinguishing the ICP discharge [Sharp, 1988b], [Long et al., 1988], [Montaser, 1998], [Maestre et al., 2002], [Bings et al., 2014]. In most cases, the use of a spray chamber improves the properties of the aerosol, unfortunately at the expense of the sample and analyte transfer rate.

##### 2.1.1.1 Pneumatic nebulizers

The nebulizers most commonly used in ICP-MS are based on the concept of pneumatic nebulization, first introduced for analytical purposes by Gouy in 1879. The solution is dispersed into a fine aerosol, with a fast-moving gas providing the kinetic energy required. Aerosol formation by nebulization usually occurs through a filmwise breakup mechanism [Montaser, 1998 (p. 115)], [Bings et al., 2014] (see also 4.3.1).

Three main groups of pneumatic nebulizers can be identified: (i) the concentric, (ii) the crossflow and (iii) the Babington nebulizer. Detailed descriptions of the operating princi-

ples can be found, for example, in the comprehensive reports by [Sharp, 1988a], [Sneddon, 1990], [Montaser, 1998], [Todoli et al., 2008], [Bings et al., 2014]. Concentric nebulizers are more frequently used in ICP spectrometry than those with cross-flow design because there is no liquid or gas capillary to adjust. Some pneumatic nebulizer designs are shown in *Figure 2-1*.

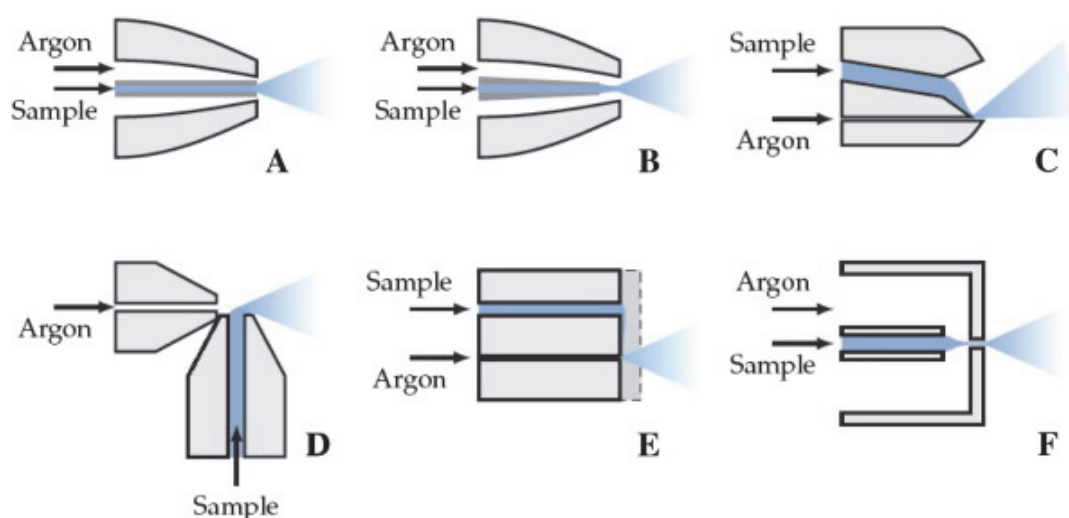


*Figure 2-1* Various design principles of pneumatic nebulizers. A: conventional concentric nebulizer, B: concentric nebulizer with recessed capillary, C: parallel-path nebulizer (also referred to Burgener nebulizer), D: cross-flow nebulizer, E: V-groove nebulizer, F: flow-focussing/blurring nebulizer. Reproduced from [Bings et al., 2014] by courtesy of Elsevier.

For the analysis of microsamples or low flow applications it is necessary to reduce the liquid flow rate to 10 - 300  $\mu\text{L min}^{-1}$ . The use of conventional pneumatic nebulizers, which operate at typical sample flow rates of 0.5 - 2  $\text{mL min}^{-1}$ , results in a dramatic loss of sensitivity of the analytical signal. Thus, many pneumatic micronebulizers have been developed to operate at extremely low sample consumption rates. One of them, which was also used in this thesis, is the MicroMist nebulizer (MMN) [Todoli et al., 2008].

### MicroMist nebulizer (MMN)

The MMN is a micro-uptake glass concentric nebulizer (see *Figure 2-1 B* and *Figure 2-2*) in which the liquid capillary is recessed with respect to the nebulizer tip. Therefore, it is able to handle solutions with high salt content without clogging the nebulizer tip.

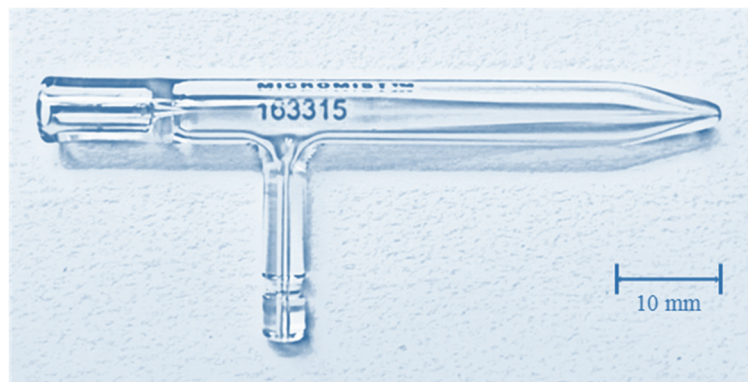


*Figure 2-2* Micro Mist nebulizer (Glass Expansion, Australia; source: E. Fasch); see also *Figure 2-1 B*.

The MicroMist nebulizer is also more robust compared to other glass micronebulizers, as the outer wall of the inner capillary consists of a conical, ground glass piece. However, it should be noted that the MMN also suffers from dimensional irreproducibility from nebulizer-to-nebulizer [Todoli et al., 2006], [Todoli et al., 2008]. This might be a possible source of uncertainty, which can have also an influence on the results provided in this thesis.

#### 2.1.1.2 Non-pneumatic aerosol generation

In contrast to pneumatic nebulization, the droplets are generated by (i) ultrasonic, (ii) mechanical, (iii) thermal or (iv) electrostatic interactions.

- (i) Ultrasonic nebulizers (USN) incorporate a piezoelectric transducer driven by an ultrasonic generator at high frequencies (typically 0.2 - 10 MHz) to convert the liquid to an aerosol. Unlike pneumatic nebulization the aerosol is generated independently of the gas flow. Even though in some cases improved detection capability and nebulization efficiency can be achieved with USNs as compared to pneumatic nebulizers, disadvantages including longer analysis time, poorer precision and higher costs must be accepted. A major drawback is the high liquid load into

the ICP and as a consequence a heating/ cooling device is required. Therefore, the usage of a desolvation membrane is advisable. [Montaser, 1998 (p. 128)].

- (ii) Mechanical droplet formation can be achieved either by active movement of the sample capillary, *e.g.*, by a bimorph transducer, or, as in Wang's oscillating capillary nebulizer, by passive movement of a long, slackly capillary. In the latter, the motion is caused by transverse and longitudinal vibrations induced by a gas flow within a flowing carrier gas stream. Active capillary movement produces monodisperse droplets at a frequency that equals the oscillating frequency of the capillary [Bings et al., 2014].
- (iii) Thermal droplet generation can be obtained by conventional thermospray and microwave-assisted nebulization. Amirav et al. showed that thermospray could be applied for the in situ formation of highly monodisperse nanoparticles [Bings et al., 2014].
- (iv) The electrospray ionization (ESI) technique is widely applied in molecular/ organic mass spectrometry. ESI has been adapted by Brennan et al. to a heat-assisted argon electrospray interface suitable for ICP-AES and ICP-MS applications. With the Ar-ESI interface liquid flow rates in the range of 2 – 4  $\mu\text{L min}^{-1}$  become manageable, which is important when hyphenating sample introduction to miniaturized ionization sources [Bings et al., 2014].

### 2.1.1.3 Spray chambers

Most pneumatic nebulizers have one thing in common: they require a spray chamber, as pneumatically generated aerosols have properties (e.g., droplet size, droplet velocity or aerosol concentration) that make it impossible to introduce them directly into the plasma (exception: direct injection nebulizer – plugged into the plasma torch without a spray chamber). Therefore, when investigating aerosol characteristics, it is always prudent to consider the nebulizer/ spray chamber combination rather than the nebulizer alone (more details about the performance requirements of a liquid sample introduction system to be used with an ICP see chapter 3). The most basic spray chambers are single pass chambers, also called cylindrical or direct spray chambers, which are simple in design. The aerosol is transported directly through the chamber into the plasma.

A comprehensive overview of various more advanced spray chamber designs and their characteristics is given by e.g. Todoli et al. [Todoli et al., 2008]. The two most important designs are described shortly hereafter.

#### Scott-type double-pass spray chamber

In ICP spectrometry this type of spray chamber has been the most widely used for many years since it was first described for this purpose by Scott et al. [Scott et al, 1974]. Commercially available ICP systems are still equipped with this old chamber design today.



Figure 2-3 Scott spray chamber (Agilent Technologies, USA; source: E. Fasch).

The Scott chamber is a dual-tube aerosol chamber, which modulates the spray in terms of droplet size, droplet velocity, aerosol concentration and reduces the turbulence within

the inner tube of the chamber by flow reversal. Scott chambers are effective in eliminating coarse droplets, but suffer from other various drawbacks, such as high dead volume, memory effects, and thus long equilibration and wash-out times. The spray chamber can be equipped with a cooling/ heating system usually using a water jacket. [Todoli et al., 2008], [Montaser, 1998].

### **Cyclonic type spray chamber**

In cyclonic spray chambers, the aerosol is introduced through a tangential inlet in the cylindrical part of the chamber. After following a downward spiral motion near the spray chamber walls to the bottom of the chamber, the aerosol changes direction and moves in an inner spiral trajectory to the top of the chamber.



*Figure 2-4 Cyclonic spray chamber (Agilent Technologies, USA; source: E. Fasch).*

It is more likely that this chamber acts as an impact wall chamber where most of the large droplets are removed and leave the chamber via the drain at the bottom. In general it should be noted that although cyclonic spray chambers can effectively eliminate large droplets, they are not suitable for transporting small droplets. The position of the nebulizer also affects the quality of the signal. Nevertheless, they are widely used in practice due to their low dead volume, fast wash-out and equilibration times and good sensitivities. The spray chamber can be equipped with a cooling/ heating system usually using Peltier cooling. [Todoli et al., 2008], [Montaser, 1998].

### **2.1.2 Solid sample introduction**

The main advantages of solid sample introduction over liquid sample introduction are: sample preparation time is reduced, no molecular ion spectral interferences occur since no solvents are present, and spatially resolved information about the sample can be gained. However, the unavailability of suitable calibration standards often limits accurate analytical feasibility.

Various techniques have been developed for transferring solid samples into the plasma. These methods include direct insertion devices, but in addition, aerosols or vapors can be generated from the solid sample using arc and spark ablation, electrothermal vaporization, or laser ablation techniques and are directly transported into the ICP [Montaser, 1998].

### **2.1.3 Gaseous sample introduction**

Gaseous sample introduction is the simplest method to introduce the sample into the ICP. It offers many advantages over liquid sample introduction, such as a transport efficiency of nearly 100 %, which helps to improve the analytical figures of merit in respect of the determination of trace and ultratrace levels of specific elements. The disadvantage is that most samples do not present themselves in gaseous form and many solid samples are very difficult to convert to the gaseous state. Sample handling could also be more difficult (e.g., sample storage is not easy, and it is necessary to ensure that no samples are lost by using leak-proof devices).

The main gaseous sample introduction methods include direct introduction, hydride generation, and chromatography techniques. Detailed descriptions can be found, e.g. in the comprehensive reports by [Sneddon, 1990], [Montaser, 1998].



## 2.2 Computational fluid dynamics (CFD)

### 2.2.1 Introduction

Computational Fluid Dynamics generally refers to the numerical solution of the governing equations for the description of flows, heat transfer or chemical reactions using computational methods. From the early beginnings in the 1950's CFD has grown to become an indispensable tool in almost every branch of fluid dynamics. Compared to other methods of fluid mechanics, such as experimental and analytical methods, CFD is a young discipline that gained industrial importance in the late 1970's – early 1980's with the development of the first general purpose commercial CFD codes. Before that, CFD was mainly used in specialized laboratories and university research departments working in aerospace and nuclear industries. It has always been closely linked to the development of efficient numerical integration methods for partial differential equations, mathematical-physical models for increasingly complex turbulent flow processes and the development of powerful digital computing systems. With the rapid increase in computer power and reduction in cost, it did not take long for CFD codes to proliferate and CFD applications to spread into almost every industrial sector. Nowadays, CFD is an integral part of the engineering design and analysis process for many companies and research organizations. CFD offers the ability to accurately predict the performance of new designs or processes before they are ever manufactured or implemented. It significantly reduces design and development time, provides detailed information otherwise not available from experiments and quickly simulates a wide range of flow conditions [Schönung, 1990], [Laurien et al., 2011], [Wendt, 1992 and 1996], [Ferziger et al, 2002].

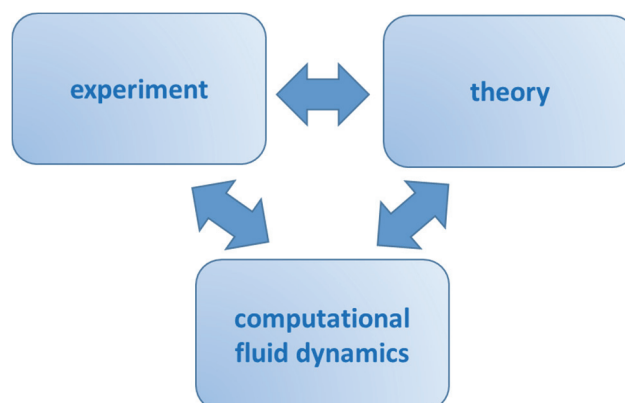


Figure 2-5 Relationship between experiment and theory – the role of CFD.

The role of computational fluid dynamics has become so fundamental that it can be considered as “third dimension” in modern fluid dynamics in addition to the classical cases of pure experiment and pure theory. This relationship is shown in *Figure 2-5* [Wendt, 1992 and 1996].

### **2.2.2 CFD investigations of sample introduction systems in ICP spectrometry**

For the first time Schaldach et al. simulated the aerosol transport in a cyclone chamber by means of computational fluid dynamics [Schaldach et al., 1999 and 2002b]. The numerical results for the argon flow confirmed the fact that a cyclone spray chamber for plasma spectrochemistry works primarily like an impact chamber through flow-line interception of the larger particles on the normal surfaces, coupled with a recirculatory turbulent deposition on the tangential surfaces [Sharp, 1988b] and not like a typical cyclone used in process engineering.

In a further publication the effect of flow spoilers was modeled [Schaldach et al., 2003a]. From these results it was concluded that the position of the spoiler had a critical influence on the performance of the chamber. Under micro-flow conditions, the optimized design with three spoilers gave the best results with regard to mass transport efficiency and wash-out time.

In reference [Kollau, 1999] a first computational parameter study of the flow situation in a Scott-type double-pass spray chamber was published. By varying parameters like spray angle, density of the introduced liquid, droplet size distribution of the primary aerosol and by focusing only on monodisperse droplets it was found that the most important parameters influencing chamber performance were nebulizer atomization and fluid density.

Schaldach et al. predicted the characteristics and the analytical performance of a Scott-type spray chamber for ICP-AES equipped with a Meinhard nebulizer in reference [Schaldach et al., 2002a]. A sample uptake rate of  $1.3 \text{ mL min}^{-1}$  and a gas flow rate of  $0.5 \text{ L min}^{-1}$  were used for the calculations. The time resolved mass flow rate at the outlet of the chamber obtained from the simulation showed a good agreement with the shape of the analytical signal.

Optimization of the geometry of a Scott chamber with the aid of computer simulation and an evolutionary strategy indicated that shorter chambers had better characteristics [Schaldach et al., 2000 and 2003b]. Three geometrical parameters were chosen for optimization, i.e., the total length of the chamber, the length of the inner tube and the diameter of the inner tube. As result, the new chamber was significantly shorter, the distance between the inner tube and the dome at the end of the chamber had been reduced, and the distance between the inner and the outer tube was enlarged. The chamber with the geometry predicted to give the best results was manufactured by a glassblower and tested on an ICP-AES instrument. The new chamber showed an experimentally obtained transport efficiency of 4.9 %, which is 2.3 times higher than the value of the original chamber. Compared with the longer chambers the wash-out time was approximately 3.5 times better [Schaldach et al., 2000 and 2003b].

Computer simulations of spray chambers for dry aerosol transport were also applied to improve the analytical figures of merit in laser ablation ICP-MS. Detailed descriptions can be found, for example, in the reports by [Koch et al., 2004], [Bleiner et al., 2007], [Autrique et al., 2008], [Van Malderen et al., 2016], [Becker, 2022]. Becker et al. stated that notable progress has been made in cell design. However, the focus of CFD has shifted to visualization and understanding of the flow field properties of the laser ablation cell, rather than systematic optimization of its design as originally proposed [Becker, 2022].

### 3. Performance Requirements of a liquid sample introduction system to be used with an ICP

#### 3.1 General considerations

Liquid sample introduction into plasmas usually involves the conversion of the sample into an aerosol. Due to the polydispersity of the aerosol droplets, it is advisable to reduce the fraction of large droplets in order to improve the quality of the aerosol and thus the analytical signal. In most cases, a common sample introduction system typically consists of a nebulizer that generates the fine spray of droplets and a spray chamber that modifies these droplets accordingly. Droplets entering the plasma undergo various processes:

- desolvation: process of heating droplets to evaporate solvent to form solid particles
- volatilization: process of converting solid particles into gas phase
- dissociation: process of breaking-up gaseous molecules into atoms
- ionization: process of charging atoms
- excitation: process of exciting both atoms and ions

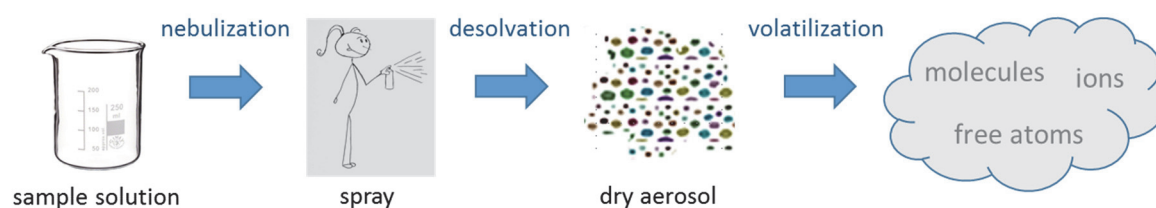


Figure 3-1 Processes when droplets enter the plasma (desolvation-volatilization-atomization).

Ideally, desolvation and volatilization processes should proceed as completely as possible. However, this assumes that due to the poor thermal conductivity of argon used as transport and plasma gas, the residence time of the droplets in the plasma is long enough for heat transfer from the plasma to the droplets to take place. The interaction time of the

droplets with the plasma is approximately in the range of 2 - 3 ms [Montaser, 1998 (p. 4)]. In addition, the liquid flow rate, the carrier gas flow rate and both the velocity and the size distribution of the droplets are of great importance [Todoli et al., 2008], [Nelms, 2005], [Bings et al., 2014].

### **3.2 Desolvation, vaporization and ionization in the ICP**

The sample is delivered into the central channel gas flow of the plasma. In most cases when pneumatic nebulization techniques are used, the aerosol may still contain small droplets of liquid. These droplets have to be dried to form solid particles and afterwards vaporized in order to subsequently dissociate into vapor phase compounds. The time-scale for the processes mentioned is in the range of several milliseconds. Once atomized the sample particles undergo excitation and ionization, which are significantly faster processes. Compared to the total population of atoms in the plasma, the proportion of atoms that can be assigned to the sample is only  $10^{-6}$  or less [Jarvis et al., 1992 (p. 14)]. The HF power used to generate an inductively coupled plasma is in the order of kilowatts and causes kinetic gas temperatures in the central channel ranging between 4000 and 7000 K. As a consequence of the skin effect energy has to diffuse from the periphery to the plasma central channel to provide the energy necessary for desolvation and vaporization. However, the energy required is relatively low (less than 100 W) in relation to the total applied power (forward power) of 1000 W [Bates et al., 1990], [Olesik, 1997], [Todoli et al., 2008]. As a rule of thumb, earlier studies suggest that droplets should be  $\sim 8 - 10 \mu\text{m}$  or less in diameter in order to be fully desolvated and atomized in the plasma [Houk et al., 1988], [Todoli et al., 2008], [Olsen et al., 1983]. Otherwise, incompletely desolvated droplets lead to local plasma cooling effects, reduced sensitivity and elevated noise levels [Olesik et al., 1991], [Hobbs et al., 1993], [Olesik, 1997], [Horner et al., 1998]. As noted previously, the energy available in the central plasma channel is relatively low. For this reason, only a limited amount of aerosol may be introduced to ensure complete desolvation and evaporation. Water as a solvent can play a useful role: on the one hand, plasma energy has to be expended for the solvent decomposition process, on the other hand, the dissociated products (i.e., molecular hydrogen and oxygen) help to locally increase thermal conductivity and heat transfer. Regarding aqueous solutions, it is reported

that the total amount of aerosol should be in the range of 20 - 40 mg min<sup>-1</sup>. [Tang et al., 1986], [Horner et al., 1998], [Todoli et al., 2008].

### 3.3 Organic solvents

The vast majority of samples analyzed with ICP techniques enter the plasma as aqueous, frequently acidic solutions. In some cases, organic solutions may be preferred, for example, when solvent extraction is used in sample pretreatment or when high-performance liquid chromatography (HPLC) uses the ICP spectrometer as a detector. In addition, organic sample matrices such as mineral oil products or highly viscous samples usually have to be analyzed in the presence of organic solvents. Unlike aqueous solutions, whose properties are only slightly altered by the addition of acids, the chemical nature and physical properties must always be taken into account when using organic solvents. Even low concentrations of organic solvents (< 2 % v/v) in water can affect the ICP signal [Olesik et al., 1990], [Todoli et al., 2008 (p. 11)].

The most relevant physical properties of a solvent that cause changes in the pneumatic aerosol formation process are as follows:

- *solution viscosity*
- *surface tension*

Thus, when organic solvents with a lower viscosity and higher surface tension as compared to water are used, a finer primary aerosol is generated in the pneumatic nebulization process. Commonly used solvents such as methanol, ethanol or acetone cause an increase in the relative volatility of the solution, which leads to both an increased aerosol transport towards the plasma and an increased solvent evaporation rate. It should be taken into consideration that excessive organic plasma loading could have devastating effects by degrading the thermal properties of the plasma and even leading to its extinction. Another detrimental effect of using organic solvents is the formation of carbon, which is often deposited on the surfaces of the cones and injector. Spectral interferences caused by carbon species can also have serious effects, especially when using the ICP-MS technique. Reducing the solvent mass delivered to the plasma can be achieved by cooling the spray chamber, reducing the solution uptake and carrier gas flow rate, mixing

the organic solvent with water, or using desolvation systems [Todoli et al., 2008], [Montaser, 1998 (p. 368)], [Montaser et al., 1992 (p. 707)], [Boorn et al., 1980], [Boorn et al., 1982], [Kreuning et al., 1989], [Wiederin et al., 1990].

### 3.4 Ideal aerosol/ sample introduction system

An ideal aerosol passing through the plasma would not alter the fundamental properties of the ICP or the optimum collection of ions by the mass spectrometer (MS) interface. In practice, however, sample aerosols of the plasma cause changes in plasma gas temperature, the electron temperature, and the electron number density and subsequently alter the processes of desolvation, vaporization, atomization, excitation, and ionization. The crucial factor in any analysis is the generation of a fine aerosol and its transport into the plasma. Unfortunately, sample introduction is still the limiting factor in ICP spectrometry [Montaser, 1998 (p. 336)].

A nebulizer converts the bulk solution into an aerosol, which is a mixture of gases, particles, and solvent vapor. The particles are solids or liquid droplets with diameters from virtually zero up to a few hundred micrometers. A distinction can be made between primary, secondary and tertiary aerosols as follows [Montaser, 1998 (p. 337)]:

<u>primary aerosol:</u>	aerosol produced at the tip of a pneumatic nebulizer (PN) or right in front of the transducer plate in an ultrasonic nebulizer (USN)
<u>secondary aerosol:</u>	some PNs further break up the primary aerosol into a finer spray by having an impact bead a short distance from the nebulizer nozzle
<u>tertiary aerosol:</u>	resulting aerosol after passing through a spray chamber (droplet size distribution shifts to smaller diameters as the solvent evaporates from the surface of droplets and larger droplets settle out of the aerosol stream)

The specifications of an ideal sample introduction system should include the following prerequisites [Montaser, 1998], [Todoli et al, 2008]:

- maximum droplet diameter  $\leq 10 \mu\text{m}$
- monodisperse droplets
- complete droplet desolvation
- 100 % analyte transport
- minimization of noise from aerosol production, filtration, transport, drain etc.
- the sample introduction system (nebulizer, spray chamber, tubing) should not contaminate the sample
- high contents of dissolved solids should be tolerated
- option of injecting suspensions
- no risk of nebulizer clogging
- total quantity of aqueous aerosol:  $20\text{-}40 \text{ mg min}^{-1}$  (for a power range of 800-1600W)



### 3.5 Parameters in aerosol droplet characterization

The following outline of the parameters to characterize the mass and particle dispersion of aerosols was made according to the references of [Hinds, 1999] and [Montaser, 1998].

The quality of an aerosol is governed by key parameters as listed in *Table 3-1*. These parameters, which are discussed in the following sections, are crucial for predicting how plasma will perform in analytical measurements.

*Table 3-1 Various key parameters in aerosol characterization.*

---

Size distributions and mean diameters

Cumulative percent volume of particles under a certain size

Span of a distribution

Velocity of particles (axial and radial)

Particle time of arrival

Aerosol concentration

Volume flux

---

#### 3.5.1 Properties of size distributions and mean diameters

Considering a monodisperse aerosol the particle diameter as a single parameter provides a full description of the droplet size. In the majority of cases, however, sample aerosols are polydisperse, which means that particles may display diameters from virtually zero up to a few hundred micrometers. Due to this wide size range that also affects the physical properties of the aerosol it is necessary to characterize the size distribution by mathematical means and descriptive statistics. For simplicity, particles are assumed to be spherical in the following considerations, hence the effect of the shape of the particles is neglected.

In a first step particle size data are sorted into a series of contiguous size intervals and number of particles for the respective size intervals. A graphical representation of grouped data is known as a histogram, where the width of the intervals represents the respective size range (horizontal x-axis). Each size range is represented by a vertical bar that lies

on the horizontal x-axis and whose height (vertical y-axis) indicates the number of particles in the respective size interval. Keep in mind that the frequency (i.e., the height of any interval) is dependent on the width of that interval which may lead to a distortion of the size distribution. Therefore, the histogram is normalized by dividing the number of particles in each size group by the width of that size interval (number/  $\mu\text{m}$ ). Consequently, the area of each vertical bar is now proportional to the number of particles in the respective size interval. Using many vertical bars and drawing a curve through their maxima results in a smooth curve known as particle size distribution curve. This is the graphical representation of the frequency function, or probability density function. This function can be used for mathematical interpretation and represents an important way to characterize dispersed quantities such as particle size, particle mass, particle volume or particle velocity.

The frequency function  $f(x)$  is defined as:

$$f(x) = \frac{df}{dx} \quad (3-1)$$

where  $dx$  is a differential interval of particle size. Standardization for sample size by dividing the frequency by the total number of particles gives a function that can be used for direct comparison of  $f(x)$  from samples of different size due to the fact that the total area equals to 1.0.

$$\int_0^{\infty} f(x)dx = 1.0 \quad (3-2)$$

The cumulative distribution function  $F(x)$  illustrates the fraction of the particles having diameters less than  $x$ .

$$F(x) = \int_0^x f(x)dx \quad (3-3)$$

Distribution functions are inter alia defined by two parameters: one parameter identifies the location or center of the distribution and the other one represents the width or breadth of the distribution. The mean, mode, median, and geometric mean are the most commonly used quantities for characterizing the location of the center of a distribution. The field of statistics provides several ways of calculating the width of distributions, with standard deviation, variance and span (see 3.5.2) being the most commonly used descriptors.

The **mean or arithmetic average diameter**  $\bar{d}_p$  of the particles is the simplest way of describing a group of different particle sizes by one value. It is calculated by

$$\bar{d}_p = \frac{\sum n_i d_i}{\sum n_i} \quad (3-4)$$

where  $n_i$  is the number of particles in group  $i$ , with a midpoint size  $d_i$ .

The **median** is the middle value that separates an ascending list of diameters into two equal halves. For a given data set, it may be thought of as the halfway point between the two extremes of the range and corresponds to a cumulative fraction of 0.5.

The **mode** is the value that occurs most frequently and corresponds to the maximum of the frequency distribution curve. It can be mathematically derived by setting the derivative of the frequency function equal to zero and solving for the diameter.

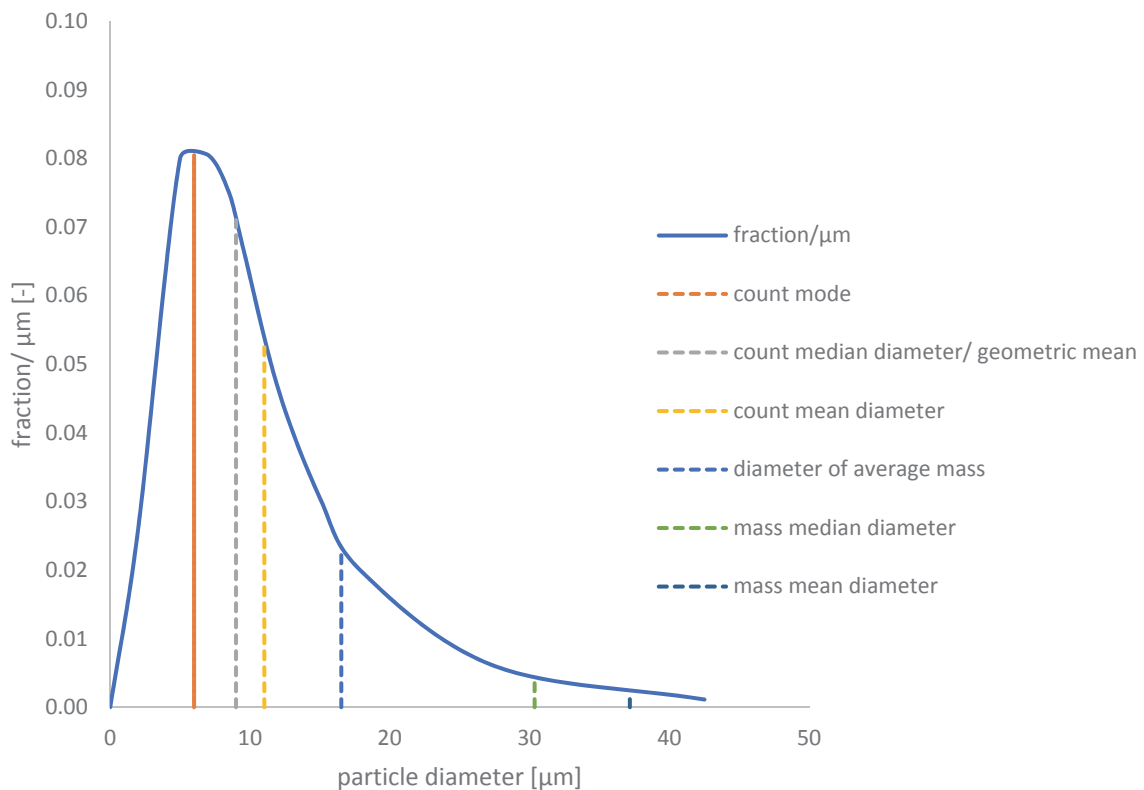


Figure 3-2 Lognormal count distribution showing the location of several different descriptors of a mean for the diameters (revised from [Hinds, 1999 (p.100)]). The quantities are calculated using the Hatch-Choate equations [Hinds, 1999 (p. 97)].

The numerical values of the mode, median, and mean are the same in a symmetrical distribution such as the normal distribution, but they may be very different in highly skewed distributions as shown in *Figure 3-2*. For this reason, the median is a commonly used measure in robust statistics because arbitrarily large or small results have less effect on the median than on the mean.

The **geometric mean**  $d_g$  is defined as the  $N$ th root of the product of  $N$  numbers:

$$d_g = \left( \prod_{i=1}^N d_i \right)^{\frac{1}{N}} \quad (3-5)$$

For the number of particles  $n$  in group  $i$ ,

$$d_g = \left( \prod_{i=1}^N d_i^{n_i} \right)^{\frac{1}{N}} \quad (3-6)$$

where  $d_i$  are characteristic diameters (e.g. midpoint sizes) as already mentioned above and  $N$  corresponds to the total number of particles measured.

Aerosol data which are skewed (i.e., long tail at large sizes) are often believed to come from a lognormal distribution (i.e., the logarithm of the particle diameter is normally distributed). If frequency is plotted against the logarithm of the particle size the smaller diameters are forced to spread and the larger size ranges are compressed. The particle diameters are said to be lognormally distributed, if the resulting plot looks like a normal distribution. In this case the arithmetic mean of  $\ln d$  is defined by

$$\ln d_g = \frac{\sum n_i \ln d_i}{N} \quad (3-7)$$

For the description of some specific types of aerosols other less common distributions turned out to be useful such as

- the Rosin-Rammler distribution (valid for coarsely dispersed dusts and sprays, primarily developed for sizing crushed coal)
- the Nukiyama-Tanasawa distribution (used for aerosols having extremely wide size ranges)

- the power function distribution (applicable to atmospheric aerosols)
- the exponential distribution (relevant to powdered materials)
- the Khrgian-Mazin distribution (applied to size distributions of cloud droplets)

Table 3-2 Names and definitions for common average diameters for lognormal and normal distributions.

distribution	median, geometric	mean diameter
count	count median diameter geometric mean $CMD = \exp\left[\frac{\sum n \ln d}{N}\right]$	count mean diameter $\bar{d} = d_{10} = \frac{\sum nd}{N}$
length	length median diameter $LMD = \exp\left[\frac{\sum nd \ln d}{\sum nd}\right]$	length mean diameter $d_{lm} = \frac{\sum nd^2}{\sum nd}$
area	surface median diameter $SMD = \exp\left[\frac{\sum nd^2 \ln d}{\sum nd^2}\right]$	surface mean diameter Sauter mean diameter $d_{sm} = d_{32} = \frac{\sum nd^3}{\sum nd^2}$
volume or mass	volume median diameter mass median diameter $MMD = \exp\left[\frac{\sum nd^3 \ln d}{\sum nd^3}\right]$	volume mean diameter mass mean diameter $d_{mm} = \frac{\sum nd^4}{\sum nd^3}$  diameter of average volume diameter of average mass $d_{\bar{m}} = \left[\frac{\sum nd^3}{N}\right]^{\frac{1}{3}}$

Source: [Montaser. 1998, (p. 346)]

Depending on how particle diameters were measured or how the data are to be utilized, some calculated quantities (moment averages) that are proportional to particle size raised to a power (moment) might be necessary. There are multiple definitions for the respective

associated measures for single average diameters because the mean values are associated with the assumptions of the distribution calculation (e.g. number, surface, volume of the particles).

*Table 3-2* gives an overview of definitions for common types of average diameters for lognormal and normal distributions.

### 3.5.2 Span of a droplet size distribution

The width of a droplet size distribution is represented by a dimensionless number known as span, which is defined as

$$span = \frac{d_{vol90} - d_{vol10}}{d_{vol50}} \quad (3-8)$$

$d_{vol90}$ ,  $d_{vol10}$  and  $d_{vol50}$  refer to droplet diameters below which the 10, 50, and 90 percentile of the cumulative aerosol volume are found. Since an aerosol should ideally be monodisperse, this means the smaller the span, the higher the quality of the aerosol for analytical ICP spectrometry.

### 3.5.3 Velocity of droplets and droplet time of arrival

The average droplet velocity  $U$  is calculated from equation (3-9).

$$U = \sum_{i=1}^{NC} \frac{n_i u_i}{N} \quad (3-9)$$

$NC$  stands for the total number of velocity classes,  $n_i$  and  $u_i$  refers to the number of counts and the velocity for the class  $i$ , respectively. The total number of droplets measured is denoted by  $N$ .

It is important to note that droplet velocities that are too high can negatively affect the performance of the plasma. For example, the residence time of the droplets in the plasma may be reduced to such an extent that adequate vaporization, atomization, excitation, and ionization can no longer be guaranteed. Furthermore, a very polydisperse aerosol with a broad velocity distribution can also deteriorate the quality of the measurement signal. Significant delays in the particle time of arrival in the plasma can occur when using

desolvation units. With ultrasonic nebulizers, these delays are observed in the millisecond range [Montaser, 1998 (p. 349)].

### 3.5.4 Volume flux of droplets and aerosol concentration

The volume flux of droplets  $F$  ( $\text{cm}^3 \text{s}^{-1} \text{cm}^{-2}$ ) is closely related to the mass transport rate (see also 3.5.5) and is defined as

$$F = \frac{\pi}{6} d_m^3 \frac{N}{At} \quad (3-10)$$

where  $d_m$  is the diameter of average volume and, accordingly, the diameter of average mass as given in *Table 3-2*.  $N$  refers to the total number of droplets passing a cross-sectional area  $A$  per unit time  $t$  [Montaser, 1998 (p. 347)].

Common measures of aerosol concentration are the mass concentration (mass of particles per unit volume of aerosol) and the number concentration (number of particles per unit volume of aerosol) [Hinds, 1999 (p. 10)].

### 3.5.5 Mass transport rate of solvent

The mass transport rate of solvent,  $S_{\text{tot}}$  ( $\text{mg min}^{-1}$  or  $\mu\text{g s}^{-1}$ ) directly indicates the mass of solvent (liquid and vapor) that is transferred into the plasma base per unit of time. It consists of two components, the aerosol (liquid) flux and the vapor stream. The phase composition plays an important role in the formation of the spatial vertical zone structure of the ICP, and in the case of organic solvents, it influences the plasma stability [Sharp, 1988b (p. 956)].

### 3.5.6 Mass transport rate of analyte

The mass transport rate of analyte,  $W_{\text{tot}}$  (usually  $\text{mg min}^{-1}$  or  $\mu\text{g s}^{-1}$ ) is a direct measure of the analyte mass reaching the plasma per unit of time. Ideally, the mass flow rate of the analyte and the mass flow rate of the aerosol are directly related to the concentration of the bulk solution, but changes may occur due to aerosol evaporation or aerosol ionic redistribution [Sharp, 1988b (p. 956)].

### 3.6 Aerosol modification processes

Primary aerosols generated from pneumatic nebulizers have coarse and polydisperse droplet size distributions. In addition, the droplet velocities and the direction of droplet movement are rather undefined. Along their passage through the spray chamber, they are subjected to various aerosol modification processes. These include evaporation, coalescence, coagulation and impact losses due to droplet inertia, in addition to gravitational settling and turbulence. An illustration of the aerosol transport phenomena is given in *Figure 3-3*. The physical and mathematical description of these phenomena can be found in *chapter 4.3*.

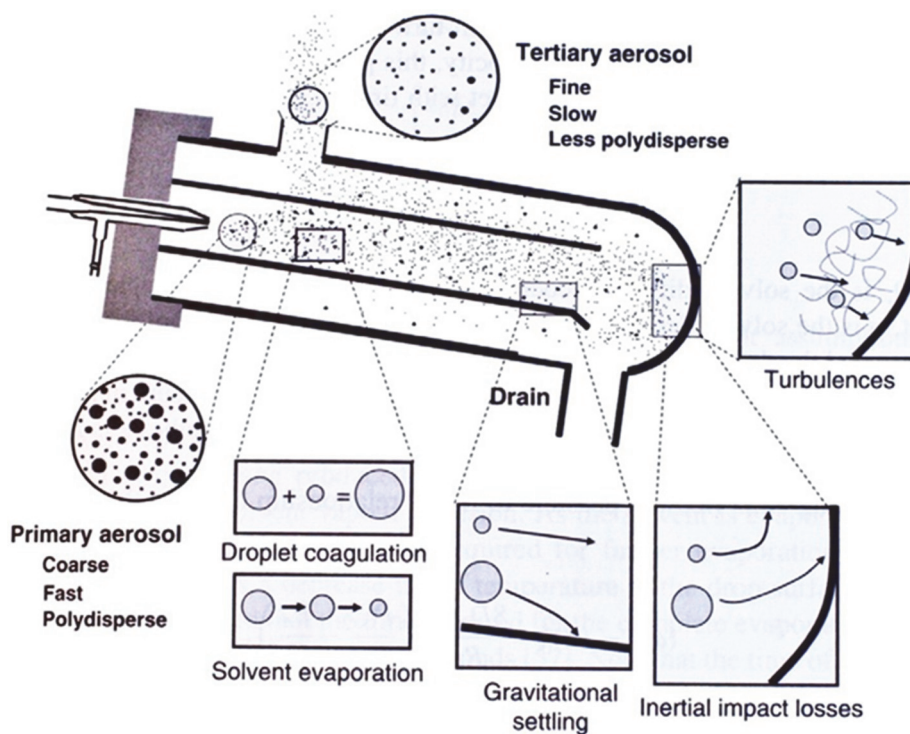


*Figure 3-3* Scheme representing the aerosol modification processes/ transport phenomena inside a Scott-type double-pass spray chamber equipped with a concentric nebulizer. Reproduced from [Todoli et al., 2008] by courtesy of Elsevier.



### 3.7 Limitations of current instrumental setups of pneumatic nebulizers and spray chambers

With reference to the previous chapters, the following conclusions can be drawn regarding the performance of conventional liquid sample introduction systems [Sharp, 1988b], [Todoli et al., 2008], [Bings et al., 2014]:

- Pneumatically generated aerosols are polydisperse with droplet sizes ranging from virtually zero to a few hundred  $\mu\text{m}$  in diameter.
- The droplets have a very heterogeneous velocity distribution and spatial droplet number density.
- Spray chambers serve as tools to adapt the properties of the aerosol generated by the nebulizer to the requirements of the ICP. The respective range of droplet diameters obtained at the plasma outlet of the spray chamber leads to a wide signal intensity distribution.
- Tertiary aerosols still provide a significant amount of partially desolvated droplets.
- The maximum analyte transport efficiencies ( $W_{\text{tot}}$ ) achievable at conventional flow rates (i.e.,  $\sim 1 \text{ mL min}^{-1}$ ) are approximately 2 - 4 %.
- The majority of useful small droplets generated by the nebulizer are lost inside the spray chamber.
- In conclusion, no general sample introduction system exists that works for all sample types. In practice, the selection of the appropriate spray chamber is not so closely linked to the sample properties as to the selection of the respective nebulizer.

### **3.8 Modeling of sample introduction systems**

Before a sample introduction system can be modeled, the most important system-inherent parameters must be determined and defined. These include the sample uptake rate, the gas flow rate of the nebulizer, and also the nebulizer efficiency. In this thesis, both mass transport and analyte transport efficiency were determined using indirect methods (see also *chapter 5.2, 5.3, and 5.4*).

Particle imaging velocimetry (PIV), Fraunhofer laser diffraction, and phase Doppler anemometry (PDA) methods were used to determine particle velocities and particle size distributions, which provide additional key parameters for characterizing the sample introduction system (see also *chapter 5.1*).

## 4. Numerical Simulation

### 4.1 Introduction

The intended goal of any CFD modeling is to represent the physical processes that occur when fluids flow around and within specific objects. The effect and interaction of phenomena like dissipation, diffusion, convection, shock waves, slip surfaces, boundary layers, and turbulence are all associated with these processes. Many important aspects of these relationships are nonlinear, meaning that they cannot be solved analytically and therefore require numerical solutions of the associated partial differential equations [Lomax et al., 2001].

Figure 4 1 illustrates the procedure of a numerical simulation from pre-processing to solution of the governing equations [Noll, 1993].

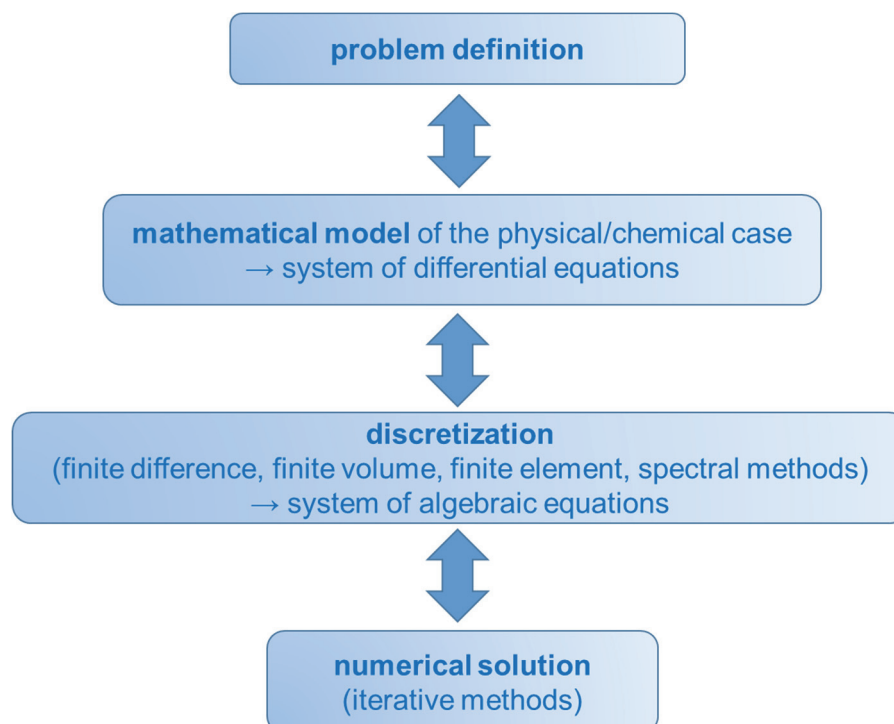


Figure 4-1 Numerical simulation of fluid flow.

Once the problem has been defined, including geometry, flow conditions and requirements of the simulation, a suitable set of governing equations and boundary conditions must be chosen. In general, the phenomena of importance for continuum fluid dynamics are subject to the laws governing conservation of mass, momentum, and energy. The resulting partial differential equations are referred to as Navier-Stokes equations. However, in the interest of computational efficiency it is always prudent to consider slightly simplified forms of these equations, as long as the simplifications retain the essential physical descriptions. Boundary conditions (i.e., solid walls, inflow and outflow boundaries, periodic boundaries, symmetry boundaries, *etc.*) have to be specified and depend on the governing equations. For processes that cannot be simulated within the specified limits, additional physical models may have to be selected. For example, turbulence is a physical process that is frequently modeled. The success of a simulation is up to the skills of the engineer in selecting the governing equations and physical models based on the simulation requirements [Lomax et al., 2001].

Due to the great complexity of the Navier-Stokes equations and their nonlinear character, it is possible to find analytical solutions only in certain particular cases. To solve these equations numerical methods have to be used. In a first step, the governing partial differential equations and boundary conditions defined by continuous variables are approximated by an equivalent of coupled algebraic equations with discrete variables (discretization). Next, an adequate numerical method and gridding strategy must be selected. Numerical methods generally used in CFD can be classified as finite difference, finite volume, finite element or spectral methods. Many different gridding strategies exist including structured, unstructured, hybrid, composite and overlapping grids. Finally, the results of the simulation must be interpreted by sophisticated flow visualization tools and error estimation techniques [Herwig, 2004].

## 4.2 Modelling of the flow

In fluid mechanics, multiphase flows represent interactive flows that involve more than one thermodynamic phase (i.e., gas, solid and liquid). In gas-droplet, gas-particle and liquid-particle flows particles and droplets constitute the so-called dispersed phase. According to Crowe et al., the Euler-Lagrange method can be used for dilute and dense two-phase flows.

In flows with a diluted particle concentration, the influence of interactions with the continuous carrier fluid or the wall as well as field forces (e.g. weight force) prevails over particle-particle collisions. In flows with a high particle load, the interaction between particles dominates and must be modeled accordingly [Crowe et al., 2012].

## 4.2.1 Governing equations of fluid dynamics

This chapter is based on [Wendt, 1992 and 1996], [Herwig, 2002].

### 4.2.1.1 Conservation principle

The basic equations are the mathematical formulations of the three fundamental physical laws of conservation as well as the ideal gas law:

- (1) conservation of mass (continuity equation)
- (2) conservation of momentum (momentum equation of Newton's second law)
- (3) conservation of energy (energy equation or first law of thermodynamics)
- (4) ideal gas law

These physical laws are used to define a proper model of the flow. For a continuum fluid the conservation laws can be derived by considering a closed volume, commonly referred to as the control volume (CV), within a finite region of the flow (*Figure 4-2*).

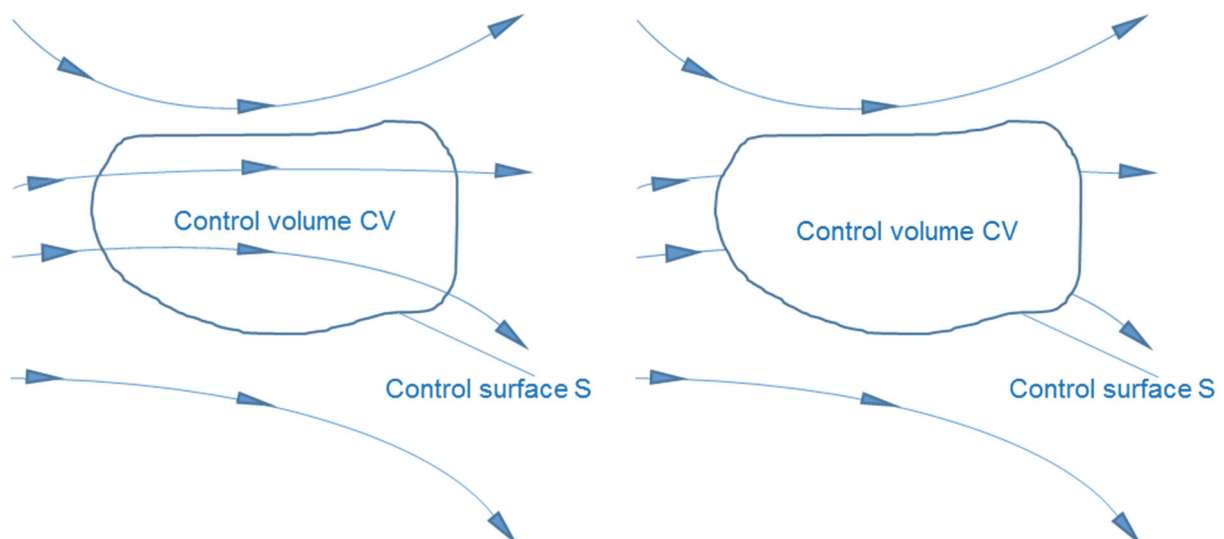


*Figure 4-2 Finite control volume approach; left side: Eulerian specification, right side: Lagrangian specification (adapted from [Wendt, 1992 and 1996 (p. 17)]).*

Instead of observing the whole flow field at once this control volume approach applies the fundamental physical principles only to the fluid inside the defined control volume and the fluid passing through the corresponding surface, respectively. Depending on whether the control volume is fixed in space with the fluid moving through it or is moving with the fluid in such a way that the same fluid particles inside the control volume are considered, the former case is called Eulerian specification of the flow field (left side of *Figure 4-2*) and the latter case is referred to as Lagrangian specification of the flow field (right side of *Figure 4-2*). If the fundamental physical principles are applied to an infinitesimally small fluid element with a differential volume  $dV$ , as shown in *Figure 4-3*, the fluid flow equations obtained are in form of a partial differential equation. The particular partial differential equations obtained from the Eulerian specification are defined as conservation form of the equations (left side of *Figure 4-3*). The equations obtained from the Lagrangian specification are called the non-conservation form of the governing equations (right side of *Figure 4-3*).

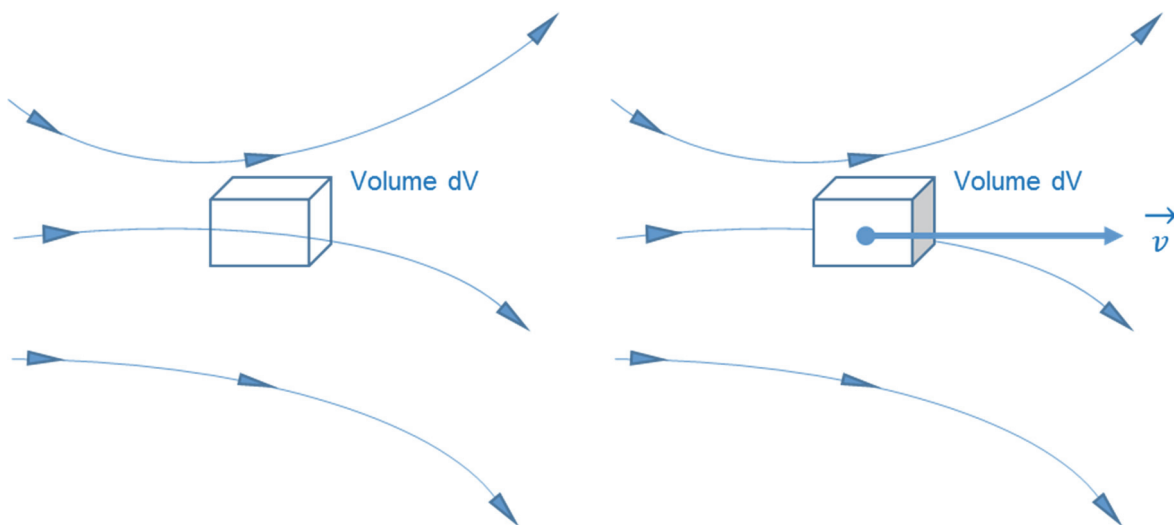


*Figure 4-3* Infinitesimal fluid element approach; left side: Eulerian specification, right side: Lagrangian specification (adapted from [Wendt, 1992 and 1996 (p. 17)]); (with a velocity vector  $\vec{v}$ ).

The differential coordinate-free form of the conservation equations can be written as follows:

continuity equation

$$\frac{\partial \rho}{\partial t} + \nabla \cdot (\rho \cdot \vec{v}) = 0 \quad (4-1)$$

momentum equation

$$\frac{\partial \rho \vec{v}}{\partial t} + \nabla \cdot (\rho \vec{v} \vec{v}) = -\nabla p + \nabla \cdot \vec{\tau} + \vec{f} \quad (4-2)$$

energy equation

$$\frac{\partial \rho e}{\partial t} + \nabla \cdot \rho \vec{v} e = -p(\nabla \cdot \vec{v}) - \nabla \cdot \vec{q} + \frac{\partial Q}{\partial t} + \Phi \quad (4-3)$$

ideal gas law

$$p = \rho \cdot R_s T \quad (4-4)$$

In these equations  $\rho$  stands for density,  $\vec{v}$  for the instantaneous, non-averaged velocity vector,  $p$  for pressure,  $\vec{\tau}$  for the stress tensor,  $\vec{f}$  for the acceleration vector due to external volume forces,  $e$  for the internal energy,  $\vec{q}$  for the heat flux vector,  $Q$  for the production of heat,  $\Phi$  for the dissipation function,  $T$  for the temperature, and  $R_s$  is the specific gas constant.

For Newtonian fluids, the divergence of the stress tensor can be written as function of the velocity gradient:

$$\nabla \cdot \vec{\tau} = -\nabla \times (\mu(\nabla \times \vec{v})) + \nabla \left[ \frac{4}{3} \mu \nabla \cdot \vec{v} \right] \quad (4-5)$$

where  $\mu$  stands for the dynamic viscosity.

For the calculation of turbulent flows in which the Reynolds-averaged equations (see 4.2.2) are solved, the increased effective stress due to the turbulent fluctuations is also taken into account in  $\vec{\tau}$ .

Using Fourier law of heat conduction  $\vec{q}$  is written as

$$\vec{q} = -k\nabla T \quad (4-6)$$

where  $k$  represents the thermal conductivity and  $T$  the temperature.

For the dissipation function  $\Phi$  this results in

$$\Phi = \nabla \cdot (\vec{\tau} \vec{v}) - (\nabla \cdot \vec{\tau}) \cdot \vec{v} \quad (4-7)$$

and describes the dissipation of kinetic energy in internal energy [Schönung, 1990].



### 4.2.1.2 Conservation of mass – continuity equation

Considering a control volume, the fundamental principle that mass is conserved means

$$\left[ \begin{array}{l} \text{net mass flow out of} \\ \text{control volume} \\ \text{through surface} \end{array} \right] = \left[ \begin{array}{l} \text{time rate of decrease} \\ \text{of mass inside control} \\ \text{volume} \end{array} \right]$$

[Wendt, 1992 and 1996 (p. 24)]

Equation (4-1) represents a differential coordinate-free form of the continuity equation. It can be transformed into a form specific for a given coordinate system (such as the Cartesian) or for other general non-orthogonal coordinate systems. The Cartesian form of the continuity equation is as follows:

$$\frac{\partial \rho}{\partial t} + \frac{\partial(\rho u_i)}{\partial x_i} = 0 \quad (4-8)$$

Here, the Einstein convention is used

$$\frac{\partial(\rho u_i)}{\partial x_i} = \frac{\partial(\rho u_x)}{\partial x} + \frac{\partial(\rho u_y)}{\partial y} + \frac{\partial(\rho u_z)}{\partial z} = 0 \quad (4-9)$$

where  $x_i$  ( $i = 1,2,3$ ) or  $(x,y,z)$  are the Cartesian coordinates and  $u_i$  or  $(u_x, u_y, u_z)$  are the Cartesian components of the velocity vector  $\vec{v}$  [Ferziger et al., 2002 (p. 5)].

In order to take into account the proportion of the continuous fluid in a two-phase flow, the general designation of density in equation (4-8) must be expanded to include the gas phase volume fraction  $\alpha_c$ . Accordingly, the bulk density of the continuous phase can be written as

$$\rho = \alpha_c \rho_c \quad \text{with} \quad \alpha_c + \alpha_d = 1 \quad (4-10)$$

where  $\alpha_d$  represents the volume fraction of the dispersed phase.

Substituting equation (4-10) into equation (4-8) gives

$$\frac{\partial(\alpha_c \rho_c)}{\partial t} + \frac{\partial(\alpha_c \rho_c u_i)}{\partial x_i} = 0 \quad (4-11)$$

[Crowe et al., 2012 (p. 20)].

### 4.2.1.3 Conservation of momentum

The momentum equation is based on Newton's 2<sup>nd</sup> law of fluid motion ( $\vec{F} = m \vec{a}$ ) which means that the net force acting on the fluid element equals its mass times the acceleration of this element [Wendt, 1992 and 1996 (p. 27)].

Applied to a control volume, this means

$$\left[ \begin{array}{l} \text{rate of momentum} \\ \text{accumulation in} \\ \text{control volume} \end{array} \right] + \left[ \begin{array}{l} \text{net efflux of} \\ \text{momentum from} \\ \text{control volume} \end{array} \right] = \left[ \begin{array}{l} \text{force on fluid} \\ \text{in control} \\ \text{volume} \end{array} \right]$$

[Crowe et al., 2012 (p. 173)].

Considering a CV the forces acting on the fluid may be divided into

- **surface forces** (pressure forces on the boundary, shear stresses at the wall, drag forces caused by the dispersed phase, surface tension, etc.)
- **body forces** (gravitational forces, electromagnetic forces, centrifugal and Coriolis forces, electromagnetic forces, etc.) [Ferziger et al., 2002 (p. 5)]

Surface forces act directly on the surface of the fluid element, whereas body forces act directly on the mass of the fluid element. Surface forces are caused by pressure - shear - and normal stress distributions acting on the surface and are also superimposed by friction forces due to the outside fluid that surrounds the fluid element [Wendt, 1992 and 1996 (p. 28)].

It is historically correct to refer to the conservation equations for the momentum of a viscous flow as Navier-Stokes equations. However, in modern computational fluid dynamic literature a "Navier-Stokes solution" of a given viscous flow problem usually is to be interpreted in such a way that the "full governing equations" (i.e., the entire conservation equations - continuity, energy and momentum) are used [Wendt, 1992 and 1996 (p. 44)].

For Cartesian coordinates and for the case that gravity is the only body force, the momentum equation is

$$\frac{\partial(\rho u_i)}{\partial t} + \frac{\partial(\rho u_j u_i)}{\partial x_j} = \frac{\partial \tau_{ij}}{\partial x_j} - \frac{\partial p}{\partial x_i} + \rho g_i \quad (4-12)$$

where  $g_i$  is the gravitational acceleration in the direction of  $x_i$ ,  $\tau_{ij}$  stands for the viscous part of the stress tensor and  $p$  for the static pressure [Ferziger et al., 2002 (p. 9)].

For Newtonian fluids, the viscous part of the stress tensor may be written as follows:

$$\tau_{ij} = \mu \left( \frac{\partial u_i}{\partial x_j} + \frac{\partial u_j}{\partial x_i} \right) - \frac{2}{3} \mu \delta_{ij} \frac{\partial u_k}{\partial x_k} \quad (4-13)$$

where  $\mu$  is the dynamic viscosity and  $\delta_{ij}$  is the Kronecker Delta ( $\delta_{ij}$  is 1 if  $i = j$  and  $\delta_{ij} = 0$  otherwise) [Ferziger et al., 2002 (p. 6)].

In analogy to the continuity equation described before, the momentum equation can be extended by the gas phase volume fraction  $\alpha_c$ . and the disperse momentum source or momentum sink  $S_d$  under the assumption that the volume boundaries are only in contact with the continuous phase:

$$\frac{\partial(\alpha_c \rho_c u_j)}{\partial t} + \frac{\partial(\alpha_c \rho_c u_j u_i)}{\partial x_j} = \frac{\partial \tau_{ij}}{\partial x_j} - \alpha_c \cdot \frac{\partial p}{\partial x_i} + \alpha_c \cdot \rho_c \cdot g_i + S_d \quad (4-14)$$

Most models use simplified mathematical approaches to solve the complex conservation equations for mass and momentum. The *Boussinesq approximation* is used if the effect of a variation of the temperature on the fluid properties involved, in particular on the density, can be neglected. When this is the case, density is treated as variable with a linear dependence only in the gravitational term, while it is assumed to be constant in the unsteady and convection terms:

$$(\rho - \rho_0)g_i = -\rho_0 g_i \beta (T - T_0) \quad (4-15)$$

$g_i$  represents the component of the gravitational acceleration  $g$  in the direction of the Cartesian coordinate  $x_i$  and  $\beta$  is the coefficient of volumetric expansion [Ferziger et al., 2002 (p. 15)].

#### 4.2.1.4 Conservation of energy

The energy equation is based on the first law of thermodynamics, which, applied on the CV, states the following

$$\left[ \begin{array}{l} \text{rate of change of} \\ \text{energy in control} \\ \text{volume} \end{array} \right] + \left[ \begin{array}{l} \text{net efflux of} \\ \text{energy through} \\ \text{control surface} \end{array} \right] = \left[ \begin{array}{l} \text{net heat} \\ \text{transfer} \\ \text{to system} \end{array} \right] - \left[ \begin{array}{l} \text{rate of work} \\ \text{done} \\ \text{by system} \end{array} \right]$$

[Crowe et al., 2012 (p. 181)].

From a mathematical point of view, the enthalpy equation represents the conservation of a scalar quantity and can be written in Cartesian coordinates for the continuous phase as follows:

$$\frac{\partial(\rho h)}{\partial t} + \frac{\partial(\rho u_j h)}{\partial x_j} = \frac{\partial}{\partial x_j} \left( \Gamma_h \frac{\partial h}{\partial x_j} \right) + S_h \quad (4-16)$$

where  $h$  is the specific enthalpy,  $S_h$  stands for the source or sink of enthalpy, and  $\Gamma_h$  is the diffusivity (diffusion coefficient) for the enthalpy, containing the dimensionless Prandtl number  $Pr$ :

$$\Gamma_h = \frac{\mu}{Pr} \quad \text{with} \quad Pr = \frac{\mu c_p}{k} \quad (4-17)$$

$c_p$  stands for the specific heat at constant pressure and  $k$  for the thermal conductivity.

Again, substituting equation (4-10) into equation (4-16) gives

$$\frac{\partial(\alpha_c \rho_c h)}{\partial t} + \frac{\partial(\alpha_c \rho_c u_j h)}{\partial x_j} = \frac{\partial}{\partial x_j} \left( \Gamma_h \frac{\partial h}{\partial x_j} \right) + S_h \quad (4-18)$$

### 4.2.1.5 Species transport

In the continuity equation, the diffusion of mass as a transport phenomenon is not taken into account since its derivation is limited to a homogeneous, non-chemically reacting gas.

The species continuity equation includes mass transport of chemical species due to a concentration gradient. Similar to the enthalpy equation, species concentration equations are also about conservation of a scalar quantity.

$$\frac{\partial(\rho m_i)}{\partial t} + \frac{\partial(\rho u_j m_i)}{\partial x_j} = \frac{\partial}{\partial x_j} \left( \Gamma_i \frac{\partial m_i}{\partial x_j} \right) + S_i \quad (4-19)$$

The concentration is usually given as a mass fraction  $m_i$ .  $S_i$  stands for the source or sink of the species  $i$ , and  $\Gamma_i$  is the diffusivity for the species  $i$ , containing the dimensionless Schmidt number  $Sc$ :

$$\Gamma_i = \frac{\mu}{Sc} \quad \text{with} \quad Sc = \frac{\mu}{\rho_c D_i} \quad (4-20)$$

where  $D_i$  is the diffusion coefficient of the species  $i$ .

Substituting equation (4-10) into equation (4-19) gives

$$\frac{\partial(\alpha_c \rho_c m_i)}{\partial t} + \frac{\partial(\alpha_c \rho_c u_j m_i)}{\partial x_j} = \frac{\partial}{\partial x_j} \left( \Gamma_i \frac{\partial m_i}{\partial x_j} \right) + S_i \quad (4-21)$$

### 4.2.1.6 Generalized form of transport equations

Due to the similarity of the transport equations as derived above, these equations can be presented in a general form:

$$\underbrace{\frac{\partial(\rho \Phi)}{\partial t}}_{\text{local temporal derivative in CV}} + \underbrace{\frac{\partial(\rho u_j \Phi)}{\partial x_j}}_{\text{convection through surface}} = \underbrace{\frac{\partial}{\partial x_j} \left( \Gamma_\Phi \frac{\partial \Phi}{\partial x_j} \right)}_{\text{diffusion through surface}} + \underbrace{S_\Phi}_{\text{source/sink in CV}} \quad (4-22)$$

The dependent variable  $\Phi$  is generally a function of space and time, i.e.,

$\Phi = \Phi(x, y, z, t)$ .  $x$ ,  $y$ ,  $z$ , and  $t$  are the independent variables. As mentioned above,  $\Gamma_\Phi$  is the associated diffusion coefficient. To adjust to the general form of the equation, all terms that do not refer to convection or diffusion are simply combined in the source term. Accordingly, values of  $\rho\Phi$  characterize different quantities to be conserved and thus different governing equations that are summarized in *Table 4-1*.

*Table 4-1 Values of  $\Phi$  and  $\Gamma_\Phi$  assigned to the corresponding transport equations.*

$\Phi$	$\Gamma_\Phi$	conserved quantity
-	-	mass
$m_i$	$\frac{\mu}{Sc}$	species
$h$	$\frac{\mu}{Pr}$	specific enthalpy
$v$	$\mu$	momentum

#### 4.2.1.7 Ideal gas law

In many applications, it is generally acceptable to neglect intermolecular forces between the gas particles and to formulate the equation of state for gases in such a way that it reflects the ideal gas law. Thus, when calculating the partial differential equations the fluid density can be determined at the given pressure and the given species concentration as below:

$$\frac{p}{\rho} = RT \sum_{j=1}^n \frac{m_j}{M_{r,j}} \quad (4-23)$$

where  $n$  represents the number of species present,  $m_j$  the mass fraction, and  $M_{r,j}$  the molecular weight of the component  $j$ .

## 4.2.2 Turbulence

*On his deathbed, Heisenberg is reported to have said, "When I meet God, I am going to ask him two questions: Why relativity? And why turbulence? I really believe he will have an answer for the first."*

*(<http://galileo.phys.virginia.edu/classes/usem/Origin/notes/05/heisenberg.html>)*

Referring to the relative movement of the fluid particles, a basic distinction is made between laminar and turbulent flow. To illustrate the nature of the flow, the physicist Osborne Reynolds carried out his famous experiment on fluid dynamics in pipes in 1883 (Figure 4-4). He injected dyed water into the middle of a water flow and found that at a certain velocity the dyed layer broke up to become turbulent. The Reynolds number ( $Re$ ), which is a measure of the ratio of inertia to viscous forces, is used as an assessment criterion for this.

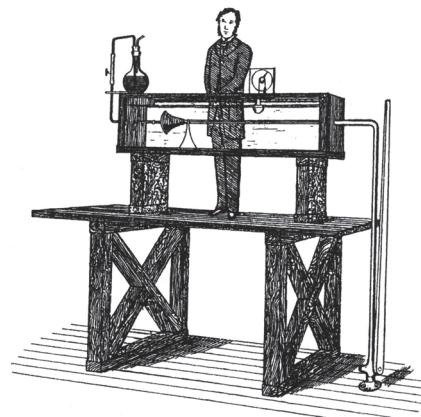


*Figure 4-4 Reynolds' experiment on fluid dynamics in pipes: water flows down to below the ground through a glass tube. Depending on the flow velocity, the nature of the flow is represented by a dyed water jet that is injected in the middle of the flow.*

*(Source: [https://commons.wikimedia.org/wiki/File:Reynolds\\_fluid\\_turbulence\\_experiment\\_1883.jpg](https://commons.wikimedia.org/wiki/File:Reynolds_fluid_turbulence_experiment_1883.jpg), 22.09.2022)*

Turbulence can generally be considered as one of the unsolved problems of classical physics, which means that there is not a single model that can describe this phenomenon in all its facets. It is a fundamental process of fluid mechanics, which has a crucial influence on the appearance of flows above so-called critical Reynolds numbers. Turbulent flows grow from well-ordered laminar flows that are characterized by fluid particles travelling smoothly in parallel layers with little or no mixing. The laminar – turbulent transition,

in which the laminar flow becomes turbulent, is associated with the critical Reynolds number (*Figure 4-5*).

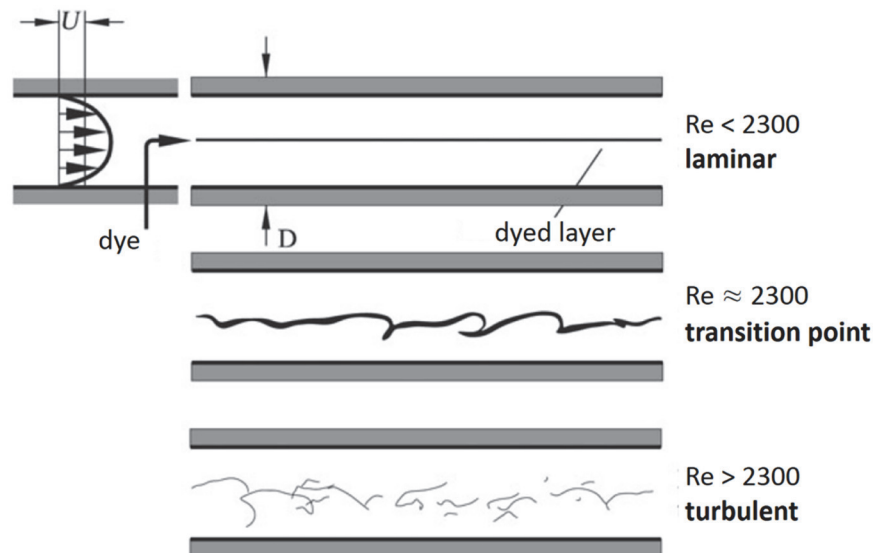


*Figure 4-5 Reynolds' experiment on fluid dynamics in pipes: laminar – turbulent transition; critical Reynolds number  $\approx 2300$  (adapted from [Laurien et al., 2011 (p. 33)] by permission from Springer).*

Turbulent flows are favored by low viscosity and higher velocities of the fluid and display three-dimensional stochastic fluctuations in time and space of various physical quantities related to particles (i.e., momentum, heat, species concentration etc.). For this reason, they are usually treated statistically, rather than deterministically [Herwig, 2004 (p. 366)]. Another effect of turbulence on the conserved quantities is that transport processes between the fluid layers take place much faster than within a laminar flow (“turbulent diffusion”). Since turbulent flows are rotational (i.e., they have non-zero vorticity), mechanisms such as vortex stretching play a key role. Due to the conservation of angular momentum, an increase of the intensity of the turbulence in the stretching direction can be observed. The transfer of momentum between different layers reduces the velocity gradients by viscous shear stress and thus also the kinetic energy of the flow. Consequently, turbulent flows are dissipative and characterized by a so-called energy cascade (*Figure 4-6*). The loss of energy is irreversibly transferred from the large scales to small-scale structures where the energy finally dissipate into heat (Kolmogorov length scale) [Ferziger et al., 2002 (p. 265)].



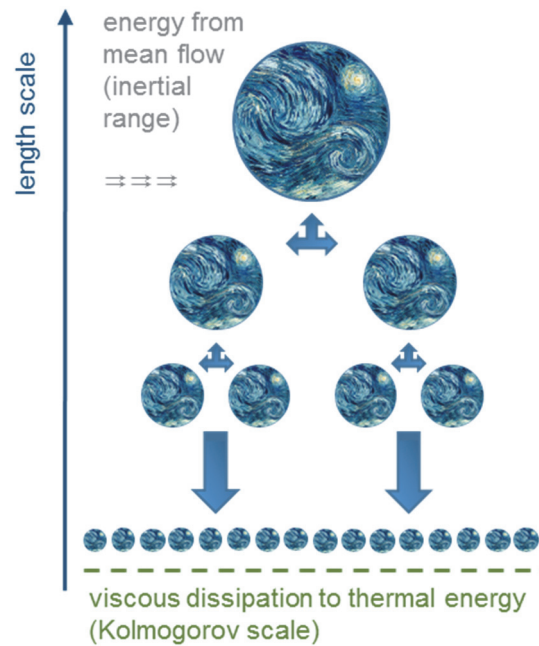


Figure 4-6 Energy cascade: transfer of energy from the mean flow via the Reynolds stresses down a cascade of progressively smaller eddies, where the smallest eddies dissipate the kinetic energy into thermal energy.

An overview of the turbulence simulation methods can be found in *Figure 4-7*.

Nowadays, one of the most accurate approach to calculating turbulence is the **Direct Numerical Simulation (DNS)**. Here, the Navier-Stokes equations are applied to directly solve the instantaneous flow properties without averaging or approximation. Only numerical discretizations are used, whose errors can be estimated and controlled. DNS can produce the information of all turbulence length scales. However, this implies that the computational mesh must be sized fine enough to resolve the Kolmogorov length scale of the flow. Consequently, the computational requirements in a DNS grows very fast for flows with increasing Reynolds number. Even if DNS proves unsuitable for most practical applications at present, it is often used to validate or improve other turbulence models [Crowe et al., 2012 (p. 201)].

Another approach takes advantage of the fact that large scale eddies are generally much more energetic than small scale ones. Consequently, they are by far the most effective vehicles for the conserved properties. On the grounds of computational parsimony, only the large scales of motion are solved for directly, while the small scales are modelled. This method is known as **Large Eddy Simulation (LES)**, a hybrid between DNS and Reynolds averaging. The basic idea behind the **Detached Eddy Simulation (DES)** is to

combine Reynolds averaging in near-wall regions with the LES method in other areas. The dynamic switching between the two models depends on the grid resolution and wall distance. Since the grid resolution is not as challenging as with pure LES, the computational cost is significantly reduced [Liu et al., 2015], [Crowe et al., 2012 (p. 277)].

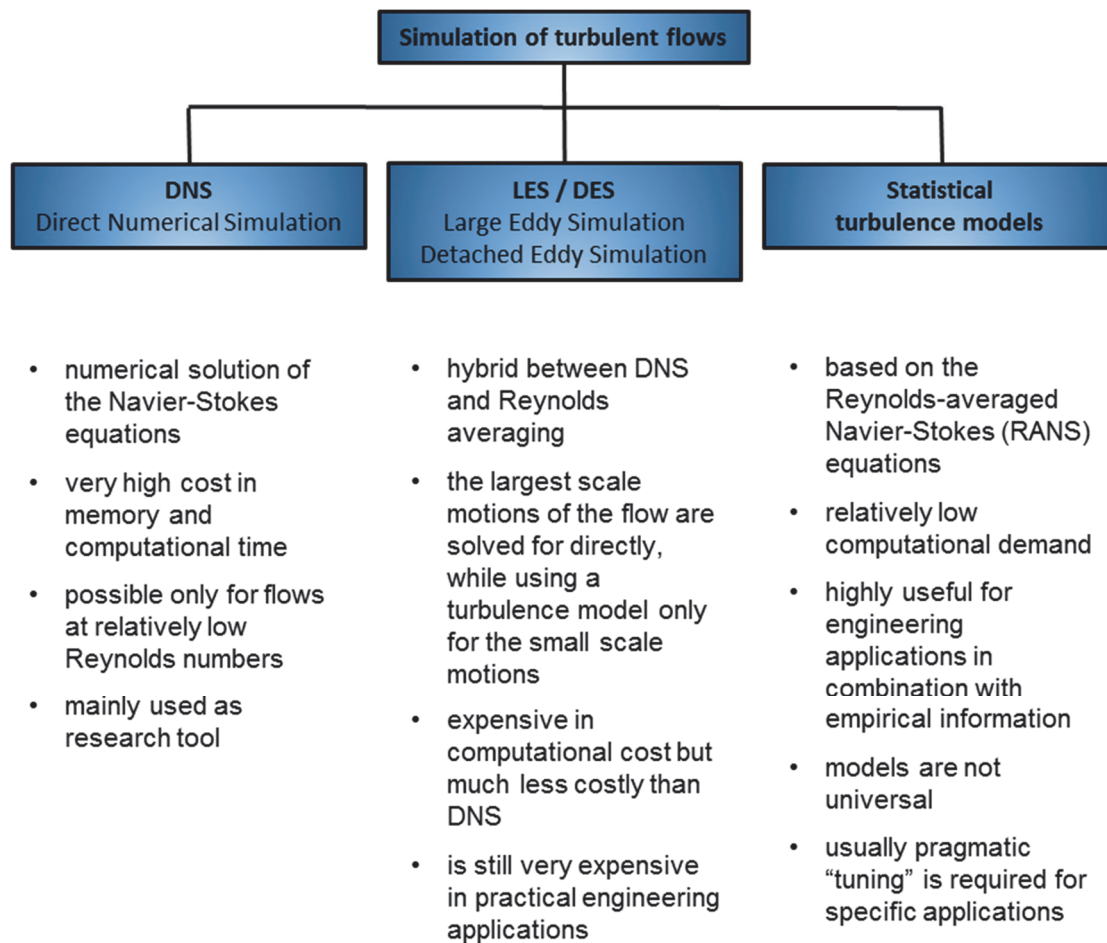


Figure 4-7 Simulation of turbulent flows – classification scheme.

Methods that are commonly used today and highly practicable in engineering applications involve averaging techniques that go back to Osborne Reynolds, who proposed them more than a hundred years ago. They are based on a mathematical technique that decomposes the flow variables of the Navier-Stokes equations into a time-averaged quantity  $\bar{\phi}$  and a fluctuation about that quantity  $\phi'$ :

$$\phi(x_i, t) = \bar{\phi}(x_i) + \phi'(x_i, t) \quad (4-24)$$

$\bar{\phi}$  is obtained either by

- time averaging for a statistical steady flow,

$$\bar{\phi}(x_i) = \lim_{T \rightarrow \infty} \frac{1}{T} \int_0^T \phi(x_i, t) dt \quad (4-25)$$

where the averaging interval  $T$  is large enough and therefore does not depend on time fluctuations, or by

- ensemble averaging for an unsteady (transient) flow,

$$\bar{\phi}(x_i, t) = \lim_{N \rightarrow \infty} \frac{1}{N} \sum_{n=1}^N \phi(x_i, t) \quad (4-26)$$

where  $N$  stands for the number of members of the ensemble that must be large enough to compensate for the effects of the fluctuations.

The resulting equations are therefore known as **Reynolds-Averaged Navier-Stokes (RANS)** equations. While the averaged terms can be easily solved for, the resulting equation contains a nonlinear term referred to as the Reynolds stress. Since this term is unknown, the equation system contains more unknowns than variables, which means that it is not closed. The ultimate goal of any turbulence modeling is to accurately predict the Reynolds stress for a given flow (“closure problem”). There are several ways to model this term, including zero equation models, one-equation models, the two-equation model and a full closure model [Crowe et al., 2012 (p. 201)], [Ferziger et al., 2002 (p. 292)].

An overview of statistical turbulence models is given in (*Figure 4-8*).

Most models can be classified as **eddy viscosity models** using the **Boussinesq approximation (turbulent-viscosity hypothesis)**, where the Reynolds stress is approximated by augmenting the molecular viscosity with a term describing a turbulent eddy viscosity  $\mu_t$ . Using this assumption, the effect of turbulence is represented as an increased viscosity:

$$-\overline{\rho u_i' u_j'} = \mu_t \left( \frac{\partial \bar{u}_i}{\partial x_j} + \frac{\partial \bar{u}_j}{\partial x_i} \right) - \frac{2}{3} \rho \delta_{ij} k \quad (4-27)$$

In equation (4-27)  $k$  is the turbulent kinetic energy:

$$k = \frac{1}{2} \overline{u_i' u_i'} = \frac{1}{2} \left( \overline{u_x' u_x'} + \overline{u_y' u_y'} + \overline{u_z' u_z'} \right) \quad (4-28)$$

The  $k$ - $\varepsilon$  model is one of the most common turbulence models in computational fluid dynamics. It is a two-equation model that uses two more transport equations to represent the turbulent properties of the flow, one for the turbulent kinetic energy  $k$  and another one for the turbulent dissipation  $\varepsilon$ . The  $k$ - $\varepsilon$  model has been proven useful for flows with isotropic turbulent viscosity, which means that the ratio between Reynolds stress and mean rate of deformations is more or less the same in all directions. In reality, turbulent flows rarely have this property. In case of flows with high degrees of anisotropy, **Reynolds stress models** are more appropriate and provide better predictions than two-equation models [Ferziger et al., 2002 (p. 294 - 307)], [Laurien et al., 2011 (p. 161 – 186)].

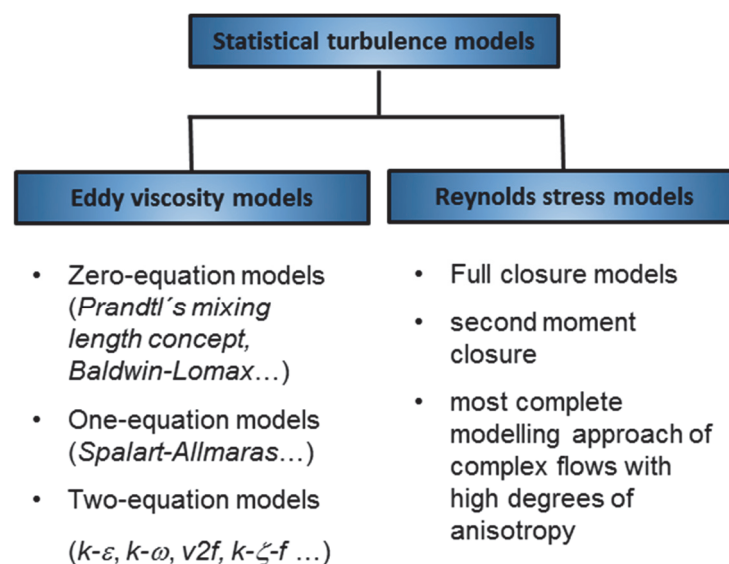


Figure 4-8 Statistical turbulence models – classification scheme.

## 4.3 Modeling of the dispersed phase

To describe multiphase flows remains challenging as the presence of multiple phases causes them to interact with the flow in which they are suspended. In this work, a gas-liquid flow is described in which the motion of liquid droplets (dispersed phase) occurs in a turbulent gas flow (Ar). This problem is non-trivial because a liquid droplet can be formed in many ways and subsequently slowed down or accelerated by both the gas flow and also gravity. The turbulent fluctuations of the gas phase affect its path, and a droplet in turn affects the turbulence. The shape of a particle is also influenced by the motion of the two phases. In addition, a droplet is subject to other events: it can be destroyed by the flow and break up into several droplets; it can collide with another one, form a stable droplet with it, or break up again into two or more droplets. Finally, it can also collide with a surface (e.g. a wall), be deposited there or form new droplets by rebounding. Furthermore, heat and mass transfer processes also take place between the droplets and the gas phase, which in turn influence the droplet size [Crowe et al., 2012], [Wieltsch, 1999].

### 4.3.1 Formation of droplets

The process of breaking up a liquid jet from a circular nozzle depends on a variety of parameters, including the effects of the internal flow of the nozzle, the jet velocity and the turbulence at the orifice exit, as well as the physical and thermodynamic states of both liquid and gas. The jet breakup generally occurs in three steps: liquid flow ejection, primary breakup, and secondary breakup. Once the jet of liquid emerges from the nozzle, it undergoes deformation that ultimately leads to the formation of first isolated liquid fragments. This process is referred to as the primary breakup mechanism. The fragments may be distorted and break down into smaller elements until they form stable droplets, and this represents the secondary breakdown mechanism. It should be noted that the initial energy of the liquid flow determines which of these processes prevails. If the initial energy is high, secondary breakup mechanisms may dominate in generating the final spray [Lin et al., 1998], [Wozniak, 2003], [Dumouchel, 2008], [Jadidi et al., 2015].

### 4.3.1.1 Primary breakup

Due to dominant forces on the jet, primary breakup phenomena result in five different breakup regimes:

- dripping regime
- Rayleigh regime
- first wind-induced regime
- second wind-induced regime
- atomization<sup>2</sup> regime

A common method to visualize the breakup regimes is to plot the unbroken length of the liquid jet  $L_{BU}$  as a function of the jet exit velocity (i.e., the volume flow rate divided by the exit section of the nozzle)  $U_L$ . This yields the so-called jet stability curve, shown in *Figure 4-9*.

The dripping regime (A in *Figure 4-9*) corresponds to the state in which drops are directly discarded at the nozzle exit without forming a continuous liquid column.

Beyond the dripping regime, a continuous liquid column is formed due to the increase of the liquid jet speed. First, the breakup length increases linearly (B in *Figure 4-9*), then passes through a maximum, and finally decreases again (C in *Figure 4-9*) with increasing jet velocity.

In the Rayleigh and first wind-induced breakup regime, the droplets detached from the end of the jet have a size comparable to the diameter of the jet. In both regimes, it is assumed that the interface of the circular liquid jet is disturbed by an axisymmetric wave. In the Rayleigh regime, an axisymmetric perturbation has a wavelength of the same order of magnitude as the jet diameter. When the amplitude of the perturbation equals the jet radius, a droplet is produced. In the first wind-induced regime the dominant perturbation evolving on the liquid jet column is still axisymmetric, as shown in *Figure 4-9*. However, the production of droplets is not as organized as in the Rayleigh regime, which may result in a broader droplet size distribution. The shape of these two regimes of the stability curve

---

<sup>2</sup> In this context, “atomization” refers to the atomization of liquids, i.e., the formation of moving droplets in a continuous gas phase, and is a common term in aerosol technology.

is relatively well understood and can be predicted by linear stability theories such as that of Sterling & Sleicher [Sterling et al., 1975].

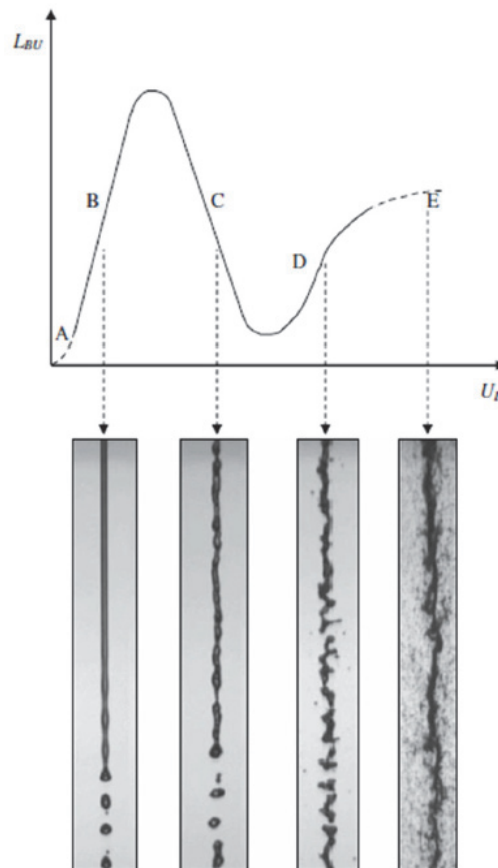


Figure 4-9 Breakup regimes in a cylindrical jet. (top) stability curve, (bottom) visualization of breakup regimes (from left to right): Rayleigh regime (B)  $Re_L = 790$ ,  $We_G = 0.06$ ; first wind-induced regime (C)  $Re_L = 5500$ ,  $We_G = 2.7$ ; second wind-induced regime (D)  $Re_L = 16500$ ,  $We_G = 24$ ; atomization regime (E)  $Re_L = 28000$ ,  $We_G = 70$  (reproduced from [Dumouchel, 2008] by courtesy of Springer).

The second wind-induced breakup regime (D in Figure 4-9) is characterized by a perturbation of the liquid jet column right at the nozzle orifice and results in a very chaotic shape. Two main breakup mechanisms are observed. Close to the nozzle exit, small droplets are detached from the liquid jet interface and further downstream the entire liquid flow breaks up into large liquid fragments. The behavior observed in this regime is due to the combined contribution of the turbulence of the liquid flow and the effect of the aerodynamic forces.

The atomization regime (E in *Figure 4-9*) corresponds to the situation where a spray is generated. The liquid jet emerging from the nozzle is completely disrupted at the orifice exit. It should be noted that the average droplet size diameters are much smaller than the jet diameter. In the second wind-induced and atomization regimes, the most influential parameters on the behavior of the liquid jet are liquid-gas interfacial forces and the internal flow structure (turbulence and cavitation) [Lin et al., 1998], [Wozniak, 2003], [Dumouchel, 2008], [Jadidi et al., 2015].

Due to its initial velocity, the droplet generally performs a relative motion with respect to the gas phase after its formation. The droplet has to displace gas, and the inertia of the gas counteracts this process, which ultimately leads to a deformation of the droplet. The cohesion force related to the surface tension  $\sigma$  counteract the increase in surface area which is caused by the deformation. Calculating the ratio between deforming inertial forces and the stabilizing surface tension gives the Weber number  $We$ . It is a dimensionless number used in fluid mechanics to characterize the nature of cylindrical liquid jet breakup.

$$We = \frac{\text{inertia force}}{\text{surface tension}}$$

In addition to these two forces, the viscous force of the liquid also has an influence on the shape of the droplet. Accordingly, the higher the viscosity of the liquid, the slower the deformation of the drop. If the ratio of the viscous force and the root of the product of the inertia force and the surface force is calculated, the Ohnesorge number  $Oh$  is obtained.

$$Oh = \frac{\text{viscous force}}{\sqrt{\text{inertia force} \cdot \text{surface tension}}} = \frac{\sqrt{We}}{Re}$$

In order to evaluate the different regimes, the values of the gaseous Weber number  $We_G$ , the liquid Weber number  $We_L$ , the Ohnesorge number  $Oh$ , and the Taylor parameter  $T$  have to be calculated. These numbers are defined as follows

$$\begin{cases} We_L = \frac{\rho_L U_L^2 d}{\sigma} & We_G = \frac{\rho_G U_L^2 d}{\sigma} & Re_L = \frac{\rho_L U_L d}{\mu_L} \\ Oh = \frac{\mu_L}{\sqrt{\rho_L d \sigma}} & T = \frac{\rho_L}{\rho_G} \left( \frac{Re_L}{We_L} \right)^2 \end{cases} \quad (4-29)$$



where  $\rho_L$  and  $\rho_G$  are the liquid and gas densities, respectively,  $U_L$  stands for the liquid average velocity,  $d$  represents the nozzle diameter,  $\mu_L$  is the liquid dynamic viscosity, and  $\sigma$  is the surface tension coefficient [Wieltsch, 1999], [Dumouchel, 2008], [Jadidi et al., 2015].

The criteria used in evaluating the jet breakup regimes are summarized in *Table 4-2*.

*Table 4-2 Criteria of cylindrical liquid jet breakup regimes (reproduced from [Jadidi et al., 2015]).*

<i>breakup regime</i>	<i>criteria</i>
Region A: dripping regime	$We_L < 8$
Region B: Rayleigh regime	$We_L > 8$
	$We_G < 0.4$ or $1.2 + 3.41Oh^{0.9}$
Region C: first wind induced regime	$1.2 + 3.41Oh^{0.9} < We_G < 13$
Region D: second wind induced regime	$13 < We_G < 40.3$
Region E: atomization regime	$40.3 < We_G$
	$\frac{\rho_G}{\rho_L} > \frac{(\sqrt{A} - 1.15)}{744} f(T)^{-2}$
	$f(T) = \frac{\sqrt{3}}{6} [1 - \exp(-10T)]$

When using pneumatic nebulizers, the energy required to break up bulk liquids into droplets is provided by the atomizing gas. This is also referred to as a coaxial jet, in which the cylindrical liquid jet is surrounded by an annular gaseous stream. The fluid emerging from the nozzle at low speed is accelerated by the gas, with the relative speed or the dynamic pressure of the gas causing the liquid to break up. To classify the different breakup regimes of a coaxial jet an additional dimensionless number has to be defined:

$$We_R = \frac{\rho_G (U_G - U_L)^2 d_L}{\sigma} \quad (4-30)$$

$We_R$  represents the relative gaseous Weber number,  $U_G$  and  $U_L$  are the average velocities of the liquid and gas phases, respectively, and  $d_L$  is the diameter of the cylindrical orifice through which the liquid jet is injected.

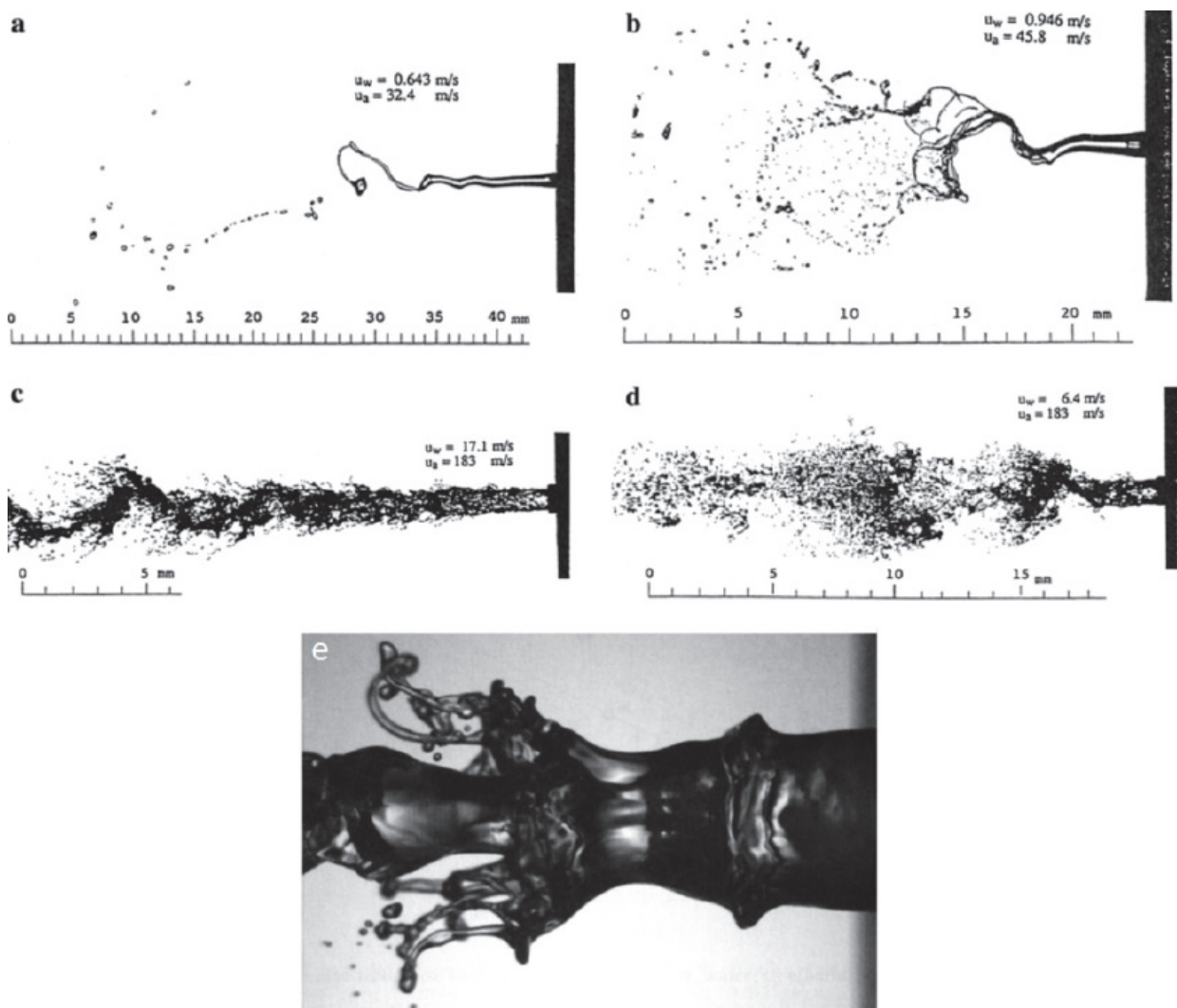


Figure 4-10 Air assisted cylindrical jet breakup regimes: (a) non-axisymmetric Rayleigh-type regime; (b) membrane-type regime; (c) fiber-type regime; (d) fiber-type regime - superpululating submode; (e) digitations-type regime (reproduced from [Jadidi et al., 2015] and [Dumouchel, 2008] by courtesy of Springer-Verlag).

Based on a morphological classification of the atomization regime, the following different types of liquid breakup in a coaxial gas flow can be specified [Dumouchel, 2008], [Jadidi et al., 2015]:

- Rayleigh-type breakup regime (axisymmetric and non-axisymmetric)
- membrane-type breakup regime
- fiber-type breakup regime (pulsating and superpulsating)
- digitations-type breakup regime

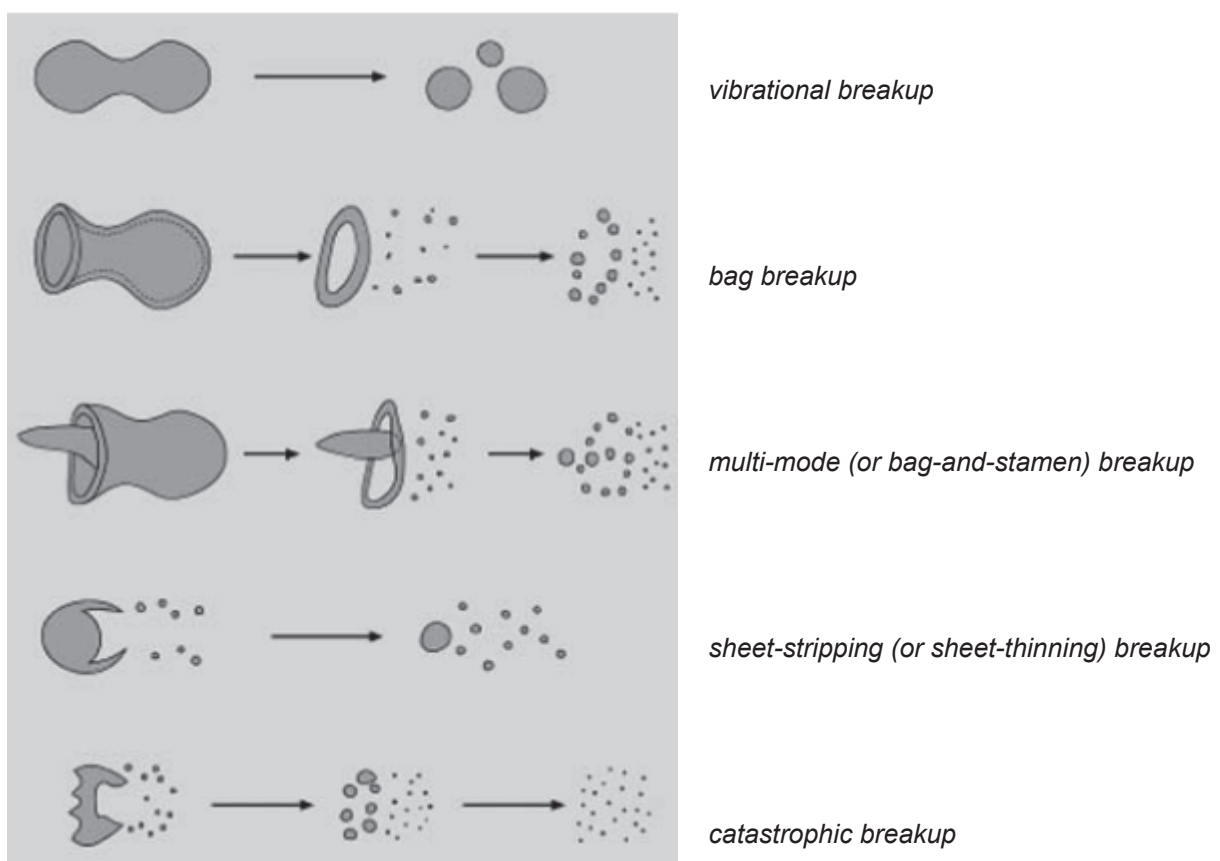
Figure 4-10 illustrates different types of air assisted cylindrical liquid jet breakup regimes. The criteria used in evaluating the respective jet breakup regimes are summarized in Table 4-3.

Table 4-3 Criteria of liquid jet breakup regimes in a coaxial gas stream [Dumouchel, 2008], [Jadidi et al., 2015].

<i>atomization regime</i>	<i>criteria</i>	<i>comment</i>
Rayleigh-type breakup regime:		generation of droplets without any liquid membrane or ligament shedding from the liquid flow
▪ axisymmetric	$We_R < 15$	
▪ non-axisymmetric	$15 < We_R < 25$	
membrane-type breakup regime	$25 < We_R < 70$	thin liquid sheets are developed, which disintegrate into droplets (much smaller than in the Rayleigh regime)
fiber-type breakup regime	$100 < We_R < 500$	thin liquid fibers peel off the jet and disintegrate, farther downstream the liquid core becomes wavy, breaks into ligaments, new fibers are peeled off again (very small droplet diameters)
▪ pulsating		
▪ superpulsating	$150 < We_R < 500$	
digitations-type breakup regime	$We_R > 200$ or lies in membrane-type regime	ligaments development with subsequent disintegration by a non-axisymmetric Rayleigh mechanism; for laminar liquid flow and turbulent gaseous flow

### 4.3.1.2 Secondary breakup

As already mentioned above, primary breakup processes take place at or near the injector orifice, while secondary breakup occurs further downstream. Secondary atomization happens when a droplet is exposed to a surrounding dispersed phase that is moving at a different velocity relative to it. This leads to deformation and fragmentation processes due to acceleration of the ambient fluid around the droplet. In the first step, the initially spherical drop is deformed. However, if the aerodynamic forces are large enough, droplet fragmentation occurs. The fragmentation process is therefore dependent on particular flow conditions and thus also leads to different types of disintegration. A possible classification of the different secondary breakup modes for Newtonian droplets is illustrated in *Figure 4-11*.



*Figure 4-11 Newtonian secondary breakup morphology (reproduced from [Guildenbecher et al., 2009] by courtesy of Springer).*

Three mechanisms for the disintegration of droplets by aerodynamic forces are mentioned:

- (1) the aerodynamic forces reach the magnitude of the surface tension forces stabilizing the droplet;
- (2) the deformation of the droplet reaches a critical value;
- (3) the occurrence of critical droplet oscillations: in this case, the deformation of the droplet reaches frequencies close to the natural frequency of the droplet, so that the decay occurs by resonance.

The resulting mechanism of the droplet disintegration is certainly a superposition of different mechanisms and leads to the respective decay modes shown in *Figure 4-11*. Furthermore, it is assumed that the transition between the different breakup modes is a function of  $We$  and  $Oh$  (see also *Table 4-4*) [Wozniak, 2003], [Jadidi et al., 2015].

*Table 4-4 Transition Weber number for Newtonian droplets with  $Oh > 0.1$  [Jadidi et al., 2015].*

<i>breakup morphology</i>	<i>transition Weber number for Newtonian drops</i>
vibrational	$\sim 11 < We < \sim 35$
multimode	$\sim 35 < We < \sim 80$
sheet-stripping	$\sim 80 < We < \sim 350$
catastrophic	$We > \sim 350$

### 4.3.2 Motion of droplets

After a droplet is formed, it is subjected to a variety of external forces that affect its state of motion. For example, gravity tries to pull it down as fast as possible, the drag force of the continuous phase wants to retard this movement and the buoyancy force tries to keep the droplet in the gas phase. In addition, various other forces exert an influence on the motion of the droplet (see also 4.2.1.3).

According to Newton's second law, the change in momentum of a particle is equal to the sum of the forces acting on the particle:

$$\frac{m_d du_d}{dt} = \sum F \quad (4-31)$$

Basically, the forces acting on a particle can be classified as follows [Crowe et al., 2012 (p. 59)]:

- **body forces:** these are forces that act on the mass of a droplet, such as gravity.
- **surface forces:** these forces are due to drag and lift and represent a momentum coupling between the continuous and the dispersed phase.

The external forces of gravity  $F_G$  and buoyancy  $F_L$  act on the particle. Their magnitude results from the density of the particle  $\rho_d$ , the density of the continuous phase displaced by the particle  $\rho_c$ , and the volume of the particle  $V_d$  as well as the acceleration due to gravity  $g$ . The resulting body force is

$$F_G + F_L = V_d (\rho_d - \rho_c) g \quad (4-32)$$

The second essential force is the steady-state drag force  $F_D$ . This force acts on a particle when there is no acceleration of the relative velocity between the particle and the transporting fluid in the respective velocity field.

$$F_D = \frac{1}{2} \rho_c C_D A_d |u_c - u_d| (u_c - u_d) \quad (4-33)$$

$\rho_c$  is the density of the continuous phase,  $C_D$  represents the drag coefficient,  $A_d$  is the representative area of the droplet (i.e., the projected area of the particle or droplet in the direction of the relative velocity) and  $u_c$  and  $u_d$  are the velocities of the continuous phase and the droplet or particle phase, respectively.

The drag coefficient of an individual particle depends on its shape, its rheological properties (deformable or undeformable), its position with respect to the flow and the flow conditions (Reynolds number, Mach number, degree of turbulence, etc.). In addition, when determining the drag coefficient for an individual particle, it is necessary to take into account whether or not its motion is unaffected by other particles.

At the smallest particle Reynolds numbers  $Re_d$  the drag coefficient has a maximum and decreases sharply with increasing particle Reynolds number. The range in which there is a linear relationship ( $Re_d \leq 0.1$ ) is known as the Stokes flow regime.

For  $750 < Re < 3.5 \cdot 10^5$  the drag coefficient is almost constant. This is referred to as inertial range or Newton flow regime. From  $Re > 3.5 \cdot 10^5$ , the drag coefficient decreases sharply and reaches a minimum at the critical Reynolds number. For the range where the particle Reynolds number is less than the critical Reynolds number, the following applies with reasonable accuracy for a spherical fluid particle [Crowe et al., 2012 (p. 67)], [Wieltsch, 1999]:

$$C_D = \frac{24}{Re_d} + \frac{4}{\sqrt{Re_d}} + 0.4 \quad (4-34)$$

For very small particle Reynolds numbers ( $Re \ll 1$ ) the drag coefficient results in:

$$C_D = \frac{24}{Re_d}.$$

In the numerical calculation, a correlation according to **Schiller and Naumann** is used for the drag coefficient [Schiller et al., 1933], [AVL FIRE™ Manual – user guide, 2019]:

$$C_D = \begin{cases} \frac{24}{Re_d} (1 + 0.15 Re_d^{0.687}) & Re_d < 10^3 \\ 0.44 & Re_d \geq 10^3 \end{cases} \quad (4-35)$$

It is also important to distinguish whether phase coupling occurs in a multiphase flow or not. If one phase influences the other without a reverse effect, the flow is characterized as **one-way coupled**. If there is a mutual effect between both phases, the flow is said to be **two-way coupled** [Crowe et al., 2012 (p. 29, 36)].

### 4.3.3 Droplet – turbulence interaction

When a droplet is introduced into a fluid flow, it takes a certain amount of time before it reaches a state of equilibrium. This period of time depends on the initial disequilibrium state and the drag forces between the fluid and particle flow. In a turbulent gas flow, inertial particles or droplets also exert an influence on the turbulence of the carrier phase. This effect is known as turbulence modulation. The presence of the disperse phase may cause either an attenuation or an augmentation of the turbulence relative to the single phase. In general, due to their inertia, large droplets react only slightly to the changed incident flow and pass through several turbulence eddies before deposition. They have longer response times until an acting force changes their direction. As droplet diameter decreases, the influence of turbulence increases. Finally, small droplets respond quickly to a change in gas velocity and follow the gas flow.

The particle relaxation time  $\tau_p$  serves as a measure of the time required to adapt to the steady state of motion. It is the ratio of the particle's momentum to the drag force it experiences:

$$\tau_p = \frac{m_d u_r}{C_D \frac{d_d^2 \pi}{4} u_r^2} \quad (4-36)$$

where  $m_d$  is the particle mass,  $u_r$  represents the relative velocity,  $d_d$  is the diameter of the particle and  $C_D$  is the drag coefficient [Crowe et al., 2012 (p. 202)], [Maier, 2003], [Wieltsch, 1999].

A similar formulation to describe the interaction between a particle and a turbulence eddy of length scale  $l$  uses the Stokes relaxation time  $\tau_v$  and the Stokes number  $St$ .

$$\tau_v = \frac{\rho_d d_d^2}{18 \mu_c} \quad (4-37)$$

where  $\mu_c$  is the viscosity of the continuous phase. As can be seen, the momentum (velocity) response time is most sensitive to the particle size  $d_d$ .

The Stokes number is an important non-dimensional parameter in dispersed flows and may be defined as



$$St = \frac{\tau_V u_{r,e}}{l} \quad (4-38)$$

where  $u_{r,e}$  is the relative velocity of the shear boundary layer under consideration and  $l$  represents the respective turbulence length scale.

The Stokes number can be used to characterize the behavior of particles in turbulent flows as follows [Crowe et al., 2012 (p. 25, 36)], [Maier, 2003]

- $St \ll 1$ : the response time of the particle is shorter, thus the particle and fluid velocities will be nearly equal (velocity equilibrium).
- $St \gg 1$ : the particle has no time to respond to the velocity changes of the continuous phase, thus the particle velocity will be almost unaffected during its passage.
- $St \sim 1$ : it can be assumed that a particle is deflected onto a curvilinear path at the edge of the turbulence eddy.
- $St = 0$ : the flow is in a velocity and thermal equilibrium, i.e., it can be regarded as a single-phase flow with modified properties.

#### 4.3.4 Droplet – wall interaction

For confined fluid-particle flows, the process of particle-wall interaction must be taken into account. In general, this interaction can be classified as follows (see also *Figure 4-12*):

- (1) hydrodynamic interaction due to proximity of the wall
- (2) mechanical interaction due to contact with the wall

Hydrodynamic forces acting on a particle approaching the wall in the normal direction prevent the particle from coming into contact with the wall. However, if the inertial forces (mechanical interaction) of the particle predominate, the hydrodynamic forces can be neglected, since a collision with the wall occurs. The reason for this is that the time for deposition is much smaller than the hydrodynamic relaxation time of the particle. Upon impact with the wall, the droplet can either stick, bounce, splash, dissolve or break. When a massive particle hits a wall surface, it usually bounces off but loses kinetic energy due to friction and inelasticity effects. However, when very small particles collide with a wall, mainly molecular forces, such as van der Waals' forces, act. Consequently, the particle deposits due to the resulting cohesive forces [Crowe et al., 2012 (p. 139)].

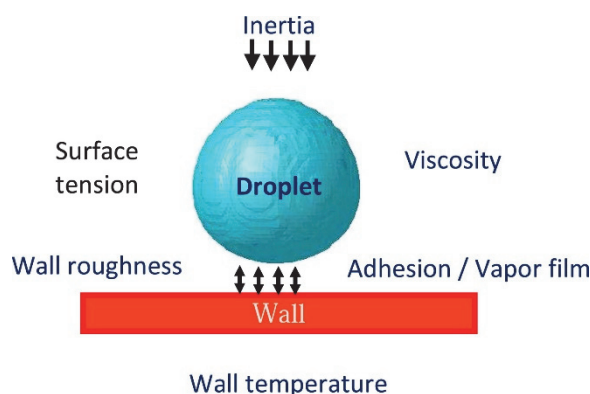


Figure 4-12 Physical forces acting on an impinging droplet (reproduced from [Mahulkar et al, 2015] by courtesy of Elsevier).

The spray-wall interaction model used in this thesis was proposed by Kuhnke [Kuhnke, 2004]. It is based on existing models, which, in contrast, also take into account the wall temperature  $T_w$  in addition to the impact parameter  $K$ . It represents the dimensionless droplet velocity and is a characteristic parameter to distinguish between different impingement regimes.

$$K = \frac{(\rho_d d_d)^{\frac{3}{4}} u_{d,\perp}^{\frac{5}{4}}}{\sigma_d^{\frac{1}{2}} \mu_d^{\frac{1}{4}}} \quad (4-39)$$

$u_{d,\perp}$  is the droplet velocity normal to the wall.

Depending on a dimensionless wall temperature  $T^*$ ,

$$T^* = \frac{T_w}{T_s} \quad (4-40)$$

where  $T_w$  and  $T_s$  are the wall temperature and the spray temperature, respectively, the Kuhnke model has four regimes shown in Figure 4-13.

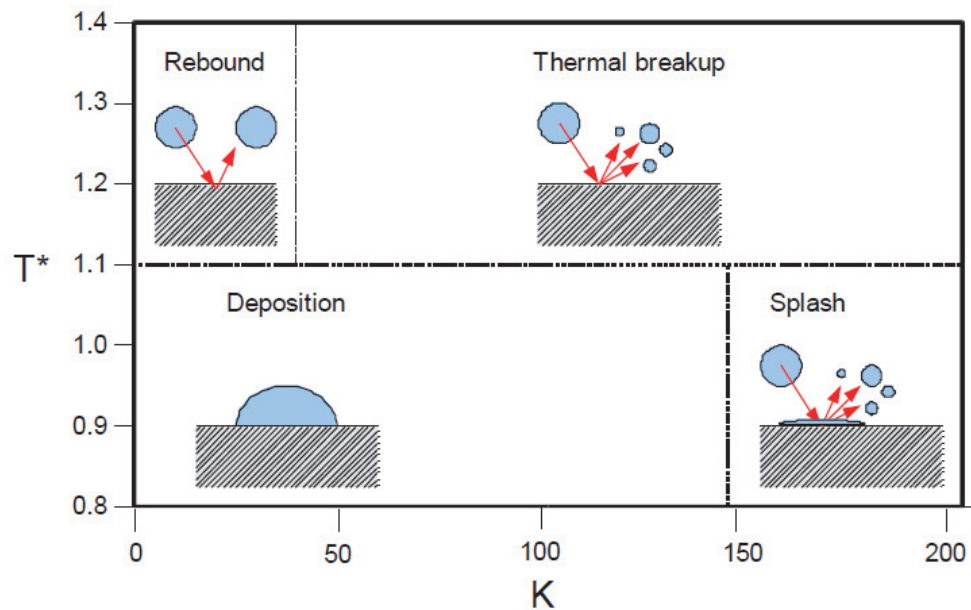


Figure 4-13 Regime map for spray/wall interaction according to Kuhnke [Kuhnke, 2004], [AVL FIRE™ Manual – Wallfilm Module, 2019 (p. 41)].

**Deposition:**  $T^* < 1.1$ , droplet velocity low; the impacting droplets are completely deposited on the wall and create a wall film.

**Splash:**  $T^* < 1.1$ , droplet velocity higher; particles are atomized to form smaller droplets after the impact. A fraction of the droplet mass is transferred to the wall film.

**Rebound:**  $T^* > 1.1$ , droplet velocity low; a vapor layer between droplet and wall is formed preventing a direct contact of the droplet with the wall and no wall film formation occurs.

**Thermal breakup:**  $T^* > 1.1$ , droplet velocity higher; no wall film is formed and the droplets disintegrate into secondary droplets.

The model can be used to calculate the mass of liquid deposited on the wall, the droplet diameters and droplet velocities after the impact.

### 4.3.5 Droplet – droplet interaction

Particle-particle interactions play an important role especially in dense flows. However, as the particle concentration in the fluid decreases, the motion of the particles is primarily determined by the forces of the fluid (drag and lift). In dense flows, the particles collide with each other or are in persistent contact. The resulting loss of kinetic energy must therefore be taken into account.

A qualitative assessment of whether a flow is dense or dilute can be made by calculating the ratio of the momentum response time  $\tau_V$  (see also 4.3.3) of a particle to the time between collisions. If this ratio is less than 1, the flow is considered dilute. In this case, the particles have sufficient time between collisions to react to the local dynamic forces of the fluid. However, if it is greater than 1, the flow is said to be dense. Here, the particle does not have time to react to the fluid dynamic forces before the next collision occurs. [Crowe et al., 2012 (p. 26)].

Particle-particle interaction regimes are commonly classified into bounce, coalescence, disruption, and fragmentation (*Figure 4-14*).

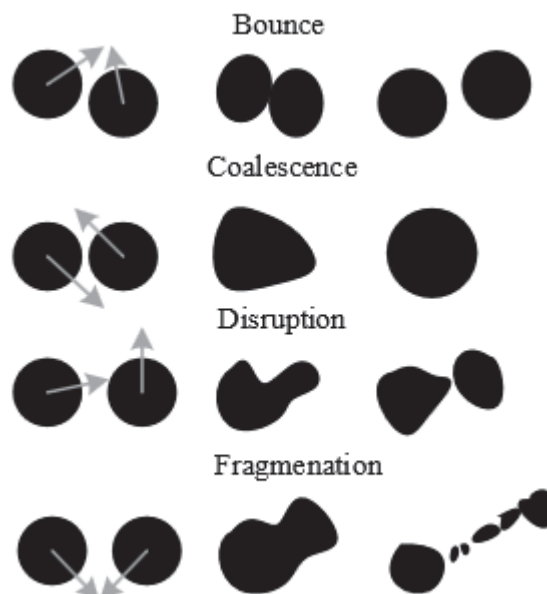


Figure 4-14 Particle-particle collision regimes. Reproduced from [Kropotova et al., 2021].

**Bounce:** Particle bounce considers the elastic collision of droplets. Due to the presence of a thin intervening gas film the surfaces of the droplets do not come into contact. No new droplets are formed and the surface of the droplet remains intact.

**Coalescence:** Particle coalescence is characterized by two droplets merging into one large droplet. Upon contact, the droplet surface disrupts. A post-collision droplet is generated whose mass is equal to the sum of the masses of the pre-collision droplets.

**Disruption:** Particle disruption involves the separation of a collision product into the same number of droplets that were present before the collision.

**Fragmentation:** Particle fragmentation occurs if a coalesced droplet breaks down catastrophically into numerous small droplets. This is the case when droplets have excessive kinetic energies [Orme, 1997].

The Weber number can be used to classify the collision regimes (see *Table 4-5*) [Kropotova et al., 2021].

*Table 4-5 Ranges of the Weber number to characterize the collision regimes.*

<i>bounce</i>	$0.7 < We < 1.5$
<i>coalescence</i>	$0 < We < 0.5$
	$2 < We < 15$ (stable coalescence)
<i>disruption</i>	$15 < We < 50$
<i>fragmentation</i>	$We > 100$

### 4.3.6 Droplet evaporation

Evaporation or condensation results in a change of phase at the surface of the droplet due to the transport of droplet vapor to or from the surface of the droplet. The driving force for this phenomenon is the difference in concentration of the droplet vapor between the droplet surface and the continuous phase. Consequently, heat and mass transfer occur between the carrier fluid and the particle cloud. Due to the relative motion of the particle-gas phase the shear force on the particle surface causes the liquid to heat up. Hence, droplet evaporation increases with enhanced droplet Reynold numbers.

A model derived by **Dukowicz** can be used to describe heat and mass transfer processes [Dukowicz, 1979], [AVL FIRE™ Manual – Spray Module, 2019 (p. 12)]. It is essentially based on the following assumptions:

- The droplets have a spherical symmetry.
- Around the droplet there is a quasi-steady gas film.
- The droplet itself has uniform temperature.
- The fluid surrounding the droplet has uniform physical properties.
- A thermal liquid-vapor equilibrium prevails at the droplet surface.

With these simplifications, it is possible to calculate an energy balance for the temperature change of the droplet, where the heat transferred either warms up the droplet or contributes to its evaporation.

$$m_d c_{p,d} \frac{dT_d}{dt} = L \frac{dm_d}{dt} + \dot{Q} \quad (4-41)$$

$c_{p,d}$  is the specific heat of a liquid droplet,  $L$  represents the latent heat of evaporation and  $\dot{Q}$  is the convective heat flux. The convective heat flux is defined by

$$\dot{Q} = \alpha A_s (T_\infty - T_s) \quad (4-42)$$

where  $\alpha$  is the convective heat transfer coefficient for the passage through the film surrounding the droplet without mass transfer and  $A_s$  is the droplet surface area.

When using the evaporation model of Dukowicz, one must be aware that the evaporation takes place in a non-condensable gas. Hence, a two-component system (i.e., the vapor and the non-condensable gas) is used in the gas-phase, even though each component may be a mixture of different species. Thus, introducing the vapor mass flux  $f_{vs}$  and the local surface heat flux  $q_s$ , the governing equation for the mass flux can be expressed as follows

$$\frac{dm_d}{dt} = \dot{Q} \frac{f_{vs}}{q_s} \quad (4-43)$$

and the droplet energy equation is written as

$$m_d c_{p,d} \frac{dT_d}{dt} = \dot{Q} \left( 1 + L \frac{f_{vs}}{q_s} \right) \quad (4-44)$$

By means of this heat balancing, the change of the temperature of the droplet or its transient diameter can now be tracked.

The ratio of  $f_{vs}$  to  $q_s$  can be calculated by assuming the Lewis number  $Le \approx 1$  and formulating a mass transfer number  $B_Y$

$$B_Y = \frac{Y_\infty - Y_{vs}}{1 - Y_{vs}} \quad (4-45)$$

that describes the ratio of the vapor content at the surface of the droplet  $Y_{vs}$  and in the surrounding phase  $Y_\infty$ . The Lewis number is defined as

$$Le = \frac{\rho c_p D}{\lambda} \quad (4-46)$$

where  $D$  and  $\lambda$  are the diffusion coefficient and the thermal conductivity, respectively.

Replacing the convective heat transfer coefficient  $\alpha$  in equation (4-42) with the Nusselt number  $Nu$ , the convective heat flux supplied from the gas to the droplet surface is

$$\dot{Q} = Nu d_d \pi (T_\infty - T_s) \quad (4-47)$$

The Nusselt number  $Nu$  is derived from the correlation proposed by Ranz and Marshall for single droplets:

$$Nu = 2 + 0.6 Re_d^{1/2} Pr^{1/3} \quad (4-48)$$

The average temperature between the local domain fluid temperature and the droplet surface temperature is used to evaluate transport properties such as vapor viscosity, specific heat, thermal conductivity etc. [AVL FIRE™ Manual – Spray Module, 2019 (p. 13)].

The model of **Abramzon and Sirignano** is based on the classical droplet vaporization model with the following extensions [Abramzon, 1989]:

- variable physical properties and non-unitary Lewis number in the gas phase
- influence of the Stefan flow (blowing) on heat and mass transfer
- transient liquid heating inside the internally circulating droplet

Gas phase calculations rely on the classical film theory, where the resistances to heat and mass transfer are modeled by fictional gas films of constant thickness. Taking into

account the relative change of the film thickness due to the presence of the Stefan flow, the film thickness is corrected by the factors  $F_T$  and  $F_M$  in this model. Subsequently, the mass change rate is described by the Sherwood and Nusselt numbers. The instantaneous droplet vaporization rate is expressed by the following equations:

$$\dot{m} = \pi \bar{\rho}_g \bar{D}_g d_d Sh^* \ln(1 + B_Y) \quad (4-49)$$

$$\dot{m} = \pi \frac{\bar{k}_g}{\bar{c}_{p,F}} \bar{\rho}_g d_d Nu^* \ln(1 + B_T) \quad (4-50)$$

where  $\bar{\rho}_g$ ,  $\bar{D}_g$  and  $\bar{k}_g$  are the average density, binary diffusion coefficient and thermal conductivity of the gas mixture in the film, respectively.  $d_d$  is the particle diameter and  $\bar{c}_{p,F}$  represents the average vapor specific heat in the film.  $B_Y$  and  $B_T$  are called the Spalding mass and heat transfer numbers (for details see [Abramzon, 1989] and [AVL FIRE™ Manual – Spray Module, 2019 (p. 14)] and are calculated as

$$B_Y = \frac{Y_s - Y_\infty}{1 - Y_s} \quad (4-51)$$

$$B_T = (1 + B_Y)^\phi - 1 \quad (4-52)$$

where  $\phi$  is

$$\phi = \frac{\bar{c}_{p,F}}{\bar{c}_{p,g}} \frac{Sh^*}{Nu^*} \frac{1}{Le} \quad (4-53)$$

$Y$  is the mass fraction, the subscripts  $s$  and  $\infty$  refer to the conditions at the droplet surface and external gas flow, respectively.

$Sh^*$  and  $Nu^*$  are the “modified” Sherwood and Nusselt numbers, which are defined as follows:

$$Sh^* = 2 + \frac{(Sh_0 - 2)}{F_M}; \quad Sh_0 = 2 + 0.552 Re^{\frac{1}{2}} Sc^{\frac{1}{3}} \quad (4-54)$$

$$Nu^* = 2 + \frac{(Nu_0 - 2)}{F_T}; \quad Nu_0 = 2 + 0.552 Re^{\frac{1}{2}} Pr^{\frac{1}{3}} \quad (4-55)$$



$Sh_0$  and  $Nu_0$  are the corresponding numbers of the non-evaporating droplet.  $F_T$  and  $F_M$  are approximated using the following correction function:

$$F(B) = (1+B)^{0.7} \frac{\ln(1+B)}{B} \quad (4-56)$$

$$F_M = F(B_Y); F_T = F(B_T) \quad (4-57)$$

The heat penetrating into the droplet (heat transfer rate) is

$$\dot{Q}_s = \dot{m} \left( \frac{\bar{c}_{p,F} (T_\infty - T_s)}{B_T} - \bar{L}(T_s) \right) \quad (4-58)$$

where  $\bar{L}$  is the latent heat of the evaporation.

The resulting algorithm for calculating the heat and mass transfer comprises the following steps [AVL FIRE™ Manual – Spray Module, 2019 (p. 15)]:

- Calculate the average physical properties  $\bar{\rho}_g$ ,  $\bar{D}_g$ ,  $\bar{c}_{p,F}$ ,  $\bar{c}_{p,g}$  and  $\bar{k}_g$ .
- Calculate  $Sh_0$  and  $Nu_0$ .
- Get  $B_Y$ ,  $F_M$ ,  $Sh^*$ , and  $\dot{m}$  from equation (4-49).
- Calculate  $B_T$  using the value from the previous iteration or time step.
- Get  $Nu^*$  and correct  $B_T$  by comparing the two mass transfer rates from equations (4-49) and (4-50). If the corrected value of  $B_T$  is too large, go back to the previous step.
- Calculate  $\dot{Q}_s$  according to equation (4-58).

The advantage of Abramzon and Sirignano's model is that the Lewis number is not limited, however the disadvantage is the iteration process.

## 4.4 Discretization

As already mentioned in chapter 4.1, discretization is required to transform the initial mathematical model (i.e., the governing partial differential equations and boundary conditions that describe the variations of the dependent variables of the fluid flow as continuous function) into a discrete equivalent. The differential equations are approximated by a system of algebraic equations for the dependent variables. Due to these approximations, it should be noted that the discretization of continuous data always yields some amount of discretization error [Schönung, 1990 (p. 36-46)], [Ferziger et al., 2002 (p. 25-35)]. There are many different discretization approaches, including the Finite Difference, Finite Volume, or the Finite Element methods. The discretization scheme used in this thesis is based on the **Finite Volume method**. The investigated flow domain is subdivided into a finite number of adjacent control volumes where all dependent variables are calculated at the centroid (i.e., computational node) of each control volume by integrating the differential form of the governing equations over each control volume. The volume integrals are converted to surface integrals using Gauß's divergence theorem. Balancing the fluxes at the surfaces of each volume yields a conservative solution, which means that the flux leaving a given volume is identical to the flux entering an adjacent volume. The advantage of the Finite Volume approach, i.e., the advantage of conservative discretization, compared to Finite Difference methods is particularly evident in complex grid geometries and curvilinear coordinates [Schönung, 1990 (p. 43)], [Ferziger et al., 2002 (p. 36, 70-89)], [Maier, 2003 (p. 83)].

With regard to the dispersed phase, the most frequently used method for the numerical discretization in the engineering environment today is based on a statistical method referred to as **Discrete Droplet Method (DDM)** [Dukowicz, 1980]. Spray droplets are introduced in the flow domain as parcels with an initial set of conditions like position, size, velocity, temperature and number of particles in the parcel. Each single parcel represents a certain number of identical non-interacting droplets. Within the Lagrangian approach droplets are tracked through the computational grid for each time step of the numerical calculation and are exposed to different flow conditions due to the turbulence field of the continuous phase. Each parcel has only one trajectory and in addition a two-way coupling between the continuous and the dispersed liquid phases is taken into account [AVL FIRE™ Manual – Spray Module, 2019], [Kuhnke, 2004].

The SIMPLE (Semi-Implicit Method for Pressure-Linked Equations) algorithm is a widely used iterative procedure to solve the Navier-Stokes equations. The sequence of the algorithm may be summarized as follows:

- estimate a pressure field  $\Rightarrow p^*$
- solve momentum equations to obtain approximated velocity components  
 $\Rightarrow u_i^*, i=1..3$
- solve pressure correction equations  $\Rightarrow p'$
- correct pressure field  $\Rightarrow p = p^* + p'$
- re-calculate the velocity field  $\Rightarrow u_i, i=1..3$
- solve further discretized equations for other dependent variables (e.g. temperature, turbulence...)
- if convergence criterion is not fulfilled re-iterate with  $p$  as a new  $p^*$

Convergence is achieved when a velocity field has been found that simultaneously fulfills the momentum and mass balance [Noll, 1993 (p. 103)].

Several solution methods are available for time discretization. Details on this can be found, for example, in [Noll, 1993].

## 4.5 Accuracy of numerical solutions

One must be aware that numerical solutions of fluid flow and heat transfer problems always represent only approximate solutions for the observable physical phenomena. In addition to the errors due to the solution algorithm, programming or setting the boundary conditions, there are three main types of systematic errors:

- **Modeling errors**, i.e., the deviation of the observable current flow from the exact solution of the mathematical model.
- **Discretization errors**, defined as the deviation of the exact solution of the conservation equations from the exact solution of the algebraic equations system by discretization of these equations.
- **Iteration errors (or convergence errors)**, caused by the iterative solution of the algebraic equation system.

Modeling errors depend on the approximations made for the dependent variables in the transport equations, especially for turbulent flow problems, two-phase flows, and combustion phenomena. However, modeling errors can also be introduced by simplifying the geometry of the solution domain or, for example, by simplifying the boundary conditions [Ferziger et al., 2002 (p. 34)].

## 4.6 Realization of numerical simulation

### 4.6.1 Software

FIRE™ (AVL LIST GMBH, Graz, Austria), a general purpose CFD-program, is used for the numerical simulation of the dynamics of the argon flow and the droplet phase inside the spray chamber. It uses finite volume methods as mentioned above with one or more of the following characteristics: steady state and time dependent flows, compressible and incompressible flows, viscous and inviscid flows, isothermal and non-isothermal flows, laminar and turbulent flows. Additional modules are available for porous media, acoustic problems, conjugate heat transfer, combustion, wall film and sprays. Following the traditional concept of a CFD program, FIRE™ consists of three modules: the pre-processor, the analysis program, and the post-processing module.

### 4.6.2 Hardware

A workstation, Precision T5600, from Dell Technologies equipped with two Intel Xeon six core processors (E5-2667) is used to perform the CFD calculations.

### 4.6.3 Numerical grid

The generation of a numerical grid is the crucial first step in applying CFD to describe physical processes. This is because only well-constructed grids guarantee the accuracy of numerical solutions and are responsible for a reasonable simulation time. Accordingly, a proper volume grid was generated that covers the physical domain of the Scott spray chamber under investigation. The geometrical dimensions of the chamber with a volume of roughly 77 mL and the volume grid of the virtual spray chamber are shown in *Figure 4-15* and *Figure 4-16*, respectively. The computational domain was divided into approximately 245,000 cells. As for the investigations preferably global information is of interest, it is sufficient to use a relatively coarse grid in order to save CPU-time. An enhanced grid density was used in regions with higher flow variations like the inflow domain and outlet region. The generated grid was a polyeder/ hexaeder type grid.

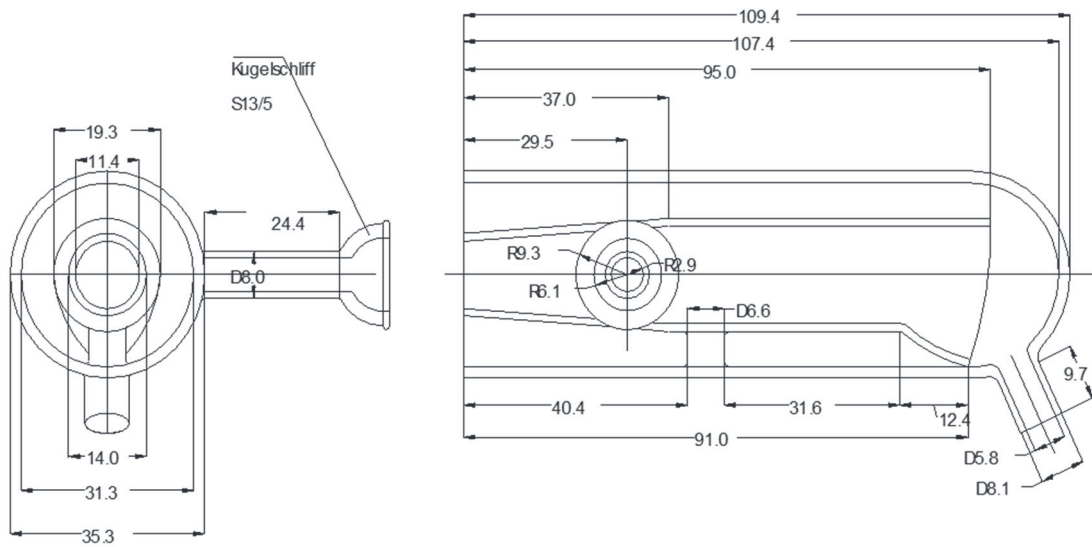
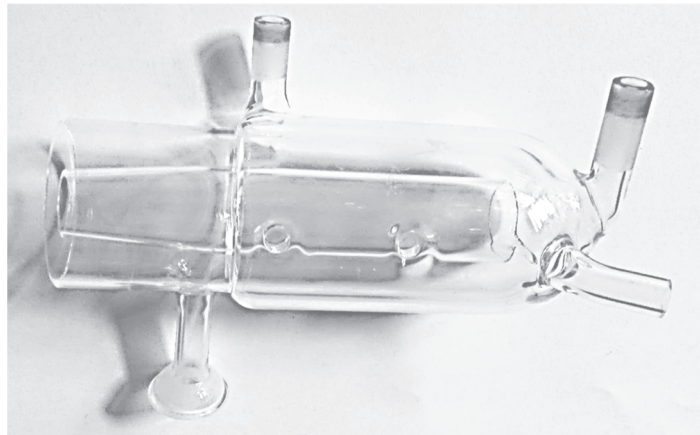


Figure 4-15 Top: photo of the investigated Scott spray chamber (source: E. Fasch); bottom: dimensions of the investigated Scott-type spray chamber (all sizes in mm).

AVL FIRE WM-Fame-Tools	
Selected object is	
[Geo Info]   Distance   Cell Info	
Mesh info	
Number of Nodes	1213746
Number of Surface Faces	29953
Number of Edge Elements	0
Number of Tria Elements	0
Number of Quad Elements	0
Number of Tet Elements	467
Number of Hex Elements	417
Number of Pyramid Elements	1610
Number of Octa Elements	0
Number of Prism Elements	2
Number of Other Elements	242614
Total Number of Elements	245110
Surface Area	0.02407500045
Volume	7.69517882146

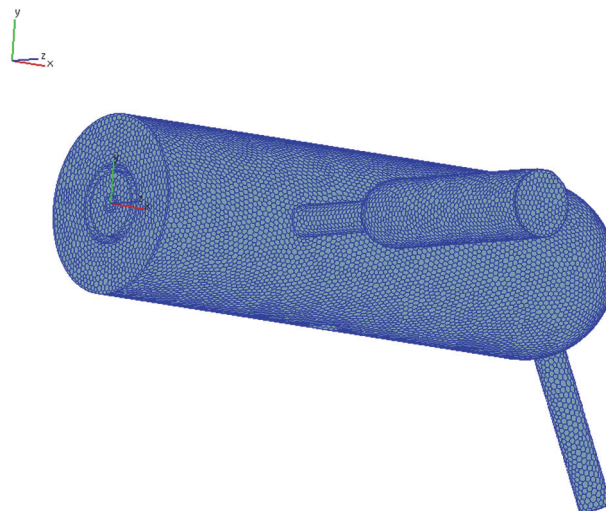


Figure 4-16 Volume grid of the virtual Scott chamber.

#### 4.6.4 Boundary conditions

The inlet boundary condition for the numerical simulation of the spray chamber is defined by the nebulizer characteristics itself. The values selected represent a nozzle where argon as a carrier gas for the sample fluid is injected. The gas velocity at the nozzle exit is set to  $276 \text{ m s}^{-1}$  at a temperature of  $219.75 \text{ K}$ . These inflow conditions are chosen according to reference [Sharp, 1988b].

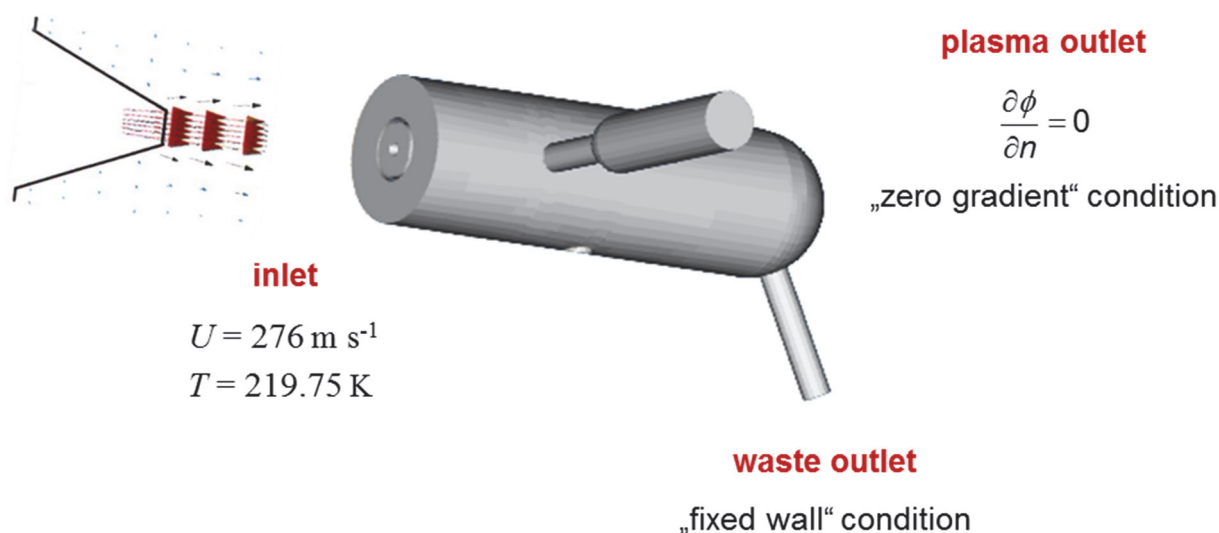


Figure 4-17 Boundary conditions for the argon gas flow.

The sample uptake- and the argon flow rate is set to  $110 \mu\text{L min}^{-1}$  and  $0.8 \text{ L min}^{-1}$ , respectively. The nozzle of the MicroMist 100 is shown in *Figure 4-18*. The nozzle diameter is  $271 \mu\text{m}$ .

A negligible outflow of gas at the waste outlet is assumed and the so - called wall boundary condition is selected. The chamber outlet to the plasma is defined by the zero gradient condition for the given pressure. Wall temperature for all wall boundaries generally are specified to be  $275.15 \text{ K}$  when the chamber cooling option is investigated or  $293.15 \text{ K}$  for the simulation at room temperature.

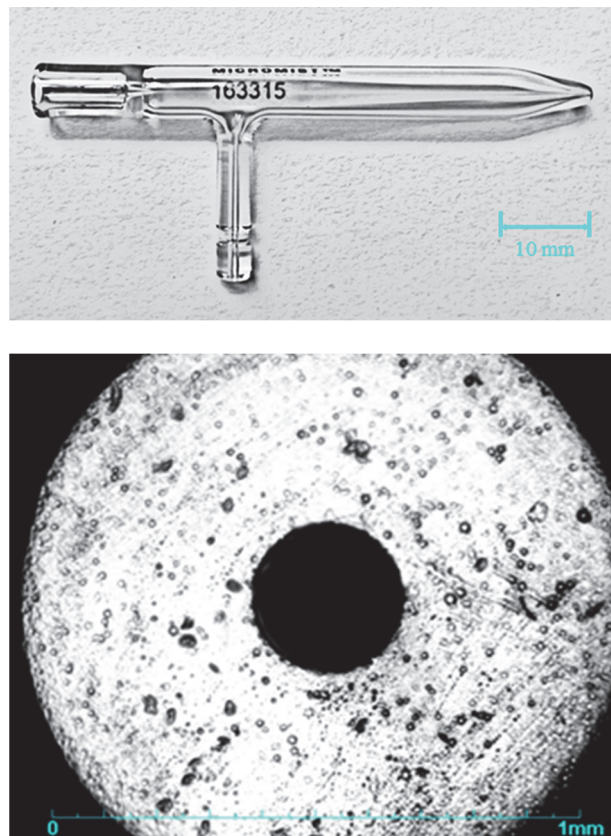


Figure 4-18 Photo of the MicroMist 100 (top) and the MicroMist 100 nebulizer nozzle (bottom); (source: E. Fasch).

## 4.6.5 Numerical model

To resolve the flow situation in a Scott-type spray chamber all numerical simulations throughout this work were processed in two steps. First, the continuous phase (i.e., argon gas flow without spray) was computed until a dynamic equilibrium (steady state) was reached. Afterwards, a transient calculation of the droplet phase was performed using the converged steady state of the gas phase as starting condition.

### 4.6.5.1 Gas flow solver

The partial differential equations describing the fundamental conservation laws (see chapter 4.2.1) are approximated in the CFD solver.



#### 4.6.5.1.1 Turbulence model

Turbulent flow conditions are modeled using the RANS (Reynolds Averaged Navier-Stokes) method. FIRE™ offers several turbulence models to choose from, including the  $k$ - $\zeta$ - $f$  model used in this work. It represents an eddy-viscosity model based on Durbin's elliptic relaxation concept ( $v2f$  model). Instead of calculating a transport equation for the velocity scale  $\bar{v}^2$ , an equation for the velocity scale ratio  $\zeta = \bar{v}^2 / k$  is solved, where  $k$  is the turbulence kinetic energy. This leads to an improvement in numerical stability in complex three-dimensional flows. Thus, the  $k$ - $\zeta$ - $f$  model is more robust and less sensitive to nonuniformities of the computational grid [Hanjalić et al., 2004]. Therefore, this model was considered the best of the models available in FIRE™ for the present simulation case.

#### 4.6.5.2 Spray

Spray calculations are based on a statistical method referred to as the **Discrete Droplet Method (DDM)** (see *chapter 4.4*). Instead of modeling the nozzle flow and the primary break-up process, the aerosol size and velocity distributions generated by the nebulizer (primary aerosols) were measured (see *chapter 5.1* and *chapter 6.3*) and used as input parameters. Droplets starting from a state of rest cause numerical problems since their distance of acceleration by the gas flow from zero to their maximum velocity is very short (approximately 1 mm [Sharp, 1988b]). This involves the production of high momentum sources in computational mesh cells close to the nozzle and causes non-monotonic and slow convergence behavior in case of coupled calculation. For this reason, droplets were provided with a predefined initial velocity obtained from experiment (*chapter 6.3*). After a time interval when argon passes through the entire chamber and reaches a steady state behavior the spray is initialized and at each time step three droplet parcels are injected. That leads to an overall number of approximately 146,000 parcels to be considered from injection start time to a final steady state gas-droplet flow field.

Of all potential effects describing the aerosol modification in the spray chamber [Sharp, 1988b] gas phase compressibility, gravitational settling, evaporation, and turbulent dispersion are considered.

Body forces are activated on particles and liquid films forming at walls. For the drag coefficient  $C_D$ , a correlation according to **Schiller and Naumann** is used in the numerical calculation (see 4.3.2).

The calculation was done assuming a two-way momentum exchange between the gas and the liquid phase. Therefore, all differential equations for the conservation of mass, momentum and energy are solved for every time step when gas and liquid coexist in the chamber.

## Evaporation model

To account for evaporation effects, the **SCR-thermolysis model** was selected. It is based on Abramzon and Sirignano's model described in chapter 4.3.6.

## Turbulent dispersion model

Particles traversing a turbulent flow are assumed to interact with the individual turbulent eddies. In each interaction, the particle is deflected according to the instantaneous velocity of the turbulent eddy and the inertia of the particle. These additional turbulence effects on the spray particles cannot be resolved by the ensemble-averaged flow field of a RANS based simulation. To account for this, the turbulent dispersion model developed by **Gosman and Ioannides** is used. This stochastic dispersion method models the effects of turbulence on spray particles by adding a fluctuating velocity term. Assuming isotropic turbulence, the particle fluctuating velocity  $u'_i$  can be determined by sampling randomly from a Gaussian distribution according to equation (4-59) with the standard deviation  $\sigma = \sqrt{\frac{2k}{3}}$  where  $k$  represents the turbulent kinetic energy of the gas at the particle location.

$$u'_i = \left( \frac{2}{3} k \right)^{\frac{1}{2}} \text{sign}(2Rn_i - 1) \text{erf}^{-1}(2Rn_i - 1) \quad (4-59)$$

$Rn_i$  is a random number from  $[0 < Rn_i < 1]$  for each vector component and  $\text{erf}^{-1}$  stands for the inverse Gaussian function. The particle fluctuating velocity  $u'_i$  is treated as a piecewise constant function of time, and is only updated when the turbulence correlation time

$t_{\text{turb}}$  has passed. This time is related on the minimum time for the eddy to break-up and the time it takes for the particle to cross an eddy. The turbulence correlation time is calculated according to the following equation

$$t_{\text{turb}} = \min \left( C_{\tau} \frac{k}{\varepsilon}, C_1 \frac{k^{\frac{3}{2}}}{\varepsilon |u_g + u' - u_d|} \right) \quad (4-60)$$

where the model constants  $C_{\tau}$  and  $C_1$  are 1 and 0.16432, respectively.  $\varepsilon$  represents the dissipation rate. If  $t_{\text{turb}}$  is smaller than the computational time step  $\Delta t$ , the spray integration time step is reduced to  $t_{\text{turb}}$  [AVL FIRE™ Manual – Spray Module, 2019 (p. 49)].

### Droplet coalescence and collision model

Droplet coalescence and droplet collision effects are neglected because of the fact that the droplet volume fraction in most areas of the spray chamber is very low [Schaldach et al., 2002a], [Kollau, 1999]. Viewed with the naked eye, a spray appears very dense (*Figure 4-19; left side*). However, if the movement of the droplets is frozen with the aid of a laser pulse, it can be seen that the instantaneous volume fraction of the liquid phase in the spray is very small (*Figure 4-19; right side*). Hence, the probability of droplet coalescence and collision phenomena is also very low.

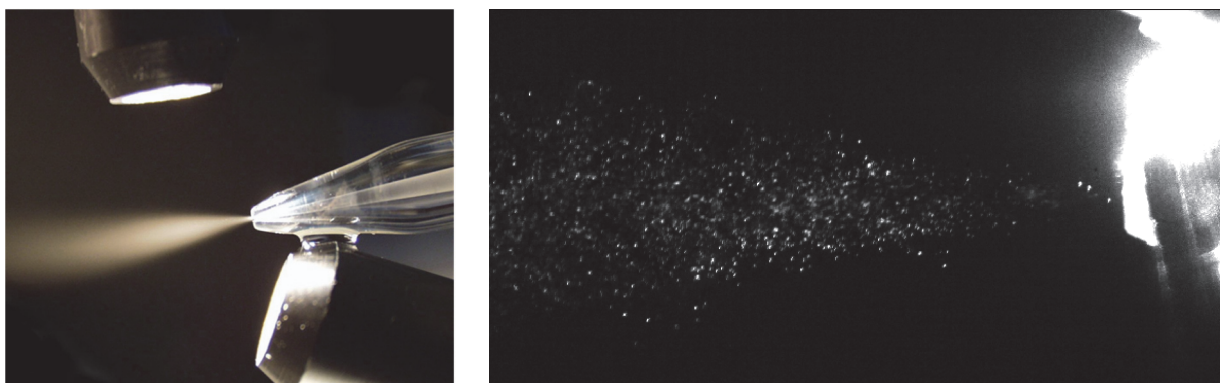


Figure 4-19 Primary aerosol of the MicroMist 100 nebulizer: photo image (left side); laser pulse image (right side) (source: E. Fasch).

### 4.6.5.3 Wall film

This chapter is based on the AVL user guide for the wall film module approaches [AVL FIRE™ Manual - Wall Film Module, 2019 (p. 7ff)]

For the present simulation case, the FIRE Wall film module was activated. The following fundamental assumptions and modeling approaches are:

- The gas and wall film flow are treated as two separate single phases.
- The film thickness is very small in contrast to the mean diameter of the gas flow.
- There is no simulation of the wavy film surface in detail. However, this is taken into account by modeling the mean film thickness with a superimposed film roughness.
- It is assumed that the mean film surface is parallel to the solid wall.
- Wall friction and interfacial shear stress dominate the film behavior.
- The wall temperature is below the Leidenfrost point.

These assumptions lead to an implementation of the wall film model as a 2D finite volume method on the wall boundaries of the gas flow geometry.

The simulation settings include solution flags for wall shear, turbulence kinetic energy (TKE), heat transfer, temperature, evaporation, entrainment, balancing, splashing and momentum equation. Similarly, the coupling flags for momentum source, vapor mass source and vapor energy source were activated for all simulation cases.

### Governing equations

The **film thickness equation** is the basic governing equation describing wall film flow. It is a slightly modified version of the continuity equation. For simplicity, only the Cartesian formulation is reproduced here as follows:

$$\frac{\partial \delta}{\partial t} + \frac{\partial \delta u_i}{\partial x_i} + \frac{\partial \delta u_j}{\partial x_j} = \frac{1}{\rho A} \underbrace{(S_{mD} - S_{mV})}_{\text{source term}} \quad (4-61)$$

where  $\delta$  is the film thickness.

The **wall film momentum equation** is derived from the standard Navier-Stokes momentum equation. For simplicity, incompressibility of the liquid building up the wall film is assumed.

$$\frac{\partial}{\partial t} u_f + (u_f \cdot \nabla) u_f = -\nabla \frac{p}{\rho_0} + \frac{\mu}{\rho_0} \Delta u_f + s_f \quad (4-62)$$

The **enthalpy balance equation** accounts for convective heat transfer within the film as well as all major heat transfer mechanisms and can be written as follows:

$$\underbrace{\frac{\partial h_i}{\partial t} \Delta V \rho_f}_{\text{change of energy stored in film}} + \underbrace{\rho_f \sum_j h_i u_{fj} ds_{ij}}_{\text{convective heat transfer within the film}} = \underbrace{\dot{H}_{s, wf}}_{\text{heat transfer from the wall to the film}} - \underbrace{\dot{H}_{s, fg}}_{\text{heat transfer between film and gas}} - \underbrace{\dot{m}_{ev} h_{ev}}_{\text{enthalpy transfer due to latent heat consumed during evaporation}} + \underbrace{\dot{H}_{s, imp}}_{\text{heat transfer via spray droplet impingement}} + \underbrace{\dot{H}_{s, ent}}_{\text{enthalpy loss via droplet entrainment}} \quad (4-63)$$

## Entrainment

When the gas velocity is high, shear forces cause droplets to be torn from the film surface back into the gas phase. These droplets are produced at or near surface waves. Within the wall film module, this phenomenon can be taken into account with the entrainment model. In this work, the **Schadel-Hanratty entrainment model** is used. The critical Weber number  $We_{cr,SH}$ , which specifies the onset of entrainment, is defined as follows:

$$We_{cr,SH} = \frac{\rho_g |\bar{u}_g - \bar{u}_f|^2 \delta}{\sigma} \quad (4-64)$$

It is a measure for the relationship between the fluid inertia and its surface tension  $\sigma$  and the average film velocity  $\bar{u}_f$ .

If the critical Weber number is greater than or equal 17 first droplets start to entrain. However, the entrainment model can account only for a mass flux that leaves the wall film. Hence, it acts as a mass source to the spray and as a mass sink to the film. The amount of mass sheared off the film per unit area and unit time is described by an empirical correlation of Schadel and Hanratty [Schadel et al., 1989].

To introduce these new droplets back to the spray, a droplet diameter has to be determined. Hence, a droplet mean diameter  $D_{vm,K}$  is calculated by using the **Kataoka droplet correlation model** [Kataoka et al., 1983].

$$D_{\text{vm,K}} = 0.028 \frac{\sigma}{\rho_g \bar{u}_g^2} Re_{\text{f,IM}}^{-\frac{1}{3}} Re_g^{\frac{2}{3}} \left( \frac{\rho_g}{\rho_f} \right)^{-\frac{1}{3}} \left( \frac{\mu_g}{\mu_f} \right)^{\frac{2}{3}} \quad (4-65)$$

where the film Reynolds number is defined as

$$Re_{\text{f,IM}} = \frac{4\bar{u}_f \delta}{\nu_f} \quad (4-66)$$

## Evaporation

The **SCR-thermolysis model** was selected (for more detailed description see chapter 4.3.6 and 4.6.5.2).

## Splashing

The **splashing model of Kuhnke** discussed in chapter 4.3.4 was chosen.

### 4.6.5.4 Thin walls

This chapter is based on the AVL user guide for the thin walls module [AVL FIRE™ Manual - Thin Walls Module, 2019].

In this work, the "**lateral heat conduction**" option is used in FIRE, which means that the solid wall boundary of the inner cylinder of the Scott chamber is modeled to solve for the heat conduction in the normal and lateral directions. The specified wall thickness is subdivided into a number of numerical cell layers that are used to solve the heat balance. The heat fluxes in normal and lateral directions are calculated based on the respective cell face areas, cell-center distances, conductivities, effective heat transfer coefficients, cell-center temperatures, as well as the fluid side and environment temperature.

The standard conduction equation (4-67) is integrated over a thin wall cell (control volume  $V$ ), yielding equation (4-68).

$$\frac{\partial \rho h}{\partial t} = \lambda \Delta T + Q; \quad dh = c_p dT \quad (4-67)$$

$h$  is the specific enthalpy,  $\rho$  stands for the density,  $t$  is the time,  $\lambda$  the thermal conductivity,  $T$  represents the temperature,  $c_p$  the specific heat and  $\Delta$  the Laplace operator. The specific source  $Q$  contains all external source terms resulting from heat exchange with the fluid or the environment (e.g., spray or wall film evaporation).

$$\frac{d}{dt} \int_V \rho h dV = \sum_{j=1}^{n_A} \int_{A_j} \lambda \overline{\nabla T}_j \cdot \overline{dA}_j + \sum_{j=1}^{n_B} \int_{B_j} q dB_j \quad (4-68)$$

The control volume  $V$  is computed as the product of the wall face area times the thickness of the respective wall cell layer. The  $n_A$  faces  $A_j$  represent the internal wall faces that are not in contact with the fluid or the environment. Heat conduction occurs only at these internal faces. The  $n_B$  faces  $B_j$  are the faces, which are in contact either with the fluid or with the environment.  $q$  are the corresponding energy sources due to spray or film evaporation and interaction with the fluid or environment.

## 5. Laboratory Experiments

Laboratory experiments served to validate the numerical model as well as the results of the numerical calculations.

### 5.1 Droplet size and velocity distribution measurements

Various measurement systems were used to characterize two-phase flow conditions, which will be briefly discussed here.

#### 5.1.1 Phase Doppler anemometry (PDA) measurements

The analysis of atomized liquids (sprays) is a very common PDA application used in combustion processes, fuel injection, spray painting, atmospheric and pharmaceutical sprays or nozzle sprays, to name a few [Montaser, 1998 (p. 358)]. It is a non-intrusive measurement method that uses the laser Doppler effect and does not require calibration. The measurement principle is based on light-scattering interferometry and allows the simultaneous measurement of statistical droplet size and velocity distributions as well as particle concentration and local size-velocity correlation. A brief description of the PDA technique is presented here for a dual-beam phase-Doppler particle size analyzer (Dantec Measurement Technology, Mahwah, NJ, USA). As shown in *Figure 5-1*, radiation from a laser is divided into four beams.

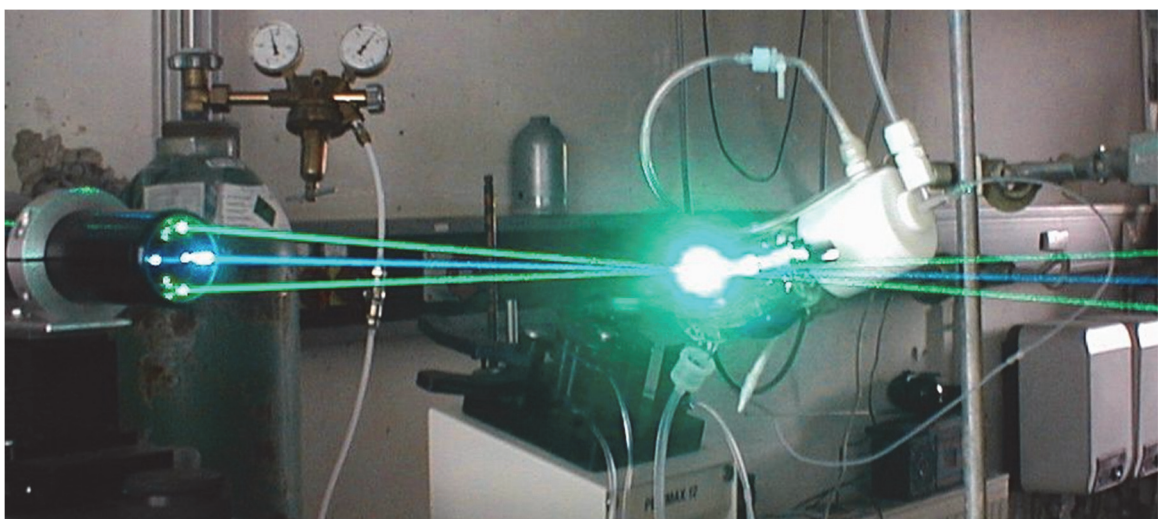


*Figure 5-1* Dual-beam phase-Doppler particle size analyzer (Dantec Measurement Technology, Mahwah, NJ, USA; source: E. Fasch).



The very small measurement volume is defined by the intersection of the four focused laser beams. Individual particles moving through the sample volume scatter light from the laser beams according to their size and velocity. The optical interference fringe pattern moves past the receiver optics at the Doppler frequency (*Figure 5-2*), which is proportional to the droplet velocity. The spatial frequency of the fringe pattern is inversely proportional to the droplet diameter.

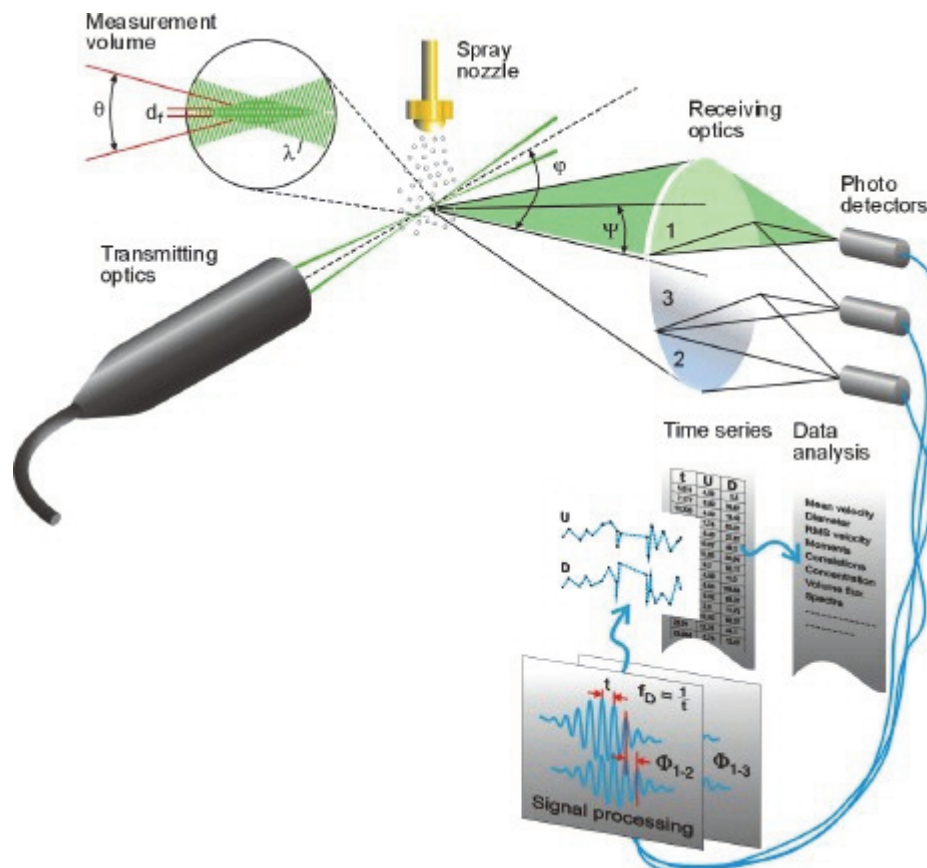


Figure 5-2 Measurement principle of phase Doppler anemometry (PDA) by courtesy of Dantec Dynamics.

With the four-beam arrangement particle sizes as well as axial and radial particle velocities are measured. Thus, a PDA system provides point measurements of spatial and temporal information for a particle field [Montaser, 1998].

### 5.1.2 Particle imaging velocimetry (PIV) measurements

Particle imaging velocimetry (PIV) is a non-intrusive whole-flow field measurement technique that provides both simultaneous and instantaneous particle velocity vectors in a

cross-section of a particle flow. PIV is essentially suitable for measurements in unsteady flows, since latent turbulent structures can be resolved. Therefore, the results are similar to CFD calculations. A light sheet illuminates the flow in the target area (*Figure 5-3*). The velocity and direction of the particles are derived by evaluating the particle motion between two light pulses. Each light pulse is recorded by the camera and provides a separate image. A map of the velocity vector over the entire target area is created by accurately measuring the displacement with sub-pixel interpolation. The technique is valid from low to supersonic velocities [Montaser, 1998].

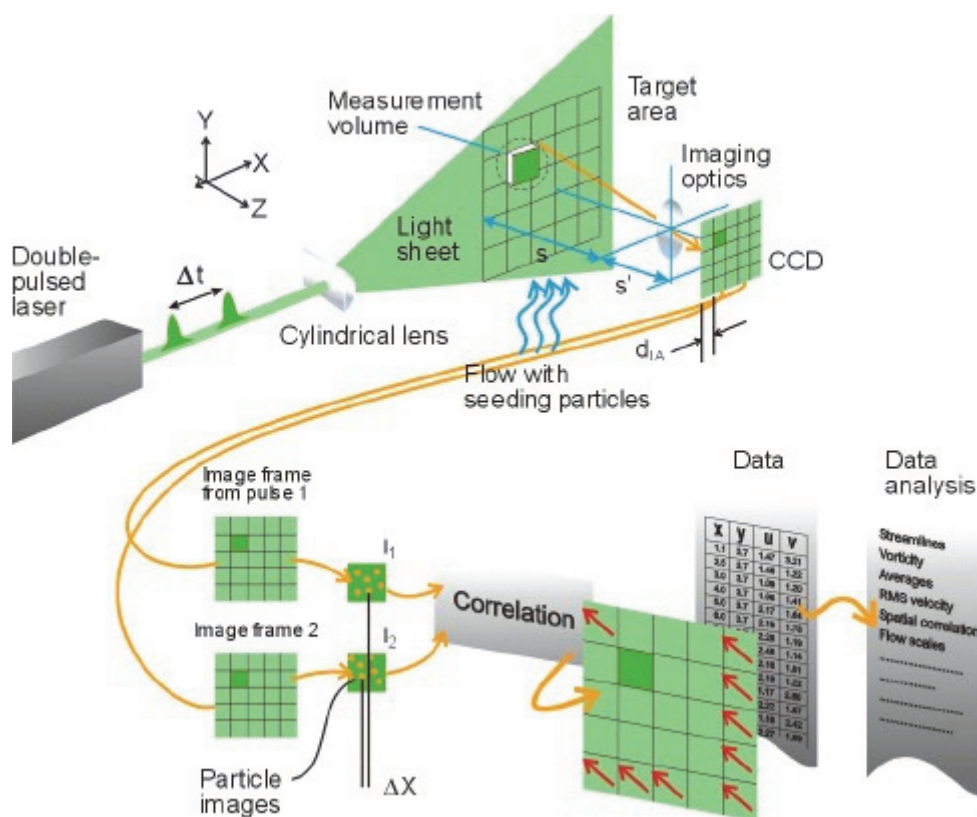
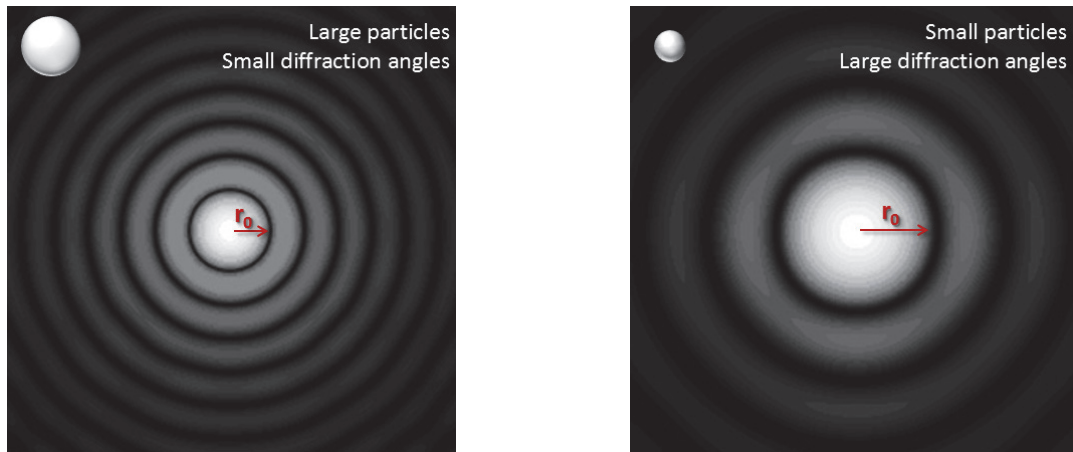


Figure 5-3 Measurement principle of particle imaging velocimetry (PIV) by courtesy of Dantec Dynamics.

### 5.1.3 Fraunhofer laser diffraction measurements

The laser diffraction / scattering method is a widely used non-intrusive technique. It is based on the phenomenon that particles scatter light in all directions, with the intensity distribution depending on the particle size. *Figure 5-4* shows characteristic scattered light patterns of individual spherical particles.



*Figure 5-4* Diffraction pattern of a large particle (left) and of a smaller particle (right) by courtesy of Sympatec (© Sympatec GmbH).

It is important to note that the spacing of the rings depends on the particle size. When investigating a particle collective, there is a superposition of the scattered light intensity patterns produced by the individual particles. Using a Fourier transform receiver lens to transfer the light intensity patterns to a multi-element photodetector, the light energy distribution can be registered. A schematic diagram of a Fraunhofer laser diffraction system is shown in *Figure 5-5*.

Fraunhofer diffraction can be used for measurements of particles down to the micrometer range. Here, only the part of the light deflection that arises exclusively from diffraction is considered. Advantageously, knowledge of the optical properties of the particles is not required. Mie scattering theory [Wozniak, 2003 (p. 110)] has to be used when the diameter of the particles is not far above the wavelength of the laser. In contrast to Fraunhofer diffraction, the optical properties of the particles must be known [Montaser, 1998], [Wozniak, 2003].

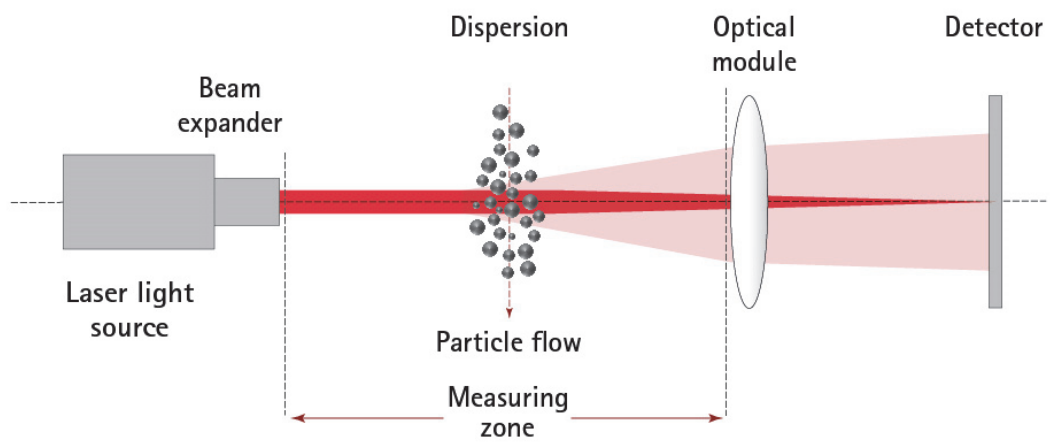


Figure 5-5 Top: Measurement principle of a Fraunhofer laser diffraction system by courtesy of Sympatec (© Sympatec GmbH); bottom: optical arrangement in the experiment (source: E. Fasch).

---

## 5.1.4 Instruments and equipment

*Table 5-1: Instruments and equipment used for laboratory experiments.*

---

Dual-beam phase–Doppler particle size analyzer	Dantec Measurement Technology, Mahwah, NJ, USA
High-Speed-PIV-Laser Nd:YLF, LDY 303HE	Litron Lasers, Warwickshire, England
High Speed Controller	LaVision, Bicester, UK
High-Speed-Kamera Imager Pro HS 4M	LaVision, Bicester, UK
Software DaVis 8.40	LaVision, Bicester, UK
Laser diffraction sensor Helos KR-Vario	Sympatec GmbH, Clausthal-Zellerfeld, Germany

---

## 5.2 Mass transport efficiency measurements using the continuous weighing method

The nebulizer mass transport efficiency obtained by the so-called “**continuous weighing method**” is defined as the fraction of the solution that leaves the spray chamber after nebulization. The solvent mass transported to the plasma per time unit  $\dot{Q}_{\text{SPL}}$  is calculated from the difference between the liquid uptake rate  $\dot{Q}_{\text{L}}$  and the nebulizer drain rate  $\dot{Q}_{\text{ND}}$  [Maessen et al. 1984], [Maessen et al. 1986]. Major uncertainty sources and their magnitudes are determined according to [Eurachem/ Citac Guide CG 4, 2012], [Guide to the Expression of Uncertainty in Measurement, JCGM GUM-6, 2020].

### 5.2.1 Specification of the measurand

The aim of this specification is to describe the measurement procedure for the determination of the solvent plasma load. This description consists of a listing of the measurement procedure, along with a mathematical expression of the measurand and the parameters dependent on it.

#### Procedure

The experimental setup is illustrated in *Figure 5-8*; the instruments and equipment used are listed in *Table 5-2*.

The measurement method consists of the following steps (see also *Figure 5-6*):

- i. The liquid uptake rate is set by selecting the appropriate pump speed of the peristaltic pump. Over a time period of 10 minutes the increase of weight of flask 1 is recorded every 20 seconds. (*Figure 5-7*). The slope ( $\text{g min}^{-1}$ ) is then calculated, which represents the value of the liquid uptake rate  $\dot{Q}_{\text{L}} = 0.108 \text{ g min}^{-1}$ .
- ii. A lead time of 60 minutes is selected to equilibrate the nebulizer/ spray chamber system. The liquid uptake rate  $\dot{Q}_{\text{L}}$  comes to  $0.108 \text{ g min}^{-1}$  (see above) and the gas flow rate  $\dot{Q}_{\text{G}}$  is set to  $0.80 \text{ L min}^{-1}$  by means of a mass flow controller. Using the appropriate tubing (see *Table 5-2*) the nebulizer drain rate  $\dot{Q}_{\text{ND}}$  should be about three times the nebulizer uptake rate  $\dot{Q}_{\text{L}}$ .

- iii. The decrease of solvent weight is recorded at ambient temperature ( $25^{\circ}\text{C} \pm 3^{\circ}\text{C}$ ). Owing to fluctuations in the transport of the liquid through the spray chamber, the decrease in weight between two subsequent measurements should exceed a minimum value. In case of water as solvent, a minimum weight decrease between 0.3 g and 0.5 g was found to be adequate [Maessen et al. 1984], [Maessen et al. 1986]. To compensate for irregularities in the liquid transport to the drain (caused for example by droplet formation), the total quantity of liquid nebulized during a complete experiment should be in the range of a few grams. During a time period of 4 hours the of solvent weight is recorded every 840 s (14 min) and yields a curve in which the slope  $b_i$  represents the solvent plasma load ( $\text{g min}^{-1}$ ) [Kreuning et al., 1987].
- iv. 5 measurement replications yield  $b_1, b_2, b_3, b_4, b_5$ .

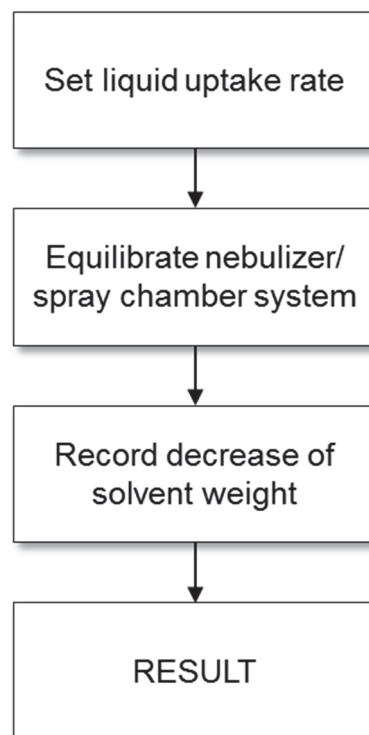


Figure 5-6 Determination of the solvent plasma load using the continuous weighing method.

Table 5-2: Instruments and equipment.

Nebulizer	MicroMist 100, Glass Expansion Pty. Ltd., Melbourne, Australia
Spray chamber	Scott-type double-pass spray chamber ( $V \sim 77$ mL)
Peristaltic pump	Perimax 12, Spetec GmbH, Erding, Germany
Tubing	Sample: Tygon black/black (ID = 0.76 mm) Nebulizer drain: Tygon purple/black (ID = 2.29 mm) Sample line: PTFE tubing (ID = 0.86 mm)
Mass flow controller	GFC 100, Kobold Instruments GmbH, Wien, Austria
Programmable logic controller (PLC)	Allen-Bradley SLC 5/05, Rockwell Automation, Linz, Austria
Balance	Mettler Toledo XS205DU, Mettler-Toledo AG, Greifensee, Schweiz
Liquid	acidified water ( $w(\text{HNO}_3) = 0.01$ )
Ar gas quality	6.0

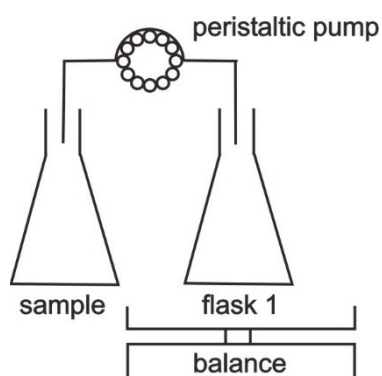


Figure 5-7 Experimental setup for determining the liquid uptake rate.



## Calculation

The measurand is the mean solvent plasma load, calculated from the 5 measurement replications of the slope of the regression line  $b_i$ , i.e., the loss of solvent weight per time unit:

$$\dot{Q}_{\text{SPL}} = \frac{b_1 + b_2 + \dots + b_5}{5} \quad (5-1)$$

where

$\dot{Q}_{\text{SPL}}$ : solvent plasma load [ $\text{g min}^{-1}$ ]

$b_i$ : slope of the regression line ( $i = 1, 2, \dots, 5$ ) [ $\text{g min}^{-1}$ ]

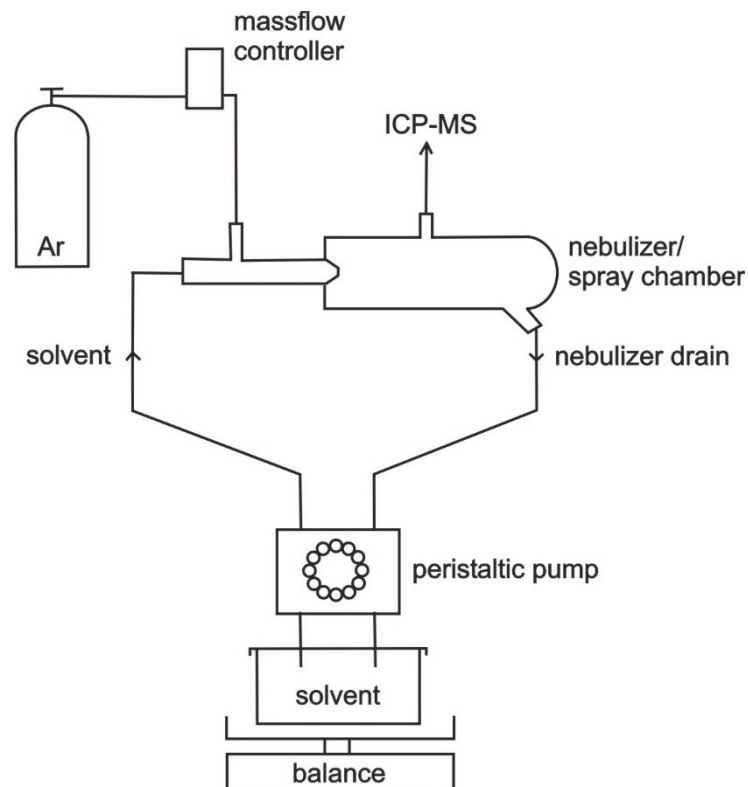
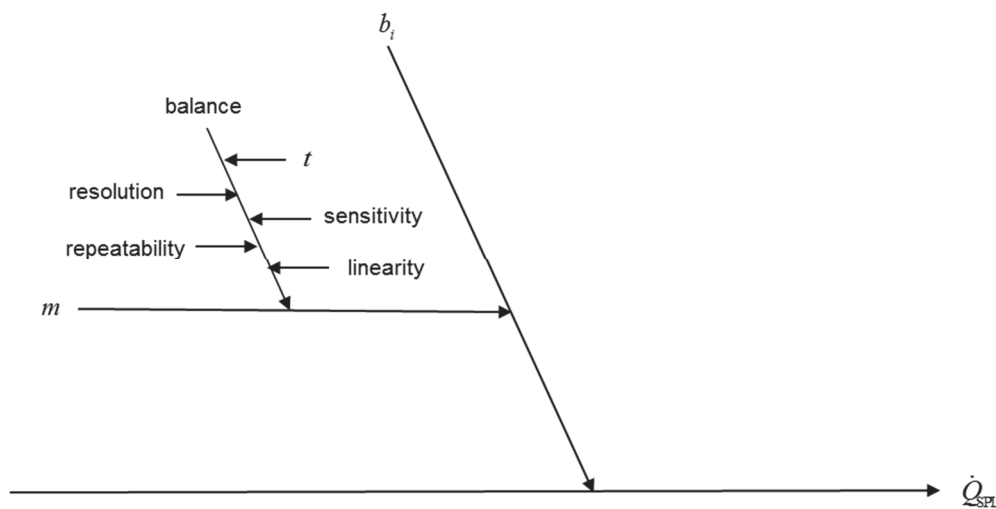


Figure 5-8 Experimental setup of the “continuous weighing method”.

## 5.2.2 Identifying and analyzing uncertainty sources

An Ishikawa diagram (*Figure 5-9*) shows the parameters affecting the calculation of the five slopes  $b_i$  ( $i = 1, 2, \dots, 5$ ) that are used in the equation for the determination of the measurand. Uncertainty sources are added for each branch that may affect the value of the measurand.



*Figure 5-9* Ishikawa diagram for mass transport measurements on nebulizer systems using the “continuous weighing method”.

Since the different repeatability terms for the calculation of the slopes  $b_i$  are reflected in the total repeatability of the result, they can be combined into one contribution as shown in *Figure 5-10*. Equation (5-1) is therefore extended by a dummy factor  $f$

$$\dot{Q}_{\text{SPL}} = \frac{b_1 + b_2 + \dots + b_5}{5} \cdot f \quad (5-2)$$

where  $f$  represents the correction term for the standard deviation of the result because of the uncertainty introduced by measurement replication.

*Figure 5-10* shows that there are actually six uncertainty components, the five already mentioned above and the one due to measurement replication.

### Slope of the regression line $b_i$

The nebulized mass of the liquid is directly quantified by weighing as difference of the liquid uptake rate  $\dot{Q}_L$  and the nebulizer drain rate  $\dot{Q}_{ND}$ . Data acquisition takes place automatically every 14 min (840 s) over a period of 4 hours. The slope is calculated from this data using linear regression.

In order to quantify the uncertainty of the slope of the regression line  $b_i$ , it is necessary to take into account, on the one hand, the uncertainty of the calculated regression slope and, on the other hand, the uncertainty of the weighing procedure itself (i.e., the uncertainty of the mass  $m$ ).

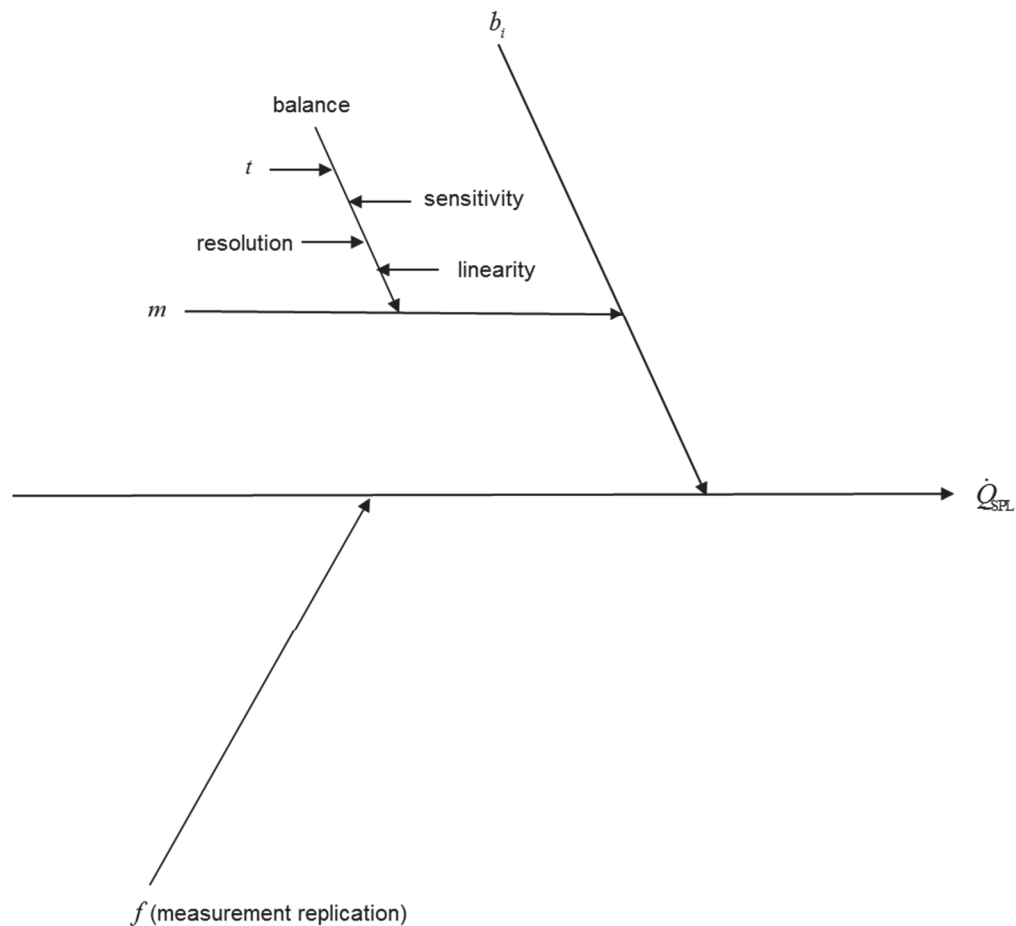


Figure 5-10 Final Ishikawa diagram with combined repeatabilities for mass transport measurements on nebulizer systems using the “continuous weighing method”.

- Linear least squares calibration  $b_i$

The estimation of uncertainty is carried out according to the statistical model for linear regression [Bennet et al., 1967], [Hartung et al., 1989], [Rösslein, 2013].

- Mass  $m$

Mass is calculated as the difference of two subsequent weighings, with the same balance in a quite narrow range. Each weighing is subject to the uncertainty of the time of the data acquisition and the uncertainty of the calibration of the balance.

Weighing intervals are preset by the balance and the uncertainty introduced by this does not need to be investigated separately. It is assumed that this uncertainty is included in the separate consideration of the repeatability (see below).

The balance manufacturer specifies the following uncertainty sources for the weighing process: the repeatability, the readability (i.e., digital resolution) of the scale and the uncertainty in the calibration function of the scale. This calibration function again has two potential uncertainty contributions, sensitivity and linearity. The influence of both the sensitivity and the linearity on the uncertainty budget is negligible, as the determination of the mass results from a measured mass difference in a narrow range on the same balance. The same applies to the uncertainty of balance readability, which is ultimately reflected in the measurement repeatability. Based on the above considerations, it is concluded that the influence of the weighing procedure can be neglected and is therefore not included in the calculation of the combined measurement uncertainty.

### **Measurement replication uncertainty $f$**

The uncertainty of the measurement replication is calculated as the standard deviation of the mean of  $b_i$ . This uncertainty component accounts for the repeatability contributions from all of the terms in the measurement equation.

### 5.2.3 Quantifying uncertainty components

The magnitude of each uncertainty component identified in 5.2.2 (see also *Figure 5-10*) needs to be quantified and converted to a standard uncertainty.

#### Slope of the regression line $b$

Calculations follow the statistical model for linear regression by assuming the relationship:

$$y = \alpha + \beta x \quad (5-3)$$

In this case it is possible to suppose that the intercept  $\alpha=0$  [Bennet et al., 1967], [Hartung et al., 1989], [Rösslein, 2013] which leads to the equation stated below:

$$y = \beta x \quad (5-4)$$

For the regression line

$$\hat{y} = \beta x_i \quad (5-5)$$

the least square estimator  $b$  for  $\beta$  is calculated using the following equation:

$$b = \frac{\sum_{i=1}^n x_i y_i}{\sum_{i=1}^n x_i^2} \quad (5-6)$$

The uncertainty of the slope of the regression line  $u(b_i)$  can be expressed as

$$u(b_i) = \frac{s_{Res}}{\sqrt{\sum_{i=1}^n x_i^2}} \quad (5-7)$$

where the square of the residual standard deviation  $s_{Res}^2$  amounts to

$$s_{Res}^2 = \frac{1}{n-1} \sum_{i=1}^n (y_i - \hat{y}_i)^2 \quad (5-8)$$

The uncertainty of the slope of the regression line is calculated as follows

$$u^2(b) = \frac{\sum_{i=1}^n u_{b_i}^2}{5} \quad (5-9)$$

Table 5-3 Residual standard deviations ( $s_{\text{Res}}$ ) and uncertainties of the different slopes ( $b_i$ ) (rounded values).

	$b_i$	$s_{\text{Res}}$	$\sum x_i^2$	$u(b_i)$
Nr.	[g min <sup>-1</sup> ]	[g]	[min <sup>2</sup> ]	[g min <sup>-1</sup> ]
1	0.025	0.040	349860	6.74E-05
2	0.026	0.047	349860	7.87E-05
3	0.025	0.027	349860	4.59E-05
4	0.026	0.037	349860	6.29E-05
5	0.027	0.039	349860	6.63E-05

$$u(b) = 5.9 \text{ E-}05 \text{ g min}^{-1}$$

### Measurement replication $f$

The uncertainty component attributable the measurement replication  $u(f)$  is calculated as the standard deviation of the mean. In this example the replication uncertainty is calculated from the set of measurements as  $6.3 \text{ E-}04 \text{ g min}^{-1}$ . This uncertainty component incorporates the uncertainty due to repeatability from all the terms in the measurement equation.

### 5.2.4 Calculating the combined standard uncertainty

$\dot{Q}_{\text{SPL}}$  is calculated according to equation (5-2):

$$\dot{Q}_{\text{SPL}} = \frac{b_1 + b_2 + \dots + b_5}{5} \cdot f \quad [\text{g min}^{-1}]$$

The values of the parameters, their standard uncertainties and relative standard uncertainties are summarized in *Table 5-4*.

Inserting  $b_i$  and the correction term for the standard deviation of the measurement replication  $f$  in (5-2) yields

$$\dot{Q}_{\text{SPL}} = \frac{b_1 + b_2 + \dots + b_5}{5} \cdot 1$$

$$\dot{Q}_{\text{SPL}} = 0.026 \text{ g min}^{-1}$$

*Table 5-4 Values and uncertainties for the measurement of the solvent plasma load using the “continuous weighing method” (rounded values).*

	Description	Value $x$	Standard uncertainty $u(x)$	Relative standard uncertainty $u(x)/x$
$b$	slope of the regression line	0.026 g min <sup>-1</sup>	5.9 E-05 g min <sup>-1</sup>	0.0023
$f$	Measurement replication	1.000	6.3 E-04 g min <sup>-1</sup> (0.026 g min <sup>-1</sup> )	0.0241

The standard uncertainty of this result equals to the square root of the sum of the squares of the uncertainties associated with each component:

$$\frac{u_c(\dot{Q}_{\text{SPL}})}{\dot{Q}_{\text{SPL}}} = \sqrt{\left( \frac{u(b \text{ (regression)})^2}{m} + \frac{u(f)^2}{f} \right)}$$

$$= \sqrt{(0.0023^2 + 0.0241^2)} = 0.024$$

$$u_c(\dot{Q}_{\text{SPL}}) = \dot{Q}_{\text{SPL}} \cdot 0.024 = 0.026 \text{ g min}^{-1} \cdot 0.024 = 0.00063 \text{ g min}^{-1}$$

$$u_c(\dot{Q}_{\text{SPL}}) = 6.3 \text{ E-04 g min}^{-1}$$

The different uncertainty components and their contributions to the combined standard uncertainty are shown in *Figure 5-11*.

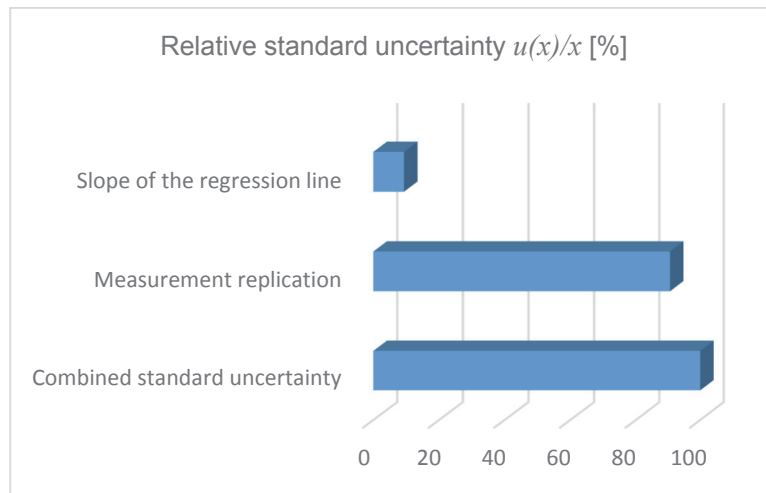


*Figure 5-11 Contributions (slope of the regression line and measurement replication) to the uncertainty budget of the different parameters on the measurement of the solvent plasma load using the “continuous weighing method”.*

The expanded uncertainty  $U$  is obtained by multiplying the combined standard uncertainty with a coverage factor. This is necessary to provide an interval that may be expected to encompass a large fraction of the distribution of values that could reasonably be attributed to the measurand. For a confidence interval of 95 % the coverage factor amounts to 2, giving:

$$U(\dot{Q}_{\text{SPL}}) = u_c(\dot{Q}_{\text{SPL}}) \cdot 2 = 6.3 \text{ E-04} \cdot 2 \text{ g min}^{-1}$$

$$U(\dot{Q}_{\text{SPL}}) = 1.3 \text{ E-03 g min}^{-1}$$

Consequently, the aerosol mass transport amounts to:

$$\dot{Q}_{\text{SPL}} = 0.026 \pm 0.0013 \text{ g min}^{-1}$$



### 5.2.5 Conclusive result

For the sample introduction system with the parameters  $\dot{Q}_G = 0.80 \text{ L min}^{-1}$  Ar and  $\dot{Q}_L = 0.108 \text{ g min}^{-1}$  acidified water ( $w(\text{HNO}_3) = 0.01$ ), a fraction of **24 %  $\pm$  1 %** of the initially introduced liquid mass is able to leave the spray chamber as aerosol and liquid vapor.

Using the “continuous weighing method” to determine the sample mass transported to the plasma it can be concluded that the dominant component of uncertainty is that attributable to the measurement replication  $u(f)$ . The continuous weighing method is known to provide accurate results but has the disadvantage of being very time consuming and labor intensive [Kreuning et al., 1987].

## 5.3 Mass transport efficiency measurements using the waste collection method

The simplest, but at the same time the most inaccurate indirect method of determining the mass transport efficiency is to collect and quantify the amount of waste (i.e., the amount of liquid which is not transported to the plasma) over a certain period of time. The mass transported to the plasma can be estimated by the difference between the amount of sample uptake mass and the mass passing to waste and divide this value by the observation time period. Although this method is found to be subject to a high degree of uncertainty [Smith et al., 1982], it makes sense to employ it to reveal trends related to the measurement of analyte transport efficiency (see *chapter 5.4*) because it is fast and simple. The major sources of uncertainty and their magnitudes are evaluated according to [Eurachem/ Citac Guide CG 4, 2012], [Guide to the Expression of Uncertainty in Measurement, 2020].

### 5.3.1 Specification

Starting from a comprehensive description of the waste collection method for determining the solvent plasma load, the measurand is defined. The various measurement steps are listed below and a mathematical statement is spelled out about the measurand and the parameters that depend on it.

#### Procedure

The measurement method is divided into the following steps as depicted in *Figure 5-12*.

- i. The liquid uptake rate  $\dot{Q}_L$  is set to  $0.11 \text{ mL min}^{-1}$  acidified water ( $w(\text{HNO}_3) = 0.02$ ) by means of a gradient pump and the gas flow rate  $\dot{Q}_G = 0.80 \text{ L min}^{-1}$  is set by a mass flow controller. Using the peristaltic pump with an appropriate tubing the nebulizer drain rate  $\dot{Q}_{\text{ND}}$  is about three times the nebulizer uptake rate  $\dot{Q}_L$ . The spray chamber temperature is adjusted to  $20 \text{ }^\circ\text{C}$  using a heating and cooling thermostat (see *Table 5-5*).
- ii. A pre-running time of 60 minutes is selected to equilibrate the nebulizer / spray chamber system.

- iii. Before the analysis, the weight of the sample vessel (empty and with sample) and that of the waste container are determined. The waste collection is started by quickly placing the sample tube into the sample vessel and the waste tube into the empty waste vessel. After 90 minutes, the waste collection is stopped by quickly removing the sample and waste tubes from their respective vessel.
- iv. Both the mass of the sample vessel and that of the waste vessel are determined by weighing.
- v. 6 measurement replications yield  $x_1, x_2, x_3, x_4, x_5, x_6$ .

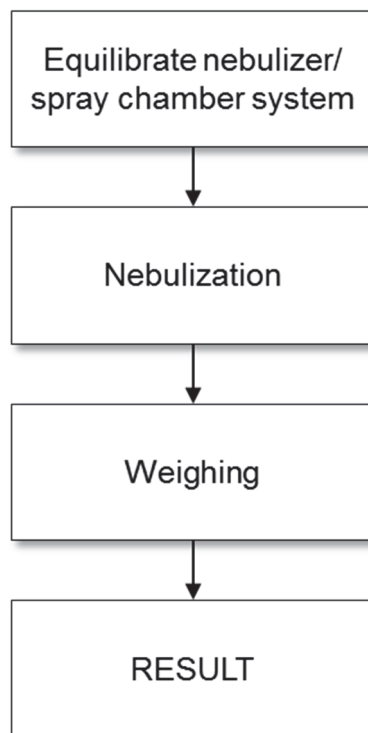


Figure 5-12 Determination of the solvent plasma load using the continuous weighing method.

Table 5-5 Instruments and equipment.

Nebulizer	MicroMist 100, Glass Expansion Pty. Ltd., Melbourne, Australia
Spray chamber	Scott-type double-pass spray chamber ( $V \sim 77$ mL)
Heating and cooling thermostat	Lauda Eco Silver, LAUDA DR. R. WOBSEER GMBH & CO. KG, 97922 Lauda-Koenigshofen, Germany
Gradient pump	GS50 Gradient Pump, Dionex Corporation, 1228 Titan Way, Sunnyvale, California 94088-3603 U.S.A.
Peristaltic pump	Perimax 12, Spetec GmbH, Erding, Germany
Tubing	Nebulizer drain: Tygon purple/black (ID = 2.29 mm) Sample line: PTFE tubing (ID = 0.86 mm)
Mass flow controller	GFC 100, Kobold Instruments GmbH, Wien, Austria
PLC	Allen-Bradley SLC 5/05, Rockwell Automation, Linz, Austria
Balance	Mettler Toledo XS205DU, Mettler-Toledo AG, Greifensee, Schweiz
sample solution	acidified water ( $w(\text{HNO}_3) = 0.02$ )
Ar gas quality	6.0

## Calculation

The measurand is the solvent plasma load  $\dot{Q}_{\text{SPL}}$ , which depends on the mean of the 6 measurement replications  $x_i$  of the loss of solvent weight per nebulization time  $t$  (i.e., the difference between the mass of the sample uptake and the mass passing to waste, divided by the nebulization time):

$$x_i = \frac{m_{\text{inlet}} - m_{\text{nebulizer drain}}}{t} \quad (5-10)$$

$$\dot{Q}_{\text{SPL}} = \frac{x_1 + x_2 + \dots + x_6}{6} \quad (5-11)$$

where

- $x_i$ : loss of solvent weight per nebulization time of measurement number  $i$   
( $i = 1,2..6$ ) [ $\text{g min}^{-1}$ ]
- $m_{\text{inlet}}$ : mass of the sample solution (before nebulization) [g]
- $m_{\text{nebulizer drain}}$ : mass of the collected sample solution passing to waste [g]
- $t$ : nebulization time [min]
- $\dot{Q}_{\text{SPL}}$ : solvent plasma load [ $\text{g min}^{-1}$ ]

### 5.3.2 Identifying and analysing uncertainty sources

A cause and effect diagram is drawn (Figure 5-13) showing the six parameters  $x_i$  ( $i = 1,2..6$ ) of the equation of the measurand as the main branches. Any further uncertainty factor is added for each branch that may influence the value of the measurand.

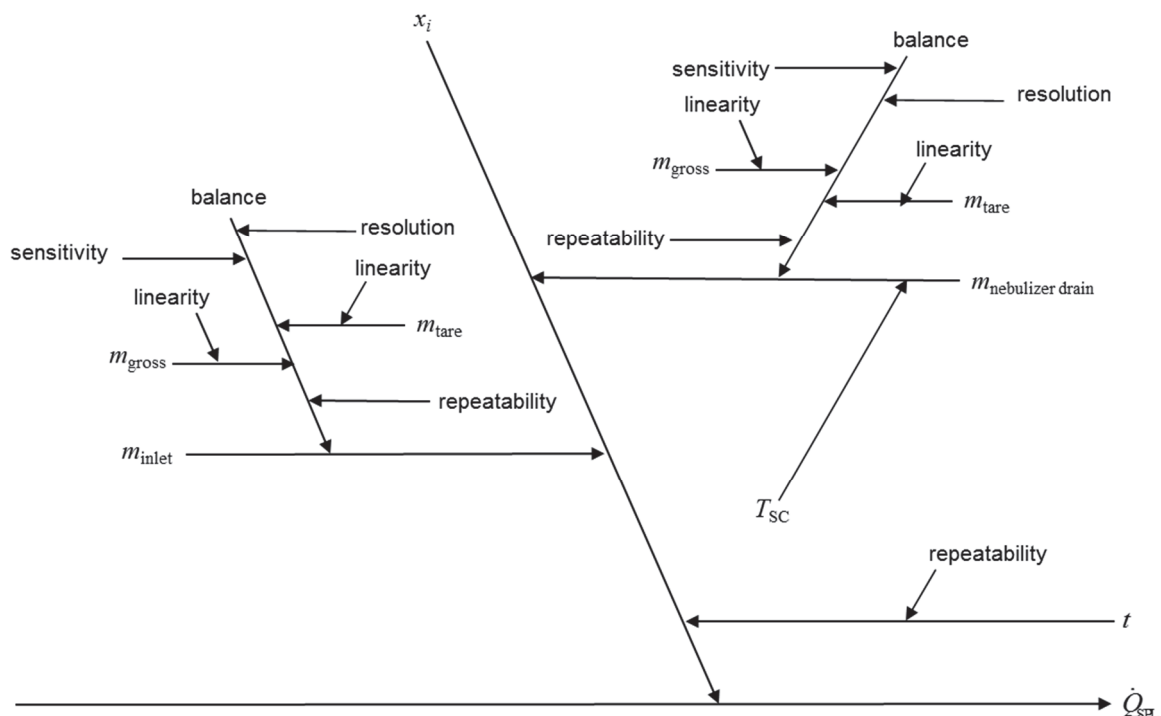


Figure 5-13 Cause and effect diagram for mass transport measurements on nebulizer systems using the "waste collection method".

Since the repeatability terms for the different  $x_i$  are reflected into the total repeatability of the result, they are combined into one factor as shown in *Figure 5-10* and *equation (5-11)* is extended by an adequate dummy factor  $f$

$$\dot{Q}_{SPL} = \frac{x_1 + x_2 + \dots + x_6}{6} \cdot f \tag{5-12}$$

where  $f$  represents the correction term for the standard deviation of the measurement replication.

*Figure 5-14* shows that there are actually seven uncertainty components, the six above mentioned and the measurement replication.

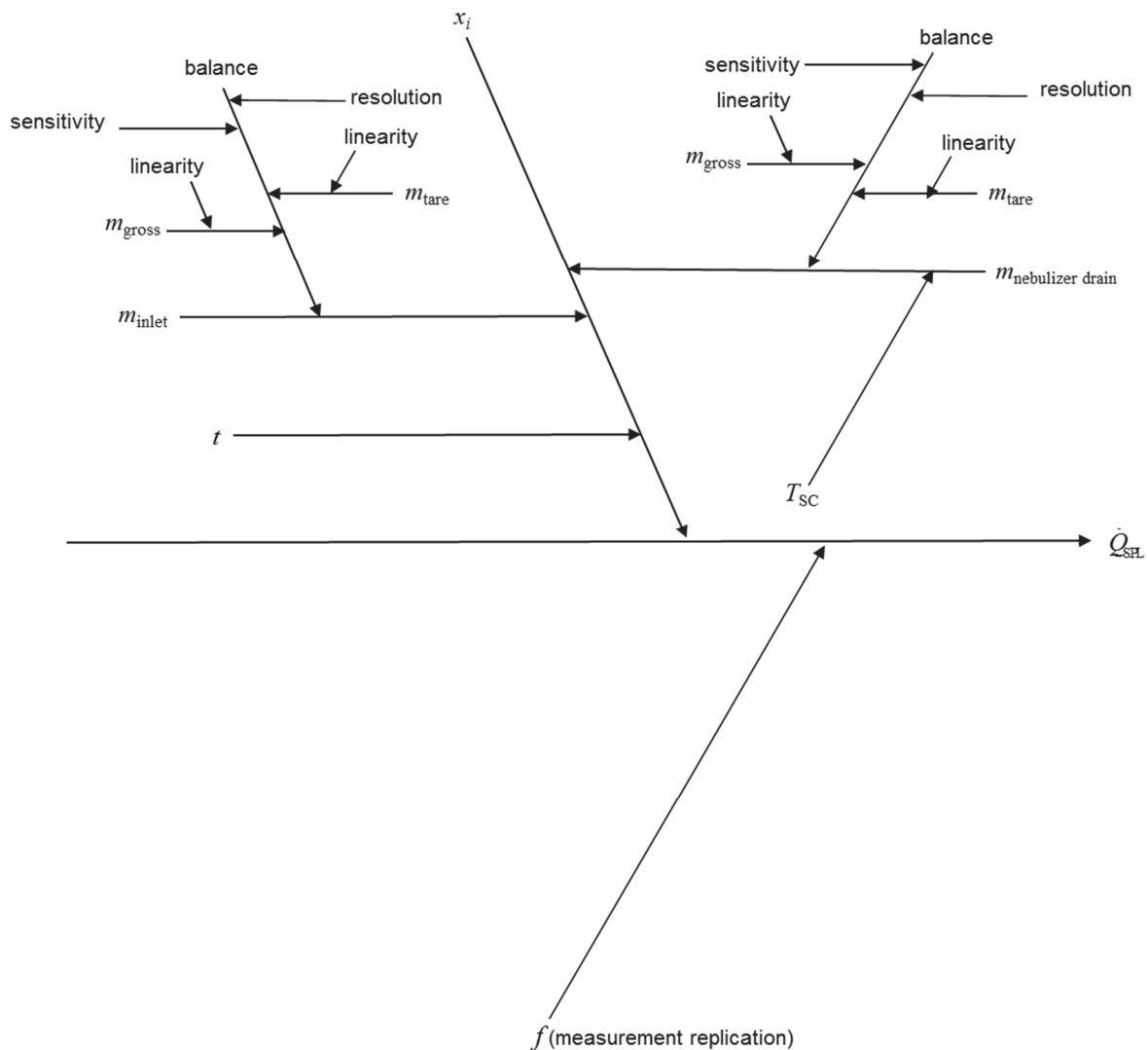


*Figure 5-14* Final cause and effect diagram with combined repeatabilities for mass transport measurements on nebulizer systems using the “waste collection method”.

## Loss of solvent weight per time unit $x_i$

The rate of the loss of solvent weight is quantified by calculating the difference between the mass of the sample uptake  $m_{\text{inlet}}$  and the mass passing to waste  $m_{\text{nebulizer drain}}$  divided by the nebulization time  $t$ .

Each  $x_i$  is influenced by three different uncertainty quantities. Two branches of the Ishikawa diagram have to be drawn for both the weighing procedure of the sample uptake and the mass passing to waste and another one for the uncertainty of the time.

- Mass  $m_{\text{inlet}}$

Mass is calculated from a measured mass difference in a narrow range on the same balance. Each of the weighings is subject to the uncertainty of the balance.

The balance manufacturer specifies the following uncertainty sources for the tared weighing process: the repeatability, the readability (i.e., digital resolution) of the scale and the uncertainty in the calibration function of the scale. This calibration function again has two potential uncertainty sources, the sensitivity and the linearity of the balance. Sensitivity is deemed to be negligible, since the determination of the mass results from a measured mass difference in a narrow range of the same balance.

- Mass  $m_{\text{nebulizer drain}}$

The uncertainty associated with the determination of the mass of the nebulizer drain begins with the same assumptions as the uncertainty of  $m_{\text{inlet}}$ . In addition, however, an uncertainty term resulting from the thermostatic control of the spray chamber must be taken into account. The uncertainty of the heating and cooling thermostat stems from the uncertainty of the accuracy of the temperature measurement, the uncertainty of temperature stability and the uncertainty of the readability of the thermostat.

- Time  $t$

Since the nebulization time period is measured manually using a stopwatch and the standard operating procedure states that the corresponding sample and waste lines are to be placed "without much delay", it can be assumed that the nebulization time must be  $> 90$  minutes. The time measurement starts after the sample and waste lines are placed and ends before they are removed from the vessels. Therefore, the nebulization time is

set to 91 minutes and the associated uncertainty is reflected accordingly via the measurement replication.

### Measurement replication $u(f)$

The uncertainty of the measurement replication is calculated as the standard deviation of the mean of the measurand  $x_i$ . This uncertainty component incorporates the repeatability from all of the terms in the measurement equation.

### 5.3.3 Quantifying uncertainty components

The magnitude of each uncertainty component identified in 5.3.2 (see also *Figure 5-14*) needs to be quantified and converted to a standard uncertainty.

#### Mass (inlet) $m_{\text{inlet}}$

Because of the combined repeatability term, it is not necessary to consider the repeatability of the balance separately. The sensitivity contribution to the uncertainty budget of the balance can also be neglected based on the above considerations. The uncertainty of the mass thus results from the uncertainty of the linearity and the uncertainty of the readability of the balance.

The certificate of the balance specifies linearity and resolution as 0.2 mg and 0.01 mg, respectively. The standard uncertainty of the mass is obtained from (according to [Rösslein, 2013 (p. 48)])

$$u(m_{\text{inlet}}) = \sqrt{3 \cdot u_{\text{linearity, balance}}^2 + 3 \cdot u_{\text{readability, balance}}^2} \quad (5-13)$$

The uncertainty of balance linearity is calculated with the aid of a rectangular distribution. For the readability term a triangular distribution is used.

- Linearity:  $u_{\text{linearity, balance}} = \frac{0.2}{\sqrt{3}} = 0.115 \text{ mg}$
- Readability:  $u_{\text{readability, balance}} = \frac{0.01}{\sqrt{6}} = 0.00408 \text{ mg}$

This gives for the standard uncertainty of the mass  $u(m_{\text{inlet}})$ :



$$u(m_{\text{inlet}}) = \sqrt{3 \cdot 0.115^2 + 3 \cdot 0.00408^2} \text{ mg}$$

$$u(m_{\text{inlet}}) = 2.0 \text{ E-04 g}$$

### Mass (nebulizer drain) $m_{\text{nebulizer drain}}$

This estimate takes into account the contributions of the balance ((according to [Rösslein, 2013 (p. 48)])) and the uncertainty of the heating and cooling device.

$$u(\text{balance}) = \sqrt{2 \cdot u_{\text{linearity, balance}}^2 + 2 \cdot u_{\text{readability, balance}}^2}$$

$$u(\text{balance}) = \sqrt{2 \cdot 0.115^2 + 2 \cdot 0.00408^2} \text{ mg}$$

$$u(\text{balance}) = 1.6 \text{ E-04 g}$$

The certificate of the heating and cooling device indicates temperature accuracy and stability as 0.3 K and 0.01 K, respectively. The readability is specified with 0.01 K. Thus, the standard uncertainty of the thermostat contribution to the uncertainty of the mass is calculated as follows:

$$u(T_{\text{SC}}) = \sqrt{u_{\text{accuracy, thermostat}}^2 + u_{\text{stability, thermostat}}^2 + u_{\text{readability, thermostat}}^2} \quad (5-14)$$

The uncertainties of temperature accuracy and temperature stability are determined with the aid of a rectangular distribution, while a triangular distribution is used for the contribution to readability.

- Accuracy:  $u_{\text{accuracy, thermostat}} = \frac{0.3}{\sqrt{3}} = 0.173 \text{ } ^\circ\text{C}$
- Stability:  $u_{\text{stability, thermostat}} = \frac{0.01}{\sqrt{3}} = 0.00577 \text{ } ^\circ\text{C}$
- Readability:  $u_{\text{readability, balance}} = \frac{0.01}{\sqrt{6}} = 0.00408 \text{ } ^\circ\text{C}$

This gives the following expression for the standard uncertainty of the spray chamber temperature  $u(T_{\text{SC}})$ :

$$u(T_{\text{SC}}) = \sqrt{0.173^2 + 0.00577^2 + 0.00408^2} \text{ } ^\circ\text{C}$$

$$u(T_{\text{SC}}) = 0.17 \text{ } ^\circ\text{C}$$

### Time $t$

For the above reasons, the nebulization time was corrected to 91 minutes and the associated uncertainty is taken into account via the measurement replication.

### Measurement replication $f$

The uncertainty component of the measurement replication  $u(f)$  is calculated as the standard deviation of the mean (see *Table 5-6*). In this example, the replication uncertainty is calculated from the series of experiments to be  $2.8 \text{ E-}03 \text{ g min}^{-1}$ . This uncertainty component incorporates the repeatability from all the terms in the measurement equation.

$$u(f) = 2.8 \text{ E-}03 \text{ g min}^{-1}$$

*Table 5-6 Results from experiment (rounded values).*

$i$	$m_{\text{inlet}}$	$m_{\text{nebulizer drain}}$	$t$	$\dot{Q}_{\text{SPL}}$
[-]	[g]	[g]	[min]	[g min <sup>-1</sup> ]
1	9.500	7.456	90	0.023
2	9.765	7.500	90	0.025
3	9.473	7.005	90	0.027
4	9.734	7.418	90	0.026
5	9.674	6.868	90	0.031
6	9.506	7.069	90	0.027

### 5.3.4 Calculating the combined standard uncertainty

$\dot{Q}_{\text{SPL}}$  is calculated according to equation (5-12):

$$\dot{Q}_{\text{SPL}} = \frac{x_1 + x_2 + \dots + x_6}{6} \cdot f \quad [\text{g min}^{-1}]$$

The values of the parameters, their standard uncertainties and relative standard uncertainties are summarized in *Table 5-7*.

*Table 5-7 Values and uncertainties for the measurement of the solvent plasma load using the “continuous weighing method” (rounded values).*

	Description	Value $x$	Standard uncertainty $u(x)$	Relative standard uncertainty $u(x)/x$
$m_{\text{inlet}}$	Balance	9.61 g	2.0 E-04 g	0.000021
$m_{\text{nebulizer drain}}$	Balance	7.22 g	1.6 E-04 g	0.000022
	Spray chamber temperature	20 °C	0.17 °C	0.0087
$t$	Time	91 min		0.011
$f$	Measurement replication	1.00	2.8 E-03 g min <sup>-1</sup> (0.027 g min <sup>-1</sup> )	0.105

Inserting  $x_i$  and the correction term for the standard deviation of the measurement replication  $f$  in (5-12) yields

$$\dot{Q}_{\text{SPL}} = \frac{x_1 + x_2 + \dots + x_6}{6} \cdot 1$$

$$\dot{Q}_{\text{SPL}} = 0.0266 \text{ g min}^{-1}$$

The standard uncertainty of this result equals to the square root of the sum of the squares of the uncertainties associated with each component:

$$\frac{u_c(\dot{Q}_{\text{SPL}})}{\dot{Q}_{\text{SPL}}} = \sqrt{\left( \frac{u(m_{\text{inlet}})^2}{m_{\text{inlet}}^2} + \frac{u(\text{balance})^2}{m_{\text{nebulizer drain}}^2} + \frac{u(T_{\text{SC}})^2}{T_{\text{SC}}^2} + \frac{u(f)^2}{f^2} \right)}$$

$$= \sqrt{(0.000021^2 + 0.000022^2 + 0.0087^2 + 0.011^2 + 0.105^2)}$$

$$= 0.106$$

$$u_c(\dot{Q}_{\text{SPL}}) = \dot{Q}_{\text{SPL}} \cdot 0.106 = 0.027 \text{ g min}^{-1} \cdot 0.106 = 0.0028 \text{ g min}^{-1}$$

$$u_c(\dot{Q}_{\text{SPL}}) = 2.8 \text{ E-03 g min}^{-1}$$

The different uncertainty components and their contributions to the combined standard uncertainty are shown in *Figure 5-15*.

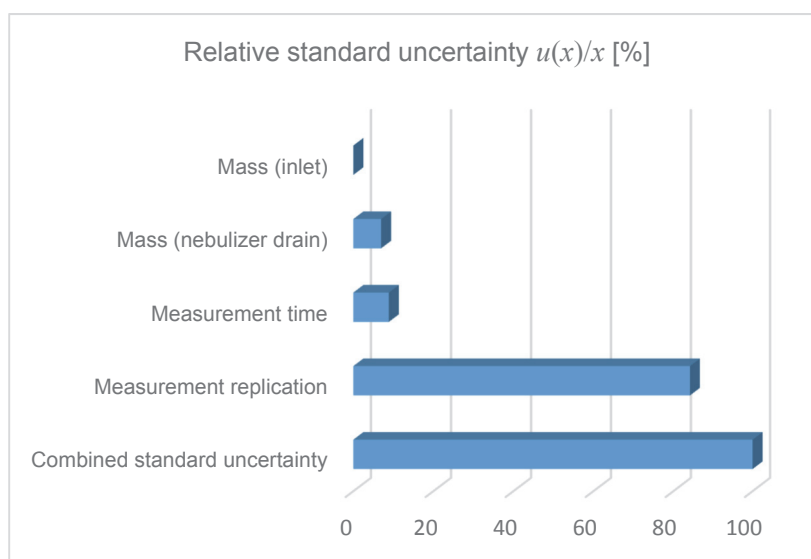


*Figure 5-15 Contributions (mass (inlet), mass (nebulizer drain), measurement time, and measurement replication) of the different parameters on the measurement uncertainty budget of the solvent plasma load using the “waste collection method”.*

The expanded uncertainty  $U$  is obtained by multiplying the combined standard uncertainty with a coverage factor. This is necessary to provide an interval that may be expected to encompass a large fraction of the distribution of values that could reasonably be attributed to the measurand. For a confidence interval of 95 % the coverage factor amounts to 2, giving:

$$U(\dot{Q}_{\text{SPL}}) = u_c(\dot{Q}_{\text{SPL}}) \cdot 2 = 2.8 \text{ E-03} \cdot 2 \text{ g min}^{-1}$$

$$U(\dot{Q}_{\text{SPL}}) = 5.7 \text{ E-03 g min}^{-1}.$$

Consequently, the aerosol mass transport amounts to:

$$\dot{Q}_{\text{SP}} = 0.027 \pm 0.0057 \text{ g min}^{-1}$$

### 5.3.5 Conclusive result

For the given sample introduction system ( $\dot{Q}_G = 0.80 \text{ L min}^{-1}$  Ar and  $\dot{Q}_L = 0.108 \text{ g min}^{-1}$  nitric acid ( $w(\text{HNO}_3) = 0.02$ ) **24 %  $\pm$  5 %** of the injected liquid mass is able to leave the spray chamber.

Using the “waste collection method” to determine the solvent mass transported to the plasma it can be concluded that the dominant component of uncertainty is obviously that of the measurement replication  $u(f)$ .

## 5.4 Analyte transport efficiency measurements

The analyte transport efficiency is determined indirectly using the waste collection measurement method described above. In addition, the sample was transported through a cryogenic trap at the plasma outlet of the spray chamber. *Table 5-8* lists the instrumentation employed. Various analyte solutions are used, which are prepared from the custom-made multi-element standard AHF CAL-7 (Inorganic Ventures, New Jersey, USA) and diluted as necessary (see *Table 5-9*). The respective standard solution is nebulized over a period of 90 minutes at different spray chamber temperatures (see chapter 6.2 for details).

*Table 5-8 Instruments and equipment.*

Nebulizer	MicroMist 100, Glass Expansion Pty. Ltd., Melbourne, Australia
Spray chamber	Scott-type double-pass spray chamber ( $V \sim 77$ mL)
Heating and cooling thermostat	Lauda Eco Silver, LAUDA DR. R. WOBSEER GMBH & CO. KG, 97922 Lauda-Koenigshofen, Germany
Gradient pump	GS50 Gradient Pump, Dionex Corporation, 1228 Titan Way, Sunnyvale, California 94088-3603 U.S.A.
Peristaltic pump	Perimax 12, Spetec GmbH, Erding, Germany
Tubing	Nebulizer drain: Tygon purple/black (i.d. = 2.29 mm) Sample line: PTFE tubing (i.d. = 0.86 mm)
Mass flow controller	GFC 100, Kobold Instruments GmbH, Wien, Austria
PLC	Allen-Bradley SLC 5/05, Rockwell Automation, Linz, Austria
Balance	Mettler Toledo XS205DU, Mettler-Toledo AG, Greifensee, Schweiz
U-tube	DURAN®-Glas, 16 mm i.d. x 20 mm o.d. x 150 mm length
sample solution	various dilutions of AHF CAL-7, Inorganic Ventures, New Jersey, USA
Ar gas quality	6.0
ICP-MS	NexION® 2000B, PerkinElmer, Waltham, MA, USA

A glass U-tube (dimensions see *Table 5-8*) is used as the cryocondenser. This tube is placed in a Dewar flask filled with crushed dry ice for approximately 30 minutes before analysis and kept there throughout the observation period.

After a nebulization period of 90 minutes, the collected condensed liquid in the U-tube is allowed to reach room temperature and both tube and liquid are weighed. The mass of the sample trapped is determined by subtracting the tare weight of the U-tube. The sample liquid is then transferred from the U-tube into a sample vessel and the mass of the sample (i.e., plasma outlet) is determined again. The mass of the waste is also determined by weighing as described in the procedure above.

Analyte concentrations in the standard solutions (i.e., Std 8, Std 9, and Std 10; see *Table 5-9*), which are trapped in the waste and in the original sample are determined by ICP-MS.

*Table 5-9 Mass fractions of REEs of the custom-made multi-element standard AHF CAL-7 in the dilutions.*

<i>Analyte</i>	<i>Atomic weight</i>	<i>Std 8 [ng/g]</i>	<i>Std 9 [ng/g]</i>	<i>Std 10 [ng/g]</i>
Y	88.905	210	242	324
La	138.905	210	242	324
Ce	140.116	420	484	648
Pr	140.907	42	48	65
Nd	144.242	210	242	324
Sm	150.360	21	24	32
Eu	151.964	8	10	13
Tb	158.925	4	5	6
Dy	162.500	21	24	32
Ho	164.930	4	5	6
Er	167.259	8	10	13
Tm	168.934	2	2	3
Yb	173.040	8	10	13
Lu	174.967	2	2	3
Gd	157.200	21	24	32
Gd	157.200	21	24	32
Th	232.038	63	73	97
U	238.050	21	24	32

Figure 5-16 shows the measurement setup to determine the analyte transport efficiency using the waste collection method.

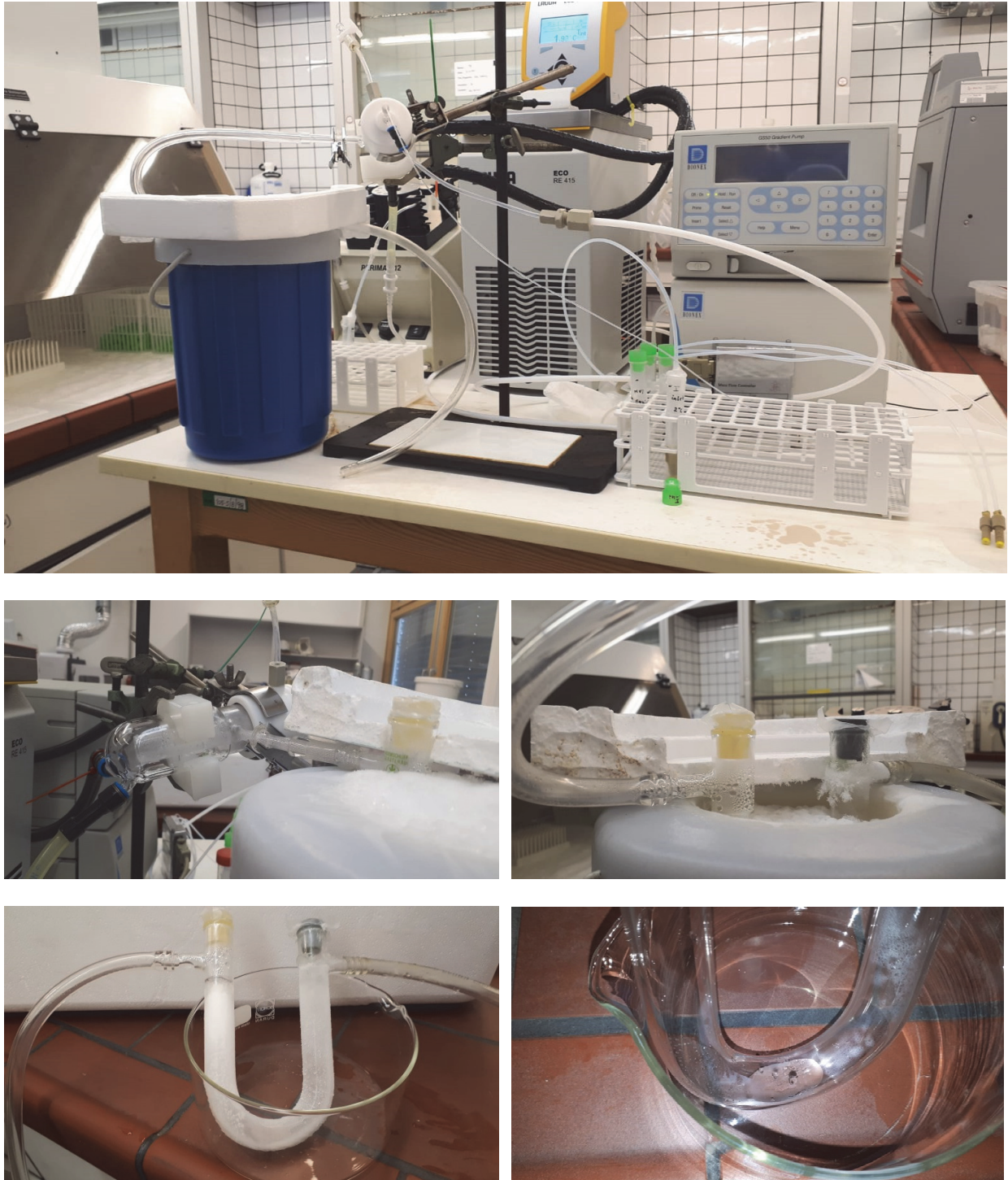


Figure 5-16 Measurement setup to determine the analyte transport efficiency using the waste collection method (source: E. Fasch).



## 6. Results and discussion

### 6.1 Mass transport efficiency (MTE)

#### 6.1.1 Mass transport efficiency - continuous weighing method

The mass transport efficiency of acidified water ( $w(\text{HNO}_3) = 0.02$ ) as a function of the liquid uptake rate was determined using the *continuous weighing method* described in chapter 5.2 with some modifications (see below). The MicroMist nebulizer was operated at 0.80 L/min argon flow, controlled by a mass flow controller (see *Table 5-2*). Measurements were carried out at two different spray chamber temperatures, i.e., 20 °C and 2 °C (*Figure 6-1*). Indirect aerosol heating/ cooling was performed via the double jacket of the spray chamber by means of a heating and cooling thermostat (see *Table 5-5*). Deviating from the original method described in chapter 5.2, the weight loss of the solvent was recorded every 10 s for one hour. The slope is then calculated from the data, which in turn represents the solvent plasma load.

*Figure 6-1* demonstrates the dependence of mass transport efficiency on both spray chamber temperature and liquid uptake rate.

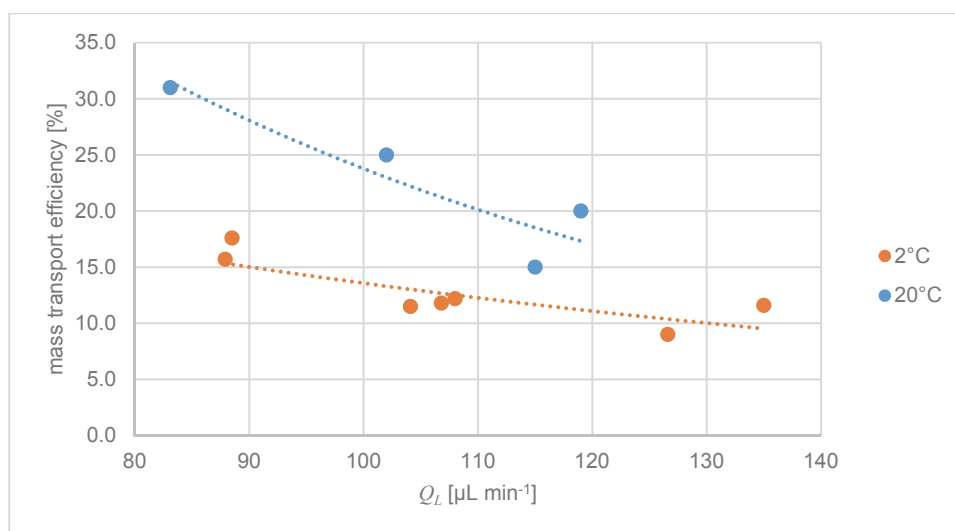


*Figure 6-1* Effect of the liquid uptake rate ( $Q_L$ ) on mass transport efficiency at two different spray chamber temperatures (i.e., 20 °C and 2 °C) at a forced argon flow rate  $Q_{Ar}$  of 0.80 L min<sup>-1</sup>.

It is well known that for a given spray chamber-nebulizer arrangement the solvent mass at the plasma outlet of the spray chamber depends on the sample uptake rate, the gas flow rate, the temperature of the spray chamber, and the solvent itself (see also 3.2). Comparing the decrease in solvent plasma load with increasing sample uptake, one can see that this is much less pronounced with a spray chamber kept at 2 °C.

Thus, at 110  $\mu\text{L min}^{-1}$  liquid flow rate, the mass transport efficiencies at spray chamber temperatures of 2 °C and 20 °C are 12 %  $\pm$  1 % and 20 %  $\pm$  3 %, respectively, as can be derived from *Figure 6-1*.

### 6.1.2 Mass transport efficiency – waste collection method

The amount of solvent mass entering the plasma to the amount of solvent mass aspirated as a function of different spray chamber temperatures was measured according to the *waste collection method* described in chapter 5.3. Similar to the continuous weighing experiments (see chapter 5.2) the MicroMist nebulizer was operated at 0.80  $\text{L min}^{-1}$  argon flow, controlled by a mass flow controller and indirect aerosol heating/ cooling was performed via the double jacket of the spray chamber by means of a heating and cooling thermostat. The sample uptake rate was set to 110  $\mu\text{L min}^{-1}$  using a gradient pump. Details on the equipment used can be found in *Table 5-8*. Measurements were carried out at different spray chamber temperatures, i.e., 2 °C, 5 °C, 10 °C, 15 °C, 20 °C, and 40 °C.

*Figure 6-2* shows the measured and calculated mass transport efficiencies as a function of the spray chamber temperature. For both the continuous weighing and the waste collection method, it can be concluded that the solvent plasma load increases significantly with increasing spray chamber temperature.

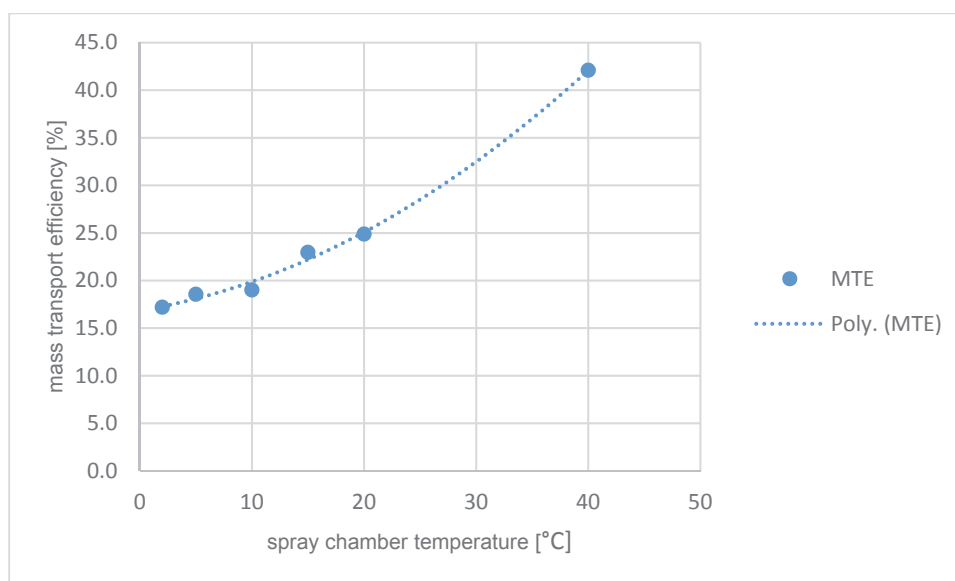


Figure 6-2 Effect of different spray chamber temperatures on mass transport efficiency (MTE) at a forced argon flow rate  $Q_{Ar}$  of  $0.80 \text{ L min}^{-1}$  and a liquid uptake rate ( $Q_L$ ) of  $110 \mu\text{L min}^{-1}$ .

Comparing the results of the waste collection method with those of the continuous weighing method, it is noticeable that the values for mass transport efficiency are generally about 5 % higher for the first method (Table 6-1).

Table 6-1 Mass transport efficiency results: waste collection vs. continuous weighing method at two different spray chamber temperatures (i.e., 2 °C and 20°C).

spray chamber temperature	mass transport efficiency [%]	
	waste collection method	continuous weighing method
2 °C	$17 \pm 2$	$12 \pm 1$
20 °C	$25 \pm 3$	$20 \pm 3$

Accordingly, there is a significant positive bias for the waste collection method, which is also predicted in the literature [Smith et al., 1982]. In general, indirect measurement methods are more prone to significant error compared to direct aerosol collection because the measurement is sensitive to even small recovery losses that occur, for example, in the spray chamber, especially at low liquid flow rates.

## 6.2 Analyte transport efficiency (ATE) – waste collection method

For purposes of determining trends in analyte transport efficiencies, it is sufficient to use the waste collection method. It is explicitly pointed out that the following results are merely estimates of the trends for varied measurement parameters and cannot be translated into absolute, quantified values. It is assumed that the entire amount of analyte not found in the waste is introduced into the plasma (i.e., any enrichment or depletion processes in the spray chamber are not considered).

### 6.2.1 Mass transport – vs. analyte transport

The analyte transport efficiency was determined as described in chapter 5.4. The collected solutions (i.e., waste and sample trapped in the cryo-condenser) and the REE standard solution (see *Table 5-8* and *Table 5-9*) used were analyzed for their analyte content by ICP-MS.

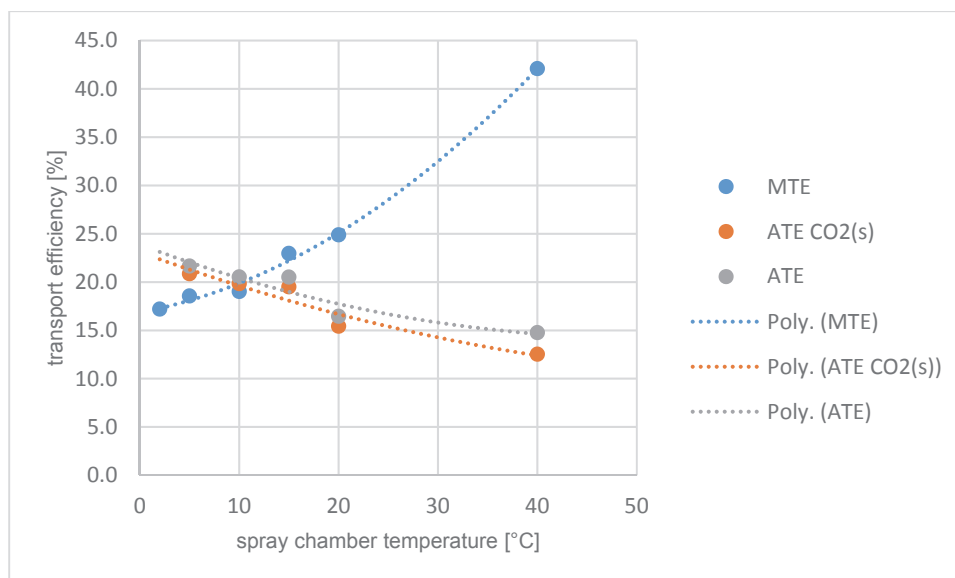


Figure 6-3 Mass transport efficiencies (MTE) vs. analyte transport efficiencies (ATE) and analyte transport efficiencies with cryogenic desolvation (ATE CO<sub>2</sub>(s)) at different spray chamber temperatures.

Figure 6-3 presents mass – and analyte transport efficiency data relating to various spray chamber temperatures. The horizontal axis indicates spray chamber temperatures in the

range from 2 °C to 40 °C and the vertical axis shows the degree of transport efficiency in relation to solvent mass and analyte mass. From the graph we can see that as the temperature of the spray chamber rises, the solvent mass transport also increases and, in parallel, the analyte mass decreases. This decline can perhaps be explained by the fact that more solvent vapor is transported to the plasma whereas less analyte containing droplets are transported with increasing spray chamber temperature. *Figure 6-3* also makes clear that the analyte transport is slightly lower in the case of cryogenic desolvation (orange line) than without its use (grey line). It is also noticeable that the percent analyte loss in the cooling trap increases at higher spray chamber temperatures, and thus also at higher aerosol temperatures.

The blue bars in the charts in *Figure 6-4* show the analyte transport of different elements as a function of varying spray chamber temperature.



*Figure 6-4* Mass transport efficiencies (MTE) vs analyte transport efficiencies (ATE) at different spray chamber temperatures [Fasch et al., 2023].

The diagrams are arranged in order of increasing spray chamber temperature. As can already be seen in *Figure 6-3*, the ratio of the transported analyte mass to the transported total mass (orange bars) also decreases significantly with increasing temperature. This obviously indicates an advantage of spray chamber cooling. If the various elements are considered, no enrichment or depletion trend can be determined with regard to the individual analytes and spray chamber temperatures. It can be deduced from the diagrams that the mass of the transported solvent increases as the spray chamber temperature rises, which increases the solvent load on the plasma. However, the mass of the analyte does not necessarily increase to the same extent. Therefore, the analyte transport efficiency remains basically the same over the temperature range under investigation. (see also *Figure 6-5*).

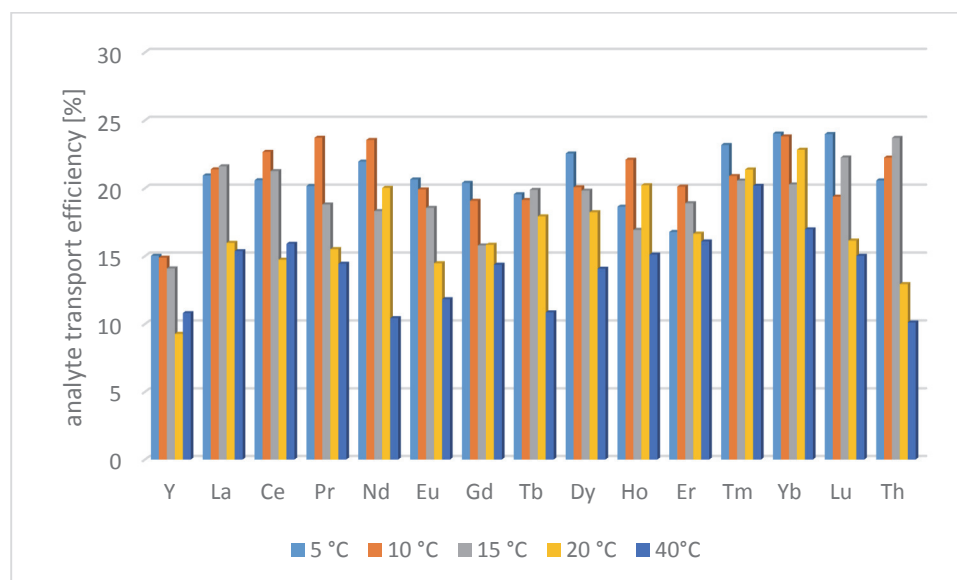


*Figure 6-5 Analyte transport efficiencies at different spray chamber temperatures.*

As appears from *Figure 6-6*, a signal drop can initially be observed in the temperature range from 2 °C to 20 °C, although the analyte transport remains more or less constant. [Fasch et al., 2022], [Fasch et al., 2023]

A possible explanation would be the increasing solvent plasma load, whereby additional plasma energy is required for desolvation and vaporization processes (see chapter 3.1). At 20 °C, a minimum of signal intensity can be observed for all analytes investigated. If the spray chamber temperature is increased further to 40 °C, the signal intensity rises again and reaches a value that is only 5 % below the maximum signal intensity measured

at 2 °C. One possible reason for this could be the beneficial role of water as a solvent. According to Todoli et al. [Todoli et al, 2008, (p. 9, 120)] it is crucial whether water is introduced into the plasma as a liquid aerosol or as water vapor. The plasma has a higher tolerance to water vapor, since the latter can increase the thermal conductivity of the plasma and hence the electron number density and the ion temperature [Long et al., 1988]. However, more detailed investigations have not been carried out on this subject.

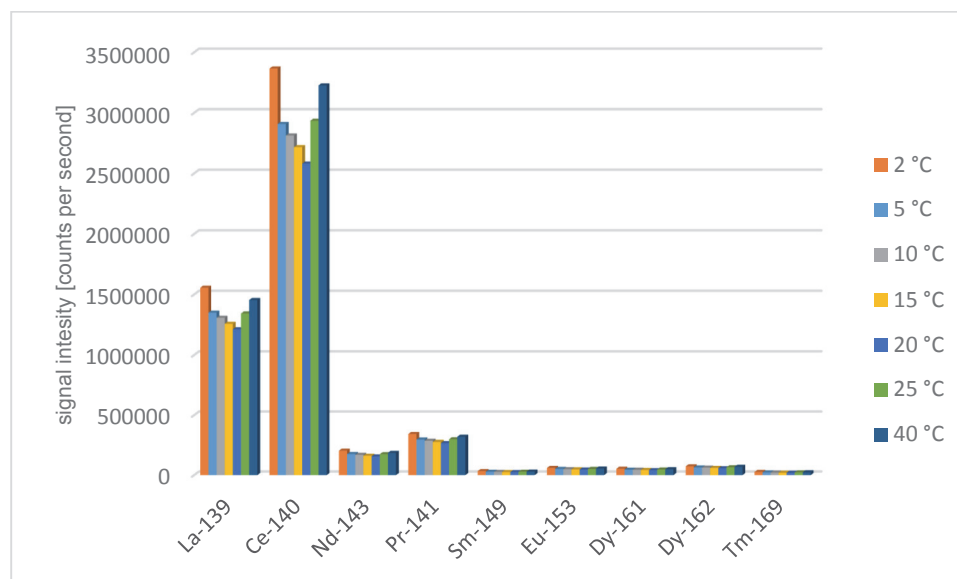


Figure 6-6 Signal intensity of standard solution Std10 at different spray chamber temperatures.

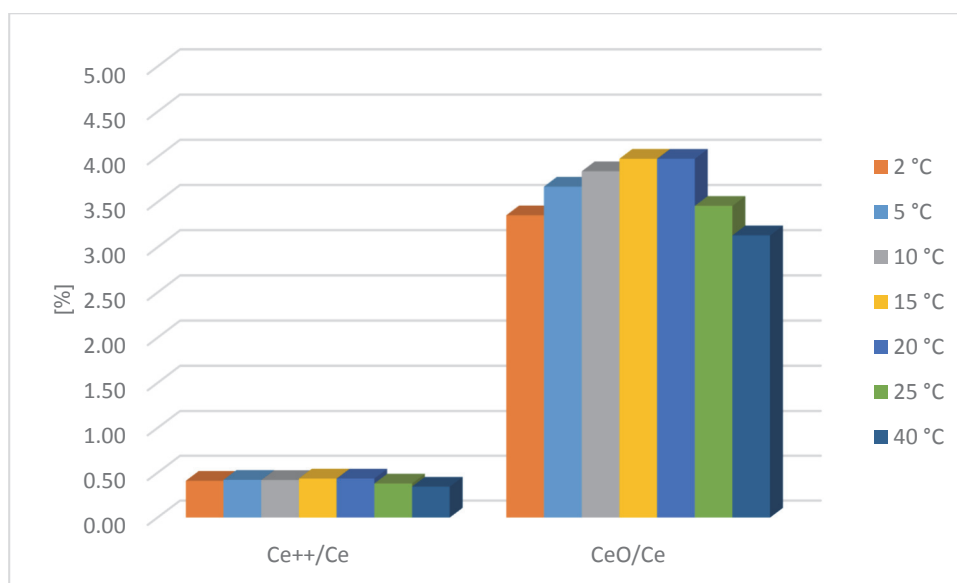
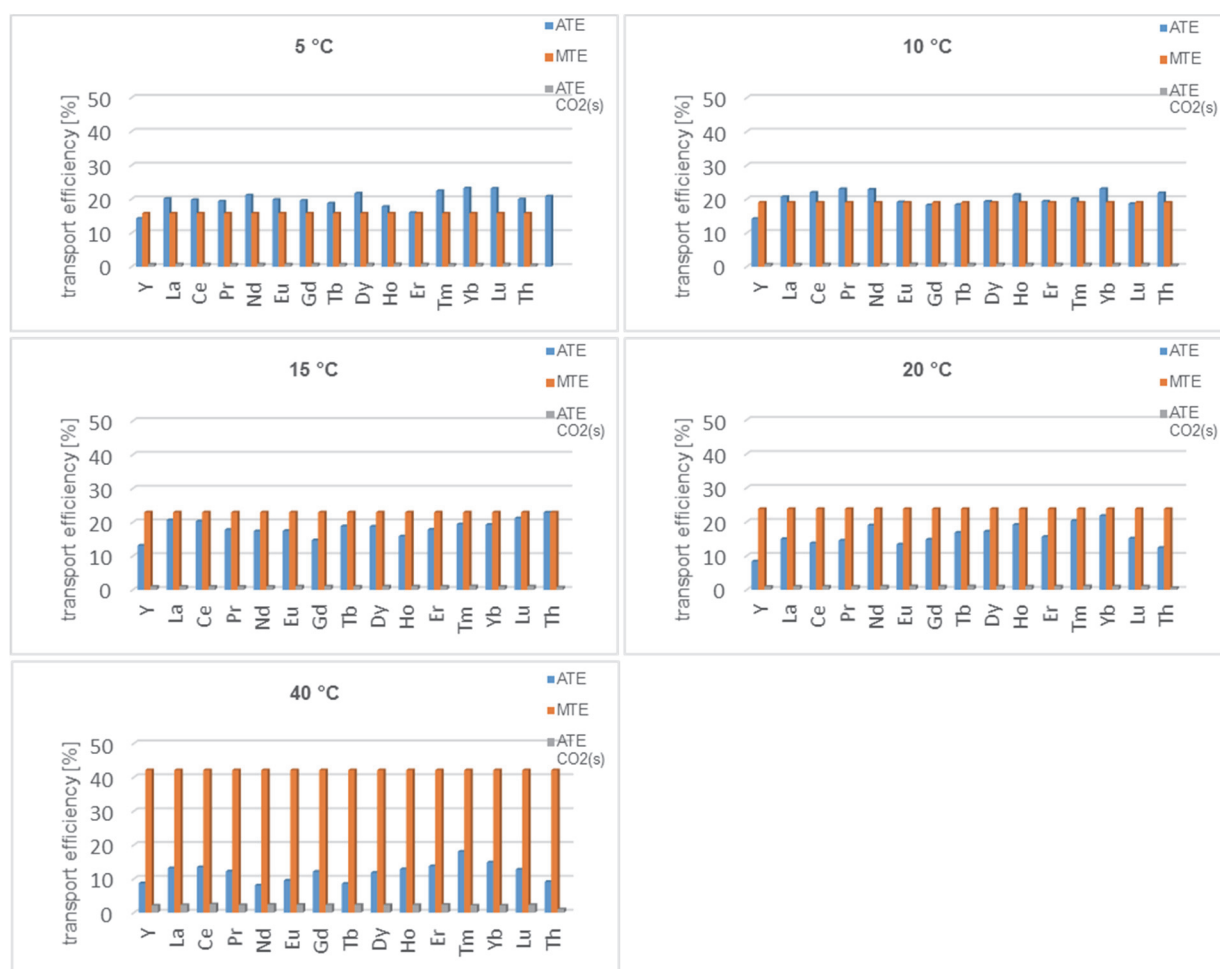


Figure 6-7 Percentage of doubly charged ions and oxide formation at different spray chamber temperatures using standard solution Std10.

Comparing the proportion of doubly charged ions and the different oxide formation rates as illustrated in *Figure 6-7* with the signal intensity in *Figure 6-6* and taking into account the different spray chamber temperatures, an inverse trend can be observed, although not very pronounced. That is, the lower the signal intensity, the higher the proportion of doubly charged ions and the higher the oxide formation. However, this effect is not significant for the formation of doubly charged ions. In the temperature range studied, the oxide formation rate varies between 3.1 and 3.8 %.



*Figure 6-8* Mass transport efficiencies (MTE) vs analyte transport efficiencies (ATE) with cryogenic desolvation at different spray chamber temperatures.

The bar graphs in *Figure 6-8* demonstrate that in the case of cryogenic desolvation, not only solvent mass but also analyte mass is removed. Again, there is no significant difference in the distribution of the mass of the individual elements measured with respect to



the analytes transported into the plasma. This trend is also confirmed when considering different spray chamber temperatures.

*Figure 6-9* shows the signal intensity in counts per second of standard solution Std10 at two different spray chamber temperatures, i.e., 2 °C and 20 °C. The signal rise is quite dramatic for the spray chamber at 2 °C compared to the spray chamber at 20 °C. In relation to the average signal intensity, this means an increase by a factor of almost 50. *Figure 6-9* further indicates that the measurements performed with the cryogenic trap result in a slight drop in signal intensity at a spray chamber temperature of 2 °C. This result is in good agreement with the fact mentioned above that there is obviously a loss of analyte in the cryogenic trap.

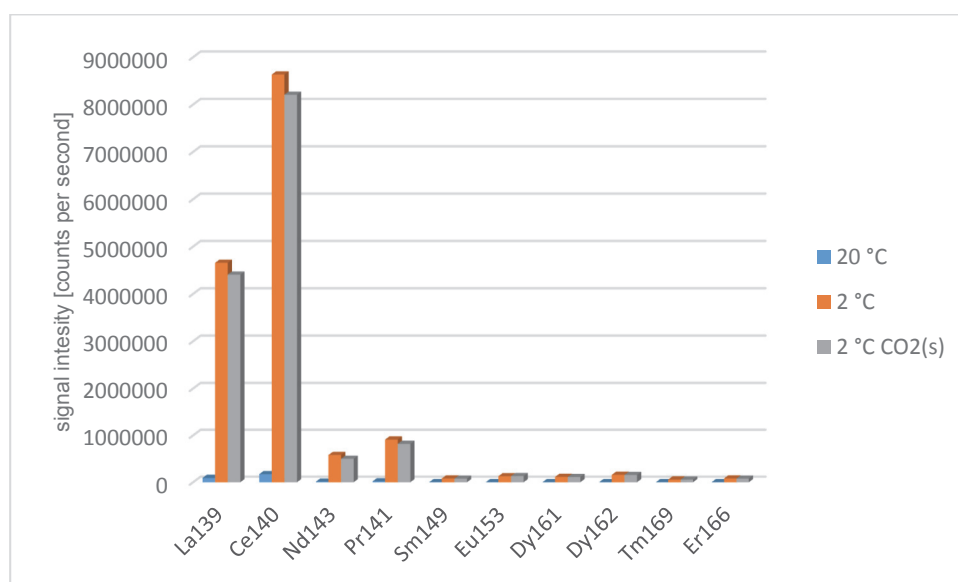


*Figure 6-9* Signal intensity of standard solution Std10 at two different spray chamber temperatures, i.e., 20 °C and 2 °C (with and without cryogenic desolvation).

As already shown in *Figure 6-1* and *Figure 6-2*, mass transport increases with increasing liquid uptake rate and temperature. If the sample reaching the plasma exit of the spray chamber is then passed through a cryogenic trap, the solvent mass can be significantly reduced. As shown in *Figure 6-10*, the deposited solvent mass increases with increasing temperature.

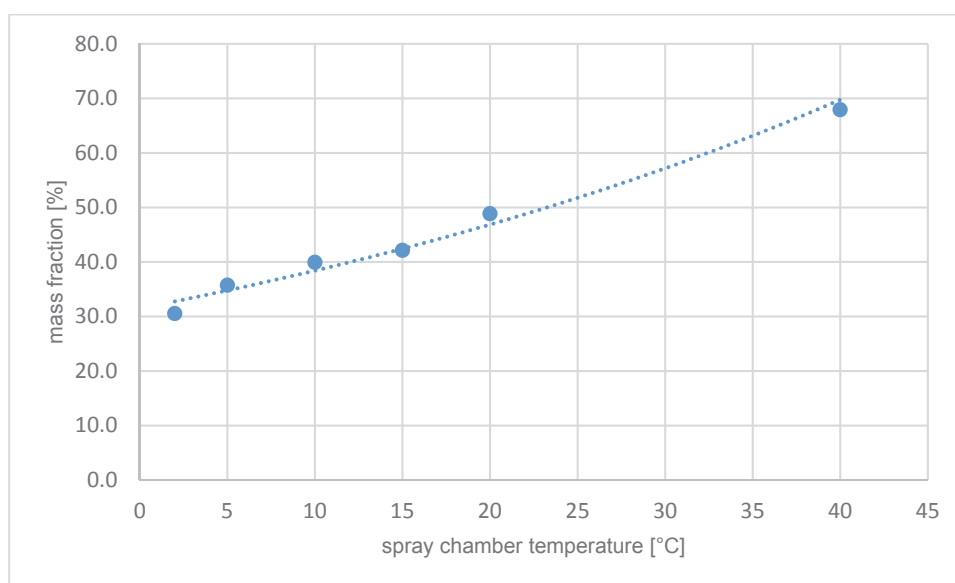


*Figure 6-10 Percentage of solvent mass deposited in the cryogenic trap.*

## 6.3 Droplet size and velocity distribution

It should be noted that any modeling of atomization or spraying processes, such as modeling the fluid dynamics of aerosols in spray chambers, requires the characteristic data of the primary aerosol as a prerequisite. Therefore, the primary aerosol must first be characterized in terms of spray size and velocity.

### 6.3.1 Spray droplet velocity and size distribution downstream of the nozzle exit in absence of the spray chamber – primary aerosol

First, the spray of an aqueous solution ( $w = 0.02 \text{ HNO}_3$ ) produced by the MicroMist nebulizer is characterized without the Scott spray chamber. This means that a free fluid jet delivered to an unconfined environment (i.e., ambient air) is investigated (*Figure 6-11*).

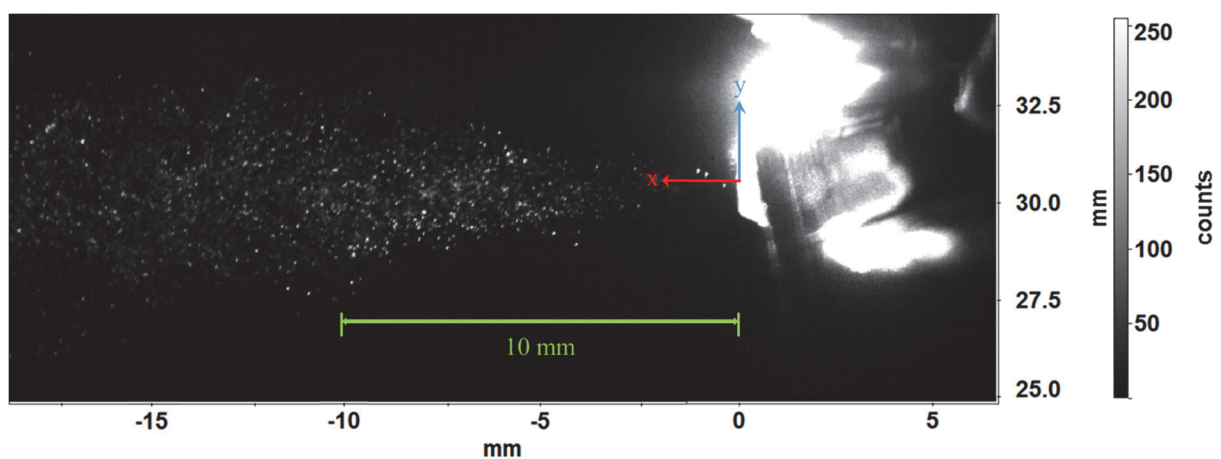


*Figure 6-11* Illuminated measurement zone by a high-speed PIV-Laser Nd: YLF, LDY 303HE (Litron) at a nebulizer gas flow rate of 0.80 L/min and a solution uptake rate of 110  $\mu\text{L}/\text{min}$ .

The nebulizer is operated at a solution uptake rate and nebulizer gas flow rate of 110  $\mu\text{L}/\text{min}$  and 0.80 L/min, respectively.

Particle imaging velocimetry (PIV) is applied to study the 2-D velocity field of the aerosol from the MicroMist nebulizer. A number of 1000 frames per measurement series is used to obtain a convergent, time-averaged result. *Figure 6-12* and *Figure 6-13* give a graphic rendition of these results at different distances from the nebulizer nozzle.

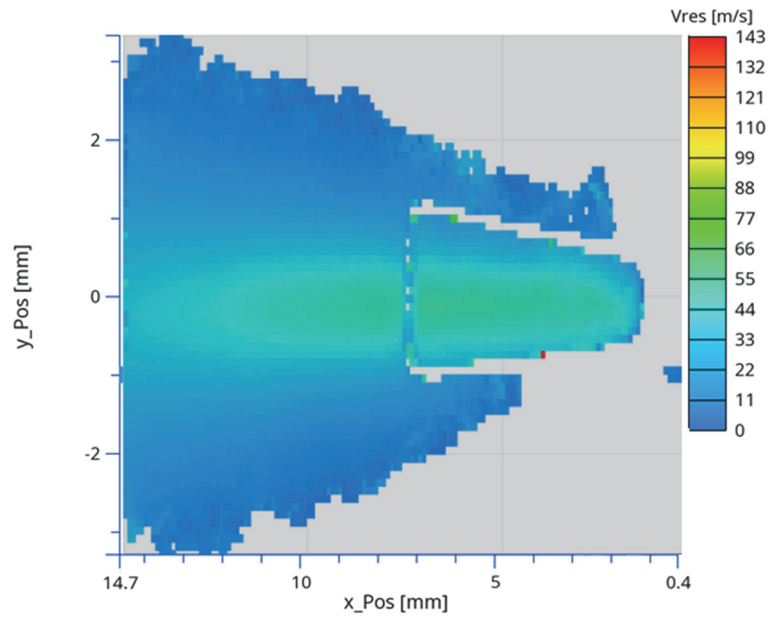


Figure 6-12 Velocity profile of the MicroMist nebulizer (PIV:  $Q_{Ar} = 0.80$  L/min;  $Q_L = 110$   $\mu$ L/min).

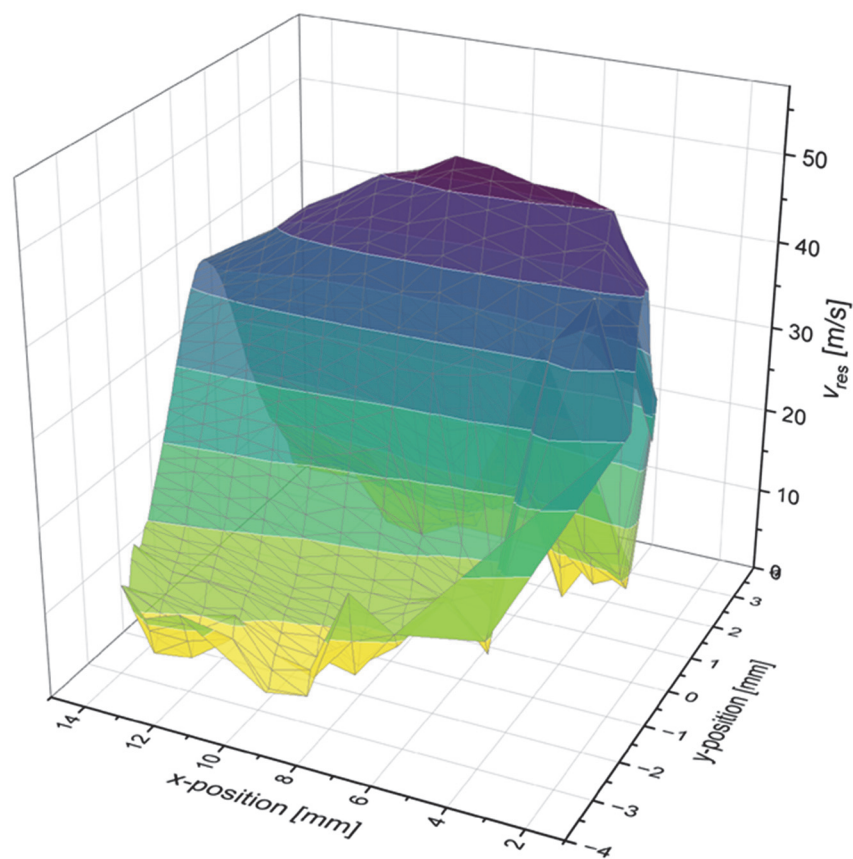
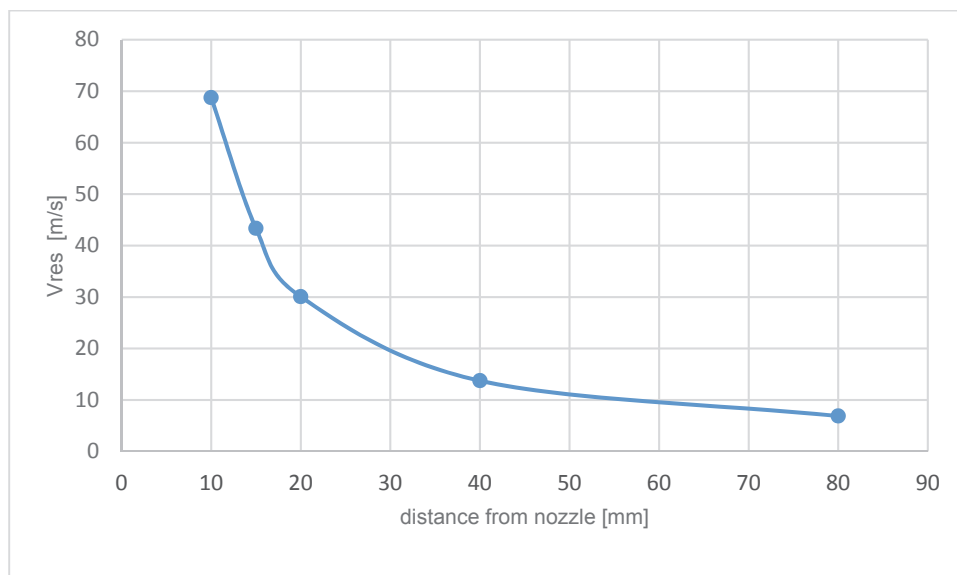


Figure 6-13 PIV measurement of the velocity profiles at various distances (x-positions) from the nebulizer tip ( $Q_{Ar} = 0.80$  L/min;  $Q_L = 110$   $\mu$ L/min).

As can be seen, the resulting velocity  $v_{res}$ , calculated from the axial and radial velocity components, first increases and reaches a maximum ( $\sim 56 \text{ m s}^{-1}$ ) at a distance of 7 mm downstream from the coordinate origin (see *Figure 6-13*). As the distance increases, the velocity decreases again. For example, the centerline velocity is about  $40 \text{ m s}^{-1}$  at a distance of 14 mm downstream.

In contrast to the PIV measurements, the primary aerosol was performed under the same experimental settings using the phase Doppler particle analyzer such that the velocity was measured at various distances from the nebulizer tip (point measurement) along the centerline of the aerosol. The resulting velocity is calculated from the axial and radial velocity component of the droplets of different sizes and represents a weighted mean value over the number of individual droplet sizes.

*Figure 6-14* clearly shows that the mean droplet velocity decreases rapidly within the first 40 mm from the nebulizer nozzle. The results from the PIV measurements confirm this trend. However, the mean velocities in the PDA measurement are higher, especially near the nozzle. This deviation can perhaps be explained by the fact that, compared to the PIV method, PDA measurements only represent point measurement results.



*Figure 6-14* PDA measurement of the mean droplet velocity weighted over the number of individual droplet sizes ( $Q_{Ar} = 0.80 \text{ L/min}$ ;  $Q_L = 110 \text{ }\mu\text{L/min}$ ).

Plotting the resulting velocity against the droplet size at various distances from the nebulizer tip, it can be seen from *Figure 6-15* that almost all droplets have nearly uniform velocity from a distance of 40 mm downstream from the center of the nozzle.

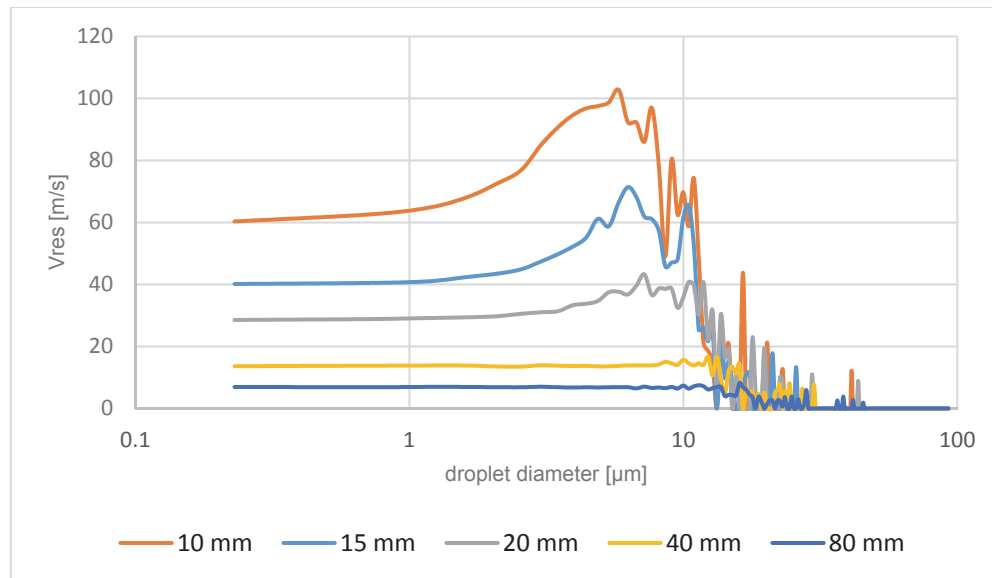


*Figure 6-15* PDA measurement of the resulting droplet velocity as a function of droplet size in various distances from the nebulizer orifice ( $Q_{Ar} = 0.80$  L/min;  $Q_L = 110$   $\mu$ L/min).

The droplet volume distribution measured with the HELOS laser diffraction system at different distances from the nebulizer (0 - 10 mm, 2.5 - 12.5 mm, and 7.5 - 17.5 mm) is illustrated in *Figure 6-16*. As can be seen from (A), the primary aerosols generated by the MicroMist have a bimodal droplet size distribution. According to published results, these maxima are likely due to oscillation of the sample capillary at characteristic frequencies [McLean et al. 1998, Todoli et al. 2002]. Another explanation could concern the measurement technique itself. The Fraunhofer laser diffraction technique always requires sphericity of the examined particles. Deviations can also result from the fact that ligaments are still present due to the primary and secondary break-up process, which may lead to the present bimodal distribution in the droplet size spectrum. Multiple scattering effects due to high particle concentrations can also distort the droplet size distribution. In this case, the scattered light is scattered again by other particles prior to reaching the detector. [Merkus, 2009], [Secker et al., 2000], [Ruth et al., unpublished results]. However, further more detailed investigations were not carried out in the present work.

It is observed that larger droplets of diameter  $\sim 24 \mu\text{m}$  are present close to the nebulizer exit. Their size decreases with distance, which is probably related to droplet break-up and evaporation processes. However, the resulting droplet density distributions also clearly show that large droplets can still be detected even at greater distances. At the distances 2.5 - 12.5 mm and 7.5 - 17.5 mm, two droplet diameter maxima of the aerosol are found at  $\sim 6 \mu\text{m}$  and  $\sim 23 \mu\text{m}$ .

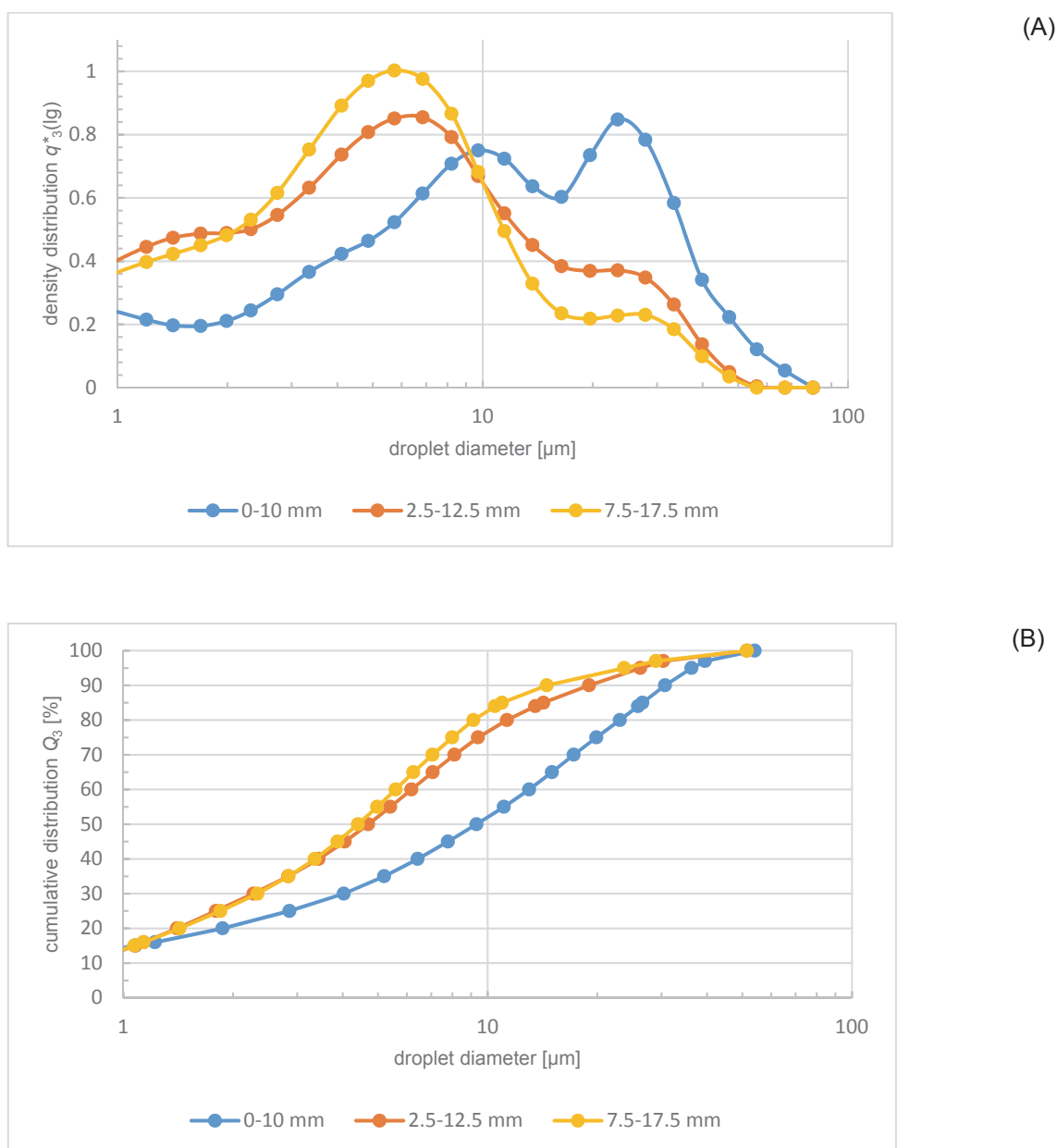


Figure 6-16 Volume - based droplet size distribution of the primary aerosol at different distances from the nebulizer nozzle measured by laser diffraction. (A) density distribution ( $q^*_3(lg)$ ) and (B) cumulative representation ( $Q_3$ ); ( $Q_{Ar} = 0.80 \text{ L/min}$ ;  $Q_L = 110 \mu\text{L/min}$ ).

The graph in *Figure 6-16 (B)* indicates the volume droplet size distribution curves, presented as the variation of the percentage of liquid sample volume contained in droplets below a given droplet diameter versus the droplet diameter for the different distances from the nebulizer nozzle. Hence, under the measurement conditions employed, the proportion of the aerosol volume contained in droplets with diameters less than 10  $\mu\text{m}$  was 52 %, 76 %, and 83 % for the distances 0 - 10 mm, 2.5 - 12.5 mm, and 7.5 - 17.5 mm, respectively.

The results of the laser diffraction measurements are summarized in *Table 6-2*.

*Table 6-2 Results for the primary aerosol measured by laser diffraction.*

		0 – 10 mm	2.5 – 12.5 mm	7.5 – 17.5 mm
Sauter mean diameter	[ $\mu\text{m}$ ]	2.2	2.2	2.0
Volume mean diameter	[ $\mu\text{m}$ ]	12.8	7.7	6.6
Particle mass specific surface	[ $\text{cm}^2 \text{g}^{-1}$ ]	28506	27542	29421
Particle volume specific surface	[ $\text{m}^2 \text{cm}^{-3}$ ]	2.85	2.76	2.94

Using the dual-beam phase–Doppler particle size analyzer, the primary aerosol was sampled at various distances from the nebulizer nozzle along the centerline of the aerosol. Note, that the droplet sizes measured by means of the two techniques are not directly comparable and therefore need to be converted first. While the size distribution in Fraunhofer laser-diffraction technique is proportional to the relative number of droplets per unit volume, the PDA technique shows proportionality to the droplet flux (i.e., the number of droplets per unit time per unit area) [Dodge, 1988].

The corresponding number and mass (volume) – based droplet size distributions for the various distances from the centerline of the nebulizer nozzle are presented in *Figure 6-17* and *Figure 6-18*. The peaks in the diagrams show that even a few large droplets have a considerable influence on the distribution due to their comparatively high mass.



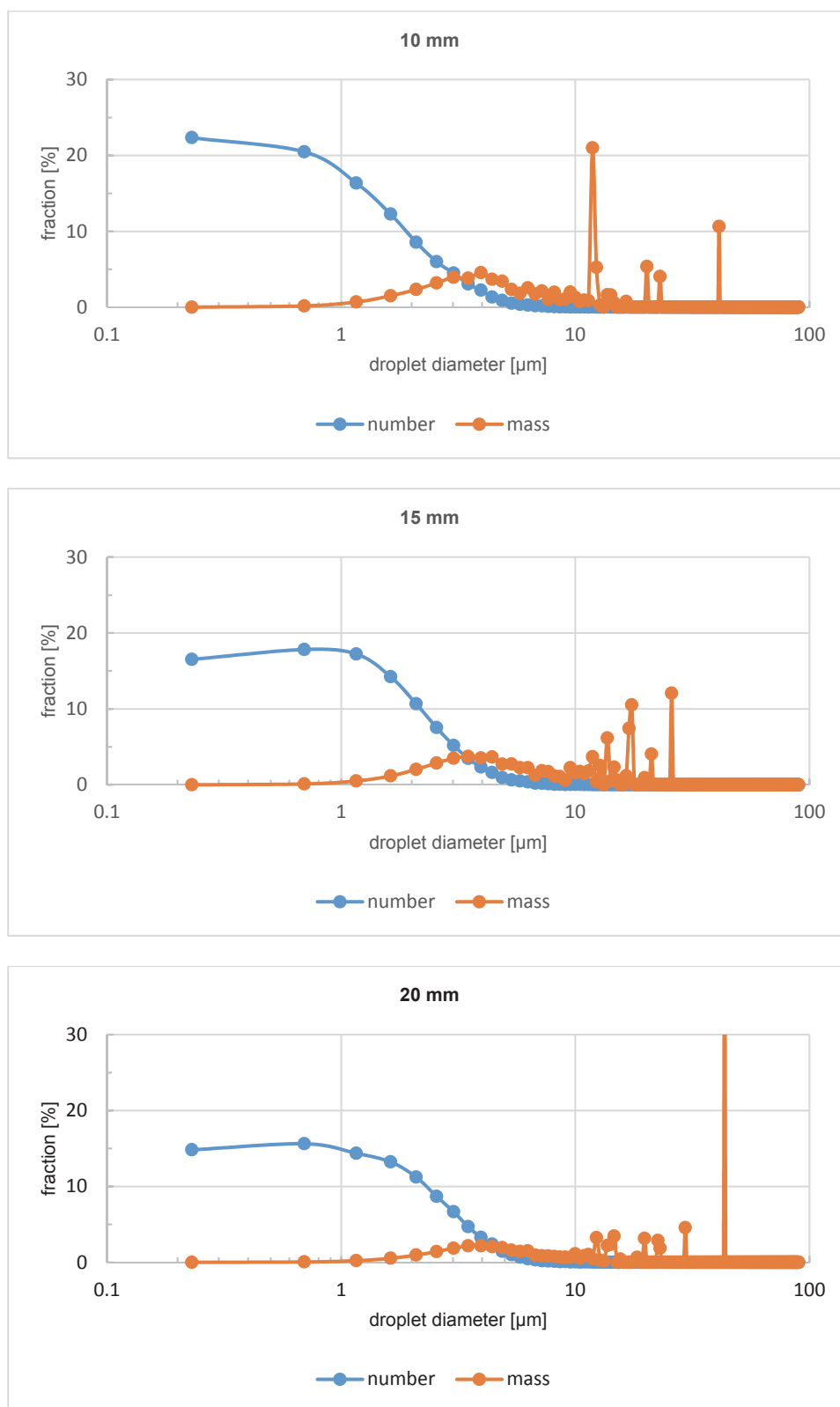


Figure 6-17 Number and mass (volume) - based droplet size distribution of the primary aerosol at various distances (i.e., 10 mm, 15 mm, 20 mm) from the nebulizer orifice measured by PDA technique. (Note: The truncated point in the bottom diagram has a mass fraction of about 48 %.)

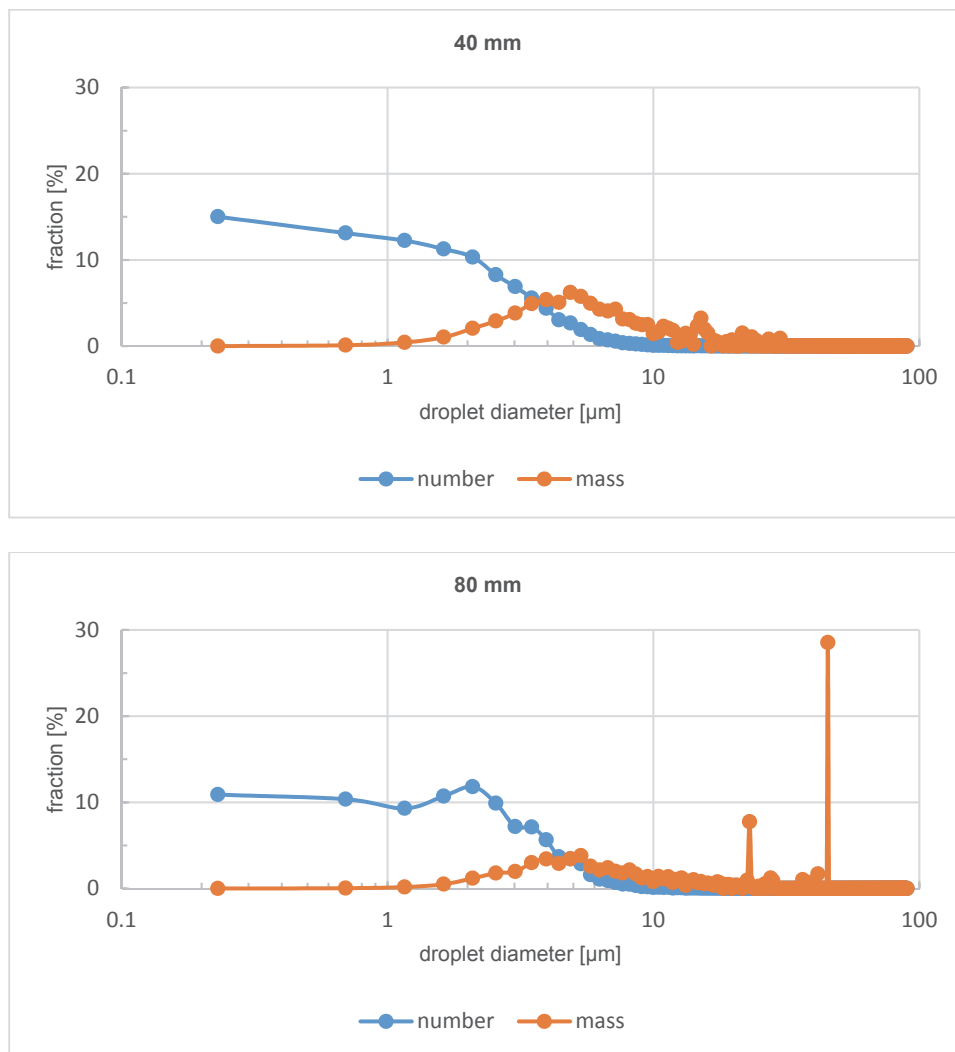


Figure 6-18 Number and mass (volume) - based droplet size distribution of the primary aerosol at various distances (i.e., 40 mm, 80 mm) from the nebulizer orifice measured by PDA technique.

The graph in *Figure 6-19* displays the mass (volume) - based distribution of the primary aerosol at a centerline distance of 10 mm from the nebulizer tip in a cumulative representation (brown line). Under the measurement conditions used, the proportion of the aerosol volume contained in droplets with a diameter of less than 10  $\mu\text{m}$  was roughly 50 %.

Characteristic droplet diameters (see *Table 3-2* for definitions) such as the mean count diameter  $d_{10}$  or the mean Sauter diameter  $d_{32}$  are summarized in *Table 6-3* and

Figure 6-20 gives a graphical representation of the development of these droplet diameters as a function of the different distances to the nebulizer nozzle.

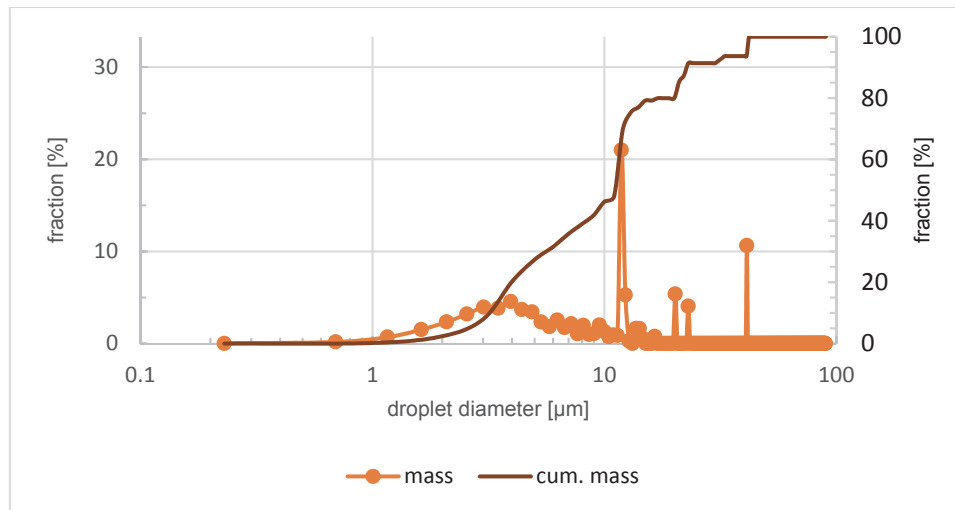


Figure 6-19 Number and mass (volume) - based droplet size distribution and a cumulative representation of the primary aerosol at a distance of 10 mm from the nebulizer tip measured by PDA technique.

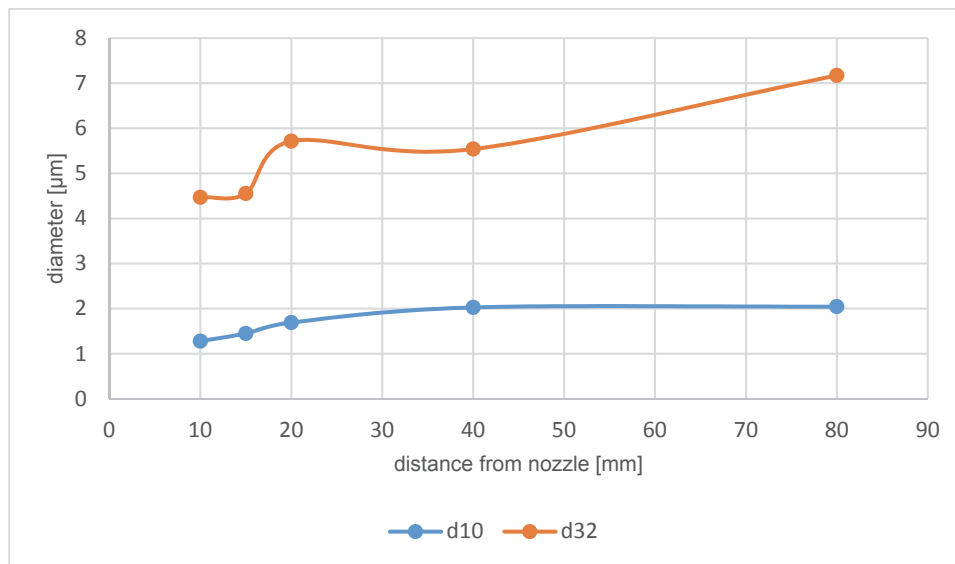


Figure 6-20 Characteristic diameters ( $d_{10}$  and  $d_{32}$ ) of the primary aerosol at various distances from the nebulizer tip measured by PDA technique.

*Table 6-3 Results for the primary aerosol measured by PDA.*

<i>distance</i> [mm]	<i>d</i> <sub>10</sub> [μm]	<i>d</i> <sub>32</sub> [μm]
10	1.3	4.5
15	1.5	4.6
20	1.7	5.7
40	2.0	5.5
80	2.0	7.2

### 6.3.2 Spray droplet velocity and size distribution downstream of the spray chamber plasma outlet – tertiary aerosol

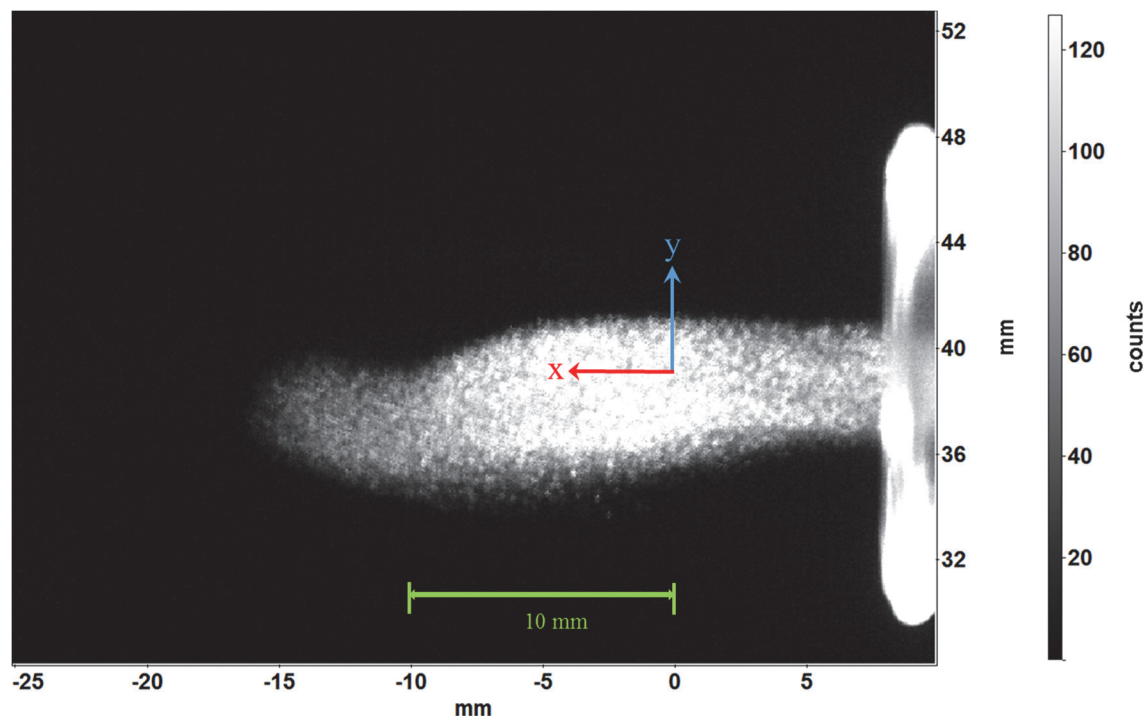
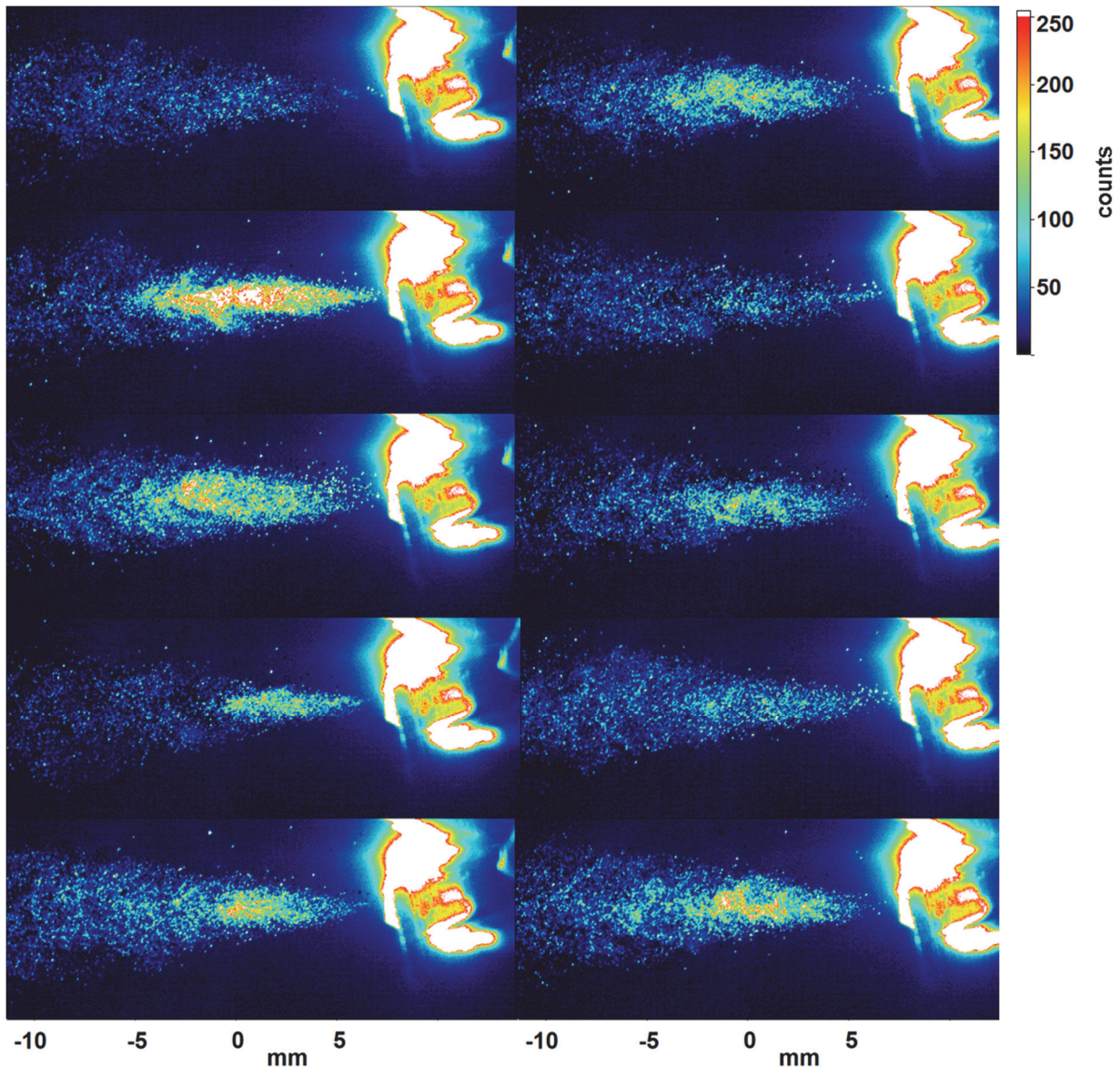


Figure 6-21 Illuminated measurement zone of the tertiary aerosol obtained at the spray chamber plasma outlet by a high-speed PIV-Laser Nd: YLF, LDY 303HE (Litron) at a nebulizer gas flow rate of 0.80 L/min and a solution uptake rate of 110  $\mu$ L/min.

Again, particle imaging velocimetry (PIV) is applied to study the 2-D velocity field of the tertiary aerosol from the MicroMist nebulizer exiting the plasma outlet of the Scott-type spray chamber.

During the measurement, an interesting observation was made. The aerosol jet broke off periodically as it exited the spray chamber. The images in *Figure 6-22* are intended to illustrate qualitatively that the droplet loading in the jet is not constant in time. The images were captured within 9 ms. However, a quantitative statement about this (e.g. droplet loading over time, detachment frequencies, etc.) is not possible based on the available data. Since a piston stroke pump was used for the measurement to feed the sample into the spray chamber, pulsations of the sample introduction system can be largely excluded as an explanation for this fact. However, one possible cause could be the flow field in the

spray chamber itself, since the resulting flow performs a rotating pendulum motion around the jet axis (see *chapter 6.4.1*).



*Figure 6-22 Images of temporally different droplet cloud densities. The acquisition of 10 images takes place within 9 ms.*

A graphical representation of the velocities at the spray chamber plasma outlet measured by PIV (point of origin see *Figure 6-21*) is given in *Figure 6-23 - Figure 6-24* and *Figure 6-25 - Figure 6-26* for the Scott chamber at 2 °C and 20 °C, respectively. At different spray chamber temperatures, the same velocities result at the outlet, which leads to the plasma (“plasma outlet”) of the spray chamber. Thus, the average velocity, measured

about 10 mm from the plasma outlet, is  $\sim 0.7 \text{ m s}^{-1}$ . The velocities measured by PDA at a distance of 1 mm from the spray chamber plasma outlet along the centerline of the aerosol give a mean velocity weighted over the number of individual droplet sizes of  $1.4 \text{ m s}^{-1}$  for both the spray chamber at  $2 \text{ }^\circ\text{C}$  and at  $20 \text{ }^\circ\text{C}$ . The results show a satisfactory agreement with the data from the numerical simulation (see *chapter 6.4.2* and *Figure 6-47*). It also appears from the numerical simulation that the argon gas flow in the tube to the plasma is about  $1 \text{ m s}^{-1}$ , indicating that the droplets largely flow with the gas flow (see *chapter 6.4.1*).

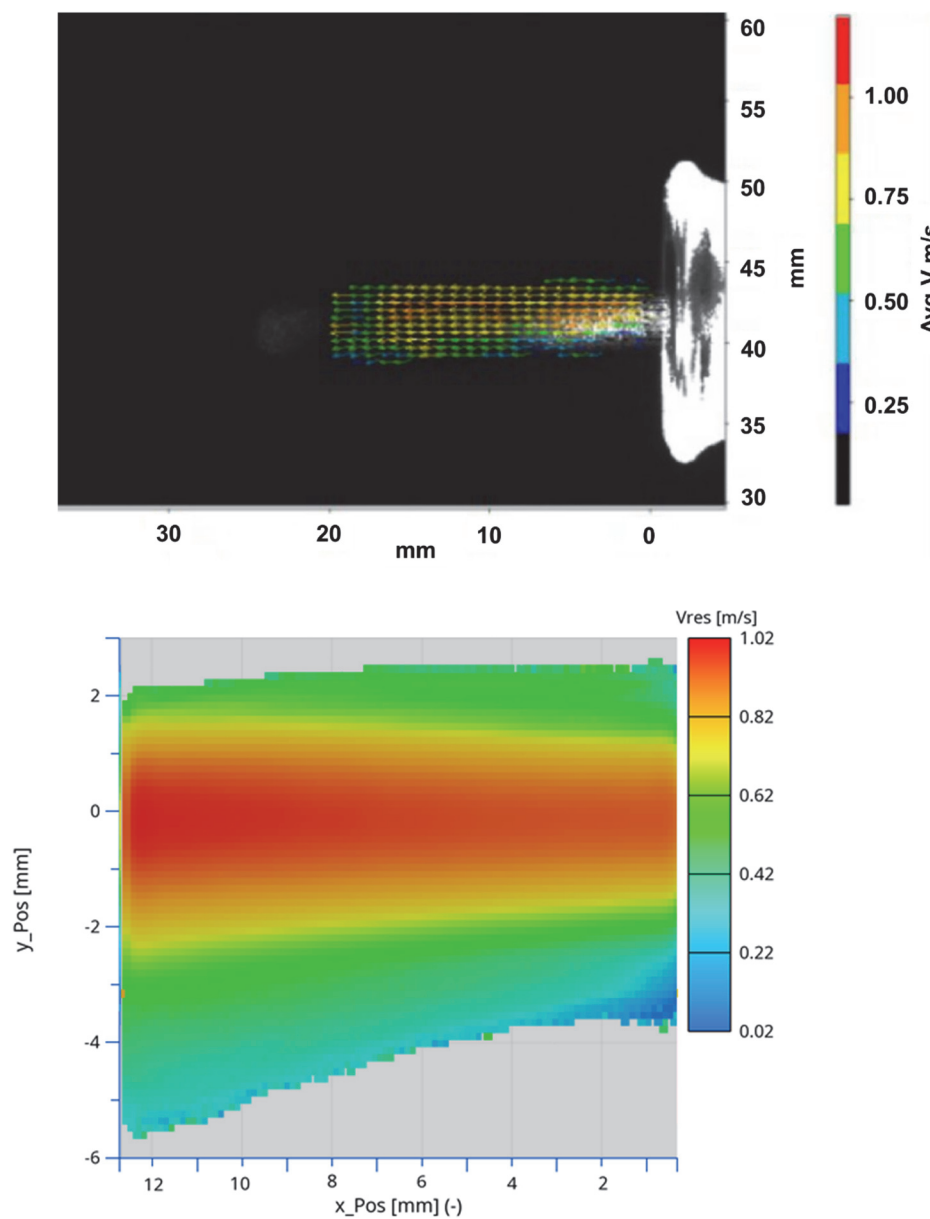


Figure 6-23 Velocity profile at the plasma outlet of the Scott chamber at  $2 \text{ }^\circ\text{C}$  (PIV:  $Q_{Ar} = 0.80 \text{ L/min}$ ;  $Q_L = 110 \text{ } \mu\text{L/min}$ ).

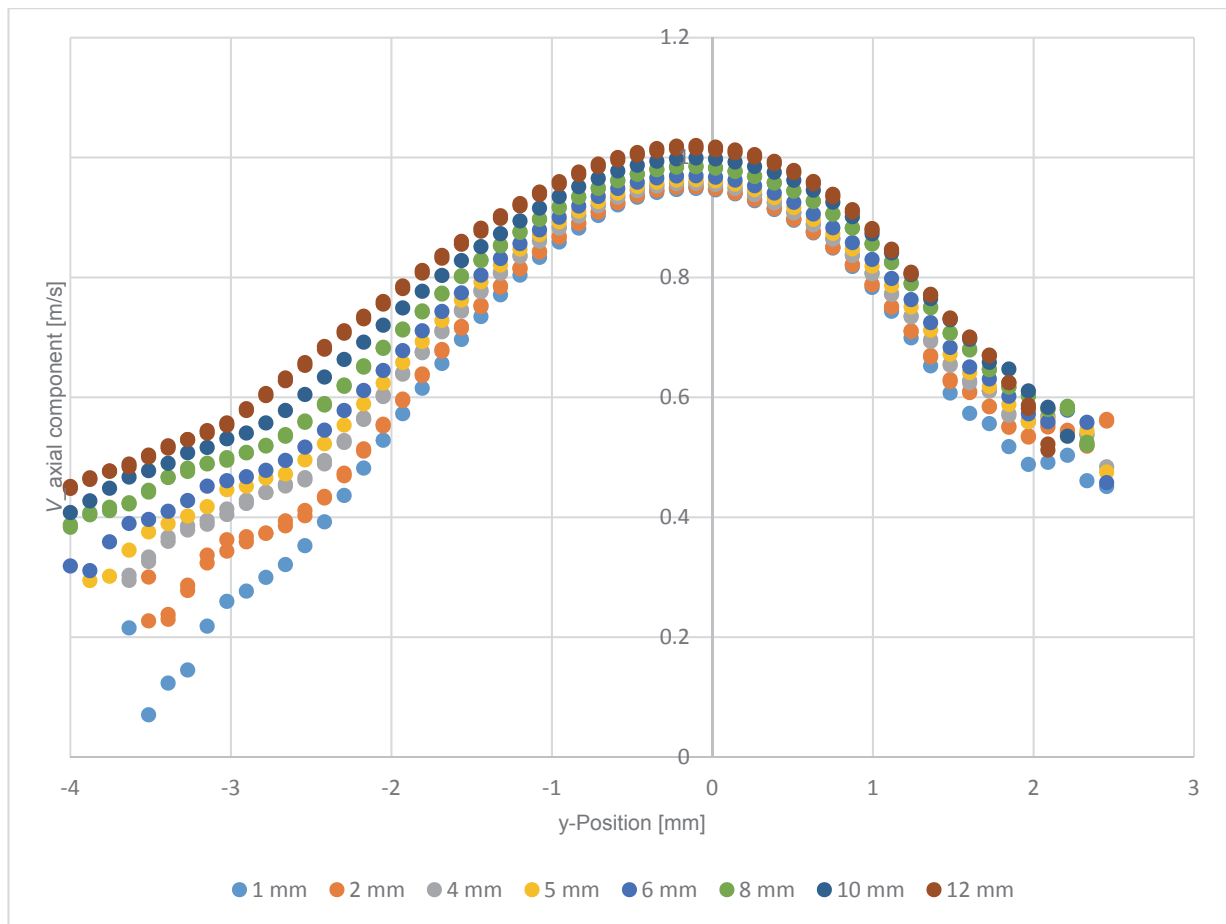


Figure 6-24 PIV measurement of the velocity profiles at various distances (x-axis: 1-12 mm) from the plasma outlet of the Scott chamber at 2 °C ( $Q_{Ar} = 0.80$  L/min;  $Q_L = 110$   $\mu$ L/min).

Comparing Figure 6-24 with Figure 6-26 shows that the dispersion properties of the carrier fluid (argon) depend on the temperature, which has an effect on the aerosol delivery rates. This results in a dispersion of the velocity field at the plasma outlet of the cooled chamber (see Figure 6-24), especially in the centerline velocity of the parabolic velocity field. Both figures illustrate the flow characteristics that result when a flow emerges from a nozzle into an environment (still air) without a wall boundary. The fluid exiting the nozzle and the fluid in the environment have different velocities. A shear layer is created between them, from which a free jet develops. The ambient fluid is sucked in and entrained. The flow field of a circular jet can be divided into different areas, each related to the decrease in the centerline velocity. The core of the jet is the region where the centerline velocity is constant and equal to the argon velocity at the plasma outlet of the Scott chamber. This region extends up to 4 to 6 diameters of the jet exit channel (i.e., approx. 23 - 35 mm) and was captured with the PIV measurements.



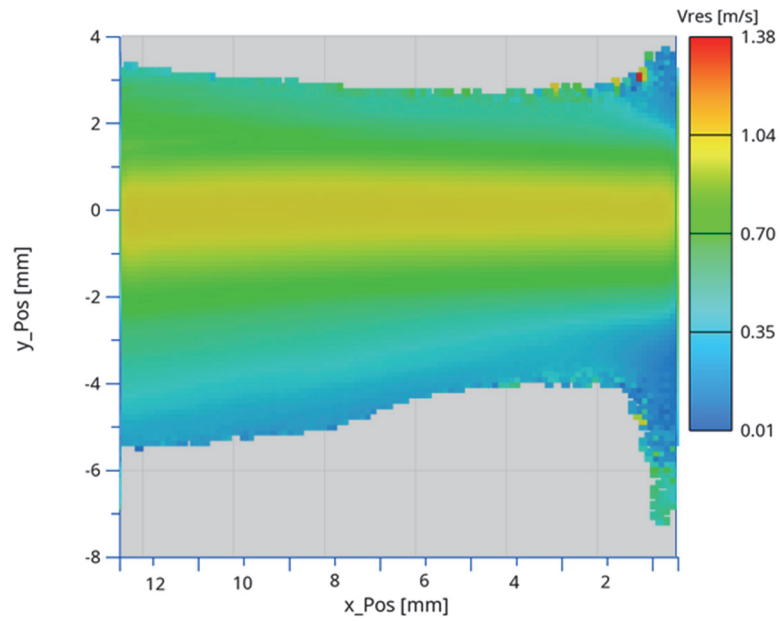


Figure 6-25 Velocity profile at the plasma outlet of the Scott chamber at 20 °C (PIV:  $Q_{Ar} = 0.80$  L/min;  $Q_L = 110$   $\mu$ L/min).

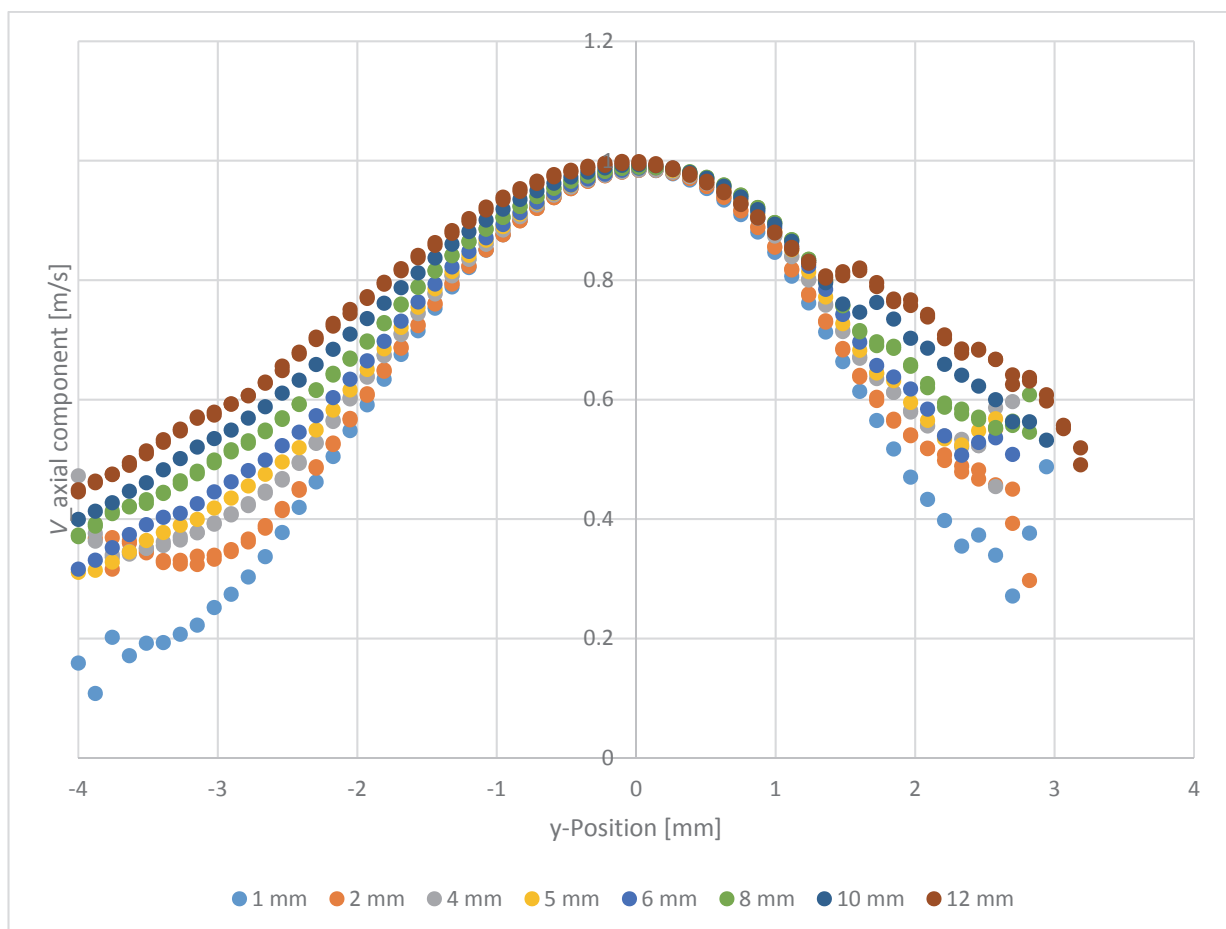
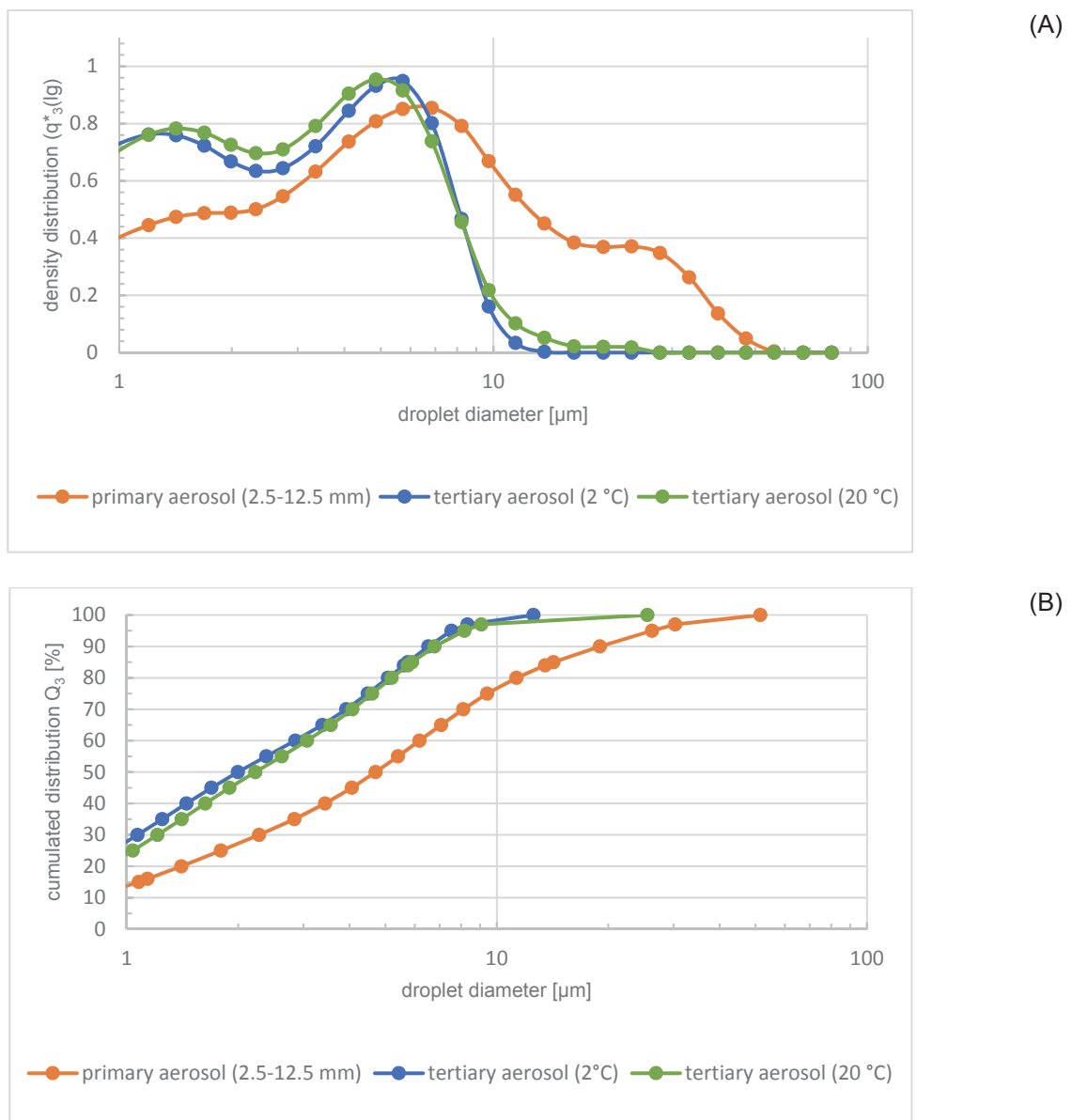


Figure 6-26 PIV measurement of the velocity profiles at various distances ( $x$ -axis: 1-12 mm) from the plasma outlet of the Scott chamber at 20 °C ( $Q_{Ar} = 0.80$  L/min;  $Q_L = 110$   $\mu$ L/min).

Thereafter, the velocity profile flattens out with increasing distance as the shear layers merge from both sides. As a result, the liquid within the jet slows down and the liquid surrounding the jet is accelerated and entrained into the jet stream [Schlichting et al., 2006], [Kmecova et al., 2019]. The fact that the slight centerline acceleration shown in *Figure 6-24* is significant should be evaluated with caution, as thermal effects due to the entry of a relatively cold jet into air at ambient temperature would probably have to be taken into account, but this has not been investigated in detail.



*Figure 6-27* Volume based droplet size distribution of the primary and tertiary aerosol measured by laser diffraction. (A) density distribution and (B) cumulative representation ( $Q_{Ar} = 0.80$  L/min;  $Q_L = 110$   $\mu\text{L}/\text{min}$ ).

*Figure 6-27* presents volume droplet size distributions of both the primary and the tertiary aerosol leaving the spray chamber at different spray chamber temperatures. From the figures it can be deduced that the spray chamber fulfills the expected filtering properties. As already mentioned, droplets with diameters larger than 10  $\mu\text{m}$  are not suitable for analytical purposes because they are not completely desolvated, vaporized and atomized in the ICP. The proportion of the aerosol volume contained in droplets less than 10  $\mu\text{m}$  in diameter was  $\sim 97\%$  and  $\sim 98\%$  for the spray chamber at 20  $^{\circ}\text{C}$  and 2  $^{\circ}\text{C}$ , respectively. Hence, large droplets are effectively removed under the given measurement conditions. The shape of the tertiary droplet size distribution is again bimodal, with maxima at 1.4 and 4.9  $\mu\text{m}$  for the spray chamber at 20  $^{\circ}\text{C}$  and 1.4 and 5.7  $\mu\text{m}$  for the spray chamber at 2  $^{\circ}\text{C}$ . As shown in *Figure 6-27 (B)*, the cut-off diameter ( $d_{\text{vol}100}$ ) of the Scott spray chamber depends on the spray chamber temperature. It is approximately 25.5  $\mu\text{m}$  and 12.6  $\mu\text{m}$  for the spray chamber at 20  $^{\circ}\text{C}$  and 2  $^{\circ}\text{C}$ , respectively.

The results of the laser diffraction measurements are summarized in *Table 6-4*.

*Table 6-4 Results for the tertiary aerosol measured by laser diffraction.*

		spray chamber at 2 $^{\circ}\text{C}$	spray chamber at 20 $^{\circ}\text{C}$
Sauter mean diameter	[ $\mu\text{m}$ ]	1.2	1.4
Volume mean diameter	[ $\mu\text{m}$ ]	2.9	3.1
Particle mass specific surface	[ $\text{cm}^2 \text{g}^{-1}$ ]	48401	43876
Particle volume specific surface	[ $\text{m}^2 \text{cm}^{-3}$ ]	4.84	4.39

## 6.4 Numerical simulation results

The following simulation results are based on a model developed with FIRE™ version 7.3 (see 8.1 Appendix A: Numerical simulations – FIRE™ v7.3). This model was able to reproduce well the modification processes of the primary aerosol in the Scott spray chamber, but not the evaporation processes prevailing in the spray chamber at the given inlet conditions. As a result, the mass of the aerosol could be calculated numerically, but not the total mass transport, since the mass of the evaporated solvent was missing. The improved model of the Scott spray chamber is presented below, with simulations performed using FIRE™ v2019.2.

### 6.4.1 Flow field in the Scott spray chamber/ Argon jet

An essential result of the simulation is the representation of the argon velocity field in the Scott double-pass spray chamber. From *Figure 6-28*, it is easy to see that the characteristics of this flow field correspond to those of a confined turbulent free jet.

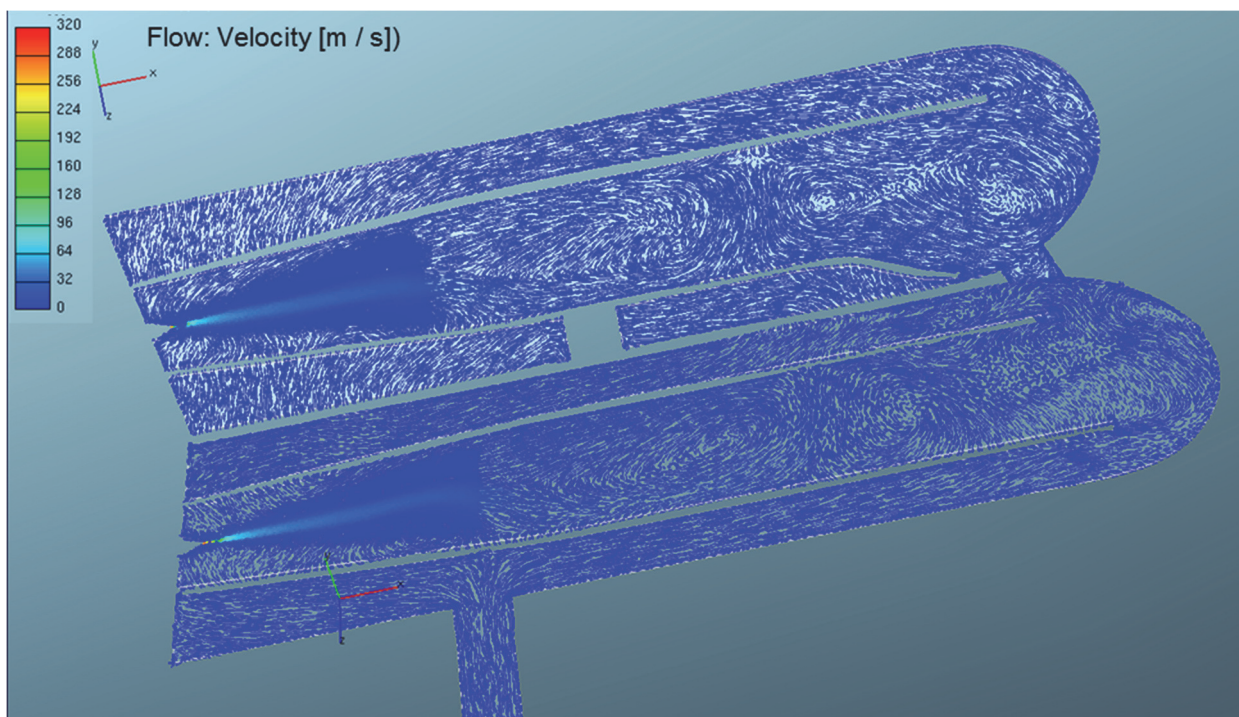


*Figure 6-28* Velocity vector field in the planes which are defined by the waste outlet and nebulizer nozzle (upper plane) and the outlet and the nebulizer nozzle (lower plane) of the Scott spray chamber.

As a result of the turbulent fluctuating motion at the edges of the jet, there is a lateral exchange of momentum, by which large areas of the initially stationary environment are captured and entrained. This suction effect of the jet causes the surrounding fluid to be sucked into the jet (entrainment effect) [Schlichting et al., 2006 (p. 662)]. It should be noted, however, that due to the confinement of the free jet by the wall of the inner tube of the spray chamber, there is no infinite reservoir of the surrounding fluid available for the entrainment process. Therefore, the jet must entrain fluid from itself, resulting in recirculation of the flow [Schlichting et al., 2006 (p. 666)], [Sharp, 1988b (p. 941)]. A single recirculating eddy is established, whose eye is located approximately at the point where the jet fills the enclosure (about 3 cm downstream from the nebulizer nozzle). This is not turbulence per se, but a reversal of the ambient flow direction. To avoid these backflow currents, an auxiliary flow would be required. Theoretically, this would have to be 11.5 times the primary jet flow, which of course would be more than impractical with regard to the injector flow of the ICP [Sharp, 1988b].

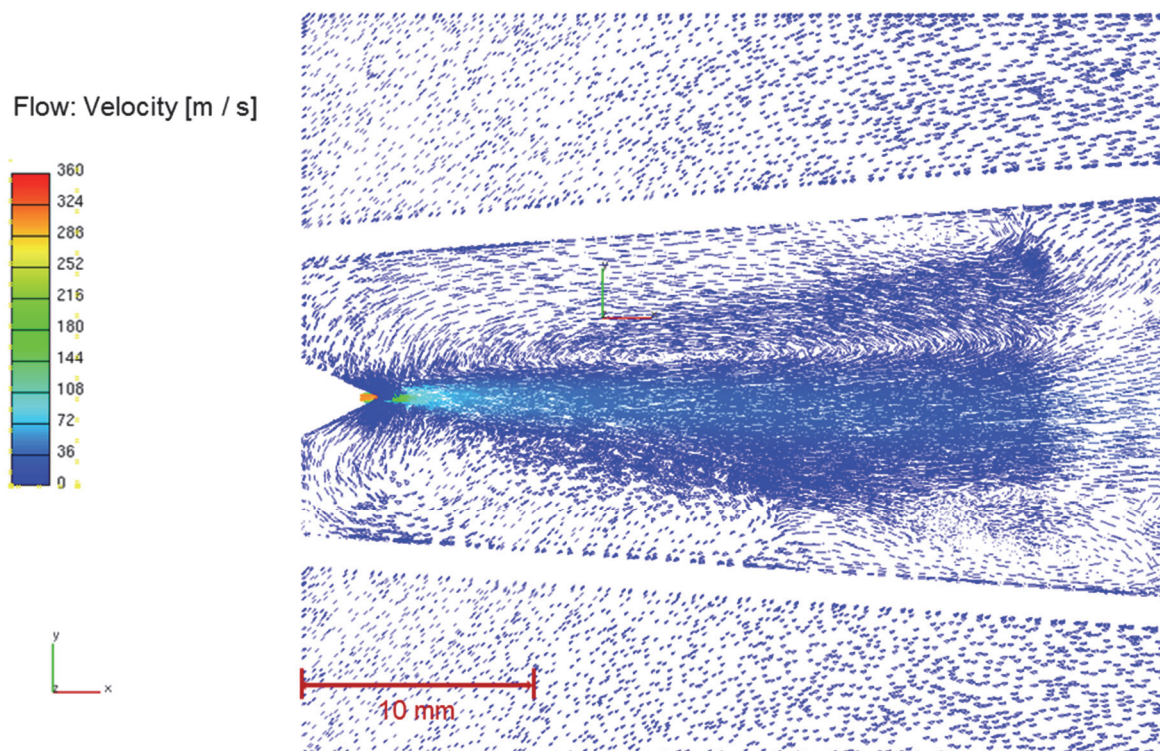
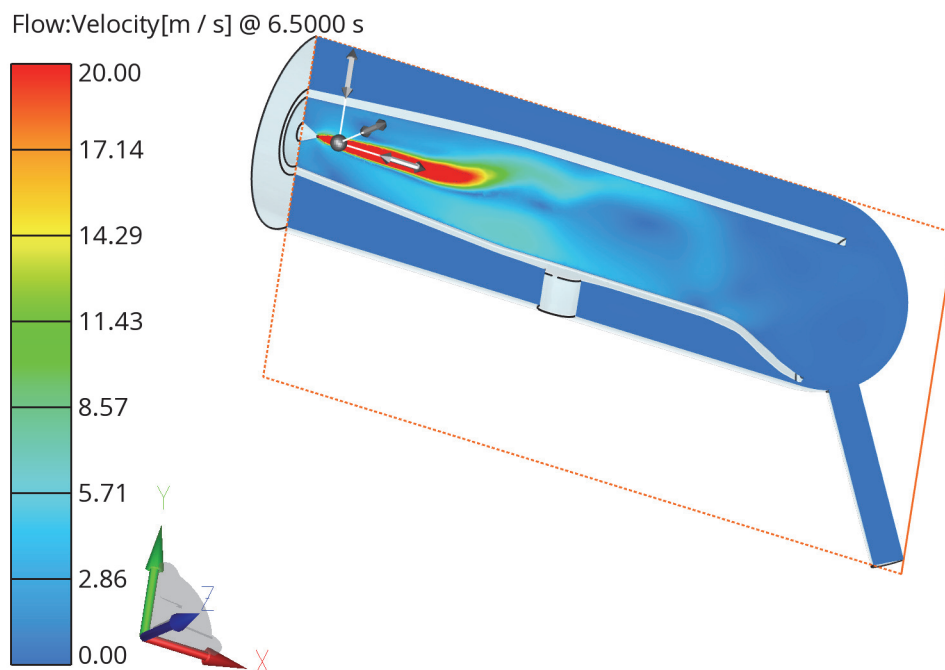


Figure 6-29 Velocity vector field near the nebulizer nozzle.

From about 3 cm downstream from the nebulizer orifice, the gas inlet centerline velocity decreases from  $276 \text{ m s}^{-1}$  to less than  $10 \text{ m s}^{-1}$  and reaches an average velocity of  $1 \text{ m s}^{-1}$  at the plasma outlet of the spray chamber. Large eddies are produced near the nebulizer nozzle (see *Figure 6-28* and *Figure 6-29*) and along the inner tube of the spray chamber, where the majority of the kinetic energy of the turbulent flow is concentrated, as a result of shear forces between the nebulizer gas jet and the relatively static gas outside the free jet boundary [Fasch et al., 2023].

Around the jet axis, the resultant flow rotates like a pendulum (*Figure 6-30*). Following a flow reversal at the end of the inner cylinder of the Scott chamber, the turbulent flow finally becomes laminar and exits the chamber in the direction of the plasma (*Figure 6-31* and *Figure 6-32*) [Fasch et al., 2023].



*Figure 6-30 Velocity field in the plane which is defined by the waste outlet and the nebulizer nozzle.*

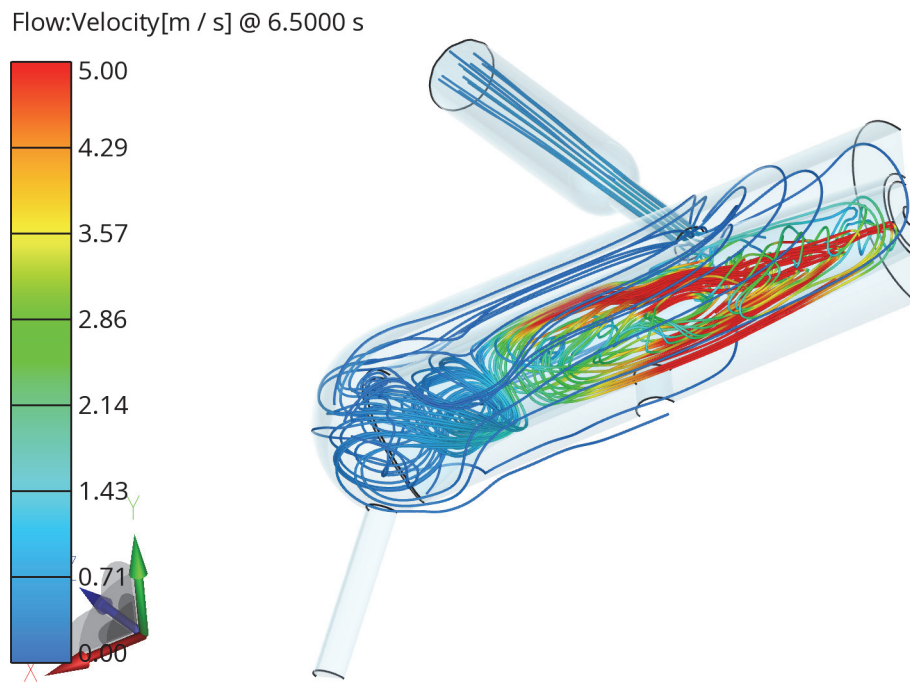


Figure 6-31 Velocity field (streamlines representation).

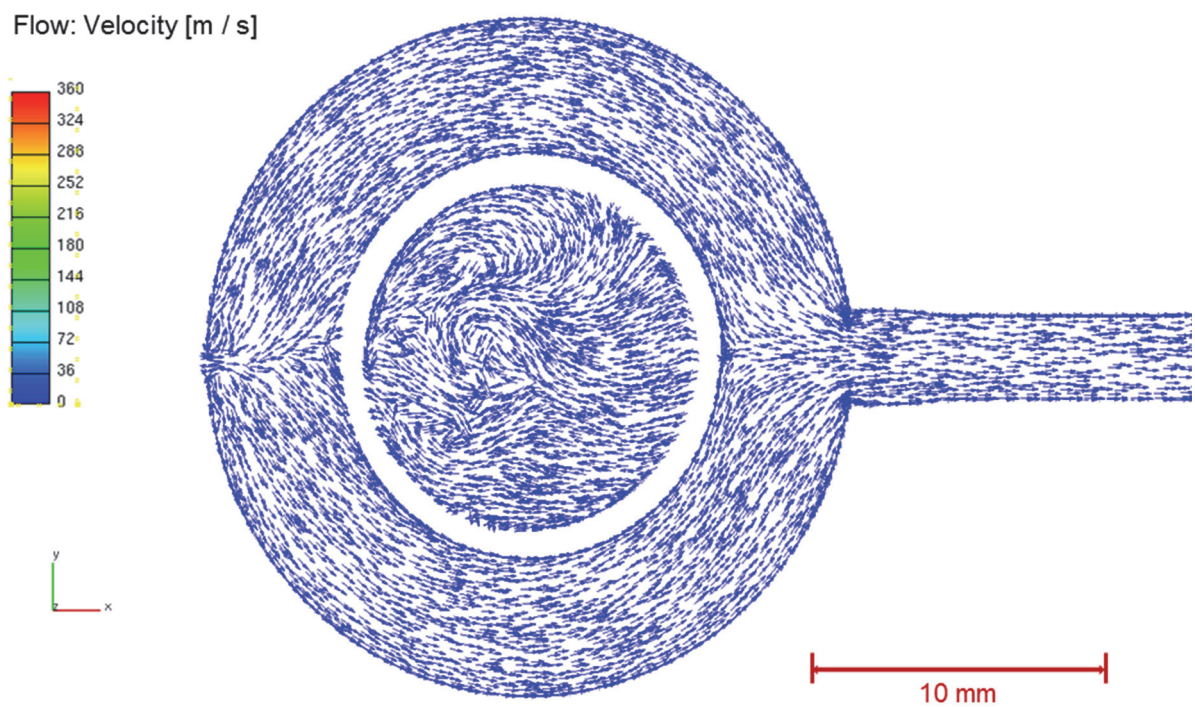


Figure 6-32 Turbulent velocity field in the inner tube of the spray chamber; laminar flow regime in the outer cylinder and at the outlet of the spray chamber [Fasch et al., 2023].

Figure 6-33 shows the pressure distribution in the Scott spray chamber. It can be seen that, with the exception of the nozzle area, ambient pressure more or less prevails.

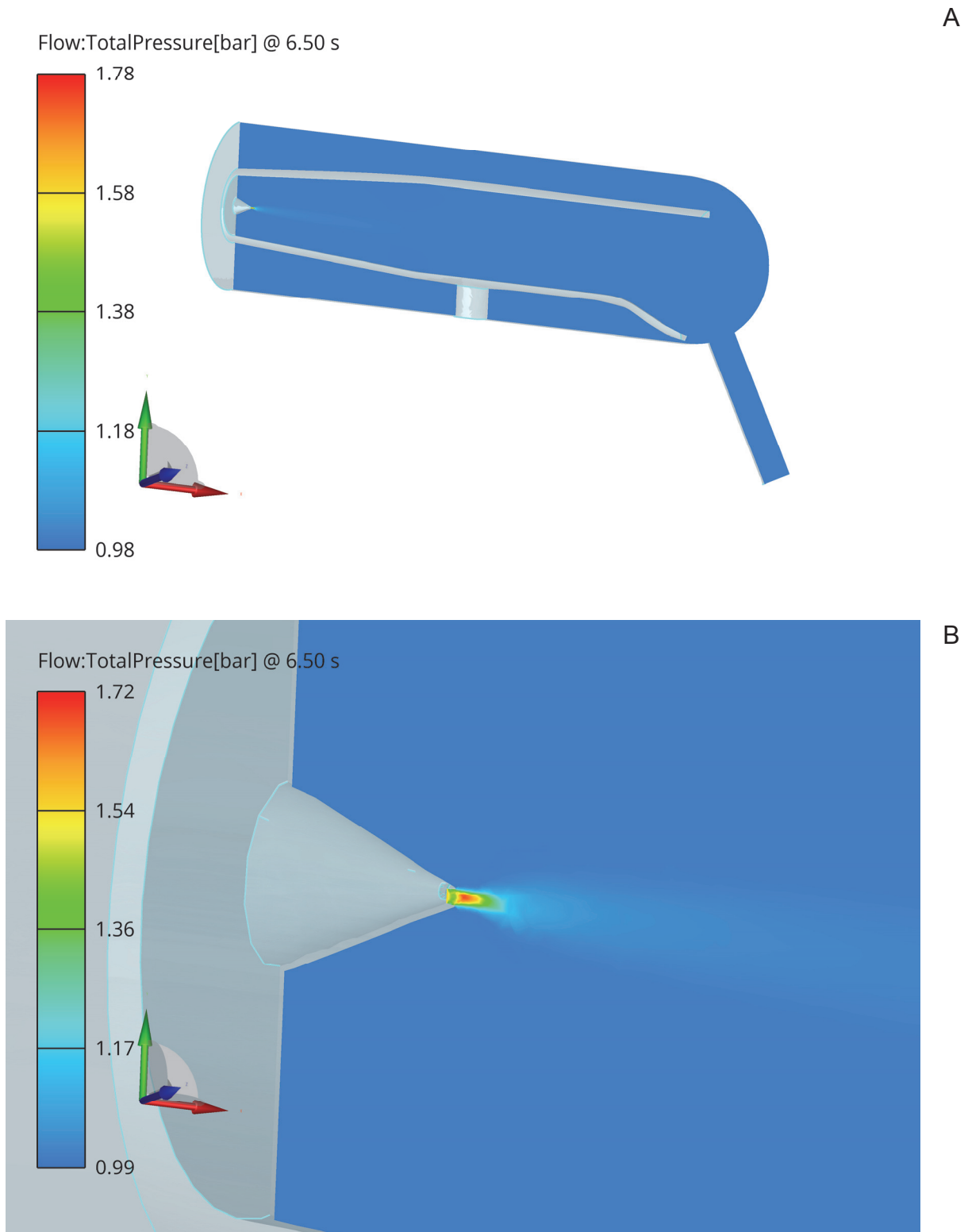
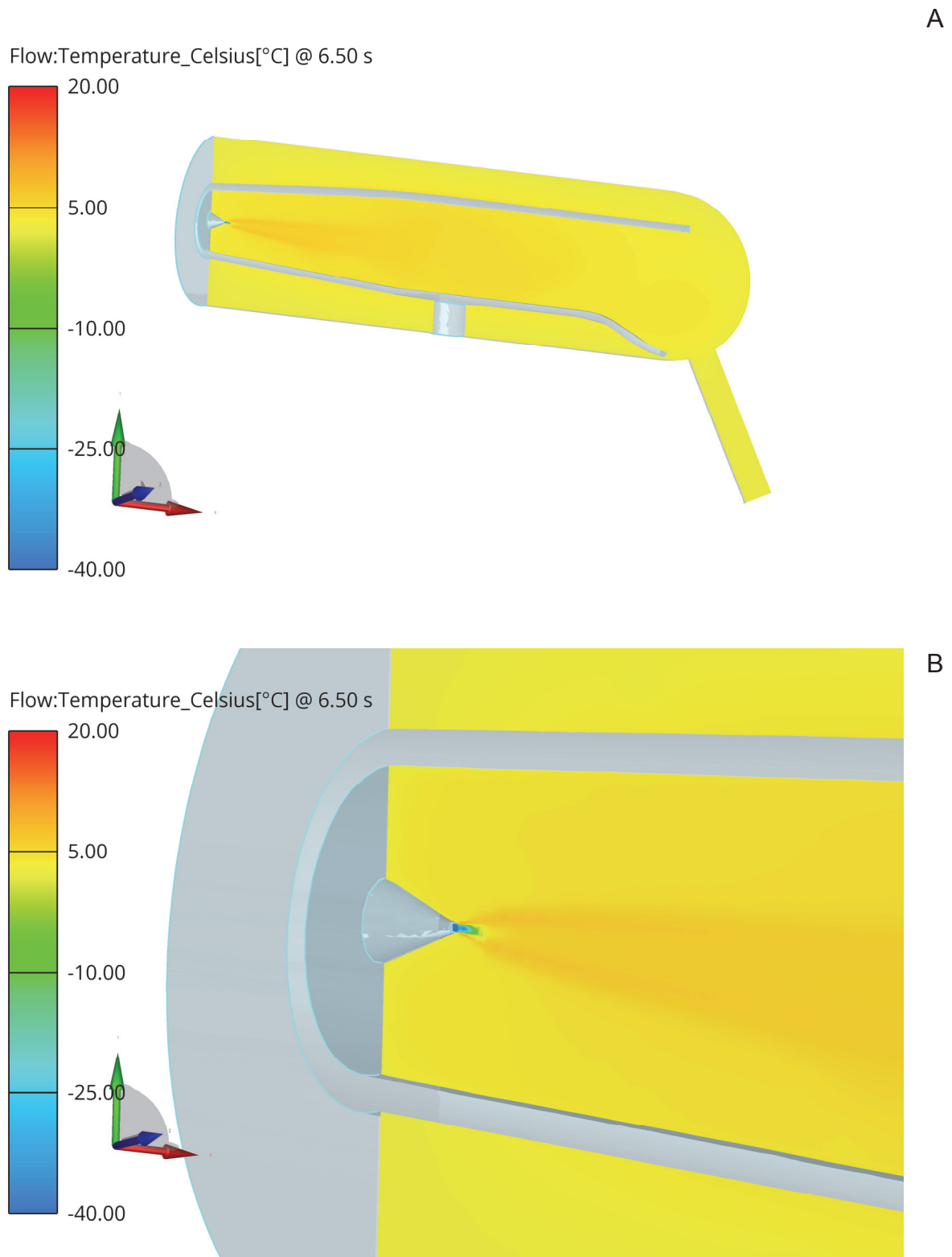


Figure 6-33 Pressure field in the Scott spray chamber (A) and in the inlet regime (B).



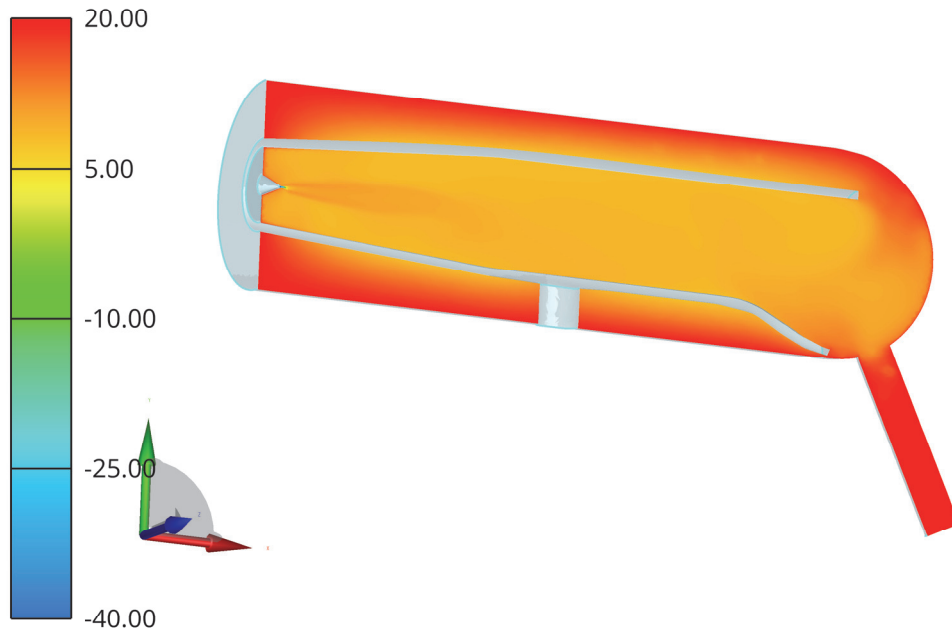
The temperature distribution for the spray chamber temperatures studied (i.e., 2 °C and 20 °C) is shown in *Figure 6-34* and *Figure 6-35*. The argon inlet temperature is -53.4 °C, as specified in the starting conditions.



*Figure 6-34* Temperature distribution in the Scott spray chamber at 2 °C (A) and in the inlet regime (B).

A

Flow:Temperature\_Celsius[°C] @ 6.50 s



B

Flow:Temperature[°C] @ 6.5000 s

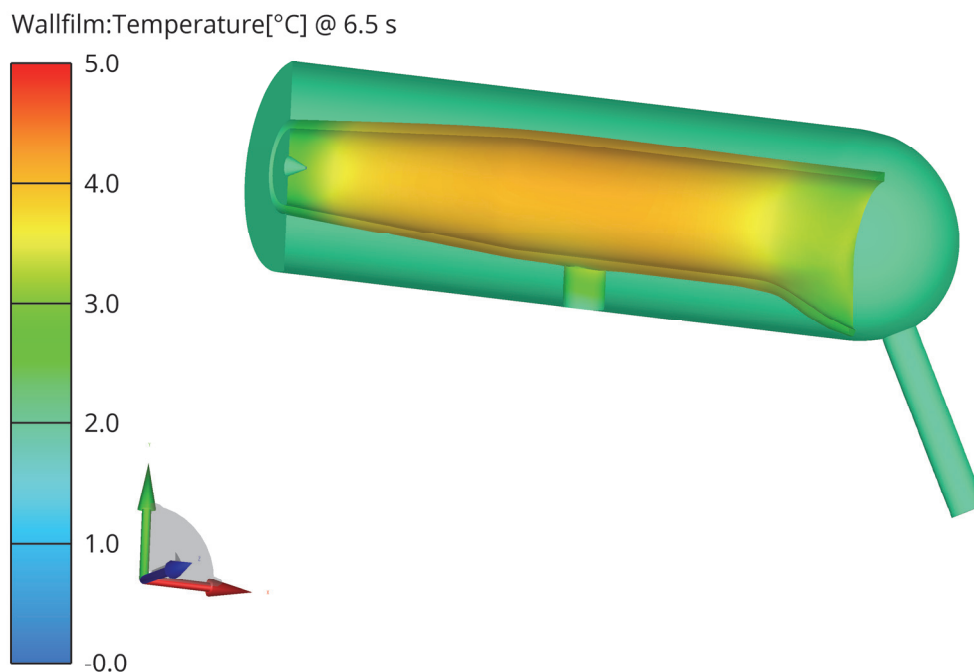


Figure 6-35 Temperature distribution in the Scott spray chamber at 20 °C (A) and in the inlet regime (B).

## 6.4.2 Numerical simulation of the droplet phase

In the spray chamber, a considerable part of the nebulized sample is deposited as a thin liquid film on the walls due to wall collisions. The velocity of the film is only 1 – 3 % compared to the average argon flow velocity because of the much higher viscosity of the liquid phase. The FIRE™ Wall Film module, which was originally developed to simulate the formation of a thin liquid gasoline film in the intake manifold of a spark ignition (SI) engine, considers all relevant physical effects. These include evaporation, secondary atomization, film rupture, and transport due to shear force and gravity. Since the wall temperature of the inner cylinder of the Scott spray chamber is difficult to access experimentally, it is calculated numerically using the FIRE™ Thin Walls module.

*Figure 6-36 and Figure 6-37 illustrate the temperature distribution of the resulting wall film in the spray chamber at 2 °C and in the spray chamber at 20 °C, respectively. The mean wall film temperature in the cooler chamber and in the warmer chamber is 4 °C and 8 °C, respectively.*



*Figure 6-36 Wall film temperature of the spray chamber at 2 °C.*

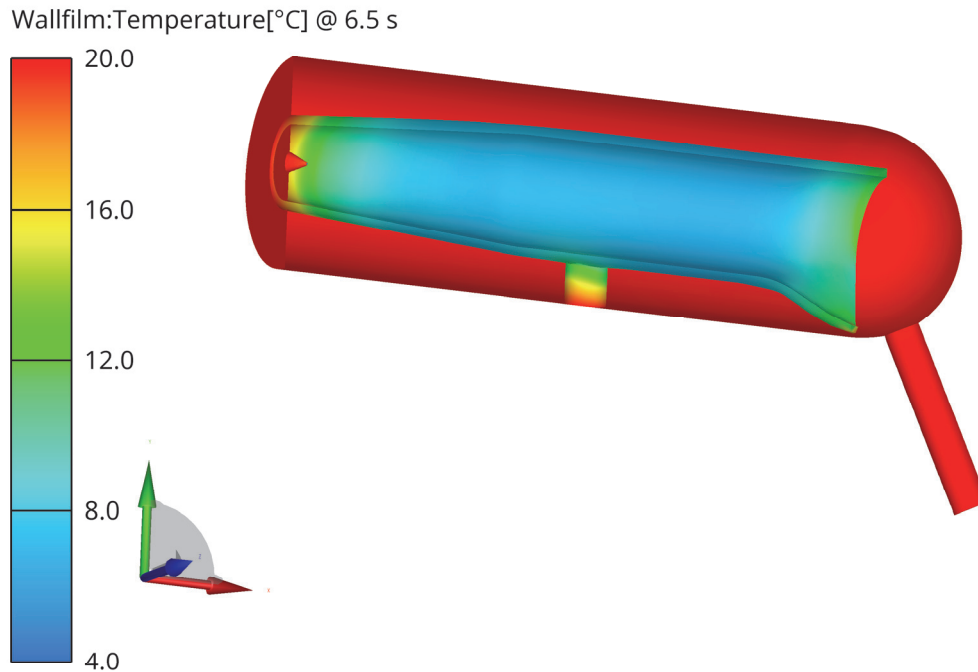
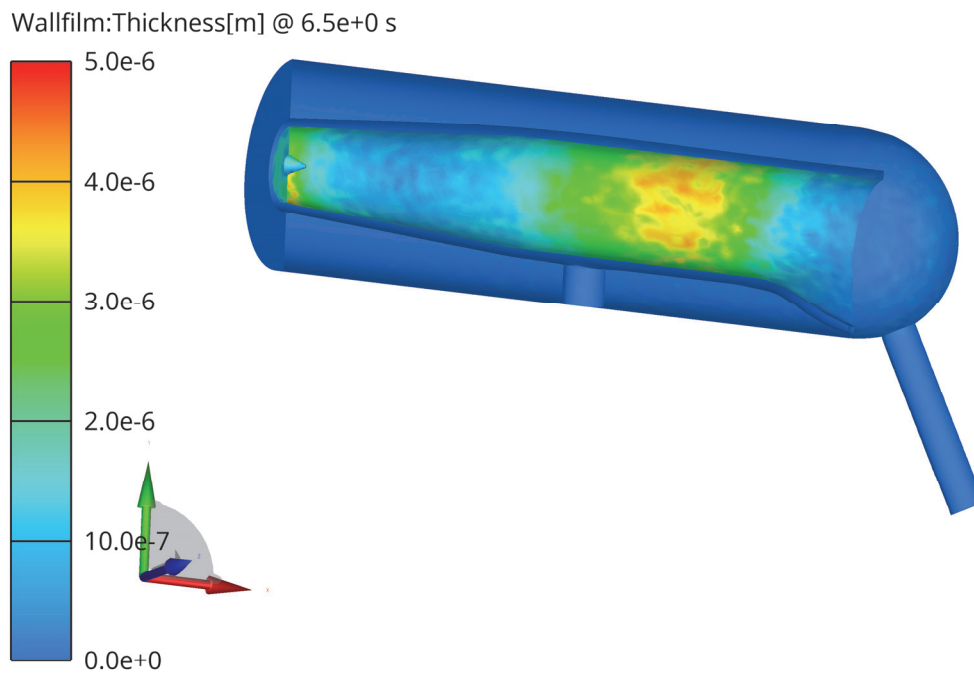


Figure 6-37 Wall film temperature of the spray chamber at 20 °C.

The wall film thickness and wall film velocity are quite similar for the cooler and warmer spray chamber and shown in *Figure 6-38* for the Scott chamber at 2 °C. The film thickness and film velocity averaged over the area are 2.2 E-03 mm and 0.26 mm s<sup>-1</sup>, respectively, for the spray chamber at 2 °C and 2.2 E-03 mm and 0.27 mm s<sup>-1</sup>, respectively, for the chamber at 20 °C.

Basically, the simulation results show that the flow field of the gas phase controls the deposition behavior in the spray chamber [Fasch et al., 2023]. From this, it can be deduced that two main mechanisms of inertial deposition are observed: droplet impaction by **flow line interception** due to the motion of the bulk flows and impactions by superimposed random components of the directional flow movement due to turbulence effects (**turbulent deposition**).

A



B

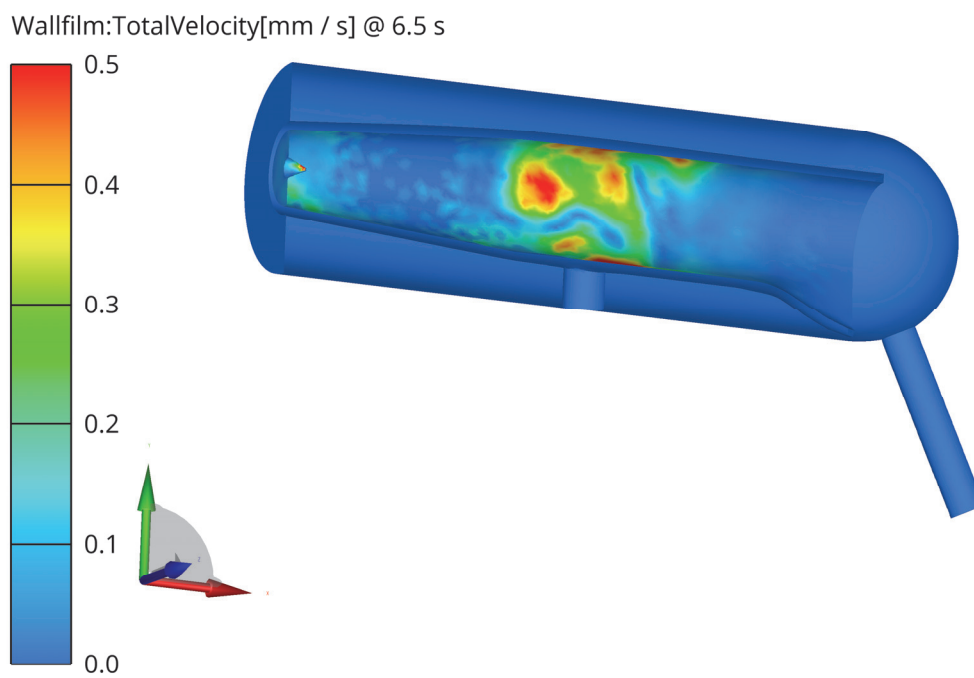
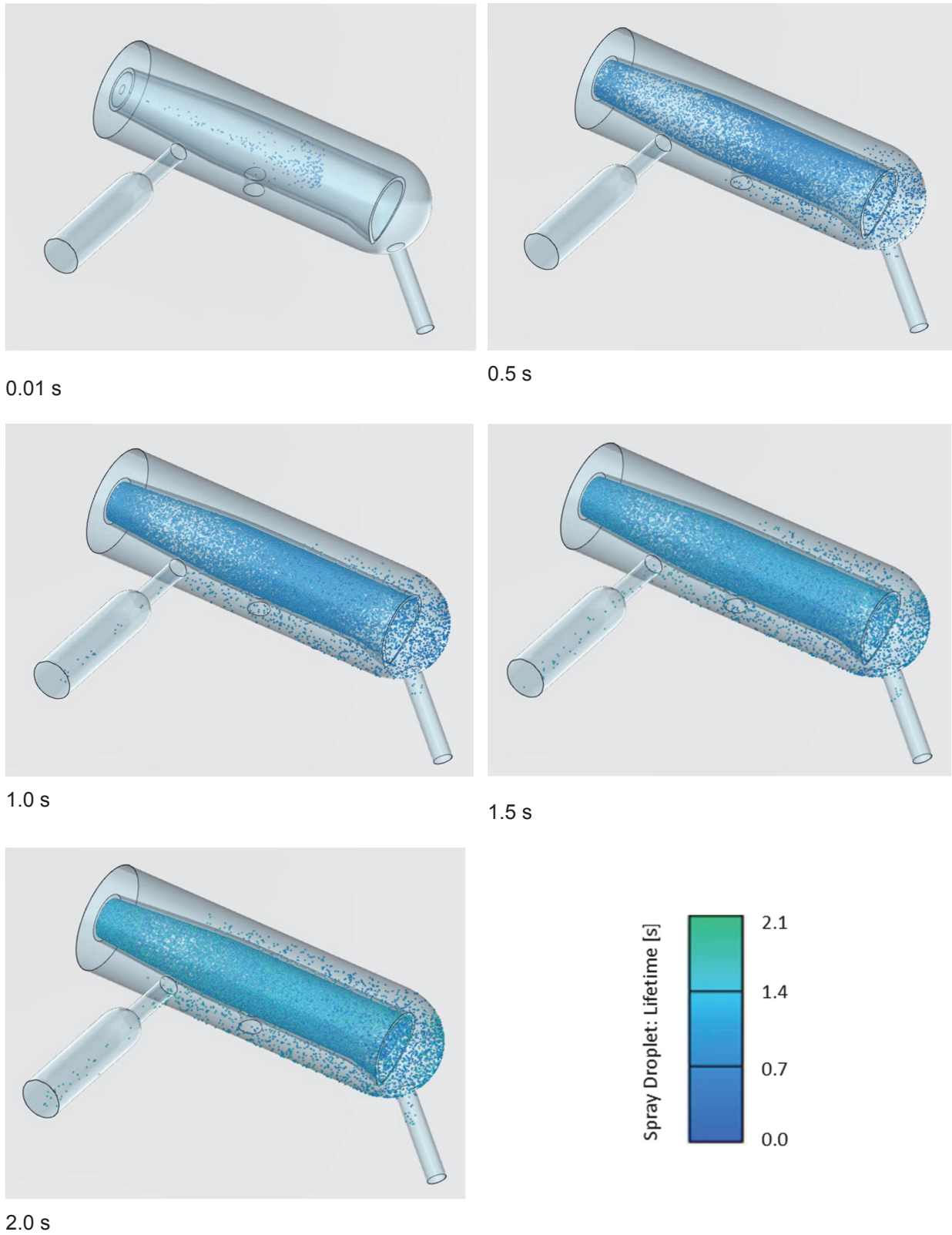


Figure 6-38 Wall film thickness (A) and wall film velocity (B) in the Scott chamber thermostatted at 2 °C.

The droplet situation in the spray chamber as a function of time after injection of the sample liquid based on droplet lifetime is displayed in *Figure 6-39* [Fasch et al., 2023].



*Figure 6-39* Various situations in the spray domain after injection of sample liquid based on droplet lifetime.

The results of the numerical simulation show that the first droplets pass through the outlet of the spray chamber after about one second.

The different deposition rates of the initially generated aerosol with respect to specified areas in the Scott chamber are illustrated for the various spray chamber temperatures in *Figure 6-40*. For this purpose, the spray chamber under investigation was divided into five different areas: bottom (i.e., inlet region including the nebulizer surface), inner pipe, dome (i.e., the wall area opposite the nebulizer nozzle), outer pipe, and wall (i.e., the inner surface of the outer cylinder of the spray chamber).

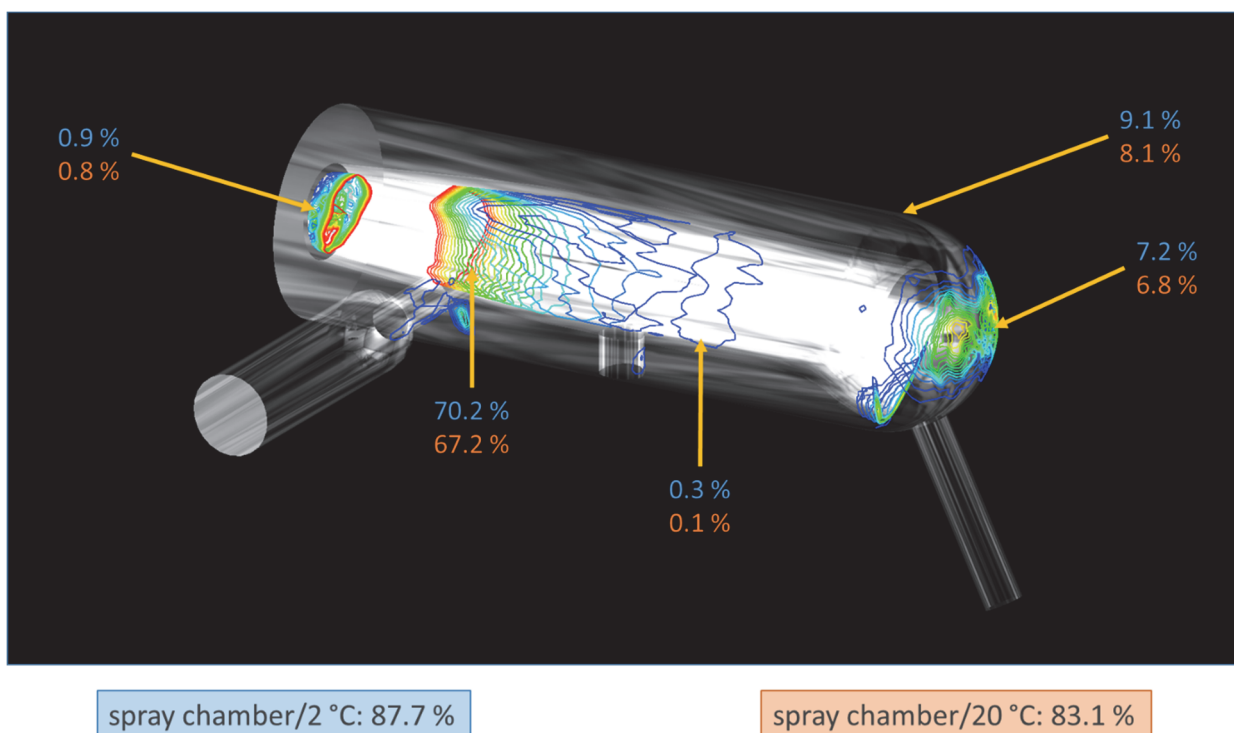


*Figure 6-40* Deposition of the originally generated aerosol related to different areas in the spray chamber [Fasch et al., 2023].

The numerical simulation shows that in the cooler spray chamber a total of 87.7 % of the introduced sample is deposited as a wall film. In the warmer chamber, the proportion is 83.1 %. Most of the introduced sample is trapped as a wall film on the surface of the inner cylinder with deposition rates of 70.2 % (spray chamber at 2 °C) and 67.2 % (spray chamber at 20 °C). Due to the strong recirculation zone close to the nebulizer nozzle, the deposition rates in this area (marked bottom) are 0.9 % and 0.8 % for the spray chamber at 2 °C and 20 °C, respectively. The aerosol deposited on the surface of the dome amounts

to 7.2 % for the cooler chamber and to 6.8 % for the warmer chamber. After reversal of the flow field, 0.3 % (spray chamber at 2 °C) and 0.1 % (spray chamber at 20 °C) of the nebulized sample deposit on the outer surface of the inner tube of the Scott chamber (marked as outer pipe). Finally, with the spray chamber at 2 °C and 20 °C, 9.1 % and 8.1 % of the introduced sample, respectively, remain trapped on the inner surface of the outer cylinder (marked as wall).



*Figure 6-41 Pictures of the investigated double-pass glass spray chamber to evidence the zones of droplet impact, nebulizing a methylene red solution (source: E. Fasch).*



Figure 6-41 shows images of the Scott spray chamber in which a dye solution (methylene red) was nebulized to highlight the zones of maximum droplet impingement. In agreement with the simulation results, the area of the inner cylinder is mainly responsible for the overall droplet deposition. Consistent with the CFD predictions, the picture further shows that droplets are also removed from the dome, but less pronounced than from the inner cylinder.

The simulated mass transport efficiencies are 11 % and 16 % for the spray chamber at 2 °C and 20 °C, respectively. These values are in good agreement with the experimentally determined mass transport efficiencies of 12 %  $\pm$  1 % (spray chamber at 2 °C) and 20 %  $\pm$  3 % (spray chamber at 20 °C). The experimental data show that higher mass transport at warmer spray chamber temperatures is not necessarily associated with higher analyte transport efficiency (see also chapter 6.2.1).

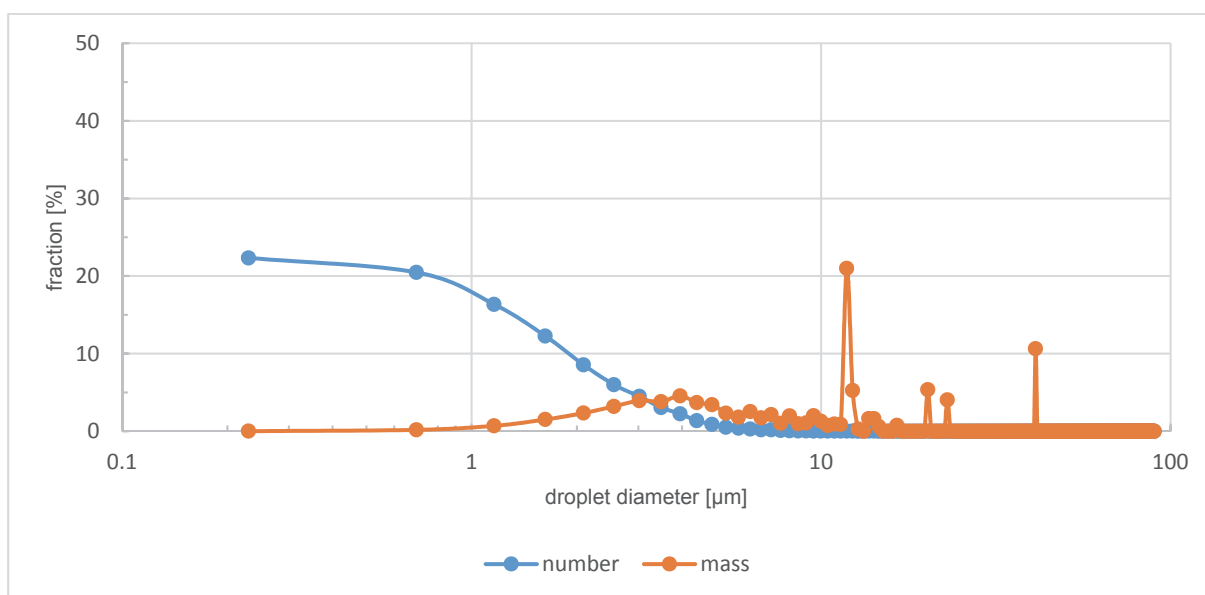
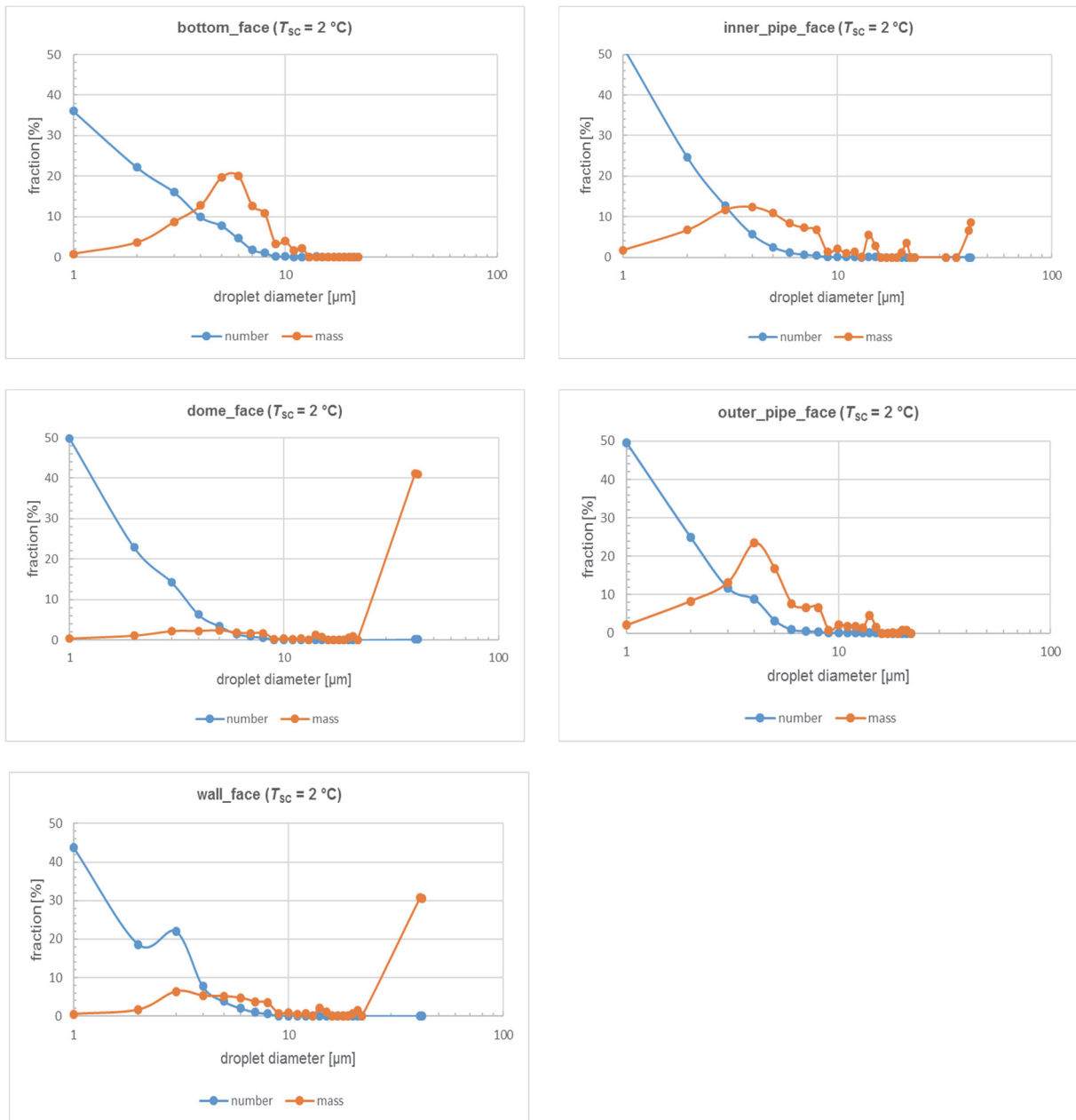


Figure 6-42 Droplet size distribution of the primary aerosol measured by the PDA method at a distance of 10 mm from the nebulizer tip.

Additionally, the numerical simulation results allow the prediction of the droplet size distributions in the considered deposition zones of the spray chamber. The number and mass based droplet size distribution of the primary aerosol measured by PDA is illustrated in Figure 6-42. This plot shows the typical polydispersity of the aerosol generated by the MicroMist nebulizer.

The volume based size distributions of the droplets deposited on the various surfaces of the Scott chamber are presented in *Figure 6-43* for the chamber at 2 °C and in *Figure 6-44* for the chamber at 20 °C.



*Figure 6-43* Calculated volume (mass) – based droplet size distributions of the aerosol deposited on various surfaces of the Scott chamber at 2° C.

Considering the inlet region including the nebulizer surface (marked bottom), the simulation shows for both spray chamber temperatures investigated a selective deposition of smaller droplets.

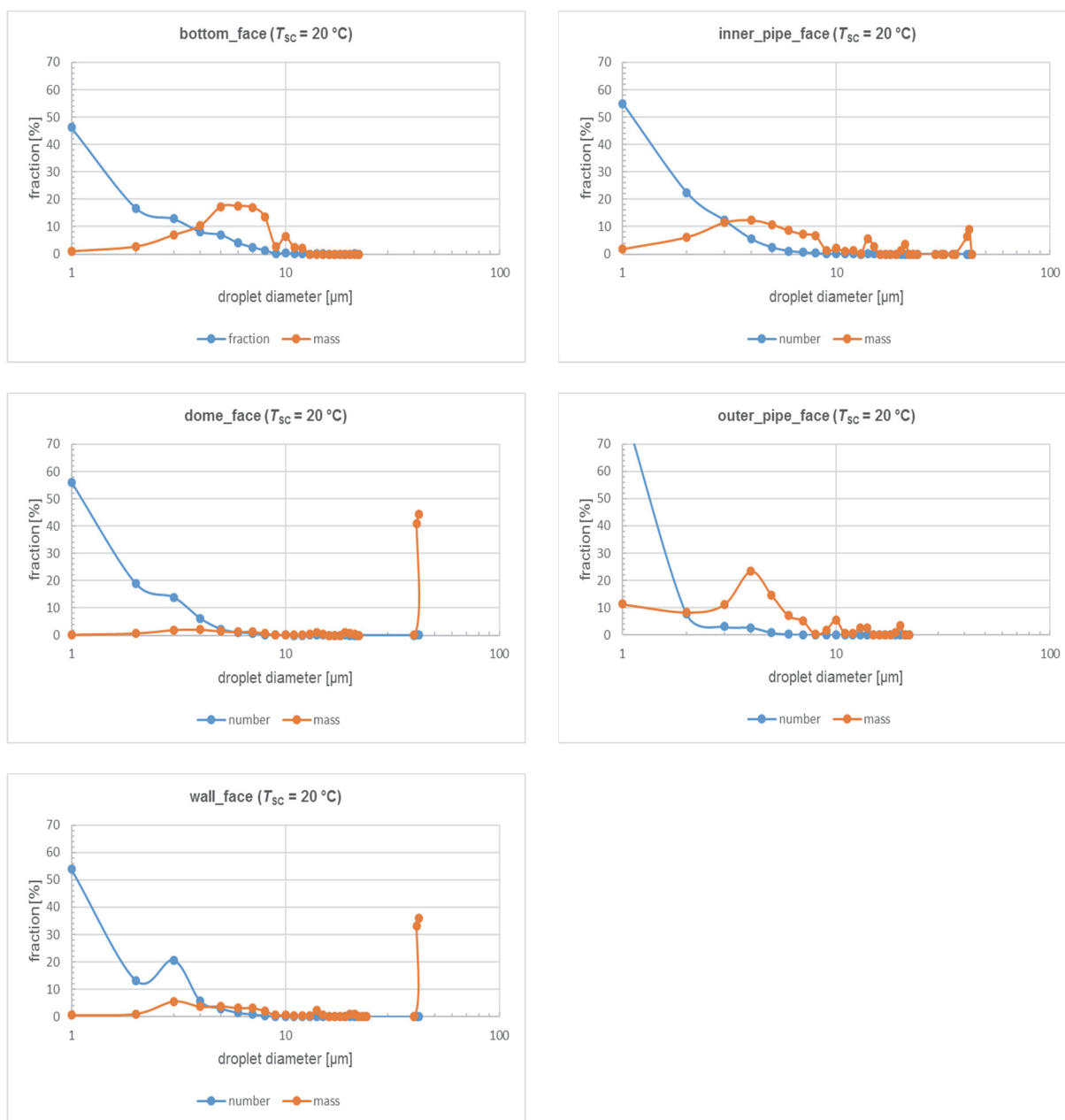


Figure 6-44 Calculated volume (mass) – based droplet size distributions of the aerosol deposited on various surfaces of the Scott chamber at 20° C.

This effect can be explained by the fact that in this region of the spray chamber it is predominantly the smaller droplets which can follow the recirculating argon flow, as these have a lower kinetic energy compared to the large droplets. This results in droplet deposition on the surface of the nebulizer nozzle and in the region behind it [Schaldach et al., 2002 (p. 1512)]. The large droplets, on the other hand, have such high momentum that they move in a straight line like cannonballs, in the direction of the nebulizer nozzle axis.

It should also be noted that this is an undesirable deposition behavior, as droplets up to a diameter of about 10  $\mu\text{m}$  are mainly deposited. The calculated count mean diameter and Sauter mean diameter (see *Table 3-2* for definition) are 2.3  $\mu\text{m}$  and 5.3  $\mu\text{m}$  for the spray chamber at 2  $^{\circ}\text{C}$  and 2.2  $\mu\text{m}$  and 5.8  $\mu\text{m}$  for the spray chamber at 20  $^{\circ}\text{C}$ , respectively. However, this effect leads to a removal of about 1 % of the droplet mass.

Most of the aerosol deposit ends up on the surface of the inner tube of the Scott chamber. The calculated droplet size distributions show that mainly droplets are collected whose size distribution corresponds more or less to that of the original aerosol. Only the droplet mass of the droplets  $> 10 \mu\text{m}$  is somewhat reduced. This behavior is the same for the spray chamber at 2  $^{\circ}\text{C}$  and the spray chamber at 20  $^{\circ}\text{C}$ , respectively. The Sauter mean diameter is 5.2  $\mu\text{m}$  for both spray chamber temperatures. This means that there is no significant temperature effect with respect to the droplet size distribution of the deposited aerosol. The only difference is that about 3 % more aerosol mass is deposited in the Scott chamber at 2  $^{\circ}\text{C}$ . It can be concluded that the inner cylinder of the Scott chamber does not exhibit any pronounced selective separation behavior.

The calculated volume (mass) - based droplet size distributions of the aerosol deposited at the dome of the spray chamber give the highest Sauter mean diameters of 19.5  $\mu\text{m}$  ( $T_{\text{SC}} = 2 \text{ }^{\circ}\text{C}$ ) and 21.5  $\mu\text{m}$  ( $T_{\text{SC}} = 20 \text{ }^{\circ}\text{C}$ ), compared to all other surfaces. Thus, the dome of the spray chamber shows a very selective separation behavior. Here, mainly the large droplets that have managed to pass through the inner cylinder of the spray chamber are trapped. Relative to the total aerosol, about 7 % of the mass is deposited on this surface. In relation to the remaining aerosol that can pass the inner cylinder, however, this mass is about 25 % ( $T_{\text{SC}} = 2 \text{ }^{\circ}\text{C}$ ) and 21% ( $T_{\text{SC}} = 20 \text{ }^{\circ}\text{C}$ ).

The residual aerosol must now undergo a flow reversal to pass through the outer tube of the Scott chamber. In contrast to the turbulent flow field that prevails in the inner tube of the spray chamber, a laminar flow field now acts on the remaining aerosol. Relative to the total mass of the aerosol introduced, the proportion separated in the outer tube is about 9.4 % ( $T_{\text{SC}} = 2 \text{ }^{\circ}\text{C}$ ) and 8.2 % ( $T_{\text{SC}} = 20 \text{ }^{\circ}\text{C}$ ), which in turn means that in relation to the rest of the active aerosol passing through the dome approximately 43 % ( $T_{\text{SC}} = 2 \text{ }^{\circ}\text{C}$ ) and 33 % ( $T_{\text{SC}} = 20 \text{ }^{\circ}\text{C}$ ) of the aerosol mass is lost again. The simulation shows for both spray chamber temperatures investigated that the residual aerosol is deposited here mainly on the inner surface of the outer cylinder (marked as wall). For the cooler spray chamber, the calculated Sauter mean diameter amounts to 11.5  $\mu\text{m}$  and 2.0  $\mu\text{m}$  for the

outer pipe face and the wall face, respectively. Looking at the warmer Scott chamber, it can be seen that the calculated Sauter mean diameter is 2.8  $\mu\text{m}$  for the outer pipe surface and 13.8  $\mu\text{m}$  for the wall surface. This means that predominantly larger droplets are deposited in the outer tube close to the dome.

Table 6-5 gives an overview of the Sauter mean diameters of the droplets deposited on the surfaces considered.

Table 6-5 Simulated Sauter mean diameters ( $d_{32}$ ) of the droplets deposited on the various surfaces of the Scott chamber at different spray chamber temperatures.

	Sauter mean diameter ( $d_{32}$ ) [ $\mu\text{m}$ ]	
	spray chamber at 2 °C	spray chamber at 20 °C
bottom_face	5.3	5.8
inner_pipe_face	5.2	5.2
dome_face	19.5	21.5
outer_pipe_face	11.5	2.8
wall_face	2.0	13.8

Basically, the inner cylinder is mainly responsible for reducing the amount of aerosol. However, evaporation effects must also be taken into account, which lead to a change in the aerosol properties, as the sample introduction system is operated at a low liquid flow rate [Todoli et al., 2008 (p. 84)]. The total sample mass flux is composed of two components: the aerosol flow (liquid) and the water vapor flow (gaseous). The calculated mass of the generated water vapor is the main component, while the transported droplet mass is calculated to be less than 1% of the introduced aerosol. It must be noted that the exact phase composition was not determined experimentally in this thesis. Droplet evaporation effects are particularly pronounced in the inlet domain of the spray chamber. In the region of the nebulizer nozzle, the argon is not yet saturated with solvent, and the relative veloc-

ities of the gas and liquid phases are very high, too. Consequently, the droplet environment is constantly renewed with dry argon, which in turn promotes further droplet evaporation [Todoli et al., 2008 (p. 79)]. With the models used in the simulation, no wall film evaporation was detected in the calculation results (see also *chapter 4.3.4*).

There are several possibilities mentioned in the literature to clarify the origin of water vapor loading: Sharp [Sharp, 1988b (p. 951)] suggests that only small droplets contribute significantly to aerosol evaporation. In his opinion, these form a temporary supersaturation of the vapor phase with respect to the bulk solution due to the surface curvature effect. The local supersaturation near the evaporating droplet therefore leads to saturation of the entire gas phase at a constant mass transfer rate. It thus contradicts the "shift-in" mechanism promoted by Gustavsson [Gustavsson, 1986], who sees the explanation in the fact that large droplets reduce their size by evaporation on their passage through the spray chamber. Sharp also found some evidence from experiments [Sharp, 1988b (p. 951)] that the water vapor loading must also originate to a certain degree from wall film evaporation effects. However, the latter could not be confirmed by the present numerical simulation, as the temperature of the inner pipe appears too low for this. (Calculated average wall film temperatures of the inner pipe: 4 °C ( $T_{SC} = 2$  °C) and 8 °C ( $T_{SC} = 20$  °C)).

Finally, the computed droplet size distributions of the aerosol exiting the Scott chamber (tertiary aerosol; *Figure 6-45* and *Figure 6-46*), show for both spray chamber temperatures investigated that the double-pass chamber serves its purpose, as most droplets larger than 10 µm are removed. This means that the whole aerosol entering the plasma should be completely vaporized. The Sauter mean diameters of the tertiary aerosol obtained by numerical simulation are 2.1 µm and 1.2 µm for the spray chamber at 2 °C and the spray chamber at 20 °C, respectively. These results are in good agreement with the values of 2.2 µm ( $T_{SC} = 2$  °C) and 1.4 µm ( $T_{SC} = 20$  °C) determined experimentally by Fraunhofer laser diffraction (see *chapter 6.3.2*).

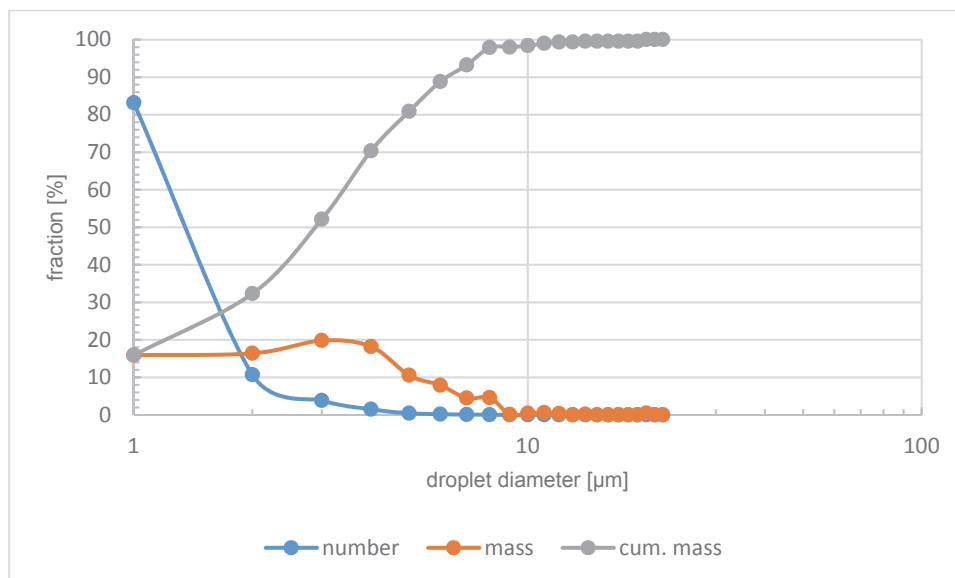


Figure 6-45 Calculated volume (mass) - based droplet size distributions of the aerosol leaving the Scott chamber (tertiary aerosol) at 2 °C.

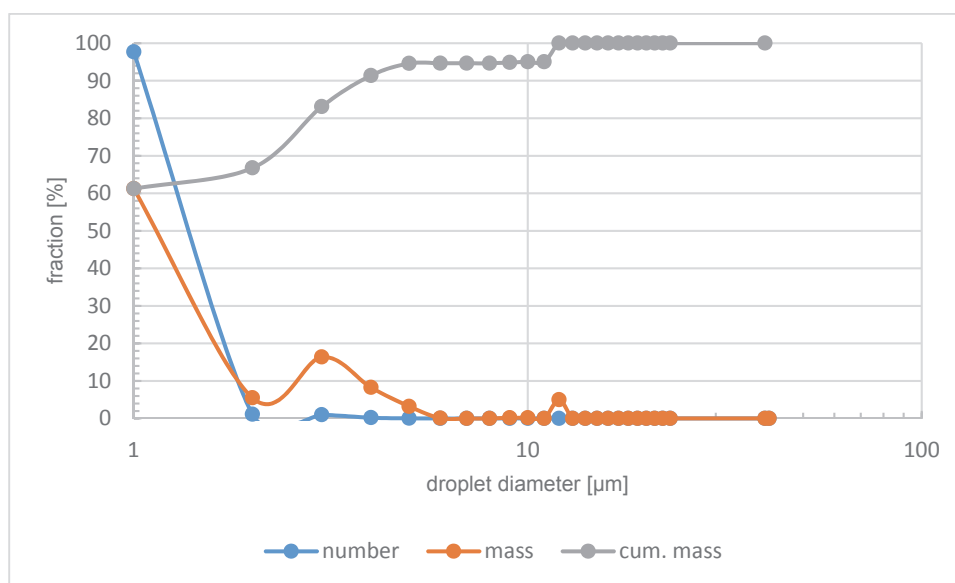
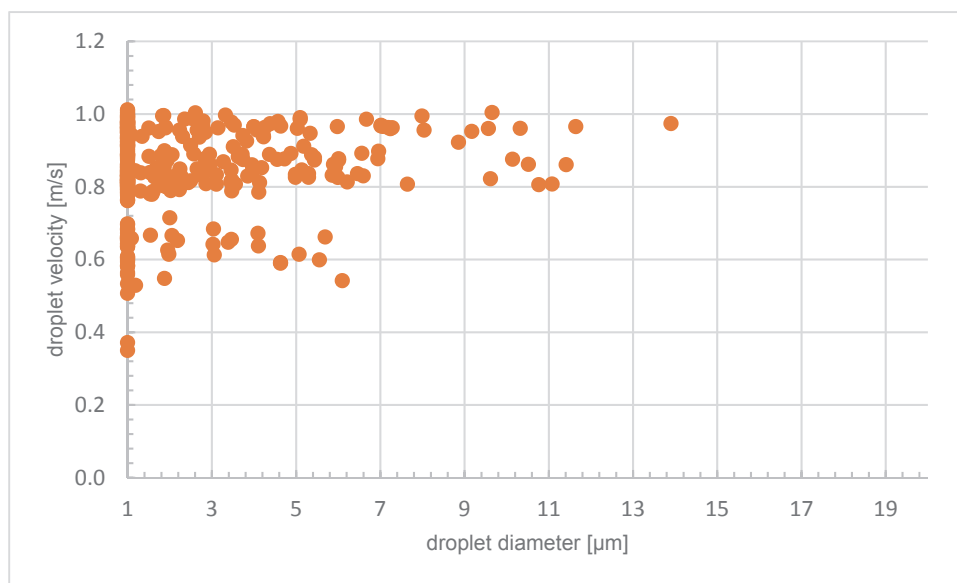


Figure 6-46 Calculated volume (mass) - based droplet size distributions of the aerosol leaving the Scott chamber (tertiary aerosol) at 20 °C.

In the tertiary aerosol of the Scott chamber at 2 °C there are more smaller droplets, which also results in a slightly larger span of 1.8  $\mu\text{m}$  compared to 1.6  $\mu\text{m}$  for the warmer spray chamber. The droplet diameter below which 99% of the cumulative aerosol volume is found amounts to 11.0  $\mu\text{m}$  for the cooler spray chamber and 10.8  $\mu\text{m}$  for the warmer spray chamber. Comparing the calculated values for  $d_{\text{vol}97}$  (refer to droplet diameters below which the 97 percentile of the cumulative aerosol volume is found (*chapter 3.5.2*))

with those obtained by laser diffraction, the results are  $7.8\ \mu\text{m}$  and  $8.3\ \mu\text{m}$  for the cooled chamber and  $10.4\ \mu\text{m}$  and  $9.1\ \mu\text{m}$  for the warmer spray chamber, respectively. Accordingly, these results show good agreement between the numerically calculated and measured data.

*Figure 6-47* illustrates the calculated velocity distribution of the droplets leaving the Scott chamber tempered to  $2\ ^\circ\text{C}$ . The results are quite similar compared to the warmer chamber and show satisfactory agreement with the experimental data from the PIV measurement (see *chapter 6.3.2*).



*Figure 6-47* Calculated velocity distribution of the droplets at the plasma outlet of the Scott chamber at  $2\ ^\circ\text{C}$ .

A graphical representation of the droplet lifetime is given in *Figure 6-48 (A)*. The plot shows that larger droplets are more likely to leave the spray chamber by a direct path than the smaller ones. The smaller droplets tend to follow the argon stream. The diagram of the droplet relaxation time in *Figure 6-48 (B)* confirms this behavior, as the relaxation time increases approximately exponentially with the droplet diameter.



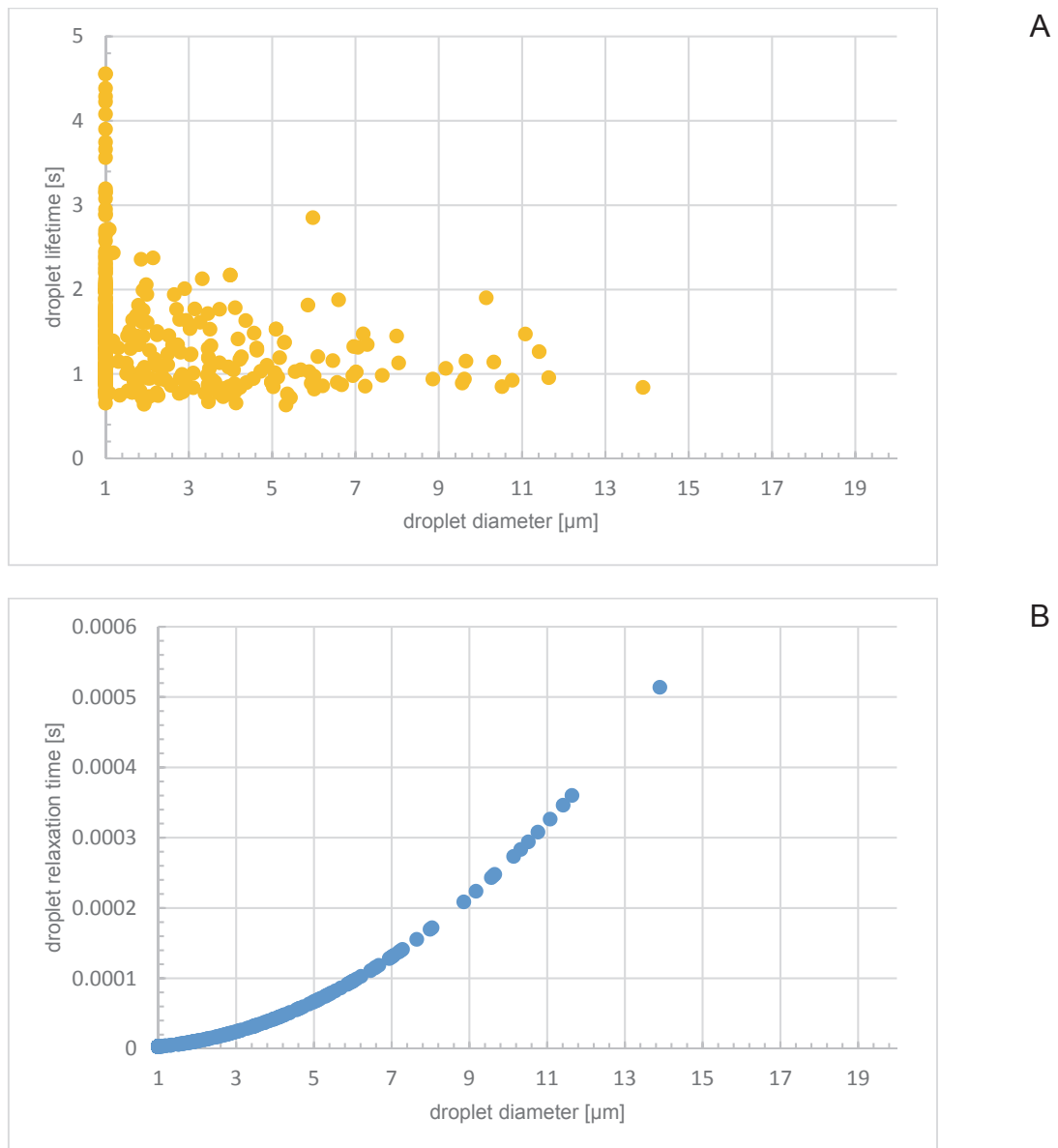


Figure 6-48 Calculated droplet lifetime (A) and droplet relaxation time (B) at the plasma outlet of the Scott chamber at 2 °C.

Table 6-6 summarizes some characteristic data, which compares measured and calculated parameters.

Table 6-6 Comparison of calculated and experimental data.

	<i>spray chamber at 2 °C</i>		<i>spray chamber at 20 °C</i>	
	calculation	experiment	calculation	experiment
mass transport	11 %	12% ± 1 %	16 %	20 % ± 3 %
Sauter diameter	2.1 μm	2.2 μm	1.2 μm	1.4 μm
$d_{vol97}$	7.8 μm	8.3 μm	10.4 μm	9.1 μm
velocity (plasma outlet)	1.0 m s <sup>-1</sup>	0.8 m s <sup>-1</sup>	1.0 m s <sup>-1</sup>	0.8 m s <sup>-1</sup>

## 6.5 Considerations for the optimization of the Scott-type spray chamber

In the following chapters, some modelling considerations for optimizing the Scott spray chamber are presented. In detail, the influence of different spray chamber parameters, e.g. the shape of the inner tube, the diameter of the outer tube, the total chamber length and some variations of the injector area were investigated using the simplified CFD model from *chapter 8.1 (Appendix A: Numerical simulations – FIRETM v7.3)*.

### 6.5.1 Spray chamber model 1

Enclosing a free jet in a spray chamber involves the establishment of a recirculating flow due to the fact that there is no availability of an infinite reservoir of fluid to feed the entrainment process. Therefore, the jet must entrain fluid from itself. Using an auxiliary gas flow to avoid recirculation and produce an uniform forward velocity is limited by the fact that the required flow must be 11.5 times the primary jet flow. Considering ICP analysis such large gas volumes are not functional [Sharp, 188b]. An attempt to improve the deposition behavior concerning the inner tube is to model its geometry.

The first numerical experiment, which does not account for evaporation effects is made with the tube under consideration having a conical shape, enlarging the diameter of the outer tube while keeping the length of the chamber constant [Fasch et al., 2007]. This leads to a total chamber volume of 118 mL. *Figure 6-49* shows the geometry of spray chamber model 1 with the corresponding flow field and impinged droplets in the cut defined by the nebulizer nozzle and the chamber outlet. The droplet distribution of the tertiary aerosol can be seen in *Figure 6-50* for the chamber at 20 °C and 2 °C.

From the results of the simulation it can be derived that both, for the cooled new chamber and the new chamber at room temperature, about 50 % more droplets exit the chamber compared with the Scott-type spray chamber. It is assumed that the new shape of the inner tube is responsible for this effect although the volume of the new chamber is enlarged. With regard to the two different chamber temperatures the development of span and Sauter mean diameters of droplets on their way to the plasma underlie the same

characteristics. Similar to the Scott chamber span values decrease in the first 7 cm downstream. Considering the shape of the droplet size distributions of plane 1 to 4 that are also placed 1, 2, 4 and 7 cm in front of the nebulizer nozzle there is no important difference identifiable. It can be concluded that the secondary aerosol modification process in this region results only in reduction of aerosol volume. After passing plane 4 the width of the droplet size distribution increases from 0.5 to 0.7.

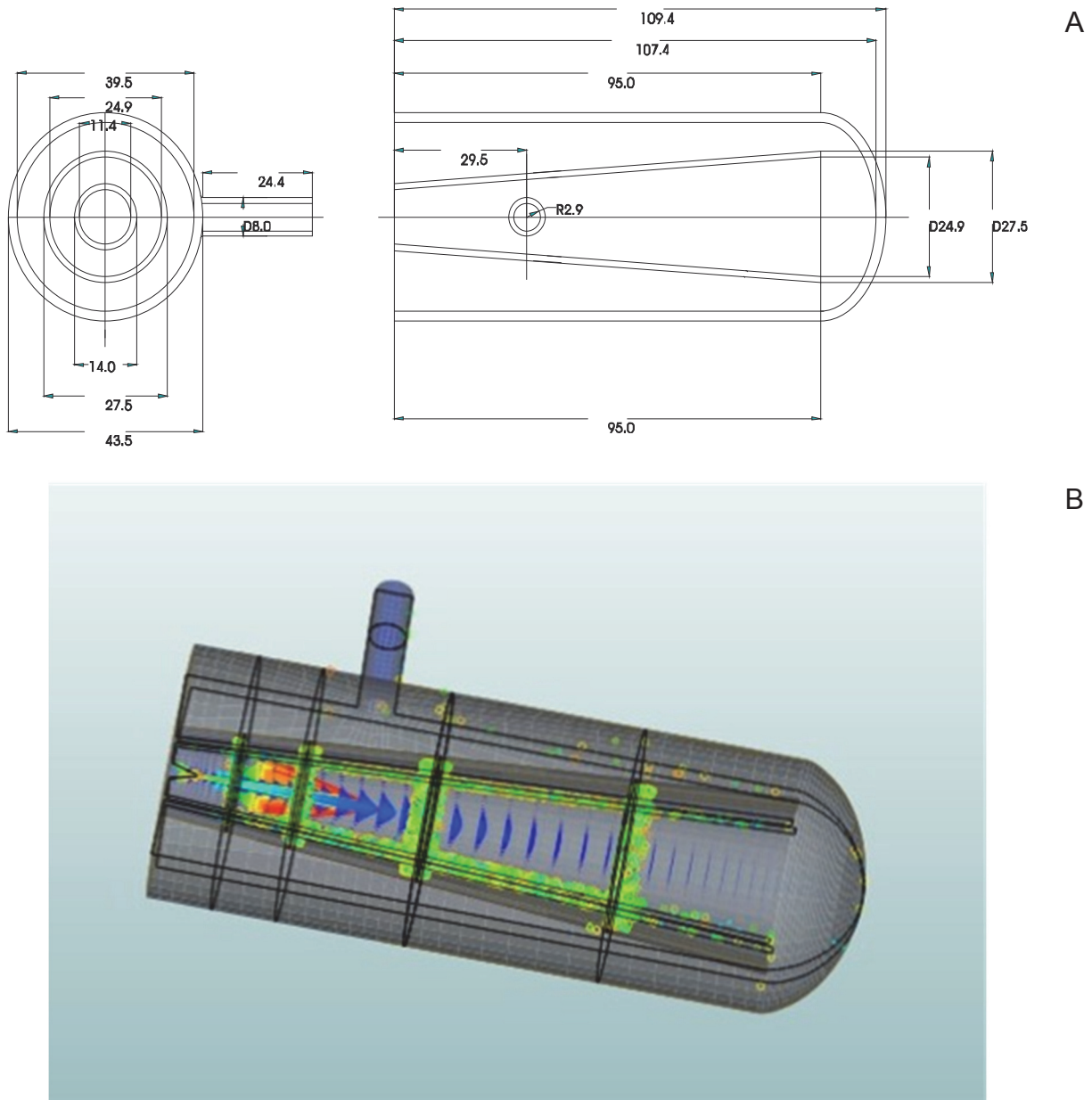


Figure 6-49 Spray chamber model 1: (A) Geometry and dimensions; (B) velocity field and impinged droplets in cut.

At the outlet to the plasma the Sauter mean diameters for the chamber at 20 °C and 2 °C amount to 7.0  $\mu\text{m}$  and 7.1  $\mu\text{m}$ , respectively and are comparable with the Sauter mean diameter of the cooled Scott chamber in *chapter 8.1*. Flow reversal leads to a loss of droplets smaller than 2  $\mu\text{m}$ . The cut-off diameter of the new chamber is 10  $\mu\text{m}$ . Comparing the two different chamber temperatures and their shapes of droplet size distributions at the chamber outlet there are no important differences. It can be concluded that the performance of the new spray chamber is similar if chamber cooling is enabled or the chamber at 20 °C is considered.

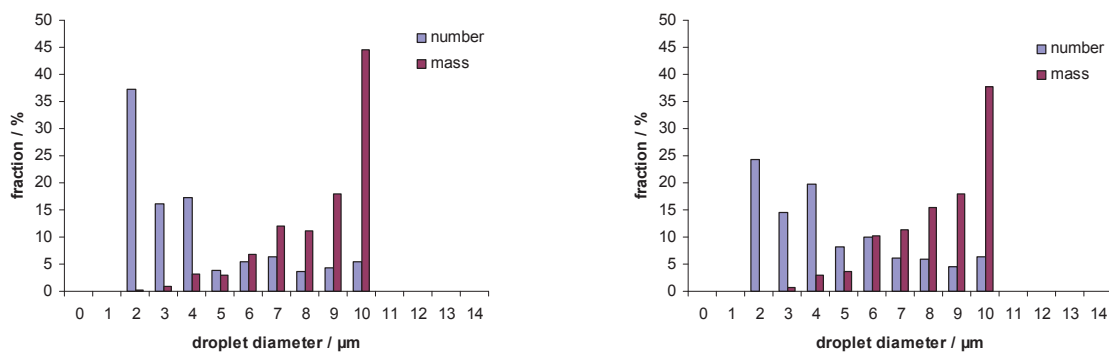


Figure 6-50 Droplet size distribution at the plasma outlet of spray chamber model 1 (spray chamber temperature left side: 20 °C; right side: 2 °C).

### 6.5.2 Spray chamber model 2 and spray chamber model 3

At present several new geometrical variations of the inner tube of the spray chamber are under investigation. Design optimization is made under the aspects of attenuating turbulences originating from the nebulization process, achieving high aerosol transport efficiencies of the small and useful droplets and getting wash-out times as short as possible. Therefore, the new virtual chamber (**spray chamber model 2**) is minimized in a way that it is half the length of the initial chamber. Two holes are introduced concerning the injector area normal to the cut defined by the nebulizer and the exit to the plasma. The idea is to take the gas from the chamber to feed the entrainment process in order to reduce the recirculating bulk flow close to the wall of the inner tube of the spray chamber and to

mobilize the small droplets, which are trapped in the recirculation zone close to the nebulizer tip and the wall boundary layer.

From *Figure 6-51* it can be derived that in the cut normal to the nebulizer and outlet region almost no recirculation occurs. Recirculation still takes place in the cut defined by the nebulizer and the outlet to the plasma.

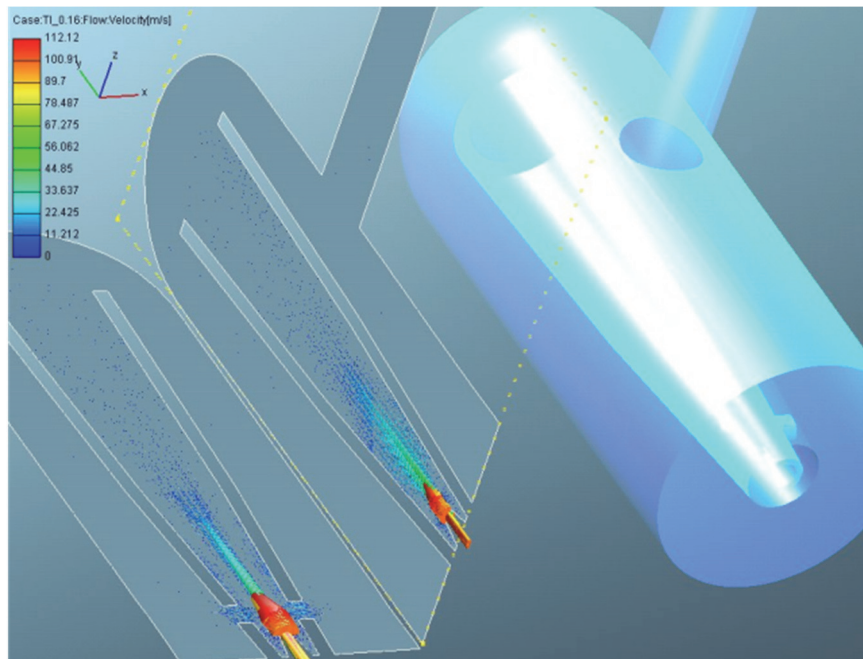


*Figure 6-51* Velocity field of spray chamber model 2.

The second geometrically modified chamber (**spray chamber model 3**) is entirely opened in the injector area which leads to a reduction of recirculation but on the other hand to a “short-circuit” of the overall flow situation (*Figure 6-52*).

From this it can be assumed that small particles will be able to follow the gas stream and rotate in the chamber area but will be incapable to leave the outlet to the plasma. It is planned to simulate the droplet phase to derive the deposition behavior and the mass transport efficiencies of the two potential geometrical modifications of the spray chamber. The next step will be the optimization of the length of the spray chamber and the optimization of the distance of the nebulizer tip and the inner tube of spray chamber 3, which probably leads to an improvement of the overall flow situation. In a future work the results of these simulations will be confirmed experimentally.

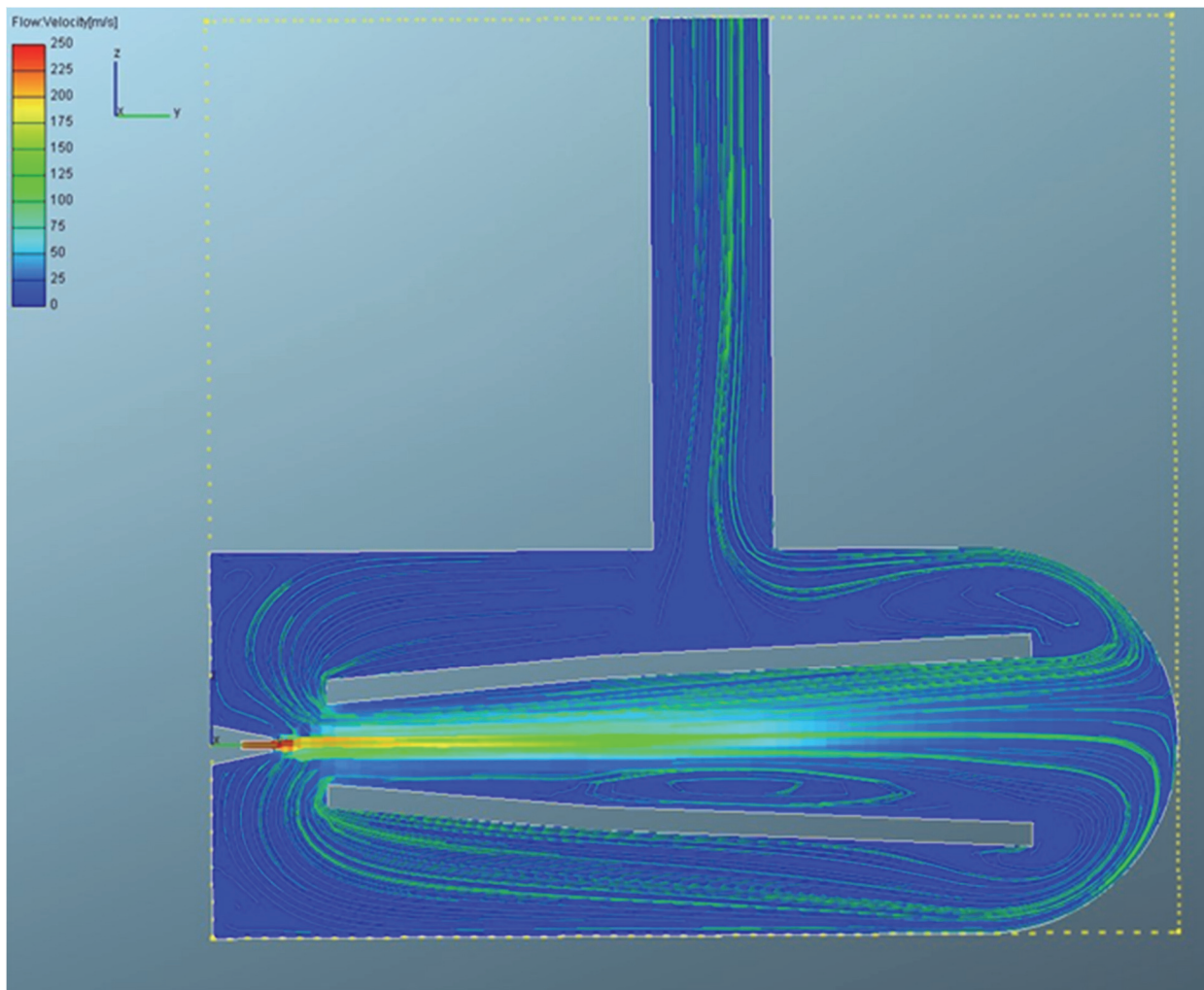


Figure 6-52 Velocity field of spray chamber model 3.

## 7. Conclusive summary and outlook

This thesis primarily describes a numerical approach to simulate the aerosol flow phenomena inside a Scott double-pass spray chamber for ICP-MS using a commercially available CFD code. The spray chamber under consideration was equipped with a micro-uptake glass concentric nebulizer (MicroMist 100 from Glass Expansion). Calculations were carried out at different spray chamber temperatures (at 2 °C and 20 °C). The results of the numerical calculations provide an approximation of the most relevant aerosol transport and modification processes such as fluid flow and turbulence, impacts, gravitational settling, evaporation, decay of turbulence occurring inside the double-pass spray chamber experimentally almost inaccessible [Fasch et al., 2022], [Fasch et al., 2023]. With the aid of CFD calculations, the flow field inside the Scott chamber and the deposition behavior of the droplets could be represented. At different surfaces of the spray chamber, the deposited droplet mass and the respective droplet size distributions could be predicted.

It was shown that a key role in aerosol modification processes could be ascribed to aerosol evaporation. This is mainly due to the fact that low liquid flow rates are used for sample introduction and the nebulizer itself, by design, produces a very fine aerosol.

The simulation also showed that the Scott chamber studied showed excellent performance concerning the separation characteristics as droplets larger than 10  $\mu\text{m}$  were almost completely removed. As already mentioned, the task of a spray chamber is to transport only droplets  $< 10 \mu\text{m}$  into the plasma, as these droplets will be vaporized completely, which in turn increases the quality of the analytical signal.

However, the tendency was confirmed that in contrast to the amount of liquid injected, only a small proportion of droplets could reach the plasma. The numerical analysis indicates that spray chamber cooling enhances the performance of the sample introduction system by reducing the solvent load on the plasma when different conditions in the spray chamber are taken into account. [Fasch et al., 2022], [Fasch et al., 2023].

To validate the numerical model, the mass transport efficiency was determined experimentally and the droplet size distribution of the tertiary aerosol was measured by laser diffraction at different spray chamber temperatures. Similarly, the velocity profile at the plasma outlet of the Scott chamber was determined experimentally using the PIV method.



A comparison with the numerically calculated values showed satisfactory agreement. It can be concluded that CFD can be used to predict the performance of spray chambers.

Measurements of the analyte transport indicate that the mass of the transported solvent increases as the spray chamber temperature rises, which increases the solvent load on the plasma. However, the mass of the analyte does not necessarily increase to the same extent and remains basically the same in the temperature range (2 °C to 40 °C) studied [Fasch et al., 2022], [Fasch et al., 2023].

In conclusion, it can be stated that due to the comparability of the experimental results with those calculated from the numerical simulation, CFD represents a suitable tool to realistically represent the flow conditions in spray chambers. Thus, the present work shows that numerical flow simulations can make important predictions about the performance of a sample introduction system for plasma mass spectrometry. The major advantage of this approach is that it can support optimization of sample introduction in advance, which can provide guidance for the production and testing of prototypes.

## 8. Appendices

### 8.1 Appendix A: Numerical simulations – FIRE™ v7.3

FIRE™ v7.3 (AVL LIST GMBH, Graz, Austria), is used for the following numerical simulation of the dynamics of the argon flow and the droplet phase inside the Scott-type double-pass spray chamber. The model presented below serves as the basis for the improved model of the Scott spray chamber discussed in *chapter 6.4*.

#### 8.1.1 Numerical simulation and boundary conditions

The inlet boundary condition for the numerical simulation of the Scott-type spray chamber is defined by the nebulizer itself. It represents a nozzle where argon as a carrier gas for the sample fluid is injected. Inflow conditions are chosen according to [Sharp, 1988b]. The sample uptake- and the argon flow rate of a micro-uptake glass concentric nebulizer (MicroMist 100, Glass Expansion Pty. Ltd., Melbourne, Australia) is set to 110  $\mu\text{L}/\text{min}$  and 0.80 L/min, respectively. The nebulizer has a nozzle diameter of 271  $\mu\text{m}$ . At the waste outlet negligible outflow of gas is assumed and the so-called wall boundary condition is used. The chamber outlet to the plasma is defined by the zero gradient condition for the pressure. Wall temperature for all wall boundaries generally are specified to be 275.15 K when chamber cooling is investigated or 293.15 K for the simulation at room temperature.

*Figure 8-1* shows the droplet size distribution of the MicroMist 100 measured 10 mm from the nebulizer tip used as input parameter for the simulation (see also *chapter 6.3.1*). Droplets starting from a state of rest cause numerical problems since their distance of acceleration by the gas flow from zero to their maximum velocity is very short (approximately 1 mm [Sharp, 1988b]). This involves production of high momentum sources in computational mesh cells close to the nozzle and causes non-monotonic and slow convergence behavior in case of coupled calculation. For this reason, droplets are provided with a predefined initial velocity. The average initial droplet velocity at the injector exit has been extracted by interpolation and averaging of the values for 1, 10 and 100  $\mu\text{m}$  particles from *Figure 32* in reference [Sharp, 1988b]. After a time period when argon passes through the entirely chamber and reaches a steady state behavior the spray is initialized and at each time step four droplet parcels are injected. That leads to an overall number

of approximately 50,000 parcels from injection start time to a final steady state gas-droplet flow field. Of all possible effects describing the aerosol modification in the spray chamber turbulent dispersion, gravitational settling, gas phase compressibility and evaporation are taken into account [Fasch et al., 2007]. Droplet coalescence and droplet collision effects are neglected because of the fact that the droplet volume fraction in most areas of the spray chamber is very low hence the probability of such phenomena is also very low [Schaldach et al, 2002a], [Kollau, 1999]. The calculation was done assuming a two-way momentum exchange between the gas and the liquid phase. Therefore, all differential equations for conservation of mass, momentum and energy are solved in every time step when gas and liquid coexist in the chamber.

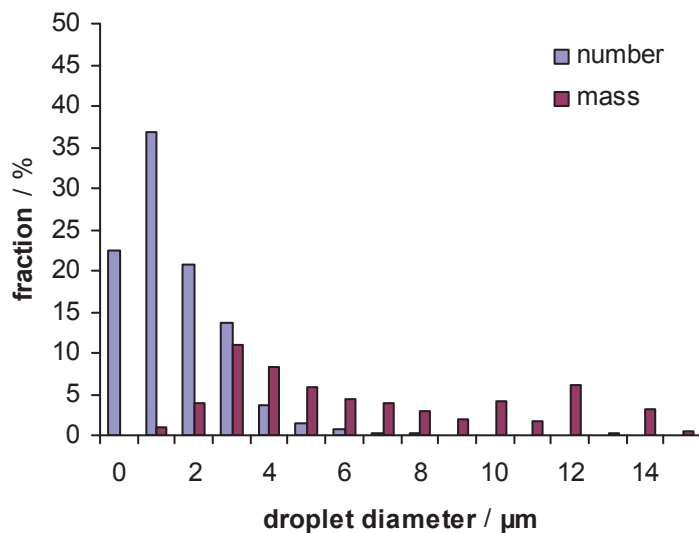


Figure 8-1 Droplet size distribution of the MicroMist 100 measured 10 mm from the nebulizer tip used as input parameter for the simulation.

## 8.1.2 Results and discussion

### 8.1.2.1 Scott-type double-pass spray chamber

A proper volume grid has to be generated for the virtual Scott spray chamber with a volume of roughly 77 mL, which consists of approximately 50,000 cells. An enhanced grid density is used in regions with higher flow variations such as the inflow domain and outlet

region to resolve phenomena at the relevant scale and therefore grid-independent solutions. In the remaining sections, a slightly coarser grid is used, which helps to ensure that the calculation time steps do not have to be too small, thus saving calculation time.

The geometrical dimensions of the chamber under investigation and the volume grid are shown in *Figure 4-15* and *Figure 8-2*, respectively.

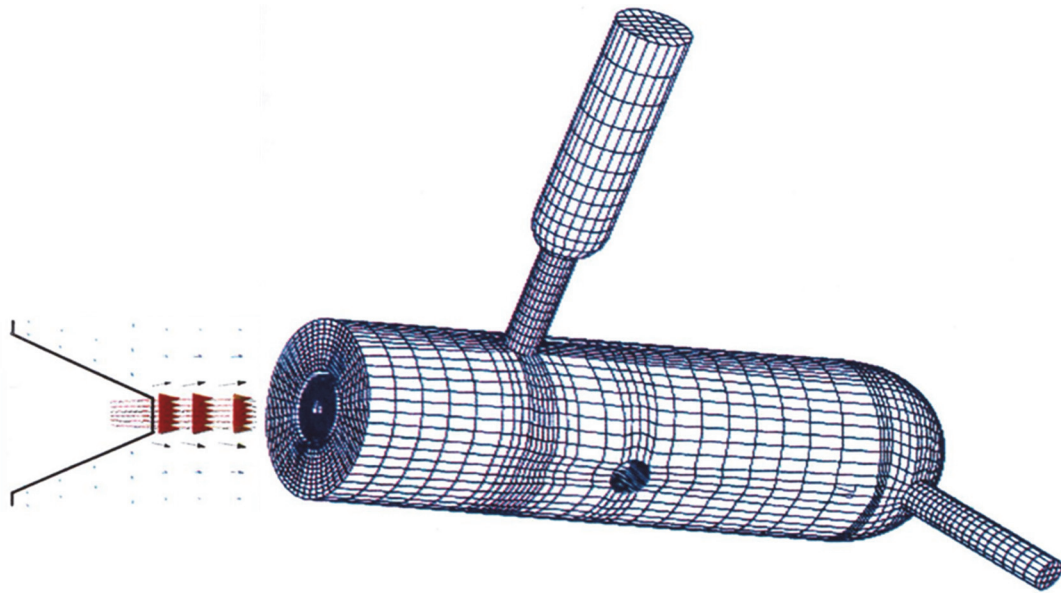


*Figure 8-2* Volume grid of the virtual Scott chamber.

To analyze the secondary aerosol modification process and the particle flow across the outlet boundary on the plasma side a special user function has to be introduced where all droplets crossing predefined planes (i.e., plane 1-4: 1, 2, 4 and 7 cm from the nebulizer tip and plane 5 at the chamber outlet) are collected. Their properties like diameter, velocity, lifetime etc. are written to a result file.

To get a first impression about the conditions and processes inside the Scott chamber *Figure 8-3* demonstrates the velocity field of the steady state gas phase. It can be easily recognized that the overall flow is strongly influenced by the characteristic of an enclosed turbulent free-jet. The turbulence due to the shearing between the nebulizer jet and the relatively static gas outside the free-jet boundary [Sharp, 1988b] creates large eddies in the vicinity of the nebulizer nozzle and along the inner tube of the spray chamber where the majority of the kinetic energy of the turbulent flow is found [Fasch et al., 2023]. In the

recirculation zone close to the nebulizer tip (*Figure 8-4 (a)*) most of the small droplets are trapped and consequently they are unable to leave the chamber.

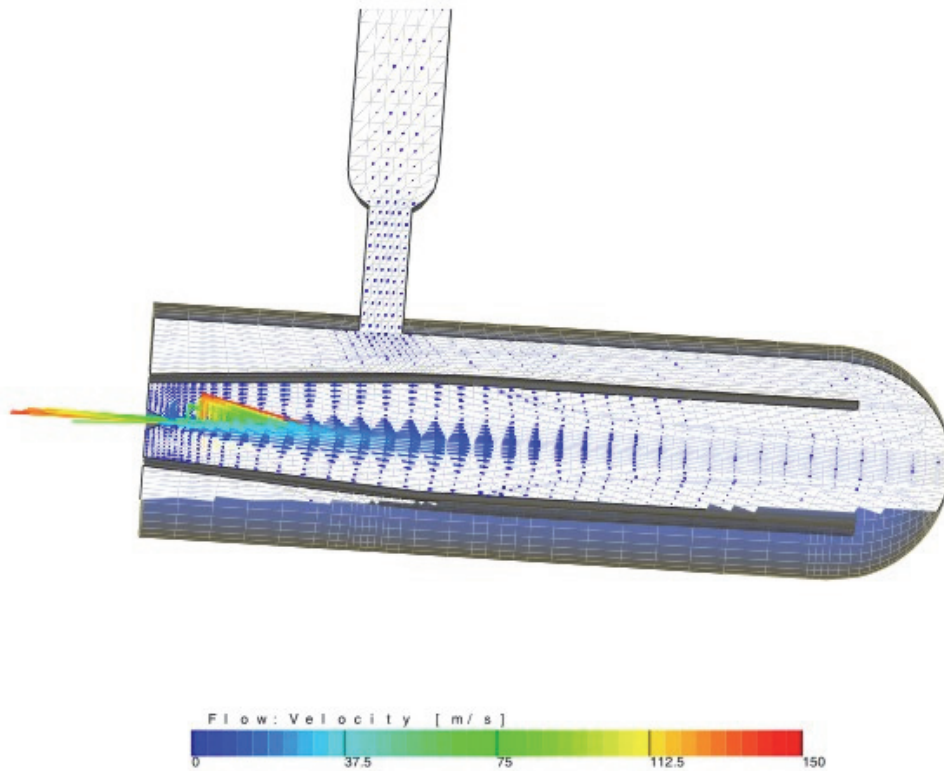


*Figure 8-3 Velocity field in the Scott chamber.*

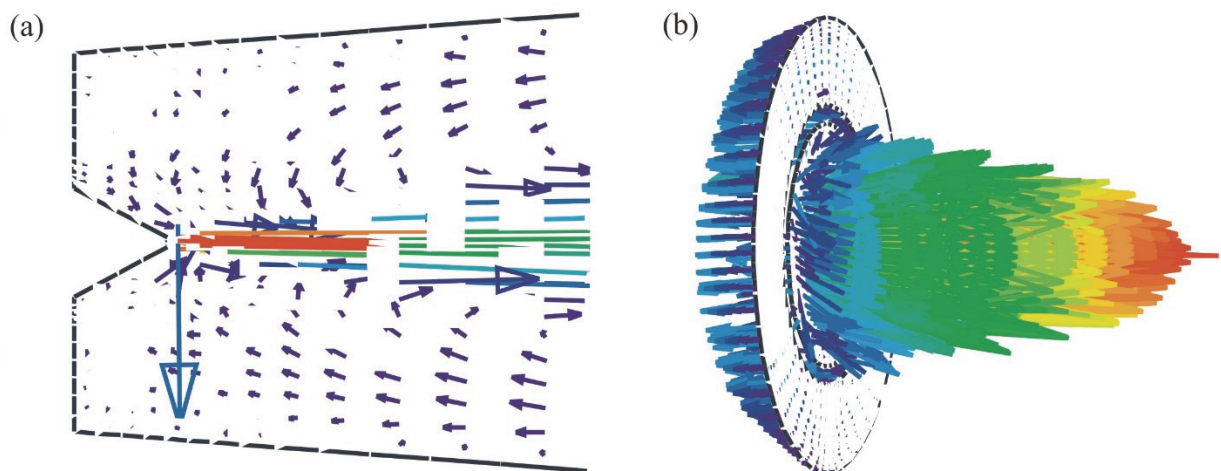


*Figure 8-4 Recirculation; (a) close to the nebulizer tip, (b) 7 cm from the nebulizer tip.*

The majority of the droplets (about 80 % of the introduced mass) are deposited in the first 7 cm on their way through the spray chamber, which can be seen in *Figure 8-5*. The reason for this precipitation behavior can be derived from the flow conditions close to the wall of the inner glass tube of the spray chamber. In this region flow reversal due to recirculation is observed. Droplets are forced to change their directions and impinge on the inner wall area of the chamber. Even at a distance of 7 cm from the nebulizer nozzle, the flow field undergoes considerable recirculation (*Figure 8-4 (b)*). In the last third of the inner tube change of flow state with regard to simultaneous decay of turbulence occurs as is evident in decreasing particle deposition rates. Geometrical dimensions of the Scott chamber are configured in a way that flow - line interception for the removal of large particles takes place. After flow reversal the flow field in the outer glass tube of the chamber becomes completely laminar. The mean velocity of the droplets at the outlet region amounts to  $1 \text{ m s}^{-1}$ .

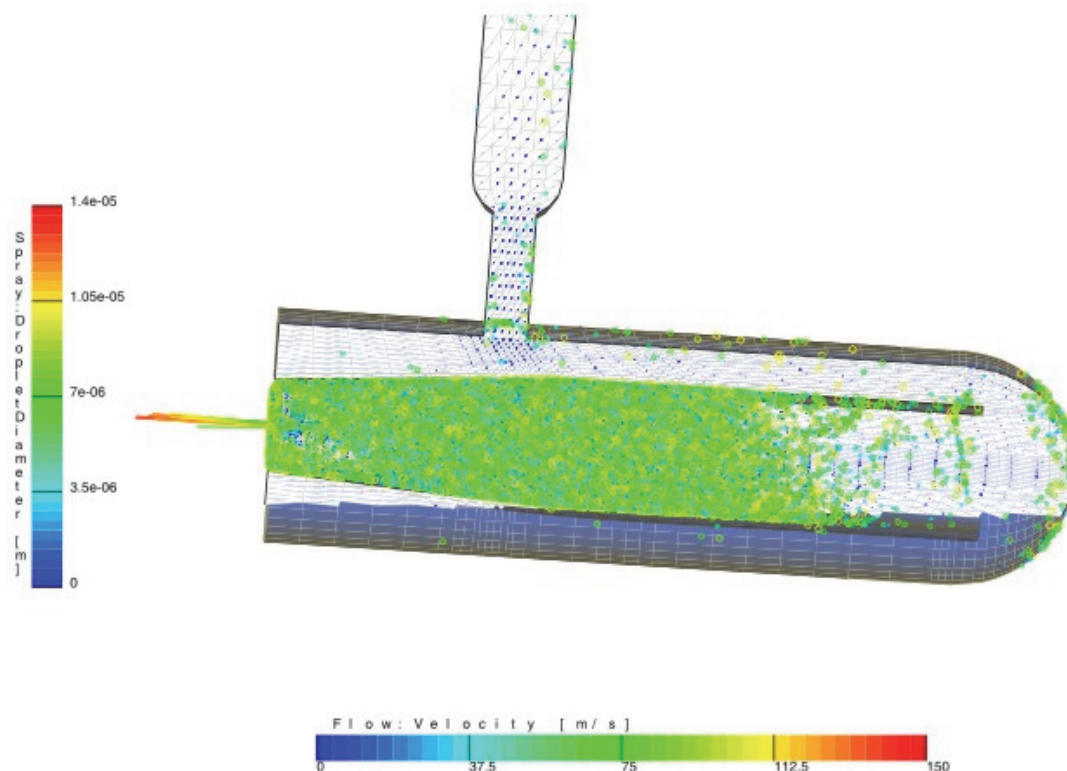


*Figure 8-5 Velocity field and impinged droplets in the Scott spray chamber*

A great advantage of CFD is that one can get information about the secondary aerosol modification processes. In case of the chamber under investigation, *Figure 8-6* shows the development of span on passage, defined as width of a distribution in terms of droplet size (*chapter 3.5.2*). As far as plane 4 for the cooled chamber and plane 3 for the chamber at room temperature droplet size distributions become narrower and afterwards on their way to the chamber outlet an increase in span for both chamber temperatures is observed. It can be concluded that span values at the outlet to the plasma are better for the cooled chamber (0.5) than for the chamber at room temperature (1.2). At 20 °C the Sauter mean diameter  $d_{32}$  amounts to 4.8  $\mu\text{m}$  and for a temperature of 2 °C to 7.5  $\mu\text{m}$  at the chamber outlet. The development of Sauter mean diameters on passage shows similar behavior with respect to the different chamber temperatures. They are slightly increasing downstream and after passing plane 4 they are decreasing again.

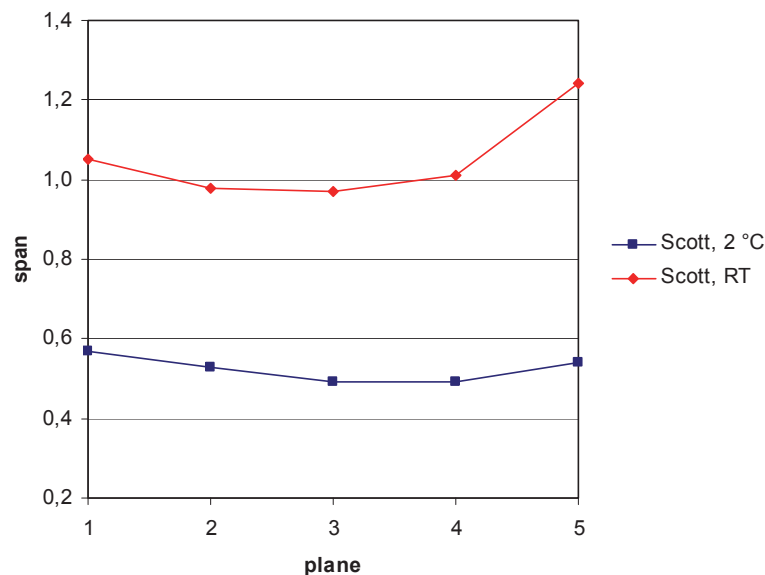


*Figure 8-6* Span values for plane 1-4 (1, 2, 4 and 7 cm from nebulizer nozzle) and plane 5 (outlet).

*Figure 8-7* show the droplet size distributions 7 cm from the nebulizer nozzle at a temperature of 20 °C and 2 °C. For the cooled chamber, they are quite similar to the distributions at the chamber exit (*Figure 8-8, right side*). After flow reversal, size fractionation is observed at room temperature. Droplets with diameters less than 2  $\mu\text{m}$  are removed from the aerosol stream and particle mass is concentrated in droplets having diameters of

9  $\mu\text{m}$  (Figure 8-8, left side). The tertiary aerosol at the chamber outlet obtained by numerical simulation shows both, for the cooled chamber and the chamber at room temperature, nearly the same behavior in droplet deposition. Small droplets ( $< 2 \mu\text{m}$ ) are removed from the aerosol flow especially due to the fact, that enclosed free jets establish recirculating flows to feed the entrainment process [Dukowicz, 1980].

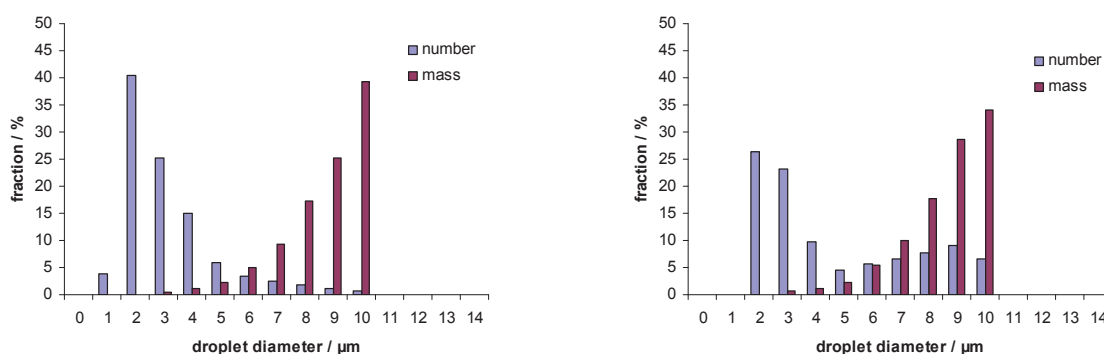


Figure 8-7 Droplet size distribution 7 cm from nebulizer nozzle at different spray chamber temperatures (left side: 20 °C; right side: 2 °C).

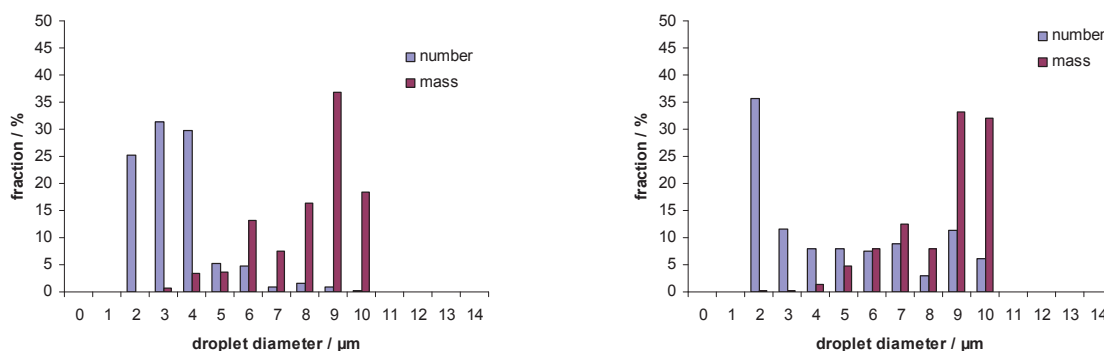


Figure 8-8 Droplet size distribution at spray chamber exit (spray chamber temperature left side: 20 °C; right side: 2 °C).

The maximum number of droplets leaving the cooled spray chamber is in the range of 2 - 3  $\mu\text{m}$  whereas the main mass is concentrated in droplets with diameters from 9 - 10  $\mu\text{m}$ . From the tertiary aerosol of the Scott chamber at room temperature, it can be



---

derived that the main mass of the droplets on their way to the plasma are about 9  $\mu\text{m}$  in diameter. The simulated value of the mass transport efficiency of the droplet (liquid) phase is 0.7 % for the cooled chamber and for the chamber at room temperature.

Similar to reference [Sharp, 1988b] the main reason for the poor mass transport efficiency is that recirculation causes a change in the direction of the bulk flow close to the wall. Hence, most of the aerosol is deposited on the inner tube of the spray chamber [Fasch et al., 2007]. Nevertheless, the combination of a MicroMist nebulizer with a Scott-chamber shows good results for ICP-MS measurements because there are no droplets larger than 10  $\mu\text{m}$ . That means that the whole aerosol entering the plasma should be completely vaporized.

Critically, in attempting to simulate the main physical phenomena in the Scott chamber, the standard evaporation model used in Fire v7.3 did not work. Accordingly, droplet evaporation effects were not taken into account, which could also be an explanation for the fact that the mean Sauter diameters at the chamber exit are too high compared to the experimentally determined values (see *chapter 6.3.2*).

## 8.2 Appendix B: List of figures

FIGURE 2-1 VARIOUS DESIGN PRINCIPLES OF PNEUMATIC NEBULIZERS. A: CONVENTIONAL CONCENTRIC NEBULIZER, B: CONCENTRIC NEBULIZER WITH RECESSED CAPILLARY, C: PARALLEL-PATH NEBULIZER (ALSO REFERRED TO BURGNER NEBULIZER), D: CROSS-FLOW NEBULIZER, E: V-GROOVE NEBULIZER, F: FLOW-FOCUSSING/BLURRING NEBULIZER. REPRODUCED FROM [BINGS ET AL., 2014] BY COURTESY OF ELSEVIER. .... 6

FIGURE 2-2 MICRO MIST NEBULIZER (GLASS EXPANSION , AUSTRALIA; SOURCE: E. FASCH); SEE ALSO FIGURE 2-1 B. .... 7

FIGURE 2-3 SCOTT SPRAY CHAMBER (AGILENT TECHNOLOGIES, USA; SOURCE: E. FASCH). .... 9

FIGURE 2-4 CYCLONIC SPRAY CHAMBER (AGILENT TECHNOLOGIES, USA; SOURCE: E. FASCH). .... 10

FIGURE 2-5 RELATIONSHIP BETWEEN EXPERIMENT AND THEORY – THE ROLE OF CFD..... 12

FIGURE 3-1 PROCESSES WHEN DROPLETS ENTER THE PLASMA (DESOLVATION-VOLATILIZATION-ATOMIZATION). .... 15

FIGURE 3-2 LOGNORMAL COUNT DISTRIBUTION SHOWING THE LOCATION OF SEVERAL DIFFERENT DESCRIPTORS OF A MEAN FOR THE DIAMETERS (REVISED FROM [HINDS, 1999 (P.100)]).THE QUANTITIES ARE CALCULATED USING THE HATCH-CHOATE EQUATIONS [HINDS, 1999 (P. 97)]. .... 22

FIGURE 3-3 SCHEME REPRESENTING THE AEROSOL MODIFICATION PROCESSES/ TRANSPORT PHENOMENA INSIDE A SCOTT-TYPE DOUBLE-PASS SPRAY CHAMBER EQUIPPED WITH A CONCENTRIC NEBULIZER. REPRODUCED FROM [TODOLI ET AL., 2008] BY COURTESY OF ELSEVIER. .... 27

FIGURE 4-1 NUMERICAL SIMULATION OF FLUID FLOW. .... 30

FIGURE 4-2 FINITE CONTROL VOLUME APPROACH; LEFT SIDE: EULERIAN SPECIFICATION, RIGHT SIDE: LAGRANGIAN SPECIFICATION (ADAPTED FROM [WENDT, 1992 AND 1996 (P. 17)]). .... 32

FIGURE 4-3 INFINITESIMAL FLUID ELEMENT APPROACH; LEFT SIDE: EULERIAN SPECIFICATION, RIGHT SIDE: LAGRANGIAN SPECIFICATION (ADAPTED FROM [WENDT, 1992 AND 1996 (P. 17)]); .... 33

FIGURE 4-4 REYNOLDS’ EXPERIMENT ON FLUID DYNAMICS IN PIPES: WATER FLOWS DOWN TO BELOW THE GROUND THROUGH A GLASS TUBE. DEPENDING ON THE FLOW VELOCITY, THE NATURE OF THE FLOW IS REPRESENTED BY A DYED WATER JET THAT IS INJECTED IN THE MIDDLE OF THE FLOW. .... 42

FIGURE 4-5 REYNOLDS’ EXPERIMENT ON FLUID DYNAMICS IN PIPES: LAMINAR – TURBULENT TRANSITION; CRITICAL REYNOLDS NUMBER  $\approx$  2300 (ADAPTED FROM [LAURIEN ET AL., 2011 (P. 33)] BY PERMISSION FROM SPRINGER). .... 43

FIGURE 4-6 ENERGY CASCADE: TRANSFER OF ENERGY FROM THE MEAN FLOW VIA THE REYNOLDS STRESSES DOWN A CASCADE OF PROGRESSIVELY SMALLER EDDIES, WHERE THE SMALLEST EDDIES DISSIPATE THE KINETIC ENERGY INTO THERMAL ENERGY. .... 44

FIGURE 4-7 SIMULATION OF TURBULENT FLOWS – CLASSIFICATION SCHEME. .... 45

FIGURE 4-8 STATISTICAL TURBULENCE MODELS – CLASSIFICATION SCHEME..... 47

FIGURE 4-9 BREAKUP REGIMES IN A CYLINDRICAL JET. (TOP) STABILITY CURVE, (BOTTOM) VISUALIZATION OF BREAKUP REGIMES (FROM LEFT TO RIGHT): RAYLEIGH REGIME (B)  $Re_L = 790$ ,  $We_G = 0.06$ ; FIRST WIND-INDUCED REGIME (C)  $Re_L = 5500$ ,  $We_G = 2.7$ ; SECOND WIND-INDUCED REGIME (D)  $Re_L = 16500$ ,  $We_G = 24$ ; ATOMIZATION REGIME (E)  $Re_L = 28000$ ,  $We_G = 70$  (REPRODUCED FROM [DUMOUCHEL, 2008] BY COURTESY OF SPRINGER). .... 50

FIGURE 4-10 AIR ASSISTED CYLINDRICAL JET BREAKUP REGIMES: (A) NON-AXISYMMETRIC RAYLEIGH-TYPE REGIME; (B) MEMBRANE-TYPE REGIME; (C) FIBER-TYPE REGIME; (D) FIBER-TYPE REGIME - SUPERPULSATING SUBMODE; (E) DIGITATIONS-TYPE REGIME (REPRODUCED FROM [JADIDI ET AL., 2015] AND [DUMOUCHEL, 2008] BY COURTESY OF SPRINGER-VERLAG)..... 53

FIGURE 4-11 NEWTONIAN SECONDARY BREAKUP MORPHOLOGY (REPRODUCED FROM [GULDENBECHER ET AL., 2009] BY COURTESY OF SPRINGER). ..... 55

FIGURE 4-12 PHYSICAL FORCES ACTING ON AN IMPINGING DROPLET (REPRODUCED FROM [MAHULKAR ET AL, 2015] BY COURTESY OF ELSEVIER). ..... 61

FIGURE 4-13 REGIME MAP FOR SPRAY/ WALL INTERACTION ACCORDING TO KUHNKE [KUHNKE, 2004], [AVL FIRE™ MANUAL – WALLFILM MODULE, 2019 (P. 41)]. ..... 62

FIGURE 4-14 PARTICLE-PARTICLE COLLISION REGIMES. REPRODUCED FROM [KROPOTOVA ET AL., 2021]. ..... 63

FIGURE 4-15 TOP: PHOTO OF THE INVESTIGATED SCOTT SPRAY CHAMBER (SOURCE: E. FASCH); BOTTOM: DIMENSIONS OF THE INVESTIGATED SCOTT-TYPE SPRAY CHAMBER (ALL SIZES IN MM). ..... 73

FIGURE 4-16 VOLUME GRID OF THE VIRTUAL SCOTT CHAMBER. .... 73

FIGURE 4-17 BOUNDARY CONDITIONS FOR THE ARGON GAS FLOW. .... 74

FIGURE 4-18 PHOTO OF THE MICROMIST 100 (TOP) AND THE MICROMIST 100 NEBULIZER NOZZLE (BOTTOM); (SOURCE: E. FASCH). 75

FIGURE 4-19 PRIMARY AEROSOL OF THE MICROMIST 100 NEBULIZER: PHOTO IMAGE (LEFT SIDE); LASER PULSE IMAGE (RIGHT SIDE) (SOURCE: E. FASCH). ..... 78

FIGURE 5-1 DUAL-BEAM PHASE-DOPPLER PARTICLE SIZE ANALYZER (DANTEC MEASUREMENT TECHNOLOGY, MAHWAH, NJ, USA; SOURCE: E. FASCH). ..... 83

FIGURE 5-2 MEASUREMENT PRINCIPLE OF PHASE DOPPLER ANEMOMETRY (PDA) BY COURTESY OF DANTEC DYNAMICS. .... 84

FIGURE 5-3 MEASUREMENT PRINCIPLE OF PARTICLE IMAGING VELOCIMETRY (PIV) BY COURTESY OF DANTEC DYNAMICS. .... 85

FIGURE 5-4 DIFFRACTION PATTERN OF A LARGE PARTICLE (LEFT) AND OF A SMALLER PARTICLE (RIGHT) BY COURTESY OF SYMPATEC (© SYMPATEC GMBH). ..... 86

FIGURE 5-5 TOP: MEASUREMENT PRINCIPLE OF A FRAUNHOFER LASER DIFFRACTION SYSTEM BY COURTESY OF SYMPATEC (© SYMPATEC GMBH); BOTTOM: OPTICAL ARRANGEMENT IN THE EXPERIMENT (SOURCE: E. FASCH). ..... 87

FIGURE 5-6 DETERMINATION OF THE SOLVENT PLASMA LOAD USING THE CONTINUOUS WEIGHING METHOD. .... 90

FIGURE 5-7 EXPERIMENTAL SETUP FOR DETERMINING THE LIQUID UPTAKE RATE. .... 91

FIGURE 5-8 EXPERIMENTAL SETUP OF THE “CONTINUOUS WEIGHING METHOD”. ..... 92

FIGURE 5-9 ISHIKAWA DIAGRAM FOR MASS TRANSPORT MEASUREMENTS ON NEBULIZER SYSTEMS USING THE “CONTINUOUS WEIGHING METHOD”. ..... 93

FIGURE 5-10 FINAL ISHIKAWA DIAGRAM WITH COMBINED REPEATABILITIES FOR MASS TRANSPORT MEASUREMENTS ON NEBULIZER SYSTEMS USING THE “CONTINUOUS WEIGHING METHOD”. ..... 94

FIGURE 5-11 CONTRIBUTIONS (SLOPE OF THE REGRESSION LINE AND MEASUREMENT REPLICATION) TO THE UNCERTAINTY BUDGET OF THE DIFFERENT PARAMETERS ON THE MEASUREMENT OF THE SOLVENT PLASMA LOAD USING THE “CONTINUOUS WEIGHING METHOD”. .. 99

FIGURE 5-12 DETERMINATION OF THE SOLVENT PLASMA LOAD USING THE CONTINUOUS WEIGHING METHOD. .... 102

FIGURE 5-13 CAUSE AND EFFECT DIAGRAM FOR MASS TRANSPORT MEASUREMENTS ON NEBULIZER SYSTEMS USING THE “WASTE COLLECTION METHOD”. ..... 104

FIGURE 5-14 FINAL CAUSE AND EFFECT DIAGRAM WITH COMBINED REPEATABILITIES FOR MASS TRANSPORT MEASUREMENTS ON NEBULIZER SYSTEMS USING THE “WASTE COLLECTION METHOD” ..... 105

FIGURE 5-15 CONTRIBUTIONS (MASS (INLET), MASS (NEBULIZER DRAIN), MEASUREMENT TIME, AND MEASUREMENT REPLICATION) OF THE DIFFERENT PARAMETERS ON THE MEASUREMENT UNCERTAINTY BUDGET OF THE SOLVENT PLASMA LOAD USING THE “WASTE COLLECTION METHOD”.	111
FIGURE 5-16 MEASUREMENT SETUP TO DETERMINE THE ANALYTE TRANSPORT EFFICIENCY USING THE WASTE COLLECTION METHOD (SOURCE: E. FASCH).	115
FIGURE 6-1 EFFECT OF THE LIQUID UPTAKE RATE ( $Q_L$ ) ON MASS TRANSPORT EFFICIENCY AT TWO DIFFERENT SPRAY CHAMBER TEMPERATURES (I.E., 20 °C AND 2 °C) AT A FORCED ARGON FLOW RATE $Q_{AR}$ OF 0.80 L MIN <sup>-1</sup> .	116
FIGURE 6-2 EFFECT OF DIFFERENT SPRAY CHAMBER TEMPERATURES ON MASS TRANSPORT EFFICIENCY (MTE) AT A FORCED ARGON FLOW RATE $Q_{AR}$ OF 0.80 L MIN <sup>-1</sup> AND A LIQUID UPTAKE RATE ( $Q_L$ ) OF 110 μL MIN <sup>-1</sup> .	118
FIGURE 6-3 MASS TRANSPORT EFFICIENCIES (MTE) VS. ANALYTE TRANSPORT EFFICIENCIES (ATE) AND ANALYTE TRANSPORT EFFICIENCIES WITH CRYOGENIC DESOLVATION (ATE CO <sub>2</sub> (s)) AT DIFFERENT SPRAY CHAMBER TEMPERATURES.	119
FIGURE 6-4 MASS TRANSPORT EFFICIENCIES (MTE) VS ANALYTE TRANSPORT EFFICIENCIES (ATE) AT DIFFERENT SPRAY CHAMBER TEMPERATURES [FASCH ET AL., 2023].	120
FIGURE 6-5 ANALYTE TRANSPORT EFFICIENCIES AT DIFFERENT SPRAY CHAMBER TEMPERATURES.	121
FIGURE 6-6 SIGNAL INTENSITY OF STANDARD SOLUTION STD10 AT DIFFERENT SPRAY CHAMBER TEMPERATURES.	122
FIGURE 6-7 PERCENTAGE OF DOUBLY CHARGED IONS AND OXIDE FORMATION AT DIFFERENT SPRAY CHAMBER TEMPERATURES USING STANDARD SOLUTION STD10.	122
FIGURE 6-8 MASS TRANSPORT EFFICIENCIES (MTE) VS ANALYTE TRANSPORT EFFICIENCIES (ATE) WITH CRYOGENIC DESOLVATION AT DIFFERENT SPRAY CHAMBER TEMPERATURES.	123
FIGURE 6-9 SIGNAL INTENSITY OF STANDARD SOLUTION STD10 AT TWO DIFFERENT SPRAY CHAMBER TEMPERATURES, I.E., 20 °C AND 2 °C (WITH AND WITHOUT CRYOGENIC DESOLVATION).	124
FIGURE 6-10 PERCENTAGE OF SOLVENT MASS DEPOSITED IN THE CRYOGENIC TRAP.	125
FIGURE 6-11 ILLUMINATED MEASUREMENT ZONE BY A HIGH-SPEED PIV-LASER Nd: YLF, LDY 303HE (LITRON) AT A NEBULIZER GAS FLOW RATE OF 0.80 L/MIN AND A SOLUTION UPTAKE RATE OF 110 μL/MIN.	126
FIGURE 6-12 VELOCITY PROFILE OF THE MICROMIST NEBULIZER (PIV: $Q_{AR}$ = 0.80 L/MIN; $Q_L$ = 110 μL/MIN).	127
FIGURE 6-13 PIV MEASUREMENT OF THE VELOCITY PROFILES AT VARIOUS DISTANCES (X-POSITIONS) FROM THE NEBULIZER TIP ( $Q_{AR}$ = 0.80 L/MIN; $Q_L$ = 110 μL/MIN).	127
FIGURE 6-14 PDA MEASUREMENT OF THE MEAN DROPLET VELOCITY WEIGHTED OVER THE NUMBER OF INDIVIDUAL DROPLET SIZES ( $Q_{AR}$ = 0.80 L/MIN; $Q_L$ = 110 μL/MIN).	128
FIGURE 6-15 PDA MEASUREMENT OF THE RESULTING DROPLET VELOCITY AS A FUNCTION OF DROPLET SIZE IN VARIOUS DISTANCES FROM THE NEBULIZER ORIFICE ( $Q_{AR}$ = 0.80 L/MIN; $Q_L$ = 110 μL/MIN).	129
FIGURE 6-16 VOLUME - BASED DROPLET SIZE DISTRIBUTION OF THE PRIMARY AEROSOL AT DIFFERENT DISTANCES FROM THE NEBULIZER NOZZLE MEASURED BY LASER DIFFRACTION. (A) DENSITY DISTRIBUTION ( $Q^*_3(LG)$ ) AND (B) CUMULATIVE REPRESENTATION ( $Q_3$ ); ( $Q_{AR}$ = 0.80 L/MIN; $Q_L$ = 110 μL/MIN).	130
FIGURE 6-17 NUMBER AND MASS (VOLUME) - BASED DROPLET SIZE DISTRIBUTION OF THE PRIMARY AEROSOL AT VARIOUS DISTANCES (I.E., 10 MM, 15 MM, 20 MM) FROM THE NEBULIZER ORIFICE MEASURED BY PDA TECHNIQUE. (NOTE: THE TRUNCATED POINT IN THE BOTTOM DIAGRAM HAS A MASS FRACTION OF ABOUT 48 %.)	132

FIGURE 6-18 NUMBER AND MASS (VOLUME) - BASED DROPLET SIZE DISTRIBUTION OF THE PRIMARY AEROSOL AT VARIOUS DISTANCES (I.E., 40 MM, 80 MM) FROM THE NEBULIZER ORIFICE MEASURED BY PDA TECHNIQUE. ....	133
FIGURE 6-19 NUMBER AND MASS (VOLUME) - BASED DROPLET SIZE DISTRIBUTION AND A CUMULATIVE REPRESENTATION OF THE PRIMARY AEROSOL AT A DISTANCE OF 10 MM FROM THE NEBULIZER TIP MEASURED BY PDA TECHNIQUE. ....	134
FIGURE 6-20 CHARACTERISTIC DIAMETERS ( $D_{10}$ AND $D_{32}$ ) OF THE PRIMARY AEROSOL AT VARIOUS DISTANCES FROM THE NEBULIZER TIP MEASURED BY PDA TECHNIQUE. ....	134
FIGURE 6-21 ILLUMINATED MEASUREMENT ZONE OF THE TERTIARY AEROSOL OBTAINED AT THE SPRAY CHAMBER PLASMA OUTLET BY A HIGH-SPEED PIV-LASER ND: YLF, LDY 303HE (LITRON) AT A NEBULIZER GAS FLOW RATE OF 0.80 L/MIN AND A SOLUTION UPTAKE RATE OF 110 $\mu$ L/MIN. ....	136
FIGURE 6-22 IMAGES OF TEMPORALLY DIFFERENT DROPLET CLOUD DENSITIES. THE ACQUISITION OF 10 IMAGES TAKES PLACE WITHIN 9 MS. ....	137
FIGURE 6-23 VELOCITY PROFILE AT THE PLASMA OUTLET OF THE SCOTT CHAMBER AT 2 °C (PIV: $Q_{AR} = 0.80$ L/MIN; $Q_L = 110$ $\mu$ L/MIN). ....	138
FIGURE 6-24 PIV MEASUREMENT OF THE VELOCITY PROFILES AT VARIOUS DISTANCES (X-AXIS: 1-12 MM) FROM THE PLASMA OUTLET OF THE SCOTT CHAMBER AT 2 °C ( $Q_{AR} = 0.80$ L/MIN; $Q_L = 110$ $\mu$ L/MIN). ....	139
FIGURE 6-25 VELOCITY PROFILE AT THE PLASMA OUTLET OF THE SCOTT CHAMBER AT 20 °C (PIV: $Q_{AR} = 0.80$ L/MIN; $Q_L = 110$ $\mu$ L/MIN). ....	140
FIGURE 6-26 PIV MEASUREMENT OF THE VELOCITY PROFILES AT VARIOUS DISTANCES (X-AXIS: 1-12 MM) FROM THE PLASMA OUTLET OF THE SCOTT CHAMBER AT 20 °C ( $Q_{AR} = 0.80$ L/MIN; $Q_L = 110$ $\mu$ L/MIN). ....	140
FIGURE 6-27 VOLUME BASED DROPLET SIZE DISTRIBUTION OF THE PRIMARY AND TERTIARY AEROSOL MEASURED BY LASER DIFFRACTION. (A) DENSITY DISTRIBUTION AND (B) CUMULATIVE REPRESENTATION ( $Q_{AR} = 0.80$ L/MIN; $Q_L = 110$ $\mu$ L/MIN). ....	141
FIGURE 6-28 VELOCITY VECTOR FIELD IN THE PLANES WHICH ARE DEFINED BY THE WASTE OUTLET AND NEBULIZER NOZZLE (UPPER PLANE) AND THE OUTLET AND THE NEBULIZER NOZZLE (LOWER PLANE) OF THE SCOTT SPRAY CHAMBER. ....	143
FIGURE 6-29 VELOCITY VECTOR FIELD NEAR THE NEBULIZER NOZZLE. ....	144
FIGURE 6-30 VELOCITY FIELD IN THE PLANE WHICH IS DEFINED BY THE WASTE OUTLET AND THE NEBULIZER NOZZLE. ....	145
FIGURE 6-31 VELOCITY FIELD (STREAMLINES REPRESENTATION). ....	146
FIGURE 6-32 TURBULENT VELOCITY FIELD IN THE INNER TUBE OF THE SPRAY CHAMBER; LAMINAR FLOW REGIME IN THE OUTER CYLINDER AND AT THE OUTLET OF THE SPRAY CHAMBER [FASCH ET AL., 2023]. ....	146
FIGURE 6-33 PRESSURE FIELD IN THE SCOTT SPRAY CHAMBER (A) AND IN THE INLET REGIME (B). ....	147
FIGURE 6-34 TEMPERATURE DISTRIBUTION IN THE SCOTT SPRAY CHAMBER AT 2 °C (A) AND IN THE INLET REGIME (B). ....	148
FIGURE 6-35 TEMPERATURE DISTRIBUTION IN THE SCOTT SPRAY CHAMBER AT 20 °C (A) AND IN THE INLET REGIME (B). ....	149
FIGURE 6-36 WALL FILM TEMPERATURE OF THE SPRAY CHAMBER AT 2 °C. ....	150
FIGURE 6-37 WALL FILM TEMPERATURE OF THE SPRAY CHAMBER AT 20 °C. ....	151
FIGURE 6-38 WALL FILM THICKNESS (A) AND WALL FILM VELOCITY (B) IN THE SCOTT CHAMBER THERMOSTATTED AT 2 °C. ....	152
FIGURE 6-39 VARIOUS SITUATIONS IN THE SPRAY DOMAIN AFTER INJECTION OF SAMPLE LIQUID BASED ON DROPLET LIFETIME. ....	153
FIGURE 6-40 DEPOSITION OF THE ORIGINALLY GENERATED AEROSOL RELATED TO DIFFERENT AREAS IN THE SPRAY CHAMBER [FASCH ET AL., 2023]. ....	154

FIGURE 6-41 PICTURES OF THE INVESTIGATED DOUBLE-PASS GLASS SPRAY CHAMBER TO EVIDENCE THE ZONES OF DROPLET IMPACT, NEBULIZING A METHYLENE RED SOLUTION (SOURCE: E. FASCH) ..... 155

FIGURE 6-42 DROPLET SIZE DISTRIBUTION OF THE PRIMARY AEROSOL MEASURED BY THE PDA METHOD AT A DISTANCE OF 10 MM FROM THE NEBULIZER TIP. .... 156

FIGURE 6-43 CALCULATED VOLUME (MASS) – BASED DROPLET SIZE DISTRIBUTIONS OF THE AEROSOL DEPOSITED ON VARIOUS SURFACES OF THE SCOTT CHAMBER AT 2° C. .... 157

FIGURE 6-44 CALCULATED VOLUME (MASS) – BASED DROPLET SIZE DISTRIBUTIONS OF THE AEROSOL DEPOSITED ON VARIOUS SURFACES OF THE SCOTT CHAMBER AT 20° C. .... 158

FIGURE 6-45 CALCULATED VOLUME (MASS) - BASED DROPLET SIZE DISTRIBUTIONS OF THE AEROSOL LEAVING THE SCOTT CHAMBER (TERTIARY AEROSOL) AT 2 °C. .... 162

FIGURE 6-46 CALCULATED VOLUME (MASS) - BASED DROPLET SIZE DISTRIBUTIONS OF THE AEROSOL LEAVING THE SCOTT CHAMBER (TERTIARY AEROSOL) AT 20 °C. .... 162

FIGURE 6-47 CALCULATED VELOCITY DISTRIBUTION OF THE DROPLETS AT THE PLASMA OUTLET OF THE SCOTT CHAMBER AT 2 °C..... 163

FIGURE 6-48 CALCULATED DROPLET LIFETIME (A) AND DROPLET RELAXATION TIME (B) AT THE PLASMA OUTLET OF THE SCOTT CHAMBER AT 2 °C..... 164

FIGURE 6-49 SPRAY CHAMBER MODEL 1: (A) GEOMETRY AND DIMENSIONS; (B) VELOCITY FIELD AND IMPINGED DROPLETS IN CUT. .... 167

FIGURE 6-50 DROPLET SIZE DISTRIBUTION AT THE PLASMA OUTLET OF SPRAY CHAMBER MODEL 1 (SPRAY CHAMBER TEMPERATURE LEFT SIDE: 20 °C; RIGHT SIDE: 2 °C)..... 168

FIGURE 6-51 VELOCITY FIELD OF SPRAY CHAMBER MODEL 2. .... 169

FIGURE 6-52 VELOCITY FIELD OF SPRAY CHAMBER MODEL 3. .... 170

FIGURE 8-1 DROPLET SIZE DISTRIBUTION OF THE MICROMIST 100 MEASURED 10 MM FROM THE NEBULIZER TIP USED AS INPUT PARAMETER FOR THE SIMULATION..... 174

FIGURE 8-2 VOLUME GRID OF THE VIRTUAL SCOTT CHAMBER. .... 175

FIGURE 8-3 VELOCITY FIELD IN THE SCOTT CHAMBER. .... 176

FIGURE 8-4 RECIRCULATION; (A) CLOSE TO THE NEBULIZER TIP, (B) 7 CM FROM THE NEBULIZER TIP. .... 176

FIGURE 8-5 VELOCITY FIELD AND IMPINGED DROPLETS IN THE SCOTT SPRAY CHAMBER..... 177

FIGURE 8-6 SPAN VALUES FOR PLANE 1-4 (1, 2, 4 AND 7 CM FROM NEBULIZER NOZZLE) AND PLANE 5 (OUTLET)..... 178

FIGURE 8-7 DROPLET SIZE DISTRIBUTION 7 CM FROM NEBULIZER NOZZLE AT DIFFERENT SPRAY CHAMBER TEMPERATURES (LEFT SIDE: 20 °C; RIGHT SIDE: 2 °C). .... 179

FIGURE 8-8 DROPLET SIZE DISTRIBUTION AT SPRAY CHAMBER EXIT (SPRAY CHAMBER TEMPERATURE LEFT SIDE: 20 °C; RIGHT SIDE: 2 °C). .... 179

## 9. References

- B. Abramzon and W. A. Sirignano**, *Droplet vaporization model for spray combustion calculations*, Int. J. Heat Mass Transfer., 1989, 32, 9, 1605-1618.
- A. Autrique, A. Bogaerts, H. Lindner, C. C. Garcia, K. Niemax**, *Design analysis of a laser ablation cell for inductively coupled plasma mass spectrometry by numerical simulation*, Spectrochim. Acta Part B, 2008, 63, 257-270.
- AVL**, *AVL FIRE™ Manual – Spray Module*, Graz, 2019.
- AVL**, *AVL FIRE™ Manual - Thin Walls Module*, Graz, 2019].
- AVL**, *AVL FIRE™ Manual – user guide*, Graz, 2019.
- AVL**, *AVL FIRE™ Manual – Wallfilm Module*, Graz, 2019.
- L. C. Bates and J. W. Olesik**, *Effect of sample aerosol transport rate on inductively coupled plasma atomic emission and fluorescence*, J. Anal. At. Spectrom., 1990, 5, 239-247.
- P. Becker, J. Koch, and D. Günther**, *Impact of ablation cell design in LA-ICP-MS quantification*, J. Anal. At. Spectrom., 2022, 37, 1846-1854.
- C. A. Bennett and N. L. Franklin**, *Statistical Analysis in Chemistry and the Chemical Industry*, John Wiley & Sons, Inc., 1967.
- N. H. Bings, J. O. Orlandini von Niessen, J. N. Schaper**, *Liquid sample introduction in inductively coupled plasma atomic emission and mass spectrometry – Critical review*, Spectrochim. Acta Part B, 2014, 100, 14-37.
- D. Bleiner, A. Bogaerts**, *Computer simulations of sample chambers for laser ablation-inductively coupled plasma spectrometry*, Spectrochim. Acta Part B, 2007, 62, 155-168.
- A. W. Boorn, M. S. Cresser and R. F. Browner**, *Evaporation Characteristics of organic solvent aerosols used in analytical atomic spectrometry*, Spectrochim Acta Part B, 1980, 35, 823-832.
- A. W. Boorn and R. F. Browner**, *Effects of Organic Solvents in Inductively Coupled Plasma Atomic Emission Spectrometry*, Anal. Chem., 1982, 54, 1402-1410.
- R. F. Browner and A. W. Boorn**, *Sample introduction: The Achilles' Heel of atomic spectroscopy*, Anal. Chem., 1984, 56, 786A-798A.

- C.T. Crowe, J.D. Schwarzkopf, M. Sommerfeld, Y. Tsuji**, *Multiphase Flows with Drop-lets and Particles, Second Edition*, CRC Press Taylor Francis Group Boca Raton London New York, 2012.
- L. G. Dodge**, *Representation of average drop sizes in sprays*, J. Propulsion, 1988, 4, 6,490-496.
- J. K. Dukowicz**, *Quasi-steady droplet change in the presence of convection, informal report*, Los Alamos Scientific Laboratory, LA-7997-MS, 1979.
- J. K. Dukowicz**, *A particle-fluid numerical model for liquid sprays*, J. Comput. Phys., 1980, 35, 229-253.
- C. Dumouchel**, *On the experimental investigation on primary atomization of liquid streams*, Exp Fluids, 2008, 45, 371-422.
- Eurachem/ Citac Guide CG 4**, *Quantifying uncertainty in analytical measurement*, 3<sup>rd</sup> edition, 2012.
- E. Fasch, H. Maier, F. Landertshamer, C. Weiß, T. Prohaska, W. Wegscheider**, *Critical comparison of experimental and computational fluid dynamic results for a sample introduction system in plasma spectrometry*, 19<sup>th</sup> European Winter Conference on Plasma Spectrochemistry, Ljubljana, Slovenia, January 29<sup>th</sup>-February 3<sup>rd</sup> 2023, Book of Abstracts, 2023, 293.
- E. Fasch, H. Maier, F. Landertshamer, C. Weiß, T. Prohaska, W. Wegscheider**, *Characterization of a sample introduction system for plasma spectrometry by computational fluid dynamics*, 28<sup>th</sup> ICP-MS Anwender\*innentreffen 2022, Montanuniversität Leoben, Austria, September 5-8 2022, Book of Abstracts, 2022, 50.
- E. Fasch, F. Landertshamer, W. Wegscheider**, *Computational fluid dynamic results for several (new) spray chambers in ICPMS*, 2007 European Winter Conference on Plasma Spectrochemistry, Taormina, Italy, 18-23 February 2007, Book of Abstracts, 2007.
- J.H. Ferziger, M. Perić**, *Computational Methods for Fluid Dynamics, Third, rev. Edition*, Springer, Berlin Heidelberg New York, 2002.
- K. Gandhi, N. Sharma, P. B. Gautam, R. Sharma, B. Mann, and V. Pandey**, *Atomic Absorption Spectroscopy and Flame Photometry. In: Advanced Analytical Techniques in Dairy Chemistry*, Springer Protocols Handbooks. Springer, New York, NY, 2022.



- Guide to the Expression of Uncertainty in Measurement**, JCGM GUM-6, 2020.
- D. R. Guildenbecher, C. López-Rivera, and P. E. Sojka**, *Secondary atomization*, *Exp Fluids*, 2009, 46, 371-402.
- A. Gustavsson**, *Comparison of an indirect and a direct method for measuring the efficiency of nebulizer systems*, *Spectrochim. Acta Part B*, 1986, 41, 291-294.
- K. Hanjalić, M. Popovac, and M. Hadžiabdić**, *A robust near-wall elliptic-relaxation eddy-viscosity turbulence model for CFD*, *Int. J. Heat and Fluid Flow*, 2004, 25, 1047-1051.
- J. Hartung, B. Elpelt, and K.-H. Klösener**, *Statistik*, 7. Auflage, R. Oldenbourg Verlag München Wien, 1989.
- H. Herwig**, *Strömungsmechanik: Eine Einführung in die Physik und die mathematische Modellierung von Strömungen*, Springer, Berlin-Heidelberg New York, 2002.
- H. Herwig**, *Strömungsmechanik A-Z*, Friedr. Vieweg & Sohn Verlag/ GWV Fachverlage GmbH, Wiesbaden, 2004.
- W. C. Hinds**, *Aerosol Technology: Properties, Behavior, and Measurement of Airborne Particles*, Second Edition, John Wiley & Sons Inc., New York/ Chichester/ Weinheim/ Brisbane/ Singapore/ Toronto, 1999.
- S. E. Hobbs and J. W. Olesik**, *Effect of desolvating droplets and vaporizing particles on ionization and excitation in argon inductively coupled plasmas*, *Spectrochim. Acta Part B*, 1993, 48, 817-833.
- J. A. Horner and G. M. Hieftje**, *Computerized simulation of mixed-solute-particle vaporization in an inductively coupled plasma*, *Spectrochim. Acta Part B*, 1998, 53, 1235-1259.
- R. S. Houk and J. J. Thompson**, *Inductively coupled plasma mass spectrometry*, *Mass Spectrometry Reviews*, 1988, 7, 425-461.
- M. Jadidi, S. Moghtadernejad and A. Dolatabadi**, *A comprehensive review on fluid dynamics and transport of suspension/liquid droplets and particles in High-Velocity Oxygen-Fuel (HVOF) thermal spray*, *Coatings*, 2015, 5, 576-645.
- K. E. Jarvis, A.L. Gray, and R. S. Houk**, *Handbook of Inductively Coupled Plasma Mass Spectrometry*, Blackie Academic & Professional, an imprint of Chapman & Hall, London Weinheim New York Tokyo Melbourne Madras, 1992.

- I. Kataoka, M. Ishii, K. Mishima**, *Generation and size distribution of droplet in annular two-phase flow*, J. Fluids Eng., 1983, 105, 230-238.
- M. Kmecova, O. Sikula, M. Krajcik**, *Circular free jets: CFD simulation with various turbulence models and their comparison with theoretical solutions*, IOP Conf. Series: Materials Science and Engineering, 2019, 471.
- J. Koch, G. Schaldach, H. Berndt, and K. Niemax**, *Numerical simulation of aerosol transport in atomic spectrometry: computer simulations of spray chambers and aerosol transport can improve the analytical figures of merit in laser ablation ICPMS*, Anal. Chem., 2004, 76, 7, 130 A-136 A.
- R. Kollau**, *Diploma Thesis*, University of Leoben, Leoben, Austria, 1999.
- G. Kreuning and F. J. M. J. Maessen**, *Organic solvent load of inductively coupled argon plasmas as a function of the liquid uptake rate and the inner gas flow rate*, Spectrochim. Acta Part B, 1987, 42, 677-688.
- G. Kreuning and F. J. M. J. Maessen**, *Effects of the solvent plasma load of various solvents on the excitation conditions in medium power inductively coupled plasmas*, Spectrochim. Acta Part B, 44, 1989, 367-384.
- S. Kropotova and P. Strizhak**, *Collisions of liquid droplets in a gaseous medium under conditions of intense phase transformations: review*, Energies, 2021,14 , 6150-6176.
- D. Kuhnke**, *Spray wall interaction modelling by dimensionless data analysis*, Dissertation, Technische Universität Darmstadt, 2004.
- E. Laurien, H. Oertel jr.**, *Numerische Strömungsmechanik: Grundgleichungen und Modelle - Lösungsmethoden – Qualität und Genauigkeit*, 4. Auflage, Vieweg + Teubner Verlag | Springer Fachmedien Wiesbaden GmbH, 2011.
- S. P. Lin, R.D. Reitz**, *Drop and spray formation from a liquid jet*, Annu. Rev. Fluid Mech., 1998, 30, 85-105.
- C. Liu, C. Liu and Wenxing Ma**, *Rans, detached Eddy simulation and large Eddy simulation of internal Torque converters flows: A comparative study*, Engineering Applications of Computational Fluid Mechanics, 2015, 9, 1, 114-125.
- H. Lomax, T. H. Pulliam, D. W. Zingg**, *Fundamentals of computational fluid dynamics*, Springer-Verlag Berlin Heidelberg New York, 2001.

- S. E. Long and R. F. Browner**, *Influence of water on conditions in the inductively coupled argon plasma*, Spectrochim. Acta, Part B, 1988, 43, 12, 1461-1471.
- F. J. M. J. Maessen, P. J. H. Seeverens and G. Kreuning**, *Analytical aspects of organic solvent load reduction in normal power ICPs by aerosol thermostating at low temperatures*, Spectrochim. Acta Part B, 1984, 39, 1171-1180.
- F. J. M. J. Maessen, G. Kreuning and J. Balke**, *Experimental control of the solvent load of inductively coupled argon plasmas and effects of the chloroform plasma load on their analytical performance*, Spectrochim. Acta Part B, 1986, 41, 3-25.
- S. Maestre, J. Mora, J. - L. Todoli**, *Studies about the origin of the non-spectroscopic interferences caused by sodium and calcium in inductively coupled plasma atomic emission spectrometry. Influence of the spray chamber design*, Spectrochim. Acta Part B, 2002, 57, 1753-1770.
- S. Maher, F. P. M. Jjunju, and S. Taylor**, *Colloquium: 100 years of mass spectrometry: Perspectives and future trends*, Rev. Mod. Phys., 2015, 87, 113.
- A. V. Mahulkar, G. B. Marin, G. J. Heynderickx**, *Droplet-wall interaction upon impingement of heavy hydrocarbon droplets on a heated wall*, Chemical Engineering Science, 2015, 130, 275-289.
- H. Maier**, *Integration der SO<sub>2</sub>-Chemisorption in die numerische 3D-Strömungssimulation von Rauchgaswäschern*, Dissertation, Technische Universität Graz, 2003.
- J. A. McLean, H. Zhang, and A. Montaser**, *A direct injection high-efficiency nebulizer for inductively coupled plasma mass spectrometry*, Anal. Chem., 1998, 70, 1012-1020.
- A. Montaser and D. W. Golightly**, *Inductively coupled plasmas in analytical atomic spectrometry*, VCH Publishers, Inc., 1992.
- A. Montaser (Ed.)**, *Inductively coupled plasma mass spectrometry*, Wiley-VCH, Inc., 1998.
- Nature Milestones in Mass Spectrometry**, Nat. Methods, 2015. Retrieved from [www.nature.com/collections/aaifehieaq](http://www.nature.com/collections/aaifehieaq) (05/2024).
- S. M. Nelms**, *ICP Mass Spectrometry Handbook*, Blackwell Publishing Ltd., Oxford, UK, 2005.

- B. Noll**, *Numerische Strömungsmechanik: Grundlagen*, Springer-Verlag, Berlin Heidelberg, 1993.
- J. W. Olesik and A. W. Moore, Jr.**, *Influence of small amounts of organic solvents in aqueous samples on argon inductively coupled plasma spectrometry*, *Anal. Chem.*, 1990, 62, 840-845.
- J. W. Olesik and J. C. Fister III**, *Incompletely desolvated droplets in argon inductively coupled plasmas: Their number, original size and effects on emission intensities*, *Spectrochim. Acta Part B*, 1991, 46, 851-868.
- J. W. Olesik**, *Investigating the fate of individual sample droplets in inductively coupled plasmas*, *Applied Spectroscopy*, 1997, 51, 5, 158A-175A.
- S. D. Olsen and A. Strasheim**, *Correlation of the analytical signal to the characterized nebulizer spray*, *Spectrochim. Acta Part B*, 1983, 38, 973-975.
- M. Orme**, *Experiments on droplet collisions, bounce, coalescence and disruption*, *Prog. Energy Combust. Sci.*, 1997, 23, 65-79.
- J. Ramos**, *Celebrating 25 years of inductively coupled plasma- mass spectrometry*, *American Laboratory*, 2008, 40, 16, 30-34.
- M. Rösslein**, *Messunsicherheit in der analytischen Chemie*, 4. provisorische Auflage (überarbeitet & ergänzte), 13. Januar 2013.
- S. A. Schadel and T. J. Hanratty**, *Interpretation of atomization rates of the liquid film in gas-liquid annular flow*, *Int. J. Multiphase Flow*, 1989, 15, 6, 893-900.
- G. Schaldach, L. Berger, Berndt**, *Proceedings of the International European Winter Conference on Plasma Spectrochemistry*, Pau, France, 1999, 65.
- G. Schaldach, L. Berger, Berndt**, *Proceedings of the International Winter Conference on Plasma Spectrochemistry*, Fort Lauderdale, USA, 2000, (ICP Information NEWSLETTER 25 Special Edition, 2000, 106).
- G. Schaldach, L. Berger, I. Rasilov, H. Berndt**, *Characterization of a double-pass spray chamber for ICP spectrometry by computer simulation (CFD)*, *Spectrochim. Acta, Part B*, 2002a, 57, 1505-1520.

- G. Schaldach, L. Berger, I. Rrazilov, H. Berndt**, *Characterization of a cyclone spray chamber for ICP spectrometry by computer simulation*, J. Anal. At. Spectrom., 2002b, 17, 334-344.
- G. Schaldach, H. Berndt, B. L. Sharp**, *An application of fluid dynamics (CFD) to the characterisation and optimisation of a cyclonic spray chamber for ICP-AES*, J. Anal. At. Spectrom., 2003a, 18, 742-750.
- G. Schaldach, L. Berger, I. Rrazilov, H. Berndt**, *Characterization of a double-pass spray chamber for ICP spectrometry by computer simulation (CFD)*, Spectrochim. Acta, Part B, 2003b, 58, 1807-1819.
- L. Schiller and A. Z. Naumann**, *VDI*, 1933, 77, 318-320.
- H. Schlichting, K. Gersten**, *Grenzschicht-Theorie, 10. überarbeitete Auflage*, Springer-Verlag Berlin Heidelberg, 2006.
- B. E. Schönung**, *Numerische Strömungsmechanik: Inkompressible Strömungen mit komplexen Berandungen*, Springer, Berlin Heidelberg New York London Paris Tokyo Hong Kong Barcelona, 1990.
- R. H. Scott, V. A. Fassel, R. N. Kniseley, and D. E. Nixon**, *Inductively coupled plasma-optical emission analytical spectrometry. A compact facility for trace analysis of solutions*, Anal. Chem., 1974, 46, 75-80.
- B. L. Sharp**, *Pneumatic nebulisers and spray chambers for inductively coupled plasma spectrometry. A review. Part 1. Nebulisers*, J. Anal. At. Spectrom., 1988a, 3, 613-652.
- B. L. Sharp**, *Pneumatic nebulisers and spray chambers for inductively coupled plasma spectrometry. A review. Part 2. Spray chambers*, J. Anal. At. Spectrom., 1988b, 3, 939-963.
- D. D. Smith and R. F. Browner**, *Measurement of aerosol transport efficiency in atomic spectrometry*, Anal. Chem., 1982, 54, 533-537.
- J. Sneddon (Ed.)**, *Sample introduction in atomic spectroscopy*, Elsevier Amsterdam-Oxford-New York-Tokyo, 1990.
- A. M. Sterling, C. A. Sleicher**, *The instability of capillary jets*, J. Fluid Mech., 68, 477-495.

- Y. Q. Tang and C. Trassy**, *Inductively coupled plasma: the role of water in axial excitation temperatures*, Spectrochim. Acta Part B, 1986, 41, 143-150.
- J. J. Thomson**, *Rays of positive electricity, Proceedings of the Royal Society, Bakerian Lecture*, 1913a, 1-20.
- J. J. Thomson**, *Rays of positive electricity and their application to chemical analyses*, Longmans, Green and Co., London, UK, 1913b.
- J. - L. Todoli and J. – M. Mermet**, *Study of matrix effects using an adjustable chamber volume in a torch-integrated sample introduction system (TISIS) in ICP-AES*, J. Anal. At. Spectrom., 2002, 17, 913-921.
- J. - L. Todoli and J. – M. Mermet**, *Sample introduction systems for the analysis of liquid microsamples by ICP-AES and ICP-MS*, Spectrochim. Acta Part B, 2006, 61, 239-283.
- J. - L. Todoli and J. – M. Mermet**, *Liquid Sample Introduction in ICP Spectrometry, A Practical Guide*, Elsevier Amsterdam-Oxford, 2008.
- S. J. M. Van Malderen, A. J. Managh, B. L. Sharp, F. Vanhaecke**, *Recent developments in the design of rapid response cells for laser ablation-inductively coupled plasma-mass spectrometry and their impact on bioimaging applications*, J. Anal. At. Spectrom., 2016, 31, 423-439.
- J.F. Wendt (Ed.)**, *Computational Fluid Dynamics, An Introduction, 2<sup>nd</sup> Edition*, Springer, Berlin Heidelberg, 1992 and 1996.
- D. R. Wiederin, R. S. Houk, R. K. Winge, and A. P. D´Silva**, *Introduction of Organic Solvents into Inductively Coupled Plasmas by Ultrasonic Nebulization with Cryogenic Desolvation*, Anal. Chem., 1990, 62, 1155-1160.
- U. Wieltsch**, *Experimentelle und numerische Untersuchung des zweiphasigen Strömungszustandes in Sprühwäschern*, Dissertation, Technische Universität, 1999.
- G. Wozniak**, *Zerstäubungstechnik: Prinzipien, Verfahren, Geräte*, Springer-Verlag Berlin Heidelberg, 2003.
- G. H. Yeoh and J. Tu**, *Computational techniques for multi-phase flows – Basics and applications*, Elsevier-Butterworth-Heinemann Oxford (UK) Burlington (USA), 2010.